A Unified Framework for Simulating Impact-Induced Detonation of a Combustible Material in an Elasto-Plastic Confiner

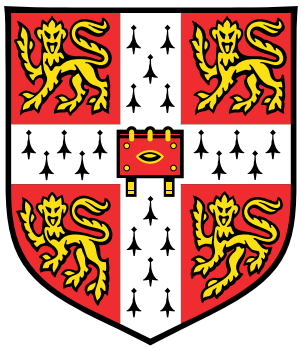

Haran Jackson

The Centre for Scientific Computing

University of Cambridge

This dissertation is submitted for the degree of

Doctor of Philosophy in Scientific Computing

Fitzwilliam College

Supervisor: Dr N. Nikiforakis

Declaration

This thesis is the result of my own work and includes nothing which is the outcome of work done in collaboration except as declared in the preface and specified in the text.

It is not substantially the same as any work that has already been submitted before for any degree or other qualification except as declared in the preface and specified in the text.

It does not exceed the prescribed word limit for the Physics and Chemistry Degree Committee.

Word Count (including abstract, tables, footnotes and appendices): 21,760

Haran Jackson
October 2019

Acknowledgements

I would like to thank my supervisor, Dr Nikos Nikiforakis, for all the help and guidance he has given me. Additionally, I would like to thank Dr Louisa Michael, Geraint Harcombe, Tomé Gouveia, Knut Sverdrup, and Bruno Dog for the many useful discussions we had.

Research Output

The working repository for my PhD project is available at github.com/haranjackson/phd. This contains all the code required to produce the tests presented within this dissertation.

Reviewing

- Journal of Computational Physics
- Czech Science Foundation (GACR) grant application

Publications

- H Jackson, N Nikiforakis, *A unified Eulerian framework for multimaterial continuum mechanics* (Journal of Computational Physics, 2019)
- H Jackson, N Nikiforakis, *A numerical scheme for non-Newtonian fluids and plastic solids under the GPR model* (Journal of Computational Physics, 2019)
- H Jackson, *The Montecinos-Balsara ADER-FV polynomial basis: convergence properties & extension to non-conservative multidimensional systems* (Computers & Fluids, 2018)
- H Jackson, *A fast numerical scheme for the Godunov-Peshkov-Romenski model of continuum mechanics* (Journal of Computational Physics, 2017)
- H Jackson, *On the eigenvalues of the ADER-WENO Galerkin predictor* (Journal of Computational Physics, 2017)

Conference Presentations

- International Conference on Computational Science 2017 (Zürich, CH), *Paper: A fast numerical scheme for the Godunov-Peshkov-Romenski model of continuum mechanics*

- SIAM International Conference on Numerical Combustion 2017 (Orlando, FL), *Mini-symposium: A new approach for cookoff modeling*
- Scientific Computation in the University of Cambridge Seminar Day 2017 (Cambridge, UK), *Poster: A numerical method based on operator splitting for the GPR model of continuum mechanics*
- Cavendish Graduate Student Conference 2016 (Cambridge, UK), *Poster: A new framework for simulating multimaterial systems and gaseous cookoff*

Open-Source Software

- ADER (pypi.org/project/ADER): The ADER method for solving any (potentially very stiff) hyperbolic system of PDEs
- NewtonKrylov (github.com/haranjackson/NewtonKrylov): A C++ implementation of the Newton-Krylov algorithm, with Python bindings
- LGMRES (github.com/haranjackson/LGMRES): A C++ implementation of the LGMRES algorithm, with Python bindings
- Julia-WENO (github.com/haranjackson/Julia-WENO): An optimized Julia implementation of the WENO reconstruction algorithm, of any order of accuracy
- ProjectionMethod (github.com/haranjackson/ProjectionMethod): A C++ implementation of Chorin's Project Method
- Euler1D (github.com/haranjackson/Euler1D): A few first- and second-order methods for solving the 1D Euler equations, implemented in C++
- LegendreGauss (github.com/haranjackson/LegendreGauss): C++ code to compute the Legendre-Gauss nodes and weights on [-1,1], based on NumPy's leggauss function

Abstract

A Unified Framework for Simulating Impact-Induced Detonation of a Combustible Material in an Elasto-Plastic Confiner

Haran Jackson

A new framework for the computational simulation of problems arising in continuum mechanics is presented. It is unified in the sense that it can describe all three major phases of matter within the same set of equations. It is able to represent inviscid fluids, Newtonian and non-Newtonian viscous fluids, elastic and plastic solids, and reactive species. These materials are presented with a variety of equations of state, and there is a clear methodology for extending the framework to more exotic materials using other constitutive equations. It is capable of accurately modeling interfaces between regions occupied by different phases, and by the vacuum.

The problem of impact-induced detonation in an elastoplastic confiner is one that incorporates the whole range of aforementioned material types, representing a challenge to existing frameworks. This new framework is shown to accurately and efficiently solve this problem.

The framework comprises a modification and extension of the Godunov-Peshkov-Romenski (GPR) model of continuum mechanics, along with a new set of operator-splitting-based numerical solvers to allow for the efficient solution of the problems that it is put to, and a new Riemann ghost fluid method for accurate simulation of material interfaces. In addition to this work, novel mathematical analyses of the structure of the GPR equations - and the numerical methods currently used to solve them - are presented in this study.

This new framework presents a range of benefits: the conceptual work required to implement a computational simulation involving many different components is greatly reduced, saving time and allowing for greater specialization of computational techniques. This has the potential to streamline development of simulation software by reducing the number of different systems of equations that require solvers, and cutting down on the amount of theoretical work required, for example in the treatment of interfaces in multimaterial problems.

Contents

List of Figures

List of Tables

Nomenclature

Roman Symbols

$\boldsymbol{B}$	Matrix of purely non-conservative components of a hyperbolic system of PDEs
$\boldsymbol{F}$	Flux vector
$\boldsymbol{H}$	$\frac{\partial E}{\partial \boldsymbol{J}}$
$\boldsymbol{J}$	Thermal impulse vector
$\boldsymbol{P}$	Vector of primitive variables
$\boldsymbol{Q}$	Vector of conserved variables
$\boldsymbol{q}$	Heat flux vector
$\boldsymbol{S}$	Vector of algebraic source terms
$\boldsymbol{v}$	Velocity
A	Distortion tensor
B_c	Prefactor in Arrhenius reaction kinetics
c_0	Adiabatic speed of sound
c_h	Characteristic velocity of heat waves
c_p	Specific heat capacity at constant pressure
c_s	Characteristic velocity of transverse perturbations
c_v	Specific heat capacity at constant volume
c_t	Coefficient in the thermal impulse contribution to the energy (denoted elsewhere in the literature by α)
E	Total specific energy
e^{ref}	Reference internal energy appearing in the Mie-Gruneisen EOS

E_a	Activation energy of a reactive species
G	Gramian matrix of the distortion tensor
K_0	Reaction rate in discrete ignition temperature reaction kinetics
p	Pressure
p^{ref}	Reference pressure appearing in the Mie-Gruneisen EOS
p_∞	Pressure constant in stiffened gas EOS
Q_c	Energy formed per unit mass of reactant
R_c	Universal gas constant
s	Entropy
T	Temperature
t	Time variable
T^{ref}	Reference temperature appearing in the Mie-Gruneisen EOS
T_i	Ignition temperature in discrete ignition temperature reaction kinetics
x	Space variable

Greek Symbols

α	Constant appearing in the Godunov-Romenski EOS
β	Constant appearing in the Godunov-Romenski EOS
δ	Kronecker delta
γ	Constant appearing in the Godunov-Romenski EOS
γ	Ratio of specific heat capacities, equal to $\frac{c_p}{c_v}$
κ	Thermal conductivity
λ	Concentration of reactive species
μ	Viscosity

ψ $\frac{\partial E}{\partial A}$

ρ Density

ρ_0 Reference density

Σ Total stress tensor

σ Viscous shear stress tensor

θ_1 Positive function controlling the rate of relaxation of the distortion tensor in the GPR model

θ_2 Positive function controlling the rate of relaxation of the thermal impulse vector in the GPR model

τ_1 Strain dissipation time

τ_2 Thermal impulse dissipation time

Other Symbols

$\|\cdot\|$ Euclidean vector norm

$\|\cdot\|_F$ Frobenius matrix norm

Acronyms / Abbreviations

ADER Arbitrary DERivative

ALE Arbitrary-Lagrangian-Eulerian

CG Continuous Galerkin

CJ Chapman-Jouguet

DG Discontinuous Galerkin

EOS Equation of State

FV Finite Volume

GFM Ghost Fluid Method

GPR Godunov-Peshkov-Romenski

RGFM Riemann Ghost Fluid Method

VOF Volume of Fluid

WENO Weighted Essentially Non-Oscillatory

ZND Zel'dovich-Neumann-Doring

Notes

Unless otherwise stated, repeated indices in vector, matrix and tensor quantities are to be summed over. If M is a matrix, then $\boldsymbol{M_i}$ is taken to be the ith column of M (note, not the ith row). MATLAB-style index notation is used, such that $M_{i:j}$ refers to the matrix consisting of the columns $i \ldots j$ of M (including columns i and j). $M_{i:j,m:n}$ refers to the submatrix of M with corners at M_{im} and M_{jn}.

Chapter 0

Introduction

0.1 Background

0.1.1 The Problem at Hand

A common theme over the course of humanity's uncovering of the Laws of Physics has been the unification of mathematical descriptions of formerly apparently-disparate physical phenomena (for example Maxwell's equations in unifying the theories of electromagnetism and optics, or the proposed Grand Unified Theories of the electromagnetic, weak, and strong interactions of the Standard Model). Computational Continuum Mechanics is yet to see ubiquitous adoption of such a unified framework, with separate models used to describe the various states of matter. These models differ not just in terms of the first-principles descriptions they posit for the materials that they purport to describe, but also in their mathematical characteristics. For example, the viscous stress terms in the Navier-Stokes equations are empirically derived, and the resulting system is parabolic in nature. By contrast, the Godunov-Romenski equations of elastoplastic deformation of metals are based on a first-principles description of the microscopic material elements of the continuum, and the model is hyperbolic in nature.

Unified models are not just aesthetically pleasing, but also practically useful. The conceptual work required to implement a computational simulation involving many different components is greatly reduced, saving time and allowing for greater specialization of computational techniques. This has the potential to streamline development of simulation software by reducing the number of different systems of equations that require solvers, and cutting down on the amount of theoretical work required, for example in the treatment of interfaces in multimaterial problems.

As an example for which a unified framework of Continuum Mechanics would be greatly beneficial, we take the problem of impact-induced detonation of a combustible material in an elastoplastic confiner. A graphical representation of this problem is shown in Figure 1 on page 2. A reactive liquid is encased in an elastoplastic solid, which is subjected to a large kinetic impulse upon impact with another solid. This initiates a reaction in the combustible material,

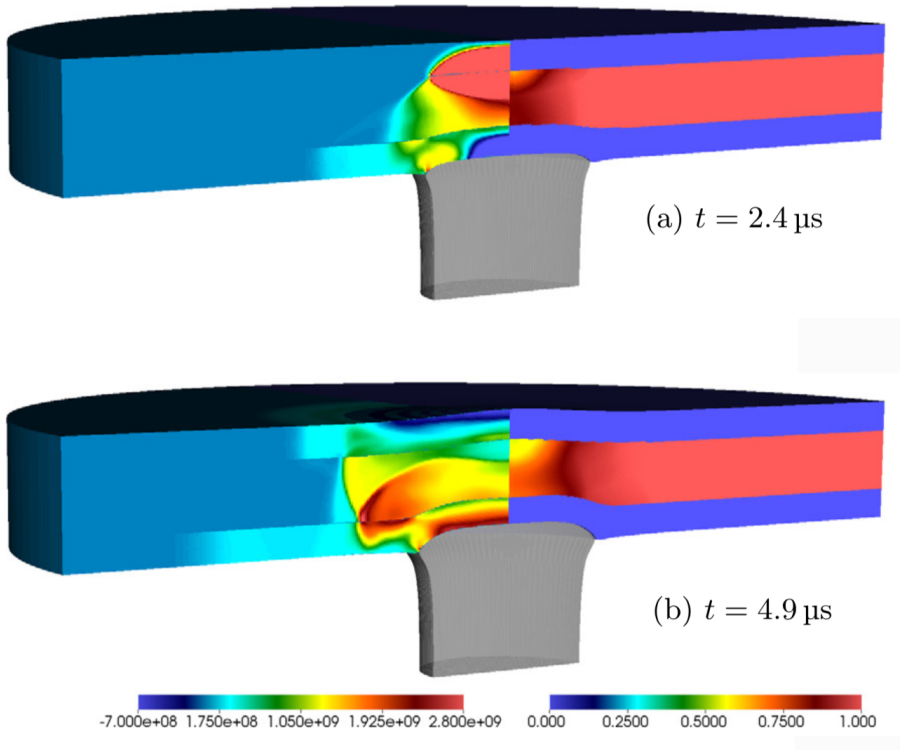

Figure 1: Impact-induced detonation of a combustible material in an elastoplastic confiner, at two different points in time (source: [84])

which propagates throughout the domain, deforming the confiner. As can be seen, three (or possibly four) states of matter are present (a solid confiner, a liquid combustible confined material, and a gaseous/vacuum surrounding environment). Without a unified framework within which to describe this problem, several different sets of equations of motion must be used, with specialized techniques to pass information across the many different inter-material interfaces present.

0.1.2 Review of Current Solutions

The definition of a multiphase system is slightly ambiguous in the literature. Here it will be taken to mean a system consisting of either two or more different materials (possibly in the same phase of matter), or two or more volumes of (possibly the same) material in different phases of matter. There are two aspects of multiphase systems that require attention: multiphase flow, and multiphase heat transfer. The latter becomes important when the phases are at different temperatures. In this study, the different phases will be

assumed to be immiscible. There are many approaches available to solve these problems, broadly including (but not limited to): Lagrangian and Arbitrary-Lagrangian-Eulerian (ALE) methods [27, 119], volume of fluid (VOF) methods [94, 108], diffuse interface methods [118], and level-set methods, including the ghost fluid method (GFM) approach [44, 97].

Without a unified model of continuum mechanics, capable of describing all phases in the same framework, different sets of equations may have to be used in the different regions occupied by different phases. These systems arise, for example, in fluid-structure interaction, or oil-water interfaces. An overview of current approaches to multiphase systems will now be given. The examples here are illustrative but not exhaustive.

There has been a huge amount of research activity in the field over the years, but current approaches can be broadly classified as either monolithic or partitioned [60]. In a monolithic scheme, all phases are described by the same set of nonlinear equations. The evolution of the interfaces is implicit to the equations, unlike in partitioned schemes. See for example [62, 85]. The system is solved by a multivariate Newton-type method. It is often ill-conditioned, due to the different scales of the state variables of the different phases. Thus, iterative solvers are required, proving inefficient unless good preconditioners are available. Codes tend to be very specialized to the specific problems they solve, and it requires expertise to develop and maintain such methods.

In a partitioned scheme, the states of the different phases are calculated separately at each time step, possibly using different models. See Rossi and Onate [114] for a recent overview of some of the common algorithmic features of these schemes. The individual systems do not suffer from the scaling-induced conditioning problems of monolithic schemes, but attention now needs to be payed to the material interfaces. Modeling them can be unstable and relatively computationally expensive (although typically not as expensive as solving the full monolithic systems). One of the great benefits of partitioned schemes is that legacy implementations of common models may be used in the domains occupied by materials that they describe. These implementations are often well-used and relatively bug free, and tend to be written efficiently for the kinds of problems that the solve. As an example of a software suite taking advantage of this, see the Caltech's Virtual Test Facility [2].

Under both types of schemes, the models describing the different phases may be formulated in either a Lagrangian, an Eulerian, or an ALE framework. Solids models tend to come in Lagrangian form, and often these are combined with ALE forms for the fluid phases, so that the fluid meshes may deform to match the deformation of the solid (see, for example, Pin et

al. [107]). These schemes tend to be very accurate, but like all Lagrangian schemes, they fail if the meshes become highly contorted. Thus, adaptive remeshing is often necessary. Some authors have coupled a Lagrangian solid scheme with an Eulerian fluid scheme, but extra care must be taken when applying the boundary conditions to the interface, which corresponds to the intersection of the Eulerian and Lagrangian meshes (see Legay et al. [73] for an implementation using level sets, or Fedkiw [46] for a GFM coupling). Some authors, such as Ryzhakov et al. [115], have found success in using the common Lagrangian formulations for the solid, and a reformulated Lagrangian model for the fluid, implementing the necessary adaptive remeshing. Yet another option is to model both the fluid and the solid in an Eulerian framework, although this now necessitates a level set method or VOF method [59] to track the interfaces. Also, these methods are more prone to losing small-scale geometric features of the media, unless methods such as AMR are employed to combat this [60].

Gavrilyuk, Favrie, et al have presented thermodynamically consistent schemes where solid-fluid interfaces are modeled with the diffuse interface method, with transverse velocities found using a ghost fluid method [43]. The fluid is governed by the compressible Euler equations, and the solid by a conservative hyperelastic model. This was later extended to encompass solids conforming to the viscoplastic model of Maxwell type materials [42], and later still to an arbitrary number of interacting hyperelastic solids and fluids governed by the compressible Euler equations [91].

Michael and Nikiforakis [84] (building on the work of Schoch et al. [120]) couple various Eulerian models of reactive and inert fluids and solids by use of a Riemann Ghost Fluid Method, with the ghost states calculated using specialized mixed-material Riemann solvers for each interaction. Whilst these techniques do not suffer from the mesh contortion issues inherent in Lagrangian formulations of continuum mechanics, and the interface coupling tends to be less computationally expensive than the iterative techniques demanded by monolithic schemes, a fair amount of theoretical work needs to be done to derive analytical relations describing the interactions between every pair of models used.

0.1.3 A New Approach

If it were possible to describe all phases with the same Eulerian model, the method of Michael and Nikiforakis could be used, with only one type of Riemann solver needed to cope with any multiphase problem posed. This would effectively be a partitioned scheme with the same system solved in each domain.

The Godunov-Peshkov-Romenski (GPR) model (proposed in 2014 by Ilya Peshkov and Eugeny Romenski [101]) represents one such opportunity. It is able to describe both fluids and solids within the same mathematical framework. In addition to this, the hyperbolic nature of the GPR model ensures that the nonphysical instantaneous transmission of information appearing in certain non-hyperbolic models (such as the Navier-Stokes equations, or Fourier heat equation) cannot occur. Additionally, the first-principles derivation of the mechanism by which viscous effects appear under the GPR model has been commented on to be more appropriate than the more phenomenological viscous law appearing in the traditional Navier-Stokes formulation (see [102]). Parallelization also tends to be easier with hyperbolic models, allowing us to leverage the great advances that have been made in parallel computing architectures in recent years [1], and the use of the vast array of effective numerical solvers designed for first-order hyperbolic systems (see [126] for an overview). As will be seen, the GPR model also includes terms for heat conduction, which do not appear in the basic formulations of many of the common models used in multiphase systems (e.g. the Euler equations, or the Navier-Stokes equations, or the Godunov-Romenski equations of solid mechanics). Heat conduction is often ignored in multiphase modeling, but such a framework based on the GPR model would almost unavoidably include it.

It is interesting to note that de Brauer et al [19, 26] have presented a method for multimaterial modeling of a similar system, including the distortion tensor of the GPR model (discussed in 0.2.1), but excluding the heat conduction terms. This method is based on level sets, similar to the method presented in this study. It should be noted, however, that de Brauer et al do not apply their method to the modeling of viscous flows.

Any unified model of continuum mechanics purporting to describe all phases of interest must be at least as descriptive as competing models tailored to each individual phase if the utmost model fidelity is required. Although the results for the GPR model applied to standard test cases have been promising, both here and in other preliminary studies [18, 34], more work is required to determine how faithfully the GPR model reproduces common agreed phenomenological results.

Thus far, the GPR model has been solved for a wide array of different fluids (inviscid and viscous Newtonian) and solids (elastic and elastoplastic) (see [18, 35, 99, 102]). It has also been extended to incorporate the effects of electrodynamics (see [36]) and general relativity (see [104]). It is yet to be formally extended to include non-Newtonian power-law fluids, however. Additionally, until this point, it has not been used to model reactive processes, such as those occurring in impact-induced detonation of combustible materials.

The GPR model has been solved solely using the ADER-WENO method ([18, 35]). ADER-WENO methods (described in Section 0.3) are extremely effective in producing arbitrarily-high order solutions to hyperbolic systems of PDEs, but in some situations their accompanying computational cost proves burdensome. Additionally, at present, there is no way of dealing with material interfaces in the GPR model.

0.1.4 Objectives of this Study

The objective of this study is to develop the GPR model in various specific ways so that it may be used to simulate the problem of impact-induced detonation of a combustible material in an elastoplastic confiner (and thus also a range of other multimaterial, multiphase physical processes - including those involving reactive species). The interfaces between these phases and the exchange of state information between them need to be dealt with in any numerical method employed. The GPR model must also be augmented in some way to capture the kinetics of the chemical reactions present. Up until now, ADER-WENO methods have been used to solve the GPR model. Whilst these are able to provide arbitrarily-high-order accuracy solutions in both space and time, they are too slow for the practical applications of the aforementioned type, even at second-order accuracy; faster numerical solvers are needed.

Thus, there are three main objectives to be addressed:

1. To combine the GPR model with the models used to describe the reactions of combustible materials
2. To develop numerical methods for solving the GPR model in a reasonable amount of time
3. To develop stable and accurate techniques to deal with the interfaces between different materials in multimaterial / multiphase problems

The outline of this study is as follows. The GPR model - and the intuition behind its derivation - are covered in 0.2.1. The numerical methods that are currently used to solve this model - and others of a similar mathematical form - are covered in Section 0.3. This includes a discussion of the WENO Method, the Discontinuous and Continuous Galerkin Methods, and the Finite Volume Method that they are applied to.

Objective 1 is addressed in Chapter 1. Analytical work is performed in Section 1.1 to enable the use of a broad set of equations of state with the GPR model (allowing for the simulation of all materials encountered in the impact-induced detonation problem). The GPR model is extended to incorporate reactive species in Section 1.2. These extensions are demonstrated to reproduce accepted numerical results in Section 1.3.

Objective 2 is addressed in Chapter 2. First, in Section 2.1, the recently-proposed improvement on the ADER-WENO method of Montecinos and Balsara [89] is extended to work in multiple dimensions. Next, a second-order operator splitting method for the GPR model is presented in Section 2.2. This method is significantly faster than even the aforementioned modified ADER-WENO method, while retaining a reasonable order of accuracy. For the first time, in 2.2.4, the relaxation mechanism of the GPR model is modified to allow for the simulation of non-Newtonian viscous fluids and elastoplastic solids (as required for the elastoplastic confiner of the impact-induced detonation problem). A second-order operator splitting method is presented for these material classes also. Many numerical tests are given in Section 2.3, to demonstrate both the physical relevance of the modifications made to the GPR model, and the accuracy of the solvers that have been derived. Discussion of the results presented is given in Section 2.4.

Objective 3 is addressed in Chapter 3. An overview of Level Sets and Ghost Fluid Methods is given in Section 3.1. A Riemann Ghost Fluid Method is derived for the GPR model in Section 3.2, for both problems involving both heat conduction and no heat conduction. This method is based on a novel eigenstructure analysis of the GPR model, which is provided in the appendix. A range of multimaterial/multiphase tests are performed in Section 3.3 to demonstrate the suitability of this method in modeling the evolution of interfaces between every possible pairing of material types. A convergence study is also provided. Discussion of the method, its limitations, and potential future improvements are given in Section 3.4.

Chapter 4 is dedicated to combining the ideas developed in the previous three chapters to solve large physical problems that incorporate phenomena necessitating all the analytical and numerical work that has been done. It is demonstrated in this chapter that the solutions to the three objectives stated above are capable of being combined into a cohesive unified continuum mechanics framework. Concluding remarks are made in Chapter 4.2. A discussion of the work produced in this study is given in Section 4.2.1, with discussion of future possible avenues of research given in Section 4.2.2.

Explicit forms of mathematical objects appearing in the GPR model are given in Chapter A.

The fluxes, sources, and non-conservative matrices are given in Section A.1. Jacobians of the conserved and primitive variables, and their fluxes and sources are given in Section A.2. An eigenstructure analysis of the GPR model is performed in Chapter B. First, the primitive system is derived in Section B.1. From this, the eigenvalues (Section B.2) and eigenvectors (Section B.3) are derived, for both the case with heat conduction and without. Parameters pertaining to the various different materials encountered in this study are given in Chapter C. Properties of common materials are given in Section C.1, and equation of state parameters are given in Section C.2.

0.2 Mathematical Model

0.2.1 Equations of Motion

The GPR model, first introduced in Peshkov and Romenski [101] - and expanded upon by Dumbser et al. [35] and Boscheri et al. [18] - takes the following form:

$$\frac{\partial \rho}{\partial t} + \frac{\partial \left(\rho v_k\right)}{\partial x_k} = 0 \tag{1a}$$

$$\frac{\partial \left(\rho v_i\right)}{\partial t} + \frac{\partial \left(\rho v_i v_k + p\delta_{ik} - \sigma_{ik}\right)}{\partial x_k} = 0 \tag{1b}$$

$$\frac{\partial A_{ij}}{\partial t} + \frac{\partial \left(A_{ik} v_k\right)}{\partial x_j} + v_k \left(\frac{\partial A_{ij}}{\partial x_k} - \frac{\partial A_{ik}}{\partial x_j}\right) = -\frac{\psi_{ij}}{\theta_1} \tag{1c}$$

$$\frac{\partial \left(\rho J_i\right)}{\partial t} + \frac{\partial \left(\rho J_i v_k + T\delta_{ik}\right)}{\partial x_k} = -\frac{\rho H_i}{\theta_2} \tag{1d}$$

$$\frac{\partial \left(\rho s\right)}{\partial t} + \frac{\partial \left(\rho s v_k + H_k\right)}{\partial x_k} = \frac{\rho}{T}\left(\frac{\psi_{kl}\psi_{kl}}{\theta_1} + \frac{H_k H_k}{\theta_2}\right) \tag{1e}$$

where ρ is density, $\mathbf{v}$ is velocity, δ is the Kronecker delta, p is pressure, σ is the sheer stress tensor, A is the distortion tensor, $\mathbf{J}$ is the thermal impulse vector, T is temperature, s is the entropy, and $\mathbf{q}$ is heat flux. $\psi = \frac{\partial E}{\partial A}$ and $\boldsymbol{H} = \frac{\partial E}{\partial \boldsymbol{J}}$, and θ_1 and θ_2 are positive functions (given below for the problems at hand).

Entropy does not decrease during the dissipative time evolution:

$$\frac{\partial \left(\rho s\right)}{\partial t} + \frac{\partial \left(\rho s v_k + H_k\right)}{\partial x_k} \geq 0 \tag{2}$$

(1e) can be replaced with the following equation, which will be used instead when solving the model in this study:

$$\frac{\partial\left(\rho E\right)}{\partial t}+\frac{\partial\left(\rho E v_k+\left(p\delta_{ik}-\sigma_{ik}\right)v_i+q_k\right)}{\partial x_k}=0 \tag{3}$$

where E is the total energy. Note that (1a), (1b), (1c), (1d), (3) can be written in the following form:

$$\frac{\partial \boldsymbol{Q}}{\partial t}+\boldsymbol{\nabla}\cdot\boldsymbol{F}+\boldsymbol{B}\cdot\nabla\boldsymbol{Q}=\boldsymbol{S} \tag{4}$$

0.2.2 Relationships between Variables

The following definitions are given:

$$p=\rho^2\left.\frac{\partial E}{\partial\rho}\right|_{s,A} \tag{5a}$$

$$\sigma=-\rho A^T\left.\frac{\partial E}{\partial A}\right|_{\rho,s} \tag{5b}$$

$$T=\left.\frac{\partial E}{\partial s}\right|_{\rho,A} \tag{5c}$$

$$\boldsymbol{q}=T\frac{\partial E}{\partial \boldsymbol{J}} \tag{5d}$$

To close the system, the EOS must be specified, from which the above quantities and the sources can be derived. E is the sum of the contributions of the energies at the molecular scale (microscale), the material element[1] scale (mesoscale), and the flow scale (macroscale):

$$E=E_1\left(\rho,s\right)+E_2\left(\rho,s,A,\boldsymbol{J}\right)+E_3\left(\boldsymbol{v}\right) \tag{6}$$

In previous studies, E_1 has been taken to be one of the following forms:

1. The ideal gas EOS:

$$E_1=\frac{p}{\rho\left(\gamma-1\right)} \tag{7}$$

[1]The concept of a *material element* corresponds to that of a fluid parcel from fluid dynamics, applied to both fluids and solids.

2. The stiffened gas EOS:

$$E_1 = \frac{p + \gamma p_\infty}{\rho\left(\gamma - 1\right)} \tag{8}$$

3. The shock Mie-Gruneisen EOS:

$$E_1 = \frac{p^{ref}}{2}\left(\frac{1}{\rho_0} - \frac{1}{\rho}\right) + \frac{p - p^{ref}}{\Gamma_0 \rho_0} \tag{9}$$

A more general set of choices for E_1 is given in Section 1.1.

Tabulated equations of state are common-place in the field (see [20, 74, 106] for a range of use cases). There is no a priori reason why they cannot be used for E_1 under the framework presented in this study, in the same manner as other hydrodynamic systems (e.g. see [17, 56]). This is out of scope of this study, however, and presents an avenue of future research. Note that E_1, c_s, c_t are permitted to depend upon ρ, p instead of ρ, s (as is the case in this study), or indeed ρ, T if the material requires it (such as materials whose shear modulus depend on temperature).

E_2 has the following quadratic form:

$$E_2 = \frac{c_s\left(\rho, s\right)^2}{4}\left\|\mathrm{dev}\left(G\right)\right\|_F^2 + \frac{c_t\left(\rho, s\right)^2}{2}\left\|\boldsymbol{J}\right\|^2 \tag{10}$$

$\|\cdot\|_F$ is the Frobenius norm[2]. c_s is the characteristic velocity of transverse perturbations. In previous studies, c_s has always been constant. In this study, it will be extended to have a ρ dependence, as outlined in Section 1.1. c_t is related to the characteristic velocity of propagation of heat waves[3]:

$$c_h = \frac{c_t}{\rho}\sqrt{\frac{T}{c_v}} \tag{11}$$

In previous studies, c_t has been taken to be constant, as it will in this study.

[2]The Frobenius norm is defined by: $\|X\|_F = \sqrt{\sum_{i,j}|X_{ij}|^2}$

[3]Dumbser et al [35] denote this variable by α, which is avoided here due to a clash with a parameter of the Godunov-Romenski EOS, used later in the study

$G = A^T A$ is the Gramian matrix of the distortion tensor, and $\operatorname{dev}(G)$ is the deviator (trace-free part) of G:

$$\operatorname{dev}(G) = G - \frac{1}{3}\operatorname{tr}(G)\, I \tag{12}$$

E_3 is the usual specific kinetic energy per unit mass:

$$E_3 = \frac{1}{2}\|\boldsymbol{v}\|^2 \tag{13}$$

The following forms are taken:

$$\theta_1 = \frac{\tau_1 c_s^2}{3\,|A|^{\frac{5}{3}}} \tag{14a}$$

$$\theta_2 = \tau_2 c_t^2 \frac{\rho T_0}{\rho_0 T} \tag{14b}$$

$$\tau_1 = \begin{cases} \frac{6\mu}{\rho_0 c_s^2} & viscous\ fluids \\ \tau_0 \left(\frac{\sigma_0}{\|\operatorname{dev}(\sigma)\|_F}\right)^n & elastoplastic\ solids \end{cases} \tag{15a}$$

$$\tau_2 = \frac{\rho_0 \kappa}{T_0 c_t^2} \tag{15b}$$

where μ is the viscosity and κ is the thermal conductivity. The justification of these choices is that classical Navier–Stokes–Fourier theory is recovered in the stiff limit $\tau_1, \tau_2 \to 0$ (see [35]). The power law for elastoplastic solids is based on the work [12].

Finally, we have the following relations:

$$\sigma = -\rho c_s^2 G \operatorname{dev}(G) \tag{16a}$$

$$\boldsymbol{q} = c_t^2 T \boldsymbol{J} \tag{16b}$$

$$-\frac{\psi}{\theta_1(\tau_1)} = -\frac{3}{\tau_1}|A|^{\frac{5}{3}} A \operatorname{dev}(G) \tag{16c}$$

$$-\frac{\rho \boldsymbol{H}}{\theta_2(\tau_2)} = -\frac{T\rho_0}{T_0 \tau_2}\boldsymbol{J} \tag{16d}$$

The following constraint also holds [101]:

$$\det(A) = \frac{\rho}{\rho_0} \tag{17}$$

0.2.3 Physical Intuition

The GPR model represents the same set of equations as the model of elastoplastic deformation originally proposed by Godunov and Romenski. Peshkov and Romenski were the first to subsequently propose that these are the equations of motion for an arbitrary continuum - not just a solid. In doing so, they were able to apply the model to fluids too. Note that material elements have not only finite size, but also internal structure (encoded in the distortion), unlike in previous continuum models.

The idea of τ_1 - the strain dissipation time - has its roots in Frenkel's "particle settled life time" (see [48]). τ_1 represents a continuous analogue of Frenkel's object. It can be thought of as the characteristic time taken for a particle to move by a distance roughly the same as the particle's size. Thus, the typical time taken for a material element to rearrange with its neighbors is characterized by τ_1 . As long as a continuum description is appropriate for the material at hand, it is thus that the GPR model seeks to describe all three major phases of matter. For example, we have the following relations:

$$\tau_1 = \begin{cases} \infty & elastic\,solids \\ 0 & inviscid\,fluids \end{cases} \tag{18}$$

The equation governing $\boldsymbol{J}$ - and its contribution to the system's total energy - are derived from Romenski's model of hyperbolic heat transfer, (see [81, 113]). These concepts were later implemented in [109, 112]. The entropy flux is the derivative of the specific internal energy with respect to $\boldsymbol{J}$, and it is in this way that $\mathbf{J}$ is defined (as the variable conjugate to the entropy flux). As remarked by Romenski, it is more convenient to evolve $\boldsymbol{J}$ and E than $\mathbf{q}$ or the entropy flux, and thus the equations take the form given here. Similarly to τ_1, τ_2 is a relaxation time, characterizing the average speed of relaxation of thermal impulse due to heat exchange between neighboring particles.

0.3 Numerical Methods

The GPR model, being non-conservative, with stiff source terms, represents a particularly challenging set of PDEs to solve. In this study they are solved by an ADER-WENO method. The method produces arbitrarily high-order solutions to hyperbolic systems of PDEs and has been shown to be particularly effective for a wide range of systems (e.g. the classical

Euler equations of gas dynamics, the special relativistic hydrodynamics and ideal magneto-hydrodynamics equations, and the Baer-Nunziato model for compressible two-phase flow - see [7, 132]). The ADER method was first devised by Toro and collaborators (see [127] in particular, and also [123, 125]). Dumbser et al [30] obviated the need for the cumbersome analytic work required by the Cauchy-Kowalewski procedure by use of a Galerkin predictor, as described in the following procedure.

First, the cell-wise constant state variable data from the current time step is reconstructed using high-order spatial polynomials according to the WENO method. This reconstruction is then extended to a reconstruction in both space and time for each individual cell in the domain, using the Galerkin method. A finite volume solver is then used to couple neighboring cells and produce the cell-wise constant data at the next time step.

0.3.1 WENO Reconstruction

First introduced by Liu et al. [78] and developed by Jiang and Shu [68], WENO methods are used to produce high order polynomial approximations to piece-wise constant data. Many variations exist. In this study, the method of [40] is used.

Consider the domain $[0, L]$. Take $K, N \in \mathbb{N}$. The order of accuracy of the resulting method will be $N + 1$. Take the set of grid points $x_i = \frac{i \cdot L}{K}$ for $i = 0, \ldots, K$ and let $\Delta x = \frac{L}{K}$. Denote cell $[x_i, x_{i+1}]$ by C_i. Given cell-wise constant data u on $[0, L]$, an order N polynomial reconstruction of u in C_i will be performed. Define the scaled space variable:

$$\chi^i = \frac{1}{\Delta x}(x - x_i) \tag{19}$$

Denoting the Gauss-Legendre abscissae on $[0, 1]$ by $\{\chi_0, \ldots, \chi_N\}$, define the nodal basis of order N: the Lagrange interpolating polynomials $\{\psi_0, \ldots, \psi_N\}$ with the following property:

$$\psi_i(\chi_j) = \delta_{ij} \tag{20}$$

If N is even, take the stencils:

$$\begin{cases} S_1 &= \left\{C_{i-\frac{N}{2}}, \ldots, C_{i+\frac{N}{2}}\right\} \\ S_2 &= \{C_{i-N}, \ldots, C_i\} \\ S_3 &= \{C_i, \ldots, C_{i+N}\} \end{cases} \tag{21}$$

If N is odd, take the stencils:

$$\begin{cases} S_1 &= \left\{C_{i-\lfloor \frac{N}{2} \rfloor}, \ldots, C_{i+\lceil \frac{N}{2} \rceil}\right\} \\ S_2 &= \left\{C_{i-\lceil \frac{N}{2} \rceil}, \ldots, C_{i+\lfloor \frac{N}{2} \rfloor}\right\} \\ S_3 &= \{C_{i-N}, \ldots, C_i\} \\ S_4 &= \{C_i, \ldots, C_{i+N}\} \end{cases} \tag{22}$$

The data is reconstructed on S_j as:

$$\sum_p \psi_p \left(\chi^i(x)\right) \hat{w}_p^{ij} \tag{23}$$

where the $\hat{w}_p^{ij}$ are solutions to the following linear system:

$$\frac{1}{\Delta x} \int_{x_k}^{x_{k+1}} \sum_p \psi_p \left(\chi^k(x)\right) \hat{w}_p^{ij} dx = u_k \qquad \forall C_k \in S_j \tag{24}$$

where u_k is the value of u in C_k. This can be written as $M_j \hat{\boldsymbol{w}}^{\boldsymbol{ij}} = \boldsymbol{u}_{[\boldsymbol{j_0}:\boldsymbol{j_N}]}$ where $\{j_0, \ldots, j_N\}$ indexes the cells in S_j. The matrices of these linear systems, along with their inverses, can be precomputed to accelerate the solution of these systems.

Define the oscillation indicator matrix:

$$\Sigma_{mn} = \sum_{\alpha=1}^{N} \int_0^1 \psi_m^{(\alpha)} \psi_n^{(\alpha)} d\chi \tag{25}$$

and the oscillation indicator for each stencil:

$$o_j = \Sigma_{mn} \hat{w}_m^{ij} \hat{w}_n^{ij} \tag{26}$$

The full reconstruction in C_i is:

$$w_i(x) = \sum_p \psi_p \left(\chi^i(x)\right) \bar{w}_p^i \tag{27}$$

where $\bar{w}_p^i = \omega_j \hat{w}_p^{ij}$ is the weighted coefficient of the pth basis function, with weights:

$$\omega_j = \frac{\tilde{\omega}_j}{\sum_k \tilde{\omega}_k} \qquad \tilde{\omega}_j = \frac{\zeta_j}{(o_j + \varepsilon)^r} \tag{28}$$

In this study, $r = 8$, $\varepsilon = 10^{-14}$, $\zeta_j = 10^5$ if S_j is a central stencil, and $\zeta_j = 1$ if S_j is a side stencil, as in [34].

The reconstruction can be extended to two dimensions by taking:

$$\upsilon^i = \frac{1}{\Delta y}(y - y_i) \tag{29}$$

and defining stencils in the y-axis in an analogous manner. The data in C_i is then reconstructed using stencil S_j as:

$$\sum_{p,q} \psi_p\left(\chi^i(x)\right) \psi_q\left(\upsilon^i(x)\right) \tilde{w}_{pq}^{ij} \tag{30}$$

where the coefficients of the weighted 1D reconstruction are used as cell averages:

$$M_j \tilde{\boldsymbol{w}}_{\boldsymbol{p}}^{\boldsymbol{ij}} = \bar{\boldsymbol{w}}_{\boldsymbol{p}}^{[\boldsymbol{j_0:j_N}]} \qquad \forall p \in \{0, \ldots, N\} \tag{31}$$

The oscillation indicator is calculated for each p in the same manner as the 1D case. The reconstruction method is easily further extensible to three dimensions, now using the coefficients $\bar{w}_{pq}$ of the weighted 2D reconstruction as cell averages.

0.3.2 Galerkin Predictors

Take a non-conservative, hyperbolic system of the form:

$$\frac{\partial \boldsymbol{Q}}{\partial t} + \frac{\partial \boldsymbol{F}(\boldsymbol{Q})}{\partial x} + B(\boldsymbol{Q}) \cdot \frac{\partial \boldsymbol{Q}}{\partial x} = \boldsymbol{S}(\boldsymbol{Q}) \tag{32}$$

where $\boldsymbol{Q}$ is the vector of conserved variables, $\boldsymbol{F}$ is the conservative nonlinear flux, B is the block matrix corresponding to the purely non-conservative component of the system, and $\boldsymbol{S}(\boldsymbol{Q})$ is the algebraic source vector.

Take the grid for the previous section, and time steps $t_0 < t_1 < \ldots$ while defining $\Delta t_n = t_{n+1} - t_n$. Combining the techniques presented in [32, 34], the Continuous Galerkin or Discontinuous Galerkin methods produce at each time step t_n a local polynomial approximation to $\boldsymbol{Q}$ on each space-time cell $C_i \times [t_n, t_{n+1}]$, using the WENO reconstruction as initial data at the start of the time step (see [7] and [30] respectively for implementations of these two variations). The order of this reconstruction in time is usually taken to be the same as the spatial order, and the same basis polynomials are used. The process involves finding the root of a non-linear system, and this process is guaranteed to converge in exact arithmetic for certain classes of PDEs (see Jackson [64]). This root finding can be computationally expensive relative to the WENO reconstruction, especially if the source terms of the PDE system are stiff.

Now define the scaled time variable:

$$\tau^n = \frac{1}{\Delta t_n} (t - t_n) \tag{33}$$

Thus, (32) becomes:

$$\frac{\partial \boldsymbol{Q}}{\partial \tau^n} + \frac{\partial \boldsymbol{F}^* (\boldsymbol{Q})}{\partial \chi^i} + B^* (\boldsymbol{Q}) \cdot \frac{\partial \boldsymbol{Q}}{\partial \chi^i} = \boldsymbol{S}^* (\boldsymbol{Q}) \tag{34}$$

where

$$\boldsymbol{F}^* = \frac{\Delta t_n}{\Delta x} \boldsymbol{F} \qquad B^* = \frac{\Delta t_n}{\Delta x} B \qquad \boldsymbol{S}^* = \Delta t_n \boldsymbol{S} \tag{35}$$

The non-dimensionalization notation and spacetime cell indexing notation will be dropped for simplicity in what follows. Now define the set of spatiotemporal basis functions:

$$\{\theta_k (\chi, \tau)\} = \{\psi_p (\chi) \psi_s (\tau) : 0 \leq p, s \leq N\} \tag{36}$$

Denoting the Galerkin predictor by $\boldsymbol{q}$, take the following set of approximations:

$$\boldsymbol{Q} \approx \boldsymbol{q} = \theta_\beta \boldsymbol{q}_\beta \tag{37a}$$

$$\boldsymbol{F}(\boldsymbol{Q}) \approx \theta_\beta \boldsymbol{F}_\beta \tag{37b}$$

$$B(\boldsymbol{Q}) \cdot \frac{\partial \boldsymbol{Q}}{\partial \chi} \approx \theta_\beta \boldsymbol{B}_\beta \tag{37c}$$

$$\boldsymbol{S}(\boldsymbol{Q}) \approx \theta_\beta \boldsymbol{S}_\beta \tag{37d}$$

for some coefficients $\boldsymbol{q}_\beta, \boldsymbol{F}_\beta, \boldsymbol{B}_\beta, \boldsymbol{S}_\beta$.

If $\{\psi_0, ..., \psi_N\}$ is a nodal basis, the *nodal basis representation* may be used:

$$\boldsymbol{F}_\beta = \boldsymbol{F}(\boldsymbol{q}_\beta) \tag{38a}$$

$$\boldsymbol{B}_\beta = B(\boldsymbol{q}_\beta) \cdot \left(\frac{\partial \theta_\gamma(\chi_\beta, \tau_\beta)}{\partial \chi} \boldsymbol{q}_\gamma \right) \tag{38b}$$

$$\boldsymbol{S}_\beta = \boldsymbol{S}(\boldsymbol{q}_\beta) \tag{38c}$$

where (χ_β, τ_β) are the coordinates of the node corresponding to basis function θ_β.

If a modal basis is used, $\boldsymbol{F}_\beta, \boldsymbol{B}_\beta, \boldsymbol{S}_\beta$ may be found from the previous values of $\boldsymbol{q}_\beta$ in the iterative processes described below.

For functions $f(\chi, \tau) = f_\chi(\chi) f_\tau(\tau)$ and $g(\chi, \tau) = g_\chi(\chi) g_\tau(\tau)$, define the following integral operators:

$$[f, g]^t = f_\tau(t) g_\tau(t) \langle f_\chi, g_\chi \rangle \tag{39a}$$

$$\{f, g\} = \langle f_\tau, g_\tau \rangle \langle f_\chi, g_\chi \rangle \tag{39b}$$

Multiplying (34) by test function θ_α, using the polynomial approximations for $\boldsymbol{Q}, \boldsymbol{F}, \boldsymbol{B}, \boldsymbol{S}$, and integrating over space and time gives:

$$\left\{ \theta_\alpha, \frac{\partial \theta_\beta}{\partial \tau} \right\} \boldsymbol{q}_\beta = -\left\{ \theta_\alpha, \frac{\partial \theta_\beta}{\partial \chi} \right\} \boldsymbol{F}_\beta + \{\theta_\alpha, \theta_\beta\} (\boldsymbol{S}_\beta - \boldsymbol{B}_\beta) \tag{40}$$

0.3.2.1 Discontinuous Galerkin Method

This method of computing the Galerkin predictor allows solutions to be discontinuous at temporal cell boundaries, and is also suitable for stiff source terms.

Integrating (40) by parts in time gives:

$$\left([\theta_\alpha, \theta_\beta]^1 - \left\{ \frac{\partial \theta_\alpha}{\partial \tau}, \theta_\beta \right\} \right) \boldsymbol{q_\beta} = [\theta_\alpha, \boldsymbol{w}]^0 - \left\{ \theta_\alpha, \frac{\partial \theta_\beta}{\partial \chi} \right\} \boldsymbol{F_\beta} + \{\theta_\alpha, \theta_\beta\} (\boldsymbol{S_\beta} - \boldsymbol{B_\beta}) \tag{41}$$

where $\boldsymbol{w}$ is the reconstruction obtained at the start of the time step with the WENO method. Define the following:

$$U_{\alpha\beta} = [\theta_\alpha, \theta_\beta]^1 - \left\{ \frac{\partial \theta_\alpha}{\partial \tau}, \theta_\beta \right\} \tag{42a}$$

$$V_{\alpha\beta} = \left\{ \theta_\alpha, \frac{\partial \theta_\beta}{\partial \chi} \right\} \tag{42b}$$

$$\boldsymbol{W_\alpha} = [\theta_\alpha, \psi_\gamma]^0 \boldsymbol{w_\gamma} \tag{42c}$$

$$Z_{\alpha\beta} = \{\theta_\alpha, \theta_\beta\} \tag{42d}$$

Thus:

$$U_{\alpha\beta} \boldsymbol{q_\beta} = \boldsymbol{W_\alpha} - V_{\alpha\beta} \boldsymbol{F_\beta} + Z_{\alpha\beta} (\boldsymbol{S_\beta} - \boldsymbol{B_\beta}) \tag{43}$$

This nonlinear system in $\boldsymbol{q_\beta}$ is solved by a Newton method. The source terms must be solved implicitly if they are stiff. Note that $\boldsymbol{W}$ has no dependence on $\boldsymbol{q}$.

0.3.2.2 Continuous Galerkin Method

This method of computing the Galerkin predictor is not suitable for stiff source terms, but it provides substantial savings on computational cost and ensures continuity across temporal cell boundaries.

$\{\psi_0, ..., \psi_N\}$ must be chosen in such a way that the first $N+1$ elements of $\{\theta_\beta\}$ have only a spatial dependence. The first $N+1$ elements of $\boldsymbol{q}$ are then fixed by demanding continuity at $\tau = 0$:

$$\boldsymbol{q}(\chi, 0) = \boldsymbol{w}(\chi) \tag{44}$$

where $\boldsymbol{w}$ is spatial the reconstruction obtained at the start of the time step with the WENO method.

For a given vector $\boldsymbol{v} \in \mathbb{R}^{(N+1)^2}$ and matrix $X \in M_{(N+1)^2,(N+1)^2}(\mathbb{R})$, let $\boldsymbol{v} = (\boldsymbol{v^0}, \boldsymbol{v^1})$ and $X = \begin{pmatrix} X^{00} & X^{01} \\ X^{10} & X^{11} \end{pmatrix}$ where $\boldsymbol{v^0}, X^{00}$ are the components relating solely to the first $N+1$ components of $\boldsymbol{v}$. We only need to find the latter components of $\boldsymbol{q}$, and thus, from (40), we have:

$$\begin{aligned} \left\{\theta_\alpha, \frac{\partial \theta_\beta}{\partial \tau}\right\}^{11} \boldsymbol{q_\beta^1} = \{\theta_\alpha, \theta_\beta\}^{11} \left(\boldsymbol{S_\beta^1} - \boldsymbol{B_\beta^1}\right) - \left\{\theta_\alpha, \frac{\partial \theta_\beta}{\partial \chi}\right\}^{11} \boldsymbol{F_\beta^1} \\ + \{\theta_\alpha, \theta_\beta\}^{10} \left(\boldsymbol{S_\beta^0} - \boldsymbol{B_\beta^0}\right) - \left\{\theta_\alpha, \frac{\partial \theta_\beta}{\partial \chi}\right\}^{10} \boldsymbol{F_\beta^0} \end{aligned} \tag{45}$$

Define the following:

$$U_{\alpha\beta} = \left\{\theta_\alpha, \frac{\partial \theta_\beta}{\partial \tau}\right\}^{11} \tag{46a}$$

$$V_{\alpha\beta} = \left\{\theta_\alpha, \frac{\partial \theta_\beta}{\partial \chi}\right\}^{11} \tag{46b}$$

$$\boldsymbol{W_\alpha} = \{\theta_\alpha, \theta_\beta\}^{10} (\boldsymbol{S_\beta} - \boldsymbol{B_\beta})^0 - \left\{\theta_\alpha, \frac{\partial \theta_\beta}{\partial \chi}\right\}^{10} \boldsymbol{F_\beta^0} \tag{46c}$$

$$Z_{\alpha\beta} = \{\theta_\alpha, \theta_\beta\}^{11} \tag{46d}$$

Thus:

$$U_{\alpha\beta} \boldsymbol{q_\beta^1} = \boldsymbol{W_\alpha} - V_{\alpha\beta} \boldsymbol{F_\beta^1} + Z_{\alpha\beta} \left(\boldsymbol{S_\beta^1} - \boldsymbol{B_\beta^1}\right) \tag{47}$$

Note that, as with the discontinuous Galerkin method, $\boldsymbol{W}$ has no dependence on the degrees of freedom in $\boldsymbol{q}$.

0.3.3 Finite Volume Scheme

Following the formulation of [34], integrating (32) over $[t_n, t_{n+1}] \times C_i$ gives:

$$\boldsymbol{Q}_i^{n+1} = \boldsymbol{Q}_i^n + \Delta t_n \left(\boldsymbol{S}_i^n - \boldsymbol{P}_i^n \right) - \frac{\Delta t_n}{\Delta x} \left(\boldsymbol{D}_{i+1}^n - \boldsymbol{D}_i^n \right) \tag{48}$$

where

$$\boldsymbol{Q}_i^n = \frac{1}{\Delta x} \int_{x_i}^{x_{i+1}} \boldsymbol{Q}\left(x, t_n\right) dx \tag{49a}$$

$$\boldsymbol{S}_i^n = \frac{1}{\Delta t_n \Delta x} \int_{t_n}^{t_{n+1}} \int_{x_i}^{x_{i+1}} \boldsymbol{S}\left(\boldsymbol{Q}\right) dx dt \tag{49b}$$

$$\boldsymbol{P}_i^n = \frac{1}{\Delta t_n \Delta x} \int_{t_n}^{t_{n+1}} \int_{x_i}^{x_{i+1}} B\left(\boldsymbol{Q}\right) \cdot \frac{\partial \boldsymbol{Q}}{\partial x} dx dt \tag{49c}$$

$$\boldsymbol{D}_i^n = \frac{1}{\Delta t_n} \int_{t_n}^{t_{n+1}} \boldsymbol{\mathcal{D}} \left(\boldsymbol{Q}^-\left(x_i, t\right), \boldsymbol{Q}^+\left(x_i, t\right) \right) dt \tag{49d}$$

$\boldsymbol{Q}^-, \boldsymbol{Q}^+$ are the left and right extrapolated states at the x_i boundary. $\boldsymbol{S}_i^n, \boldsymbol{P}_i^n, \boldsymbol{D}_i^n$ are calculated using an $N+1$-point Gauss-Legendre quadrature, replacing $\boldsymbol{Q}$ with $\boldsymbol{q_h}$.

M, as defined in Section 0.3.2, is a diagonalizable matrix with decomposition $M = R\Lambda R^{-1}$ where the columns of R are the right eigenvectors and Λ is the diagonal matrix of eigenvalues. Define the following matrix:

$$|M| = R\,|\Lambda|\,R^{-1} \tag{50}$$

Using these definitions, the interface terms arising in the FV formula have the following form:

$$\boldsymbol{\mathcal{D}}\left(\boldsymbol{q}^-, \boldsymbol{q}^+\right) = \frac{1}{2}\left(\boldsymbol{F}\left(\boldsymbol{q}^-\right) + \boldsymbol{F}\left(\boldsymbol{q}^+\right) + \hat{B} \cdot \left(\boldsymbol{q}^+ - \boldsymbol{q}^-\right) - \hat{M} \cdot \left(\boldsymbol{q}^+ - \boldsymbol{q}^-\right) \right) \tag{51}$$

$\hat{M}$ is chosen to either correspond to a Rusanov / Lax-Friedrichs flux [126]:

$$\hat{M} = \max\left(\max\left|\Lambda\left(\boldsymbol{q}^-\right)\right|, \max\left|\Lambda\left(\boldsymbol{q}^+\right)\right| \right) \tag{52}$$

or a Roe flux [38]:

$$\hat{M} = \left| \int_0^1 M\left(\boldsymbol{q}^- + z\left(\boldsymbol{q}^+ - \boldsymbol{q}^-\right)\right) dz \right| \tag{53}$$

or a simplified Osher–Solomon flux [37]:

$$\hat{M} = \int_0^1 \left| M\left(\boldsymbol{q}^- + z\left(\boldsymbol{q}^+ - \boldsymbol{q}^-\right)\right)\right| dz \tag{54}$$

$\hat{B}$ takes the following form:

$$\hat{B} = \int_0^1 B\left(\boldsymbol{q}^- + z\left(\boldsymbol{q}^+ - \boldsymbol{q}^-\right)\right) dz \tag{55}$$

It was found that the Osher-Solomon flux would often produce slightly less diffusive results, but that it was more computationally expensive, and also had a greater tendency to introduce numerical artifacts.

0.3.4 Time Step and Boundary Conditions

Let Λ_i^n be the set of eigenvalues of the GPR system evaluated at $\boldsymbol{Q_i^n}$. $C_{cfl} < 1$ is a constant (usually taken to be 0.9, unless the problem being simulated is particularly demanding, requiring a lower value). A semi-analytic form for Λ is given in Section B.2. The eigenvalues determine the speed of propagation of information in the solution to the Riemann Problem at the cell interfaces, and the time step is chosen to ensure that the characteristics do not enter into other cells between t_n and t_{n+1}:

$$\Delta t_n = \frac{C_{cfl} \cdot \Delta x}{\max_i |\Lambda_i^n|} \tag{56}$$

Transmissive boundary conditions (allowing material and heat to pass through) are implemented by setting the state variables in the boundary cells to the same value as their non-boundary neighbors. Reflective boundary conditions are implemented in the same way, except that the directions of the velocity and thermal impulse vectors in the boundary cells are reversed.

Chapter 1

Objective 1: Extending the GPR Model

1.1 Equations of State

1.1.1 Mie-Gruneisen Models

It is required to specify the microscale energy E_1 appearing in (6). In this study, several different possible choices for E_1 are put into the same framework by expressing them in the following Mie-Gruneisen form [83]:

$$E_1(\rho, p) = e(\rho, p) = e^{ref}(\rho) + \frac{p - p^{ref}(\rho)}{\rho\Gamma(\rho)} \tag{1.1a}$$

$$T = T^{ref}\phi(\rho) + \frac{e - e^{ref}}{c_v} = T^{ref}\phi(\rho) + \frac{p - p^{ref}(\rho)}{c_v\rho\Gamma(\rho)} \tag{1.1b}$$

$$\phi(\rho) = \exp\left(\int_{\rho_0}^{\rho} \frac{\Gamma\left(\rho'\right)}{\rho'} d\rho'\right) \tag{1.1c}$$

The forms taken by e^{ref}, p^{ref}, Γ for various different instances of this class are given in Table 1.1 on page 24. The first five entries in the table are standard results. The sixth is derived thus. The Godunov-Romenski hyperelastic EOS is given by:

$$E(\rho, s, A) = \frac{c_0^2}{2\alpha^2}\left(\left|A^TA\right|^{\alpha/2} - 1\right)^2 + c_vT_0\left|A^TA\right|^{\gamma/2}\left(e^{s/c_v} - 1\right) + \frac{b_0^2}{4}\left|A^TA\right|^{\beta/2}\left\|\mathrm{dev}\left(A^TA\right)\right\|^2 \tag{1.2}$$

Using the relation $\det(A) = \frac{\rho}{\rho_0}$, this can be thought of as taking the form:

$$E_1(\rho, s) + \frac{c_s(\rho)^2}{4}\left\|\mathrm{dev}(G)\right\|_F^2 \tag{1.3}$$

where $c_s = b_0\left(\frac{\rho}{\rho_0}\right)^{\beta}$. Considering only the microscale energy component, note that we have:

$$p = \rho^2\frac{\partial E_1}{\partial\rho} = \rho\left(\frac{c_0^2}{\alpha}\left(\left(\frac{\rho}{\rho_0}\right)^{\alpha} - 1\right)\left(\frac{\rho}{\rho_0}\right)^{\alpha} + \gamma c_vT_0\left(\frac{\rho}{\rho_0}\right)^{\gamma}\left(e^{s/c_v} - 1\right)\right) \tag{1.4}$$

Therefore:

$$E_1 - \frac{c_0^2}{2\alpha^2}\left(\left(\frac{\rho}{\rho_0}\right)^{\alpha} - 1\right)^2 = \frac{p}{\gamma\rho} - \frac{c_0^2}{\gamma\alpha}\left(\left(\frac{\rho}{\rho_0}\right)^{\alpha} - 1\right)\left(\frac{\rho}{\rho_0}\right)^{\alpha} \tag{1.5}$$

Thus E_1 can be put in Mie-Gruneisen form:

$$E_1 = \frac{p - \frac{c_0^2\rho}{\alpha}\left(\left(\frac{\rho}{\rho_0}\right)^{\alpha} - 1\right)\left(\frac{\rho}{\rho_0}\right)^{\alpha}}{\gamma\rho} + \frac{c_0^2}{2\alpha^2}\left(\left(\frac{\rho}{\rho_0}\right)^{\alpha} - 1\right)^2 \tag{1.6}$$

The following quantities are required when computing the eigenstructure of the system:

$$\frac{\partial T}{\partial \rho} = \frac{1}{c_v}\left(\frac{\partial e}{\partial \rho} - \frac{de^{ref}}{d\rho}\right) \tag{1.7a}$$

$$\frac{\partial T}{\partial p} = \frac{1}{c_v}\frac{\partial e}{\partial p} \tag{1.7b}$$

$$\frac{\partial e}{\partial \rho} = \frac{de^{ref}}{d\rho} - \frac{\frac{dp^{ref}}{d\rho}\rho\Gamma(\rho) + \left(\Gamma(\rho) + \rho\Gamma'(\rho)\right)\left(p - p^{ref}(\rho)\right)}{\left(\rho\Gamma(\rho)\right)^2} \tag{1.8a}$$

$$\frac{\partial e}{\partial p} = \frac{1}{\rho\Gamma(\rho)} \tag{1.8b}$$

The relevant functions for each of the EOSs used in this study are given in Table 1.2 on page 25.

Although this is a versatile class of equations of state - and it is fit for the purposes that the model is put to here - it should be noted that many other choices are available.

1.1.2 Variable Transverse Perturbation Speed

Taking (1.1a) and using the fact that $p = \rho^2 e_\rho$, we have:

$$e_\rho - \frac{\Gamma}{\rho}e = \frac{p^{ref}}{\rho^2} - \frac{\Gamma}{\rho}e^{ref} \tag{1.9}$$

Equation of State	$p^{ref}(\rho)$	$e^{ref}(\rho)$	$\Gamma(\rho)$	T^{ref}
Ideal Gas	0	0	$\gamma-1$	0
Stiffened Gas	$-p_\infty$	$\frac{p_\infty}{\rho}$	$\gamma-1$	0
Shock Mie-Gruneisen	$\frac{c_0^2\left(\frac{1}{\rho_0}-\frac{1}{\rho}\right)}{\left(\frac{1}{\rho_0}-s\left(\frac{1}{\rho_0}-\frac{1}{\rho}\right)\right)^2}$	$\frac{p^{ref}}{2}\left(\frac{1}{\rho_0}-\frac{1}{\rho}\right)$	$\Gamma_0\frac{\rho_0}{\rho}$	0
JWL	$Ae^{-\frac{R_1\rho_0}{\rho}}+Be^{-\frac{R_2\rho_0}{\rho}}$	$\frac{A}{\rho_0R_1}e^{-\frac{R_1\rho_0}{\rho}}+\frac{B}{\rho_0R_2}e^{-\frac{R_2\rho_0}{\rho}}$	Γ_0	0
Cochran-Chan	$A\left(\frac{\rho}{\rho_0}\right)^{\epsilon_1}-B\left(\frac{\rho}{\rho_0}\right)^{\epsilon_2}$	$\frac{A}{\rho_0(\epsilon_1-1)}\left(\left(\frac{\rho}{\rho_0}\right)^{\epsilon_1-1}-1\right)-\frac{B}{\rho_0(\epsilon_1-1)}\left(\left(\frac{\rho}{\rho_0}\right)^{\epsilon_2-1}-1\right)$	Γ_0	0
Godunov-Romenski	$\frac{c_0^2\rho}{\alpha}\left(\left(\frac{\rho}{\rho_0}\right)^{\alpha}-1\right)\left(\frac{\rho}{\rho_0}\right)^{\alpha}$	$\frac{c_0^2}{2\alpha^2}\left(\left(\frac{\rho}{\rho_0}\right)^{\alpha}-1\right)^2$	γ	T_0

Table 1.1: $e^{ref}, p^{ref}, \Gamma, T^{ref}$ for different kinds of Mie-Gruneisen equations of state

Equation of State	$\frac{dp^{ref}}{d\rho}$	$\frac{de^{ref}}{d\rho}$	$\Gamma'(\rho)$
Ideal Gas	0	0	0
Stiffened Gas	0	$-\frac{p_\infty}{\rho^2}$	0
Shock Mie-Gruneisen	$\frac{c_0^2\rho_0^2(s(\rho_0-\rho)-\rho)}{(s(\rho-\rho_0)-\rho)^3}$	$\frac{1}{2}\left(\frac{dp^{ref}}{d\rho}\left(\frac{1}{\rho_0}-\frac{1}{\rho}\right)+\frac{p^{ref}}{\rho^2}\right)$	$-\Gamma_0\frac{\rho_0}{\rho^2}$
JWL	$\frac{AR_1\rho_0}{\rho^2}e^{-\frac{R_1\rho_0}{\rho}}+\frac{BR_2\rho_0}{\rho^2}e^{-\frac{R_2\rho_0}{\rho}}$	$\frac{A}{\rho^2}e^{-\frac{R_1\rho_0}{\rho}}+\frac{B}{\rho^2}e^{-\frac{R_2\rho_0}{\rho}}$	0
Cochran-Chan	$\frac{\epsilon_1 A}{\rho}\left(\frac{\rho}{\rho_0}\right)^{\epsilon_1}-\frac{\epsilon_2 B}{\rho}\left(\frac{\rho}{\rho_0}\right)^{\epsilon_2}$	$\frac{A}{\rho^2}\left(\frac{\rho}{\rho_0}\right)^{\epsilon_1}-\frac{B}{\rho^2}\left(\frac{\rho}{\rho_0}\right)^{\epsilon_2}$	0
Godunov-Romenski	$\frac{c_0^2}{\alpha}\left(\frac{\rho}{\rho_0}\right)^{\alpha}\left(\left(1+\alpha\right)\left(\frac{\rho}{\rho_0}\right)^{\alpha}-1\right)+\alpha\left(\frac{\rho}{\rho_0}\right)^{\alpha}\Big)$	$\frac{c_0^2}{\alpha\rho^2}\left(\left(\frac{\rho}{\rho_0}\right)^{\alpha}-1\right)\left(\frac{\rho}{\rho_0}\right)^{\alpha}$	0

Table 1.2: $\frac{de^{ref}}{d\rho}$, $\frac{dp^{ref}}{d\rho}$, Γ' for different kinds of Mie-Gruneisen equations of state

The solutions to this equation for different forms of Γ, p^{ref}, e^{ref} take the form below, where f is an arbitrary function of s, g depends on the form of Γ, and $\hat{e}$ is a particular solution of the equation (which will be equal to e^{ref} if $p^{ref} = \rho^2 \frac{\partial e^{ref}}{\partial \rho}$).

$$e = f(s)\, g(\rho) + \hat{e}(\rho) \tag{1.10}$$

We have:

$$p = \rho^2 e_\rho = \rho^2 \left(f(s)\, g^{'}(\rho) + \hat{e}^{'}(\rho) \right) \tag{1.11}$$

Thus:

$$\frac{\frac{p}{\rho^2} - \hat{e}^{'}(\rho)}{g^{'}(\rho)} = f(s) = \frac{e - \hat{e}(\rho)}{g(\rho)} \tag{1.12}$$

Therefore:

$$E_1(\rho, p) = e(\rho, p) = \hat{e}(\rho) + \frac{g(\rho)}{g^{'}(\rho)} \left(\frac{p}{\rho^2} - \hat{e}^{'}(\rho) \right) \tag{1.13}$$

We now add another term to the energy, giving it the following form:

$$E(\rho, p) = e(\rho, p) = f(s)\, g(\rho) + \hat{e}(\rho) + B(\rho)\, h(A) \tag{1.14}$$

We then have:

$$p = \rho^2 \left(f(s)\, g^{'}(\rho) + \hat{e}^{'}(\rho) + B^{'}(\rho)\, h(A) \right) \tag{1.15}$$

Thus:

$$\frac{\frac{p}{\rho^2} - \hat{e}^{'}(\rho) - B^{'}(\rho)\, h(A)}{g^{'}(\rho)} = f(s) = \frac{e - \hat{e}(\rho) - B(\rho)\, h(A)}{g(\rho)} \tag{1.16}$$

Therefore:

$$e = \frac{g(\rho)}{g^{'}(\rho)} \left(\frac{p}{\rho^2} - \hat{e}^{'}(\rho) - B^{'}(\rho)\, h(A) \right) + \hat{e}(\rho) + B(\rho)\, h(A) \tag{1.17}$$

Noting that $\frac{g(\rho)}{g'(\rho)} = \frac{\rho}{\Gamma(\rho)}$, this can be expressed as:

$$E(\rho,p) = e(\rho,p) = E_1(\rho,p) + \left(B(\rho) - \frac{\rho}{\Gamma(\rho)}B'(\rho)\right)h(A) \tag{1.18}$$

If the EOS comprises a microscale energy component of Mie-Gruneisen type, and a mesoscale energy component with speed of transverse vibrations dependent upon ρ, then this provides a method to recover the EOS in terms of ρ and p (by substituting $B(\rho) = \frac{c_s^2(\rho)}{4}$ and $h(A) = \left\|\mathrm{dev}\left(A^TA\right)\right\|_F^2$).

1.2 Reactive Materials

We now wish to simulate the mixture of two miscible materials, labelled 1 and 2. Let λ be the mass fraction of material 1. Let material 1 undergo a chemical reaction at rate K to form material 2. The GPR model can be extended to incorporate these factors thus:

$$\frac{\partial\rho}{\partial t} + \frac{\partial(\rho v_k)}{\partial x_k} = 0 \tag{1.19a}$$

$$\frac{\partial(\rho v_i)}{\partial t} + \frac{\partial(\rho v_i v_k + p\delta_{ik} - \sigma_{ik})}{\partial x_k} = 0 \tag{1.19b}$$

$$\frac{\partial A_{ij}}{\partial t} + \frac{\partial(A_{ik}v_k)}{\partial x_j} + v_k\left(\frac{\partial A_{ij}}{\partial x_k} - \frac{\partial A_{ik}}{\partial x_j}\right) = -\frac{\psi_{ij}}{\theta_1(\tau_1)} \tag{1.19c}$$

$$\frac{\partial(\rho J_i)}{\partial t} + \frac{\partial(\rho J_i v_k + T\delta_{ik})}{\partial x_k} = -\frac{\rho H_i}{\theta_2(\tau_2)} \tag{1.19d}$$

$$\frac{\partial(\rho E)}{\partial t} + \frac{\partial(\rho E v_k + (p\delta_{ik} - \sigma_{ik})v_i + q_k)}{\partial x_k} = 0 \tag{1.19e}$$

$$\frac{\partial(\rho\lambda)}{\partial t} + \frac{\partial(\rho\lambda v_k)}{\partial x_k} = -\rho K \tag{1.19f}$$

The EOS is modified to include:

$$E_r(\lambda) = -Q_c(1-\lambda) \tag{1.20}$$

There are many different reaction rate laws that can be used to determine the form of K appearing in (1.19f).

In discrete ignition temperature reaction kinetics, no reaction occurs below the ignition temperature, T_i. Above T_i, the reaction proceeds at a constant rate $K_0 > 0$:

$$K = \begin{cases} K_0\lambda & T` \geq T_i \\ 0 & T < T_i \end{cases} \tag{1.21}$$

A more sophisticated model of reaction kinetics was devised by Svante Arrhenius in 1889 [5, 6]:

$$K = B_c e^{-\frac{E_a}{R_c T}}\lambda \tag{1.22}$$

where B_c is some prefactor (with units of frequency), and E_a is the activation energy of the reactive species.

A more sophisticated model yet is the ignition and growth model [72]:

$$\begin{aligned} K = {} & I\lambda^b \left(\frac{\rho}{\rho_0} - 1 - a\right)^x H\left(\phi_I - \phi\right) \\ & + G_1\lambda^c\phi^d p^y H\left(\phi_{G1} - \phi\right) \\ & + G_2\lambda^e\phi^g p^z H\left(\phi - \phi_{G2}\right) \end{aligned} \tag{1.23}$$

where $\phi = 1-\lambda$, H is the Heaviside function, and $I, G_1, G_2, a, b, c, d, e, g, x, y, z, \phi_I, \phi_{G1}, \phi_{G2}$ are constants depending on the material being modeled.

1.3 Numerical Results

1.3.1 Seven-Wave Elastic Riemann Problem

This test is taken from [11]. The aim of the test is to validate the Mie-Gruneisen formulation of the Godunov-Romenski EOS presented in 1.1.1, and the formulation of the mesoscale GPR energy for the Godunov-Romenski EOS presented in 1.1.2.

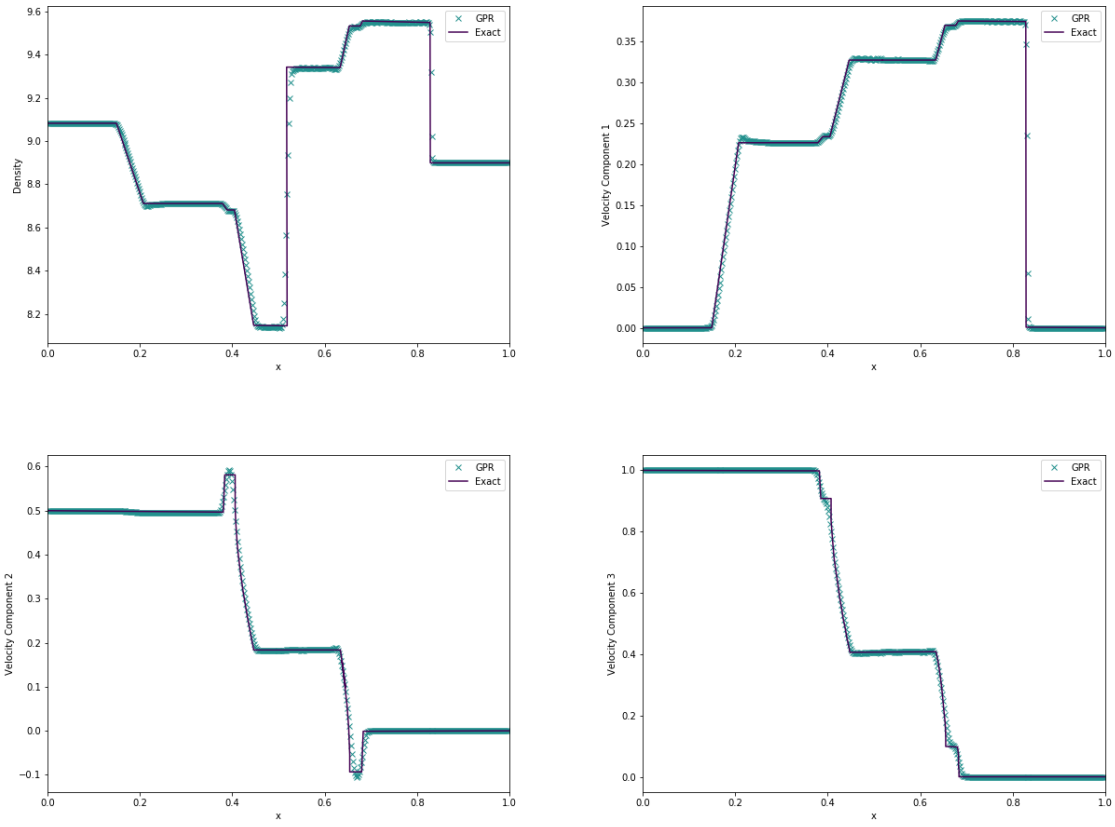

Figure 1.1: Density and velocity for the 7-wave elastic Riemann problem

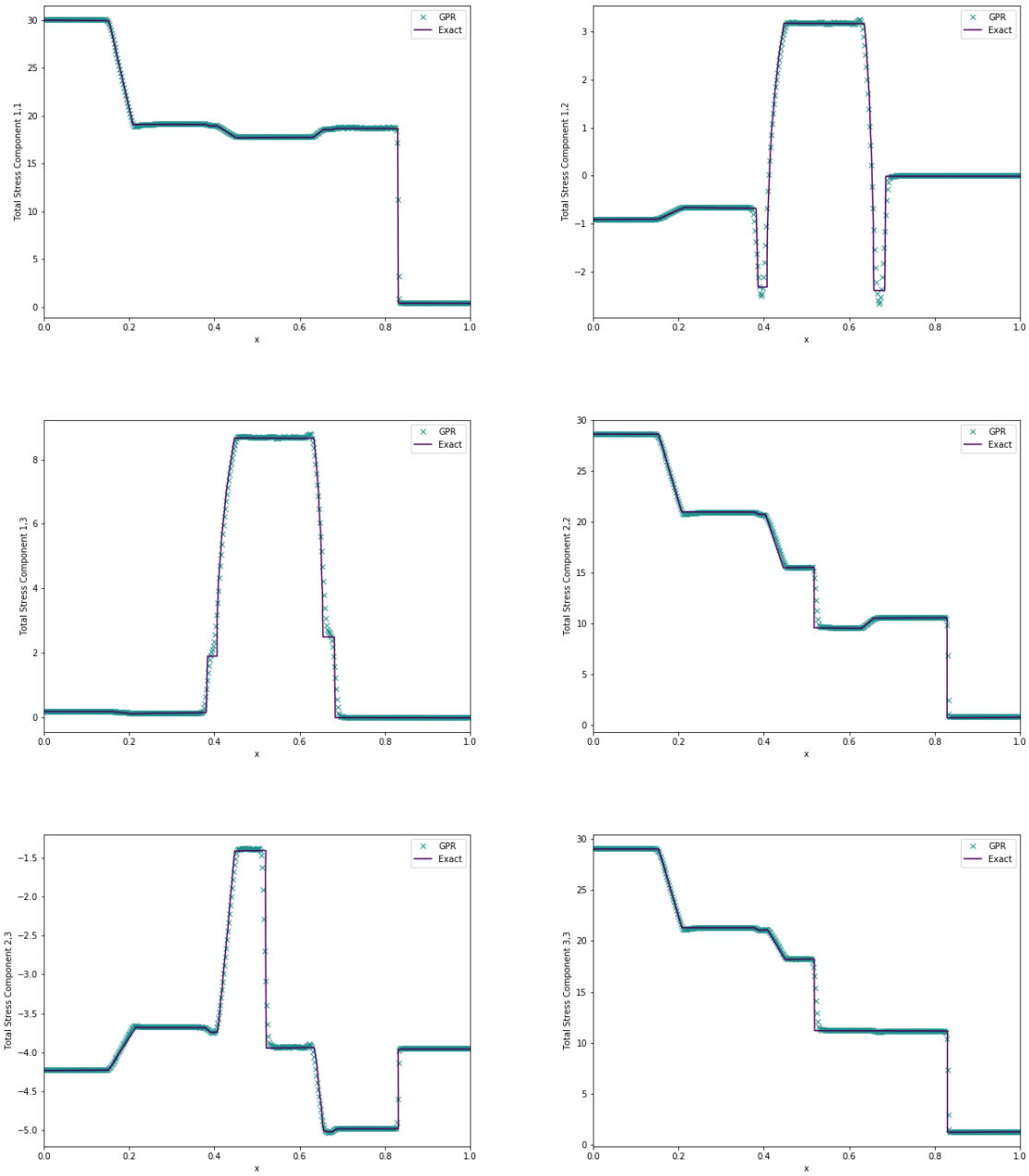

Figure 1.2: Total stress for the 7-wave elastic Riemann problem

	ρ	p	$\boldsymbol{v}$	A	$\boldsymbol{J}$	λ
$x < 0.25$	1.4	1	$\mathbf{0}$	$\sqrt[3]{1.4} \cdot I_3$	$\mathbf{0}$	0
$x \geq 0.25$	0.887565	0.191709	$(-0.577350, 0, 0)$	$\sqrt[3]{0.887565} \cdot I_3$	$\mathbf{0}$	1

Table 1.3: Initial conditions for the viscous shock-induced detonation test

1.3.2 Shock-Induced Detonation

The GPR model is now combined with discrete ignition temperature reaction kinetics to model a ZND detonation wave[1] in a viscous, reactive, ideal gas. The test consists of a CJ wave with speed 1, traveling into a region of totally unburnt gas. The initial conditions are taken from Helzel et al. [55] and are given in Table 1.3 on page 31.

The material parameters are taken to be: $\gamma = 1.4$, $c_v = 2.5$, $\rho_0 = 1$, $p_0 = 1$, $c_s = 1$, $c_t = 1$, $\mu = 10^{-4}$, $P_r = 0.75$, $Q_c = 1$, $K_0 = 250$, $T_i = 0.25$. The results for grids of 400 and 1600 cells at time $t = 0.5$ are found in Figure 1.3 on page 32. They are to be compared with those by Hidalgo and Dumbser [58]. The simulation with 400 cells corresponds well with that found in [58], and the simulation with 1600 cells is very close to Hidalgo's total variation diminishing reference solution calculated with 10,000 cells.

The von Neumann spike is well resolved, with the thin reaction zone behind it (corresponding to the region in which the concentration decreases from 1 to 0). The CJ state is maintained correctly behind the reaction zone. The spurious wave in the density is explained in [58] as being due to initialization errors occurring as a result of using exact algebraic conditions for an ideal (infinitely thin) CJ detonation wave, which are solved with a viscous model with finite reaction rate.

1.3.3 Heating-Induced Deflagration

As a step towards modeling the slow cooking off problem, the GPR model is now applied to the situation presented by Clarke, Kassoy and Riley [23–25]. Here, the domain $x \in [0, 8.5 \times 10^{-6}]$

[1] Zel'dovich [133], von Neumann [128], and Doring [28] independently proposed this detonation model, whereby reactive gas is compressed to high pressure by an infinitely thin shock wave into a *von Neumann spike*, initiating the reaction. The reaction zone is located behind the spike. In the reference frame of the shock, the gas moves supersonically ahead of the shock, subsonically in the reaction zone, and sonically in the region behind the reaction zone (which is described by the Chapman-Jouget state [21, 70]. The energy released in the reaction is transported acoustically to the shock to support it.

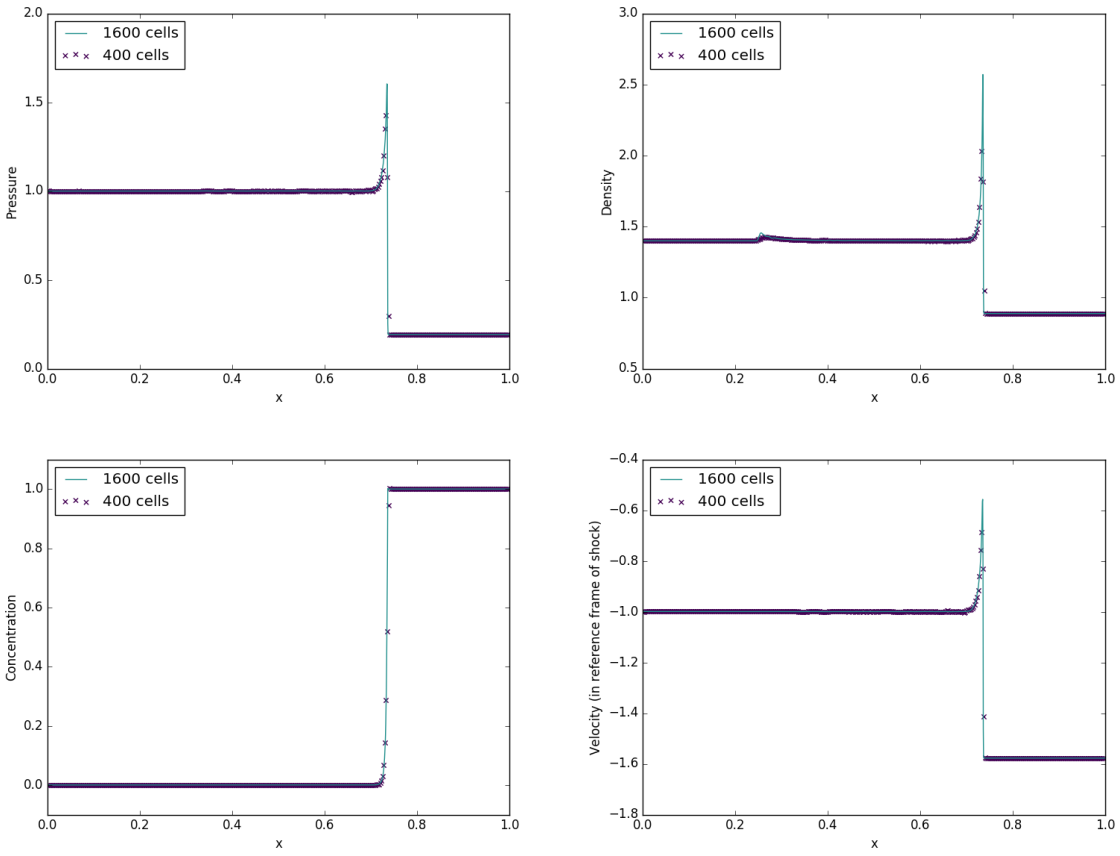

Figure 1.3: Pressure, density, concentration of reactant, and velocity (in the reference frame of the shock) in the viscous shock-induced detonation test

is occupied by an ideal gas with initial conditions $\rho = \rho_0 = 1.176$, $p = p_0 = 101325$, $\boldsymbol{v} = \mathbf{0}$, $A = I_3$, $\boldsymbol{J} = \mathbf{0}$ and material parameters $\gamma = 1.4$, $c_v = 718$, $c_s = 55$, $c_t = 500$, $\mu = 1.98\times10^{-5}$, $P_r = 0.72$. These values are chosen to be similar to air at room temperature.

Thermal energy is added at the left boundary at a high power of $\frac{\gamma p_0 c_0}{P_r(\gamma-1)}$ (around $1.7 \times 10^8 Wm^{-2}$). The test is performed with both a combustible and an inert gas. In the former case, the initial concentration is set to $\lambda = 1$. Arrhenius reaction kinetics are used, with $Q_c = 6\gamma c_v T_0$, $B_c = 7 \times 10^{10}$, $\epsilon = \frac{1}{20}$. The subsequent evolutions of the systems for 400 cells are shown in Figure 1.4 on page 34. Non-dimensionalized time and length variables t^*, x^* are used, as in [24]:

$$t = \frac{\mu}{p_0\gamma}t^* \tag{1.24a}$$

$$x = \frac{\mu c_0}{p_0\gamma}x^* \tag{1.24b}$$

There are no analogues for c_t and c_s in the models used by Clarke et al. c_s is given the experimentally-derived value for CH_3Cl at 30Â°C given in [35]. c_t is chosen by trial and error so that the GPR results corresponded with those in [24]. The results presented here are thus close, but not identical to those of Clarke et al.

Note that heating the inert gas produces an acoustic wave of constant pressure, propagating ahead of the temperature curve. This pressure wave is also present in the heating of the combustible gas, where it proceeds in front of the combustion wave. The temperature increase accompanying this acoustic wave is not enough to ignite the reactive gas, and the thin reaction zone lags behind the acoustic wavefront. Although the combustion wave is referred to as a detonation wave in [24], it would now commonly be called a deflagration wave, as it travels subsonically and is not coincident with the shock wave. This phenomenon of a second, faster shock overtaking the combustion wave demonstrated experimentally by Kapila et al. [71], with a full mathematical analysis provided by Short [121], where it is shown to result from the steep temperature gradient at the time of ignition.

1.3.4 Heating-Induced Detonation

It is now demonstrated that the heating-induced deflagration test can result in detonation if the temperature gradient upon ignition is less steep. This test is identical to the previous

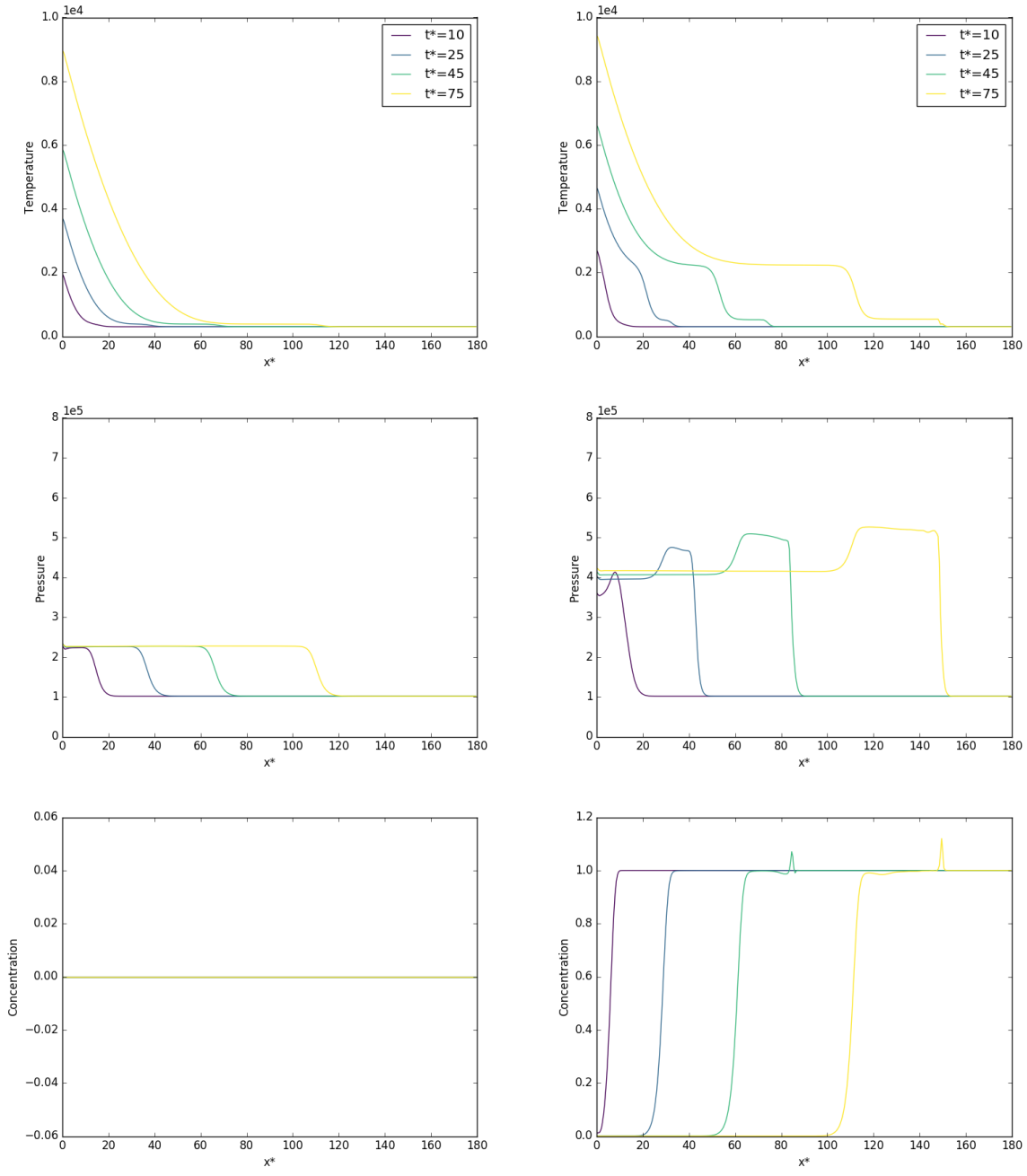

Figure 1.4: Temperature, pressure, and concentration of reactant in the heating-induced deflagration test with inert gas (left) / reactive gas (right)

test, with one exception: ϵ is given the higher value of $\frac{1}{15}$. Thus, the activation energy is effectively lower, or equivalently, the whole gas volume is relatively closer to the ignition temperature when the gas at the left boundary ignites. The results of this test are shown in Figure 1.5 on page 36.

The von Neumann spike is present and well resolved, with a thin reaction zone appearing behind it in the concentration plot. Unlike in 1.3.2, the system does not relax to the CJ state behind the detonation wave, as thermal energy is continually added to the reflective left boundary. The region behind the reaction zone is thus complex.

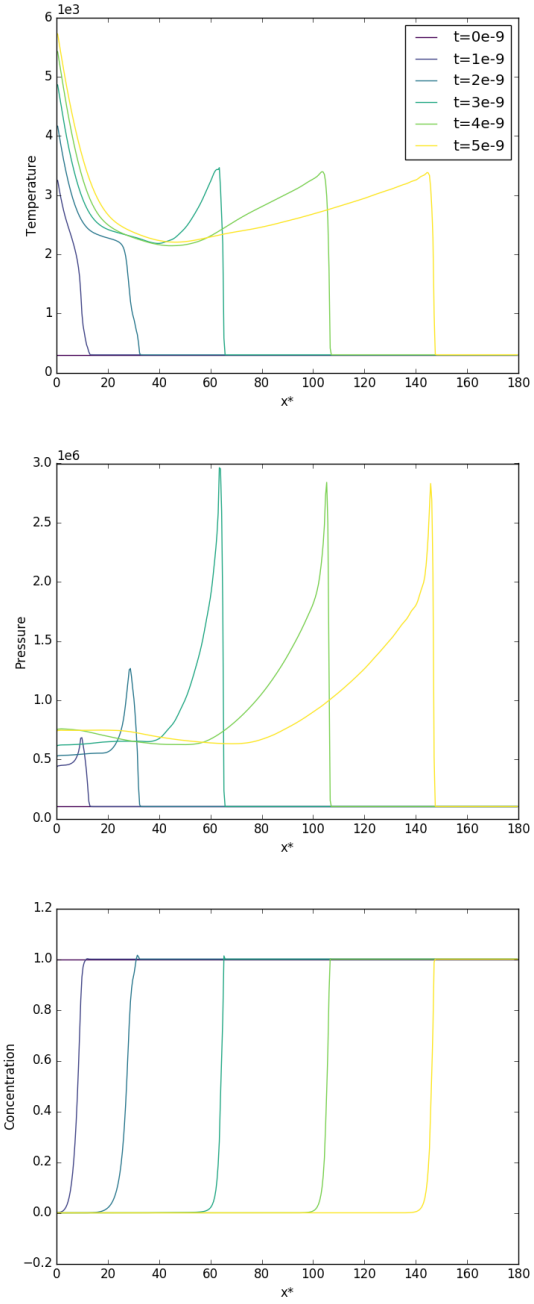

Figure 1.5: Temperature, pressure, and concentration of reactant in the heating-induced detonation test

Chapter 2

Objective 2: Improved Numerical Methods

2.1 Extending the Montecinos-Balsara ADER Method

The material in this section is published in [64, 65].

Hyperbolic systems of PDEs can be solved to arbitrary orders of accuracy by using the ADER-WENO method. These PDE systems may be non-conservative and non-homogeneous, and contain stiff source terms. ADER-WENO requires a spatiotemporal polynomial reconstruction of the data in each spacetime cell, at each time step. This reconstruction is obtained as the root of a nonlinear system, resulting from the use of a Galerkin method. It was proved in [64] that for traditional choices of basis polynomials, the eigenvalues of certain matrices appearing in these nonlinear systems are always 0, regardless of the number of spatial dimensions of the PDEs or the chosen order of accuracy of the ADER-WENO method. This guarantees fast convergence to the Galerkin root for certain classes of PDEs.

Montecinos and Balsara have presented a new, more efficient class of basis polynomials for the one-dimensional ADER-WENO method. This new class of basis polynomials, originally presented for conservative systems, is extended to multidimensional, non-conservative systems here, and the corresponding property regarding the eigenvalues of the Galerkin matrices is proved.

2.1.1 Method of Montecinos and Balsara

[89] have proposed a new, more efficient class of basis polynomials. While the method was given for conservative, one-dimensional systems in the original paper, it is extended here to general non-conservative, multidimensional systems.

Take a non-homogeneous, non-conservative, hyperbolic system of the form:

$$\frac{\partial \boldsymbol{Q}}{\partial t} + \boldsymbol{\nabla} \cdot \overrightarrow{\boldsymbol{F}}(\boldsymbol{Q}) + \overrightarrow{\boldsymbol{B}}(\boldsymbol{Q}) \cdot \nabla \boldsymbol{Q} = \boldsymbol{S}(\boldsymbol{Q}) \tag{2.1}$$

where $\boldsymbol{Q}$ is the vector of conserved variables, $\overrightarrow{\boldsymbol{F}} = (\boldsymbol{F_1}, \boldsymbol{F_2}, \boldsymbol{F_3})$ and $\overrightarrow{\boldsymbol{B}} = (B_1, B_2, B_3)$ are respectively the conservative nonlinear fluxes and matrices corresponding to the purely non-conservative components of the system, and $\boldsymbol{S}(\boldsymbol{Q})$ is the algebraic source vector.

Define spatial variables $x^{(1)}, x^{(2)}, x^{(3)}$. Take the space-time cell:

$$C = \left[x_{i_1}^{(1)}, x_{i_1+1}^{(1)}\right] \times \left[x_{i_2}^{(2)}, x_{i_2+1}^{(2)}\right] \times \left[x_{i_3}^{(3)}, x_{i_3+1}^{(3)}\right] \times [t_n, t_{n+1}] \tag{2.2}$$

Define the scaled spatial and temporal variables:

$$\chi^{(k)} = \frac{x^{(k)} - x_{i_k}^{(k)}}{x_{i_k+1}^{(k)} - x_{i_k}^{(k)}} \tag{2.3a}$$

$$\tau = \frac{t - t_n}{t_{n+1} - t_n} \tag{2.3b}$$

Thus, C becomes:

$$\left(\chi^{(1)},\chi^{(2)},\chi^{(3)},\tau\right) \in [0,1]^4 \tag{2.4}$$

By rescaling $\overrightarrow{\boldsymbol{F}}, \overrightarrow{\boldsymbol{B}}, \boldsymbol{S}$ by the appropriate constant factors, and defining $\tilde{\nabla} = \left(\partial_{\chi^{(1)}}, \partial_{\chi^{(2)}}, \partial_{\chi^{(3)}}\right)$, within C equation (2.1) becomes:

$$\frac{\partial \boldsymbol{Q}}{\partial \tau} + \tilde{\boldsymbol{\nabla}} \cdot \overrightarrow{\boldsymbol{F}}(\boldsymbol{Q}) + \overrightarrow{\boldsymbol{B}}(\boldsymbol{Q}) \cdot \tilde{\nabla} \boldsymbol{Q} = \boldsymbol{S}(\boldsymbol{Q}) \tag{2.5}$$

A basis $\{\psi_0, ..., \psi_N\}$ of P_N and inner product $\langle \cdot, \cdot \rangle$ are now required to produce a polynomial reconstruction of $\boldsymbol{Q}$ within C. Traditionally, this basis has been chosen to be either nodal ($\psi_i(\alpha_j) = \delta_{ij}$ where $\{\alpha_0, \ldots, \alpha_N\}$ are a set of nodes, e.g. the Gauss-Legendre abscissae - see [33]), or modal (e.g. the Legendre polynomials - see [7]).

[89] take the following approach. $\langle \cdot, \cdot \rangle$ is taken to be the usual integral product on $[0, 1]$. Supposing that $N = 2n + 1$ for some $n \in \mathbb{N}$, Gauss-Legendre nodes $\{\alpha_0, \ldots, \alpha_n\}$ are taken. The basis $\Psi = \{\psi_0, ..., \psi_N\} \subset P_N$ is taken with the following properties for $i = 0, \ldots, n$:

$$\begin{cases} \psi_i(\alpha_j) = \delta_{ij} & \psi_i'(\alpha_j) = 0 \\ \psi_{n+1+i}(\alpha_j) = 0 & \psi_{n+1+i}'(\alpha_j) = \delta_{ij} \end{cases} \tag{2.6}$$

Define the following subsets:

$$\Psi^0 = \{\psi_i : 0 \leq i \leq n\} \tag{2.7a}$$
$$\Psi^1 = \{\psi_i : n+1 \leq i \leq 2n+1\} \tag{2.7b}$$

The WENO method (as used in [31]) produces an order-N polynomial reconstruction:

$$w\left(\chi^{(1)}, \chi^{(2)}, \chi^{(3)}\right) \tag{2.8}$$

of the data at time t_n in:

$$\left[x_{i_1}^{(1)}, x_{i_1+1}^{(1)}\right] \times \left[x_{i_2}^{(2)}, x_{i_2+1}^{(2)}\right] \times \left[x_{i_3}^{(3)}, x_{i_3+1}^{(3)}\right] \tag{2.9}$$

It is used as initial data in the problem of finding the Galerkin predictor. Taking representation:

$$w = w_{abc}\psi_a\left(\chi^{(1)}\right)\psi_b\left(\chi^{(2)}\right)\psi_c\left(\chi^{(3)}\right) \tag{2.10}$$

we have for $0 \leq i, j, k \leq n$:

$$w_{ijk} = w\left(\alpha_i, \alpha_j, \alpha_k\right) \tag{2.11a}$$
$$w_{(n+i+1)jk} = \partial_{\chi^{(1)}} w\left(\alpha_i, \alpha_j, \alpha_k\right) \tag{2.11b}$$
$$w_{i(n+j+1)k} = \partial_{\chi^{(2)}} w\left(\alpha_i, \alpha_j, \alpha_k\right) \tag{2.11c}$$
$$w_{ij(n+k+1)} = \partial_{\chi^{(3)}} w\left(\alpha_i, \alpha_j, \alpha_k\right) \tag{2.11d}$$

Take the following temporal nodes, where $\tau_1, \ldots, \tau_N$ are the usual Legendre-Gauss nodes on $[0, 1]$ and $\tau_0 = 0$ or $\tau_0 = 1$ if we are performing a Continuous Galerkin / Discontinuous Galerkin reconstruction, respectively:

$$\{\tau_0, \ldots, \tau_N\} \tag{2.12}$$

Define $\Phi = \{\phi_0, ..., \phi_N\} \subset P_N$ to be the set of Lagrange interpolating polynomials on the temporal nodes. We now define the spatiotemporal polynomial basis $\Theta = \Phi \otimes \Psi \otimes \Psi \otimes \Psi =$

$\{\theta_\beta\}$ for $0 \leq \beta \leq (N+1)^4 - 1$. Define subsets $\Theta^{\iota\xi\kappa} = \Phi \otimes \Psi^\iota \otimes \Psi^\xi \otimes \Psi^\kappa = \left\{\theta_\mu^{\iota\xi\kappa}\right\}$ where $\iota, \xi, \kappa \in \{0, 1\}$ for $0 \leq \mu \leq (N+1)(n+1)^3 - 1$.

Denoting the Galerkin predictor by $\boldsymbol{q}$, take the following set of approximations:

$$\boldsymbol{Q} \approx \theta_\beta \boldsymbol{q}_\beta = \theta_\mu^{\iota\xi\kappa} \boldsymbol{q}_\mu^{\iota\xi\kappa} \tag{2.13a}$$
$$\overrightarrow{\boldsymbol{F}}(\boldsymbol{Q}) \approx \theta_\beta \overrightarrow{\boldsymbol{F}}_\beta = \theta_\mu^{\iota\xi\kappa} \overrightarrow{\boldsymbol{F}}_\mu^{\iota\xi\kappa} \tag{2.13b}$$
$$\overrightarrow{\boldsymbol{B}}(\boldsymbol{Q}) \cdot \tilde{\nabla} \boldsymbol{Q} \approx \theta_\beta \boldsymbol{B}_\beta = \theta_\mu^{\iota\xi\kappa} \boldsymbol{B}_\mu^{\iota\xi\kappa} \tag{2.13c}$$
$$\boldsymbol{S}(\boldsymbol{Q}) \approx \theta_\beta \boldsymbol{S}_\beta = \theta_\mu^{\iota\xi\kappa} \boldsymbol{S}_\mu^{\iota\xi\kappa} \tag{2.13d}$$

for some coefficients $\boldsymbol{q}_\beta, \overrightarrow{\boldsymbol{F}}_\beta, \boldsymbol{B}_\beta, \boldsymbol{S}_\beta$. The *nodal basis representation* is used for the coefficients of Θ^{000}:

$$\overrightarrow{\boldsymbol{F}}_\mu^{000} = \overrightarrow{\boldsymbol{F}}\left(\boldsymbol{q}_\mu^{000}\right) \tag{2.14a}$$
$$\boldsymbol{B}_\mu^{000} = B_1\left(\boldsymbol{q}_\mu^{000}\right) \boldsymbol{q}_\mu^{100} + B_2\left(\boldsymbol{q}_\mu^{000}\right) \boldsymbol{q}_\mu^{010} + B_3\left(\boldsymbol{q}_\mu^{000}\right) \boldsymbol{q}_\mu^{001} \tag{2.14b}$$
$$\boldsymbol{S}_\mu^{000} = \boldsymbol{S}\left(\boldsymbol{q}_\mu^{000}\right) \tag{2.14c}$$

In general, we have:

$$\overrightarrow{\boldsymbol{F}}_\mu^{\iota\xi\kappa} = \partial_\chi^\iota \partial_\upsilon^\xi \partial_\zeta^\kappa \left(\overrightarrow{\boldsymbol{F}}(\boldsymbol{Q})\right) \tag{2.15a}$$
$$\boldsymbol{B}_\mu^{\iota\xi\kappa} = \partial_\chi^\iota \partial_\upsilon^\xi \partial_\zeta^\kappa \left(\overrightarrow{\boldsymbol{B}}(\boldsymbol{Q}) \cdot \tilde{\nabla} \boldsymbol{Q}\right) \tag{2.15b}$$
$$\boldsymbol{S}_\mu^{\iota\xi\kappa} = \partial_\chi^\iota \partial_\upsilon^\xi \partial_\zeta^\kappa \left(\boldsymbol{S}(\boldsymbol{Q})\right) \tag{2.15c}$$

where the right-hand-side is evaluated at the nodal point corresponding to μ. The full expressions are omitted here for brevity's sake, but note that for a one-dimensional system:

$$\boldsymbol{F}_1{}_\mu^{100} = \frac{\partial \boldsymbol{F}\left(\boldsymbol{q}_\mu^{000}\right)}{\partial \boldsymbol{Q}} \cdot \boldsymbol{q}_\mu^{100} \tag{2.16a}$$
$$\begin{aligned} \boldsymbol{B}_\mu^{100} = &\left(\frac{\partial B_1\left(\boldsymbol{q}_\mu^{000}\right)}{\partial \boldsymbol{Q}} \cdot \boldsymbol{q}_\mu^{100}\right) \cdot \boldsymbol{q}_\mu^{100} \\ &+ B_1\left(\boldsymbol{q}_\mu^{000}\right) \cdot \left(\frac{\partial^2 \theta_\kappa^{000}(\chi_\mu, \tau_\mu)}{\partial \chi^2} \boldsymbol{q}_\mu^{000} + \frac{\partial^2 \theta_\kappa^{100}(\chi_\mu, \tau_\mu)}{\partial \chi^2} \boldsymbol{q}_\mu^{100}\right) \end{aligned} \tag{2.16b}$$
$$\boldsymbol{S}_\mu^{100} = \frac{\partial \boldsymbol{S}\left(\boldsymbol{q}_\mu^{000}\right)}{\partial \boldsymbol{Q}} \cdot \boldsymbol{q}_\mu^{100} \tag{2.16c}$$

where χ_μ, τ_μ are the spatial and temporal coordinates where $\theta_\mu^{100} = 0$ and $\partial_\chi \theta_\mu^{100} = 1$. Note that $\frac{\partial B_1}{\partial \boldsymbol{Q}}$ is a rank 3 tensor.

Consider functions f, g of the following form:

$$f\left(\tau, \chi^{(1)}, \chi^{(2)}, \chi^{(3)}\right) = f_\tau(\tau) f_1\left(\chi^{(1)}\right) f_2\left(\chi^{(2)}\right) f_3\left(\chi^{(3)}\right) \tag{2.17a}$$

$$g\left(\tau, \chi^{(1)}, \chi^{(2)}, \chi^{(3)}\right) = g_\tau(\tau) g_1\left(\chi^{(1)}\right) g_2\left(\chi^{(2)}\right) g_3\left(\chi^{(3)}\right) \tag{2.17b}$$

Define the following integral operators:

$$[f, g]^t = f_\tau(t) g_\tau(t) \langle f_1, g_1 \rangle \langle f_2, g_2 \rangle \langle f_3, g_3 \rangle \tag{2.18a}$$

$$\{f, g\} = \langle f_\tau, g_\tau \rangle \langle f_1, g_1 \rangle \langle f_2, g_2 \rangle \langle f_3, g_3 \rangle \tag{2.18b}$$

Multiplying (2.13b) by test function θ_α, using the polynomial approximations for $\boldsymbol{Q}, \overrightarrow{\boldsymbol{F}}, \overrightarrow{\boldsymbol{B}}, \boldsymbol{S}$, and integrating over space and time gives:

$$\left\{\theta_\alpha, \frac{\partial \theta_\beta}{\partial \tau}\right\} \boldsymbol{q}_\beta = \{\theta_\alpha, \theta_\beta\} (\boldsymbol{S}_\beta - \boldsymbol{B}_\beta) - \left\{\theta_\alpha, \frac{\partial \theta_\beta}{\partial \chi^{(k)}}\right\} \boldsymbol{F}_{k\beta} \tag{2.19}$$

2.1.2 Discontinuous Galerkin Method

This method of computing the Galerkin predictor allows solutions to be discontinuous at temporal cell boundaries, and is also suitable for stiff source terms. Integrating (2.19) by parts in time gives:

$$\left([\theta_\alpha, \theta_\beta]^1 - \left\{\frac{\partial \theta_\alpha}{\partial \tau}, \theta_\beta\right\}\right) \boldsymbol{q}_\beta = [\theta_\alpha, \boldsymbol{w}]^0 + \{\theta_\alpha, \theta_\beta\} (\boldsymbol{S}_\beta - \boldsymbol{B}_\beta) - \left\{\theta_\alpha, \frac{\partial \theta_\beta}{\partial \chi^{(k)}}\right\} \boldsymbol{F}_{k\beta} \tag{2.20}$$

where $\boldsymbol{w}$ is the reconstruction obtained at the start of the time step with the WENO method. Take the following ordering:

$$\theta_{(N+1)^3 h + (N+1)^2 i + (N+1) j + k}(\tau, \chi, \upsilon, \zeta) = \phi_h(\tau) \psi_i(\chi) \psi_j(\upsilon) \psi_k(\zeta) \tag{2.21}$$

where $0 \leq h, i, j, k \leq N$. Thus, define the following:

$$U_{\alpha\beta} = [\theta_\alpha, \theta_\beta]^1 - \left\{ \frac{\partial \theta_\alpha}{\partial \tau}, \theta_\beta \right\} = \left(R^1 - M^{\tau,1} \right) \otimes \left(M^\chi \right)^3 \tag{2.22a}$$

$$V^k_{\alpha\beta} = \left\{ \theta_\alpha, \frac{\partial \theta_\beta}{\partial \chi^{(k)}} \right\} = M^\tau \otimes \left(M^\chi \right)^{k-1} \otimes M^{\chi,1} \otimes \left(M^\chi \right)^{3-k} \tag{2.22b}$$

$$\boldsymbol{W}_\alpha = [\theta_\alpha, \Psi_\gamma]^0 \, \boldsymbol{w}_\gamma = R^0 \otimes \left(M^\chi \right)^3 \tag{2.22c}$$

$$Z_{\alpha\beta} = \{\theta_\alpha, \theta_\beta\} = M^\tau \otimes \left(M^\chi \right)^3 \tag{2.22d}$$

where $\{\Psi_\gamma\} = \Psi \otimes \Psi \otimes \Psi$ and:

$$\begin{cases} M^\tau_{ij} = \langle \phi_i, \phi_j \rangle & M^{\tau,1}_{ij} = \left\langle \phi_i', \phi_j \right\rangle \\ M^\chi_{ij} = \langle \psi_i, \psi_j \rangle & M^{\chi,1}_{ij} = \left\langle \psi_i, \psi_j' \right\rangle \\ R^1_{ij} = \phi_i(1) \, \phi_j(1) & \boldsymbol{R^0_i} = \phi_i(0) \end{cases} \tag{2.23}$$

Thus:

$$U_{\alpha\beta} \boldsymbol{q}_\beta = \boldsymbol{W}_\alpha + Z_{\alpha\beta} \left(\boldsymbol{S}_\beta - \boldsymbol{B}_\beta \right) - V^{(k)}_{\alpha\beta} \boldsymbol{F}_{k\beta} \tag{2.24}$$

Take the definitions:

$$\begin{cases} D &= \left(M^\chi \right)^{-1} M^{\chi,1} \\ E &= \left(R^1 - M^{\tau,1} \right) \end{cases} \tag{2.25}$$

Noting that $E\mathbf{1} = \boldsymbol{R^0}$, we have, by inversion of U:

$$\begin{aligned} \boldsymbol{q} = &\left(\mathbf{1} \otimes I^3 \right) \boldsymbol{w} + \left(E^{-1} M^\tau \otimes I^3 \right) \left(\boldsymbol{S} - \boldsymbol{B} \right) \\ &- \left(E^{-1} M^\tau \otimes I^{k-1} \otimes D \otimes I^{3-k} \right) \boldsymbol{F}_k \end{aligned} \tag{2.26}$$

Thus, we have:

$$\begin{aligned} \boldsymbol{q}_{hijk} = &\boldsymbol{w}_{ijk} + \left(E^{-1} M^\tau \right)_{hm} \left(\boldsymbol{S}_{mijk} - \boldsymbol{B}_{mijk} \right) \\ &- \left(E^{-1} M^\tau \right)_{hm} \left(D_{in} \left(\boldsymbol{F}_1 \right)_{mnjk} + D_{jn} \left(\boldsymbol{F}_2 \right)_{mink} + D_{kn} \left(\boldsymbol{F}_3 \right)_{mijn} \right) \end{aligned} \tag{2.27}$$

Note then that $\boldsymbol{q}^{\iota\xi\kappa}$ is a function of $\boldsymbol{S}^{\iota\xi\kappa}, \boldsymbol{B}^{\iota\xi\kappa}, \overrightarrow{\boldsymbol{F}}$:

$$\boldsymbol{q}^{\iota\xi\kappa} = \mathcal{F}\left(\boldsymbol{S}^{\iota\xi\kappa}\right) + \mathcal{F}\left(\boldsymbol{B}^{\iota\xi\kappa}\right) + \mathcal{G}_{\iota\xi\kappa}\left(\overrightarrow{\boldsymbol{F}}^{000}, \ldots, \overrightarrow{\boldsymbol{F}}^{111}\right) \tag{2.28}$$

where $\mathcal{F}, \mathcal{G}_{\iota\xi\kappa}$ are linear functions. Note in turn that, by (2.15c):

$$\boldsymbol{S}^{\iota\xi\kappa} = \mathcal{H}\left(\bigcup_{(0,0,0) \leq (a,b,c) \leq (\iota,\xi,\kappa)} \boldsymbol{q}^{abc}\right) \tag{2.29}$$

where $\mathcal{H}$ is a nonlinear function.

In the case of stiff source terms, the following Picard iteration procedure can be used to solve (2.27), as adapted from [89]:

$$\begin{aligned}\left(\boldsymbol{q}^{\iota\xi\kappa}\right)_{m+1} = \mathcal{F}\left(\mathcal{H}\left(\left(\boldsymbol{q}^{\iota\xi\kappa}\right)_{m+1} \cup \bigcup_{\substack{(0,0,0) \leq (a,b,c) \leq (\iota,\xi,\kappa) \\ (a,b,c) \neq (\iota,\xi,\kappa)}} \left(\boldsymbol{q}^{abc}\right)_m\right)\right) \\ + \mathcal{F}\left(\left(\boldsymbol{B}^{\iota\xi\kappa}\right)_m\right) + \mathcal{G}_{\iota\xi\kappa}\left(\left(\overrightarrow{\boldsymbol{F}}^{000}\right)_m, \ldots, \left(\overrightarrow{\boldsymbol{F}}^{111}\right)_m\right)\end{aligned} \tag{2.30}$$

2.1.3 Continuous Galerkin Method

This method of computing the Galerkin predictor is not suitable for stiff source terms, but is less computationally expensive and ensures continuity across temporal cell boundaries. The first $N+1$ elements of $\boldsymbol{q}$ are fixed by imposing the following condition:

$$\boldsymbol{q}(\chi, 0) = \boldsymbol{w}(\chi) \tag{2.31}$$

For $\boldsymbol{v} \in \mathbb{R}^{(N+1)^2}$ and $X \in M_{(N+1)^2,(N+1)^2}(\mathbb{R})$, let:

$$\boldsymbol{v} = \left(\boldsymbol{v}^{\boldsymbol{0}}, \boldsymbol{v}^{\boldsymbol{1}}\right) \tag{2.32a}$$

$$X = \begin{pmatrix} X^{00} & X^{01} \\ X^{10} & X^{11} \end{pmatrix} \tag{2.32b}$$

where $\boldsymbol{v}^{\mathbf{0}}, X^{00}$ are the components relating solely to the first $N+1$ components of $\boldsymbol{v}$. We only need to find the latter components of $\boldsymbol{q}$, and thus, from (2.19), we have:

$$\begin{aligned}\left\{\theta_\alpha, \frac{\partial \theta_\beta}{\partial \tau}\right\}^{11} \boldsymbol{q}_\beta^1 = \{\theta_\alpha, \theta_\beta\}^{11} \left(\boldsymbol{S}_\beta^1 - \boldsymbol{B}_\beta^1\right) - \left\{\theta_\alpha, \frac{\partial \theta_\beta}{\partial \chi^{(k)}}\right\}^{11} \boldsymbol{F}_{k\beta}^{\,1} \\ + \{\theta_\alpha, \theta_\beta\}^{10} \left(\boldsymbol{S}_\beta^0 - \boldsymbol{B}_\beta^0\right) - \left\{\theta_\alpha, \frac{\partial \theta_\beta}{\partial \chi^{(k)}}\right\}^{10} \boldsymbol{F}_{k\beta}^{\,0}\end{aligned} \tag{2.33}$$

Define the following:

$$U_{\alpha\beta} = \left\{\theta_\alpha, \frac{\partial \theta_\beta}{\partial \tau}\right\}^{11} \tag{2.34a}$$

$$V_{\alpha\beta}^k = \left\{\theta_\alpha, \frac{\partial \theta_\beta}{\partial \chi^{(k)}}\right\}^{11} \tag{2.34b}$$

$$\boldsymbol{W}_\alpha = \{\theta_\alpha, \theta_\beta\}^{10} \left(\boldsymbol{S}_\beta - \boldsymbol{B}_\beta\right)^0 - \left\{\theta_\alpha, \frac{\partial \theta_\beta}{\partial \chi^{(k)}}\right\}^{10} \boldsymbol{F}_{k\beta}^{\,0} \tag{2.34c}$$

$$Z_{\alpha\beta} = \{\theta_\alpha, \theta_\beta\}^{11} \tag{2.34d}$$

Thus:

$$U_{\alpha\beta} \boldsymbol{q}_\beta^1 = \boldsymbol{W}_\alpha + Z_{\alpha\beta} \left(\boldsymbol{S}_\beta^1 - \boldsymbol{B}_\beta^1\right) - V_{\alpha\beta}^k \boldsymbol{F}_{k\beta}^{\,1} \tag{2.35}$$

Note that, as with the discontinuous Galerkin method, $\boldsymbol{W}$ has no dependence on the degrees of freedom in $\boldsymbol{q}$. As the source terms are not stiff, the following iteration is used:

$$U_{\alpha\beta} \left(\boldsymbol{q}_\beta^1\right)_{m+1} = \boldsymbol{W}_\alpha + Z_{\alpha\beta} \left(\left(\boldsymbol{S}_\beta^1\right)_m - \left(\boldsymbol{B}_\beta^1\right)_m\right) - V_{\alpha\beta}^k \left(\boldsymbol{F}_{k\beta}^{\,1}\right)_m \tag{2.36}$$

2.1.4 Convergence Properties

In [64] it was proved that for traditional choices of polynomial bases, the eigenvalues of $U^{-1}V^i$ are all 0 for any $N \in \mathbb{N}$, for $i = 1, 2, 3$. This implies that in the conservative, homogeneous case ($\overrightarrow{\boldsymbol{B}} = \boldsymbol{S} = \mathbf{0}$), owing to the Banach Fixed Point Theorem, existence and uniqueness of a solution are established, and convergence to this solution is guaranteed. As noted in [39], in the linear case it is implied that the iterative procedure converges after at most $N+1$ iterations. A proof of this result for the Montecinos-Balsara polynomial basis

class is now provided here. For the theory in linear algebra required for this section, please consult a standard textbook on the subject, such as [93].

Take the definitions (2.23), (2.25). Consider that:

$$U^{-1}V^k = E^{-1}M^\tau \otimes I^{k-1} \otimes D \otimes I^{3-k} \tag{2.37}$$

Therefore:

$$\left(U^{-1}V^k\right)^m = \left(E^{-1}M^\tau\right)^m \otimes \left(I^{k-1}\right)^m \otimes D^m \otimes \left(I^{3-k}\right)^m \tag{2.38}$$

A matrix X is nilpotent ($X^k = 0$ for some $k \in \mathbb{N}$) if and only if all its eigenvalues are 0. Note that $U^{-1}V^k$ is nilpotent if $D^m = 0$ for some $m \in \mathbb{N}$.

Note that if $p \in P_N$ then $p = a_j\psi_j$ for some unique coefficient vector $\boldsymbol{a}$. Thus, taking inner products with ψ_i, we have $\langle\psi_i, \psi_j\rangle\, a_j = \langle\psi_i, p\rangle$ for $i = 0, ..., N$. This produces the following result:

$$p = a_j\psi_j \Leftrightarrow \boldsymbol{a} = \left(M^\chi\right)^{-1}\boldsymbol{x},\ x_i = \langle\psi_i, p\rangle \tag{2.39}$$

Taking $\boldsymbol{a} \in \mathbb{R}^{N+1}$, define:

$$p = a_0\psi_0 + \ldots + a_N\psi_N \in P_N \tag{2.40}$$

Note that:

$$\left(M^{\chi,1}\boldsymbol{a}\right)_i = \left\langle\psi_i, \psi_0'\right\rangle a_0 + \ldots + \left\langle\psi_i, \psi_N'\right\rangle a_N = \left\langle\psi_i, p'\right\rangle \tag{2.41}$$

Thus, by (2.39):

$$\left(\left(M^\chi\right)^{-1} M^{\chi,1}\boldsymbol{a}\right)_i \psi_i = \left(D\boldsymbol{a}\right)_i \psi_i = p' \tag{2.42}$$

By induction:

$$\left(D^m\boldsymbol{a}\right)_i \psi_i = p^{(m)} \tag{2.43}$$

for any $m \in \mathbb{N}$. As $p \in P_N$, $D^{N+1}\boldsymbol{a} = \mathbf{0}$. As $\boldsymbol{a}$ was chosen arbitrarily, $D^{N+1} = 0$. No specific choice has been made for $N \in \mathbb{N}$ and thus the result holds in general.

Thus, in the case that $\overrightarrow{\boldsymbol{B}} = \boldsymbol{S} = \mathbf{0}$, existence and uniqueness of a solution are established, and convergence to this solution is guaranteed for the iterative solution to (2.24) in the Discontinuous Galerkin case, and (2.35) in the Continuous Galerkin case.

2.2 Operator Splitting Methods

The material in this section is published in [63] and [66].

A new second-order numerical scheme based on an operator splitting is proposed for the GPR model. The homogeneous part of the system is solved with a finite volume method based on a WENO reconstruction, and the temporal ODEs are solved using some analytic results presented here. Whilst it is not possible to attain arbitrary-order accuracy with this scheme (as with ADER-WENO schemes used previously), the attainable order of accuracy is often sufficient, and solutions are computationally cheap when compared with other available schemes. The new scheme is compared with an ADER-WENO scheme for various test cases, and a convergence study is undertaken to demonstrate its order of accuracy.

A method for modeling non-Newtonian fluids (dilatants and pseudoplastics) by a power law under the GPR model is also presented, along with a new numerical scheme for solving this system. The scheme is also modified to solve the corresponding system for power-law elastoplastic solids. The method is found to perform favorably against problems with known exact solutions, and numerical solutions published in the open literature. It is simple to implement, and to the best of the authors' knowledge it is currently the only method for solving this modified version of the GPR model.

2.2.1 Strang Splitting

Note that (1a), (1b), (1c), (1d), (3) can be written in the following form:

$$\frac{\partial \boldsymbol{Q}}{\partial t} + \boldsymbol{\nabla} \cdot \boldsymbol{F}(\boldsymbol{Q}) + \boldsymbol{B}(\boldsymbol{Q}) \cdot \nabla \boldsymbol{Q} = \boldsymbol{S}(\boldsymbol{Q}) \tag{2.44}$$

As described in [126], a viable way to solve inhomogeneous systems of PDEs is to employ an operator splitting. That is, the following subsystems are solved:

$$\frac{\partial \boldsymbol{Q}}{\partial t} + \boldsymbol{\nabla} \cdot \boldsymbol{F}(\boldsymbol{Q}) + \boldsymbol{B}(\boldsymbol{Q}) \cdot \nabla \boldsymbol{Q} = \boldsymbol{0} \tag{2.45a}$$

$$\frac{d\boldsymbol{Q}}{dt} = \boldsymbol{S}(\boldsymbol{Q}) \tag{2.45b}$$

The advantage of this approach is that specialized solvers can be employed to compute the results of the different subsystems. Let $H^{\delta t}, S^{\delta t}$ be the operators that take data $\boldsymbol{Q}(x,t)$ to $\boldsymbol{Q}(x,t+\delta t)$ under systems (2.45a) and (2.45b) respectively. A second-order scheme (in time) for solving the full set of PDEs over time step $[0, \Delta t]$ is obtained by calculating $\boldsymbol{Q}_{\boldsymbol{\Delta t}}$ using a Strang splitting:

$$\boldsymbol{Q}_{\boldsymbol{\Delta t}} = S^{\frac{\Delta t}{2}} H^{\Delta t} S^{\frac{\Delta t}{2}} \boldsymbol{Q}_{\boldsymbol{0}} \tag{2.46}$$

In the scheme proposed here, the homogeneous subsystem will be solved using a WENO reconstruction of the data, followed by a finite volume update, and the temporal ODEs will be solved with appropriate ODE solvers. It should be noted that there are other choices of solvers for the homogeneous system that could have been made (e.g. see MUSCL, SLIC, and WAF, among others in [126]). The WENO method was chosen due to the arbitrarily high-order spatial reconstructions it is able to produce. This new scheme will be referred to here as *the Split-WENO method*.

Noting that $\frac{d\rho}{dt} = 0$ over the ODE time step, the operator S entails solving the following systems:

$$\frac{dA}{dt} = \frac{-3}{\tau_1} (\det A)^{\frac{5}{3}} A \operatorname{dev}(G) \tag{2.47a}$$

$$\frac{d\boldsymbol{J}}{dt} = -\frac{1}{\tau_2} \frac{T\rho_0}{T_0 \rho} \boldsymbol{J} \tag{2.47b}$$

These systems can be solved concurrently with a stiff ODE solver. The Jacobians of these two systems to be used in an ODE solver are given in A.2 and A.2. However, these systems can also be solved separately, using the analytical results presented in 2.2.3 and 2.2.4, under specific assumptions. The second-order Strang splitting is then:

$$\boldsymbol{Q}_{\boldsymbol{\Delta t}} = D^{\frac{\Delta t}{2}} T^{\frac{\Delta t}{2}} H^{\Delta t} T^{\frac{\Delta t}{2}} D^{\frac{\Delta t}{2}} \boldsymbol{Q}_{\boldsymbol{0}} \tag{2.48}$$

where $D^{\delta t}, T^{\delta t}$ are the operators solving the distortion and thermal impulse ODEs respectively, over time step δt. This allows us to bypass the relatively computationally costly process of solving these systems numerically.

The constraint (17) is enforced by rescaling the singular values of the distortion all by the same factor at each time step, to ensure that $\det A = \frac{\rho}{\rho_0}$.

2.2.2 Homogeneous System

A WENO reconstruction of the cell-averaged data is performed at the start of the time step (as described in [40]). Focusing on a single cell C_i at time t_n, we have $\boldsymbol{w}^n(\boldsymbol{x}) = \boldsymbol{w}^n{}_p \Psi_p(\boldsymbol{\chi}(\boldsymbol{x}))$ in C_i where Ψ_p is a tensor product of basis functions in each of the spatial dimensions. The flux in C is approximated by $\boldsymbol{F}(\boldsymbol{x}) \approx \boldsymbol{F}(\boldsymbol{w}_p)\Psi_p(\boldsymbol{\chi}(\boldsymbol{x}))$. $\boldsymbol{w}_p$ are stepped forwards half a time step using the update formula:

$$\begin{aligned}\frac{\boldsymbol{w}_{\boldsymbol{p}}^{n+\frac{1}{2}} - \boldsymbol{w}_{\boldsymbol{p}}^{n}}{\Delta t/2} = &- \boldsymbol{F}\left(\boldsymbol{w}_{\boldsymbol{k}}^{n}\right) \cdot \nabla \Psi_k(\boldsymbol{\chi}_{\boldsymbol{p}}) \\ &- \boldsymbol{B}\left(\boldsymbol{w}_{\boldsymbol{p}}^{n}\right) \cdot \left(\boldsymbol{w}_{\boldsymbol{k}}^{n} \nabla \Psi_k(\boldsymbol{\chi}_{\boldsymbol{p}})\right)\end{aligned} \tag{2.49}$$

i.e.

$$\boldsymbol{w}_{\boldsymbol{p}}^{n+\frac{1}{2}} = \boldsymbol{w}_{\boldsymbol{p}}^{n} - \frac{\Delta t}{2\Delta x}\begin{pmatrix}\boldsymbol{F}\left(\boldsymbol{w}_{\boldsymbol{k}}^{n}\right) \cdot \nabla \Psi_k(\boldsymbol{\chi}_{\boldsymbol{p}}) \\ +\boldsymbol{B}\left(\boldsymbol{w}_{\boldsymbol{p}}^{n}\right) \cdot \left(\boldsymbol{w}_{\boldsymbol{k}}^{n} \nabla \Psi_k(\boldsymbol{\chi}_{\boldsymbol{p}})\right)\end{pmatrix} \tag{2.50}$$

where $\boldsymbol{\chi}_{\boldsymbol{p}}$ is the node corresponding to Ψ_p. This evolution to the middle of the time step is similar to that used in the second-order MUSCL and SLIC schemes (see [126]) and, as with those schemes, it is integral to giving the method presented here its second-order accuracy.

Integrating (2.45a) over C gives:

$$\boldsymbol{Q}_{\boldsymbol{i}}^{\boldsymbol{n+1}} = \boldsymbol{Q}_{\boldsymbol{i}}^{\boldsymbol{n}} - \Delta t_n \left(\boldsymbol{P}_{\boldsymbol{i}}^{\boldsymbol{n+\frac{1}{2}}} + \boldsymbol{D}_{\boldsymbol{i}}^{\boldsymbol{n+\frac{1}{2}}}\right) \tag{2.51}$$

where

$$\boldsymbol{Q}_i^n = \frac{1}{V}\int_C \boldsymbol{Q}\left(\boldsymbol{x}, t_n\right) d\boldsymbol{x} \tag{2.52a}$$

$$\boldsymbol{P}_i^{n+\frac{1}{2}} = \frac{1}{V}\int_C \boldsymbol{B}\left(\boldsymbol{Q}\left(\boldsymbol{x}, t_{n+\frac{1}{2}}\right)\right)\cdot\nabla\boldsymbol{Q}\left(\boldsymbol{x}, t_{n+\frac{1}{2}}\right) d\boldsymbol{x} \tag{2.52b}$$

$$\boldsymbol{D}_i^{n+\frac{1}{2}} = \frac{1}{V}\oint_{\partial C} \boldsymbol{\mathcal{D}}\left(\boldsymbol{Q}^-\left(\boldsymbol{s}, t_{n+\frac{1}{2}}\right), \boldsymbol{Q}^+\left(\boldsymbol{s}, t_{n+\frac{1}{2}}\right)\right) d\boldsymbol{s} \tag{2.52c}$$

where V is the volume of C and $\boldsymbol{Q}^-, \boldsymbol{Q}^+$ are the interior and exterior extrapolated states at the boundary of C, respectively.

Note that (2.45a) can be rewritten as:

$$\frac{\partial \boldsymbol{Q}}{\partial t} + \boldsymbol{M}\left(\boldsymbol{Q}\right)\cdot\nabla\boldsymbol{Q} = \boldsymbol{0} \tag{2.53}$$

where $\boldsymbol{M} = \frac{\partial \boldsymbol{F}}{\partial \boldsymbol{Q}} + \boldsymbol{B}$. Let $\boldsymbol{n}$ be the normal to the boundary at point $\boldsymbol{s} \in \partial C$. For the GPR model, $\hat{M} = \boldsymbol{M}\left(\boldsymbol{Q}\left(\boldsymbol{s}\right)\right)\cdot\boldsymbol{n}$ is a diagonalizable matrix with decomposition $\hat{M} = \hat{R}\hat{\Lambda}\hat{R}^{-1}$ where the columns of $\hat{R}$ are the right eigenvectors and $\hat{\Lambda}$ is the diagonal matrix of eigenvalues. Define also $\hat{\boldsymbol{F}} = \boldsymbol{F}\cdot\boldsymbol{n}$ and $\hat{B} = \boldsymbol{B}\cdot\boldsymbol{n}$. Using these definitions, the interface terms arising in the FV formula have the following form:

$$\begin{aligned}\boldsymbol{\mathcal{D}}\left(\boldsymbol{Q}^-, \boldsymbol{Q}^+\right) = \frac{1}{2}\left(\hat{\boldsymbol{F}}\left(\boldsymbol{Q}^+\right) + \hat{\boldsymbol{F}}\left(\boldsymbol{Q}^-\right)\right) \\ + \frac{1}{2}\left(\tilde{B}\left(\boldsymbol{Q}^+ - \boldsymbol{Q}^-\right) + \tilde{M}\left(\boldsymbol{Q}^+ - \boldsymbol{Q}^-\right)\right)\end{aligned} \tag{2.54}$$

$\tilde{M}$ is chosen to either correspond to a Rusanov/Lax-Friedrichs flux (see [126]):

$$\tilde{M} = \max\left(\max\left|\hat{\Lambda}\left(\boldsymbol{Q}^+\right)\right|, \max\left|\hat{\Lambda}\left(\boldsymbol{Q}^-\right)\right|\right) \tag{2.55}$$

or a Roe flux (see [38]):

$$\hat{M} = \left|\int_0^1 M\left(\boldsymbol{q}^- + z\left(\boldsymbol{q}^+ - \boldsymbol{q}^-\right)\right) dz\right| \tag{2.56}$$

or a simplified Osher–Solomon flux (see [37, 38]):

$$\tilde{M} = \int_0^1 \left|\hat{M}\left(\boldsymbol{Q}^- + z\left(\boldsymbol{Q}^+ - \boldsymbol{Q}^-\right)\right)\right| dz \tag{2.57}$$

where

$$\left|\hat{M}\right| = \hat{R}\left|\hat{\Lambda}\right|\hat{R}^{-1} \tag{2.58}$$

$\tilde{B}$ takes the following form:

$$\tilde{B} = \int_0^1 \hat{B}\left(\boldsymbol{Q}^- + z\left(\boldsymbol{Q}^+ - \boldsymbol{Q}^-\right)\right) dz \tag{2.59}$$

It was found that the Osher-Solomon flux would often produce slightly less diffusive results, but that it was more computationally expensive, and also had a greater tendency to introduce numerical artifacts.

$\boldsymbol{P}_i^{n+\frac{1}{2}}, \boldsymbol{D}_i^{n+\frac{1}{2}}$ are calculated using an $N+1$-point Gauss-Legendre quadrature, replacing $\boldsymbol{Q}\left(\boldsymbol{x}, t_{n+\frac{1}{2}}\right)$ with $\boldsymbol{w}^{n+\frac{1}{2}}(\boldsymbol{x})$.

2.2.3 Thermal Impulse ODEs

Taking the EOS for the GPR model (6) and denoting by $E_2^{(A)}, E_2^{(J)}$ the components of E_2 depending on A and $\boldsymbol{J}$ respectively, we have:

$$\begin{aligned} T &= \frac{E_1}{c_v} \\ &= \frac{E - E_2^{(A)}(\rho, s, A) - E_3(\boldsymbol{v})}{c_v} - \frac{1}{c_v} E_2^{(J)}(\boldsymbol{J}) \\ &= c_1 - c_2 \|\boldsymbol{J}\|^2 \end{aligned} \tag{2.60}$$

where:

$$c_1 = \frac{E - E_2^{(A)}(A) - E_3(\boldsymbol{v})}{c_v} \tag{2.61a}$$

$$c_2 = \frac{c_t^2}{2c_v} \tag{2.61b}$$

Over the time period of the ODE (2.47b), $c_1, c_2 > 0$ are constant. We have:

$$\frac{dJ_i}{dt} = -\left(\frac{1}{\tau_2}\frac{\rho_0}{T_0\rho}\right) J_i\left(c_1 - c_2\|\boldsymbol{J}\|^2\right) \tag{2.62}$$

Therefore:

$$\frac{d}{dt}\left(J_i^2\right) = J_i^2\left(-a + b\left(J_1^2 + J_2^2 + J_3^2\right)\right) \tag{2.63}$$

where

$$a = \frac{2\rho_0}{\tau_2 T_0 \rho c_v}\left(E - E_2^{(A)}(A) - E_3(\boldsymbol{v})\right) \tag{2.64a}$$

$$b = \frac{\rho_0 c_t^2}{\tau_2 T_0 \rho c_v} \tag{2.64b}$$

Note that this is a generalized Lotka-Volterra system in $\{J_1^2, J_2^2, J_3^2\}$. It has the following analytical solution:

$$\boldsymbol{J}(t) = \boldsymbol{J}(0)\sqrt{\frac{1}{e^{at} - \frac{b}{a}\left(e^{at} - 1\right)\|\boldsymbol{J}(0)\|^2}} \tag{2.65}$$

2.2.4 Distortion ODEs

Let $k_0 = \frac{3}{\tau_1}\left(\frac{\rho}{\rho_0}\right)^{\frac{5}{3}} > 0$ and let A have singular value decomposition $U\Sigma V^T$. Then:

$$G = \left(U\Sigma V^T\right)^T U\Sigma V^T = V\Sigma^2 V^T \tag{2.66}$$

$$\operatorname{tr}(G) = \operatorname{tr}\left(V\Sigma^2 V^T\right) = \operatorname{tr}\left(\Sigma^2 V^T V\right) = \operatorname{tr}\left(\Sigma^2\right) \tag{2.67}$$

Therefore:

$$\begin{aligned}\frac{dA}{dt} &= -k_0 U\Sigma V^T\left(V\Sigma^2 V^T - \frac{\operatorname{tr}(\Sigma^2)}{3} I\right) \\ &= -k_0 U\Sigma\left(\Sigma^2 - \frac{\operatorname{tr}(\Sigma^2)}{3}\right) V^T \\ &= -k_0 U\Sigma \operatorname{dev}\left(\Sigma^2\right) V^T\end{aligned} \tag{2.68}$$

It is a common result that[1]:

$$d\Sigma = U^T dA V \tag{2.69}$$

and thus:

$$\frac{d\Sigma}{dt} = -k_0 \Sigma \operatorname{dev}\left(\Sigma^2\right) \tag{2.70}$$

Using a fast 3×3 SVD algorithm (such as in [82]), U, V, Σ can be obtained, after which the following procedure is applied to Σ, giving $A(t) = U\Sigma(t) V^T$.

Denote the singular values of A by a_1, a_2, a_3. Then:

$$\Sigma \operatorname{dev}\left(\Sigma^2\right) = \begin{pmatrix} a_1\left(a_1^2 - \hat{a}\right) & 0 & 0 \\ 0 & a_2\left(a_2^2 - \hat{a}\right) & 0 \\ 0 & 0 & a_3\left(a_3^2 - \hat{a}\right) \end{pmatrix} \tag{2.71}$$

where

$$\hat{a} = \frac{a_1^2 + a_2^2 + a_3^2}{3} \tag{2.72}$$

Letting $x_i = \frac{a_i^2}{\det(A)^{\frac{2}{3}}} = \frac{a_i^2}{\left(\frac{\rho}{\rho_0}\right)^{\frac{2}{3}}}$ we have:

$$\frac{dx_i}{d\tau} = -3x_i\left(x_i - \bar{x}\right) \tag{2.73}$$

where $\tau = \frac{2}{\tau_1}\left(\frac{\rho}{\rho_0}\right)^{\frac{7}{3}} t$ and $\bar{x}$ is the arithmetic mean of x_1, x_2, x_3. This ODE system travels along the surface $\Psi = \{x_1, x_2, x_3 > 0, x_1 x_2 x_3 = 1\}$ to the point $x_1, x_2, x_3 = 1$. This surface is symmetrical in the planes $x_1 = x_2$, $x_1 = x_3$, $x_2 = x_3$. As such, given that the system is autonomous, the paths of evolution of the x_i cannot cross the intersections of these planes with Ψ. Thus, any non-strict inequality of the form $x_i \geq x_j \geq x_k$ is maintained for the whole history of the system. By considering (2.73) it is clear that in this case x_i is monotone decreasing, x_k is monotone increasing, and the time derivative of x_j may switch sign.

[1] This does not necessitate the U, V are constant. See section 3.2 of [49] for a full derivation.

Note that we have:

$$\begin{cases} \frac{dx_i}{d\tau} = -x_i\left(2x_i - x_j - x_k\right) = -x_i\left(2x_i - x_j - \frac{1}{x_i x_j}\right) \\ \frac{dx_j}{d\tau} = -x_j\left(2x_j - x_k - x_i\right) = -x_j\left(2x_j - x_i - \frac{1}{x_i x_j}\right) \end{cases} \tag{2.74}$$

Thus, an ODE solver can be used on these two equations to effectively solve the ODEs for all 9 components of A. Note that:

$$\frac{dx_j}{dx_i} = \frac{x_j}{x_i}\frac{2x_j - x_i - \frac{1}{x_i x_j}}{2x_i - x_j - \frac{1}{x_i x_j}} \tag{2.75}$$

This has solution:

$$x_j = \frac{c + \sqrt{c^2 + 4\left(1-c\right)x_i^3}}{2x_i^2} \tag{2.76}$$

where

$$c = -\frac{x_{i,0}\left(x_{i,0}x_{j,0}^2 - 1\right)}{x_{i,0} - x_{j,0}} \in (-\infty, 0] \tag{2.77}$$

In the case that $x_{i,0} = x_{j,0}$, we have $x_i = x_j$ for all time. Thus, the ODE system for A has been reduced to a single ODE, as $x_j\left(x_i\right)$ can be inserted into the RHS of the equation for $\frac{dx_i}{d\tau}$. However, it is less computationally expensive to evolve the system presented in (2.74).

2.2.4.1 Bounds on the Solutions

If any of the relations in $x_i \geq x_j \geq x_k$ are in fact equalities, equality is maintained throughout the history of the system. This can be seen by noting that the time derivatives of the equal variables are in this case equal. If $x_j = x_k$ then $x_i = \frac{1}{x_j^2}$. Combining these results, the path of the system in (x_i, x_j) coordinates is in fact confined to the curved triangular region:

$$\left\{(x_i, x_j) : x_i \leq x_i^0 \cap x_i \geq x_j \cap x_i \geq \frac{1}{x_j^2}\right\} \tag{2.78}$$

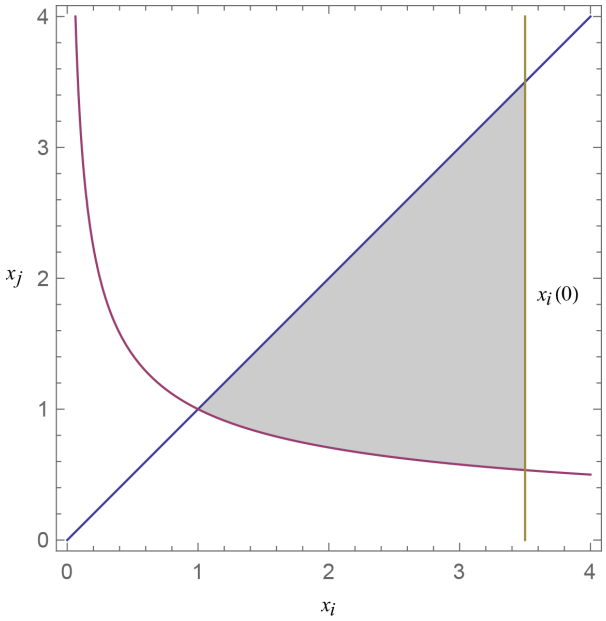

Figure 2.1: Region to which x_i, x_j are confined in the evolution of the distortion ODEs (shaded)

This is demonstrated in Figure 2.1 on page 54. By (2.74), the rate of change of x_i at a particular value $x_i = x_i^*$ is given by:

$$-x_i^* \left(2x_i^* - x_j - \frac{1}{x_i^* x_j} \right) \tag{2.79}$$

Note that:

$$\frac{d}{dx_j} \left(2x_i^* - x_j - \frac{1}{x_i^* x_j} \right) = -1 + \frac{1}{x_i^* x_j^2} = 0 \tag{2.80}$$
$$\Rightarrow x_j = \frac{1}{\sqrt{x_i^*}}$$

$$\frac{d^2}{dx_j^2} \left(2x_i^* - x_j - \frac{1}{x_i^* x_j} \right) = \frac{-2}{x_i^* x_j^3} < 0 \tag{2.81}$$

Thus, x_i decreases fastest on the line $x_i = \frac{1}{x_j^2}$ (the bottom boundary of the region given in Figure 2.1 on page 54), and slowest on the line $x_i = x_j$. The rates of change of x_i along

these two lines are given respectively by:

$$\frac{dx_i}{d\tau} = -2x_i\left(x_i - \sqrt{\frac{1}{x_i}}\right) \tag{2.82a}$$

$$\frac{dx_i}{d\tau} = -x_i\left(x_i - \frac{1}{x_i^2}\right) \tag{2.82b}$$

These have implicit solutions:

$$\tau = \left(f\left(\sqrt{x_i}\right) + g\left(\sqrt{x_i}\right)\right) - \left(f\left(\sqrt{x_i^0}\right) + g\left(\sqrt{x_i^0}\right)\right) \equiv F_1\left(x_i; x_i^0\right) \tag{2.83a}$$

$$\tau = \left(f\left(x_i\right) - g\left(x_i\right)\right) - \left(f\left(x_i^0\right) - g\left(x_i^0\right)\right) \equiv F_2\left(x_i; x_i^0\right) \tag{2.83b}$$

where

$$f\left(x_i\right) = \frac{1}{6}\log\left(\frac{x_i^2 + x_i + 1}{\left(x_i - 1\right)^2}\right) \tag{2.84a}$$

$$g\left(x_i\right) = \frac{1}{\sqrt{3}}\tan^{-1}\left(\frac{2x_i + 1}{\sqrt{3}}\right) \tag{2.84b}$$

As (2.73) is an autonomous system of ODEs, it has the property that its limit $x_1 = x_2 = x_3 = 1$ is never obtained in finite time, in precise arithmetic. In floating point arithmetic we may say that the system has converged when $x_i - 1 < \epsilon$ (machine epsilon) for each i. This happens when:

$$\tau > F_2\left(1 + \epsilon; x_i^0\right) \tag{2.85}$$

This provides a quick method to check whether it is necessary to run the ODE solver in a particular cell. If the following condition is satisfied then we know the system in that cell converges to the ground state over the time interval in which the ODE system is calculated:

$$\frac{2}{\tau_1}\left(\frac{\rho}{\rho_0}\right)^{\frac{7}{3}}\Delta t > F_2\left(1 + \epsilon; \max\left\{x_i^0\right\}\right) \tag{2.86}$$

If the fluid is very inviscid, resulting in a stiff ODE, the critical time is lower, and there is more chance that the ODE system in the cell reaches its limit in Δt. This check potentially saves a lot of computationally expensive stiff ODE solves. The same goes for if the flow is

slow-moving, as the system will be closer to its ground state at the start of the time step and is more likely to converge over Δt. Similarly, if the following condition is satisfied then we know for sure that an ODE solver is necessary, as the system certainly will not have converged over the timestep:

$$\frac{2}{\tau_1}\left(\frac{\rho}{\rho_0}\right)^{\frac{7}{3}}\Delta t < F_1\left(1+\epsilon; \max\left\{x_i^0\right\}\right) \tag{2.87}$$

2.2.4.2 Newtonian Fluids

We now explore cases when even the reduced ODE system (2.73) need not be solved numerically. Define the following variables:

$$m = \frac{x_1 + x_2 + x_3}{3} \tag{2.88a}$$

$$u = \frac{(x_1 - x_2)^2 + (x_2 - x_3)^2 + (x_3 - x_1)^2}{3} \tag{2.88b}$$

It is a standard result that $m \geq \sqrt[3]{x_1 x_2 x_3}$. Thus, $m \geq 1$. Note that u is proportional to the internal energy contribution from the distortion. From (2.73) we have:

$$\frac{du}{d\tau} = -18\left(1 - m\left(m^2 - \frac{5}{6}u\right)\right) \tag{2.89a}$$

$$\frac{dm}{d\tau} = -u \tag{2.89b}$$

Combining these equations, we have:

$$\frac{d^2m}{d\tau^2} = -\frac{du}{d\tau} = 18\left(1 - m\left(m^2 - \frac{5}{6}u\right)\right) \tag{2.90}$$

Therefore:

$$\begin{cases} \frac{d^2m}{d\tau^2} + 15m\frac{dm}{d\tau} + 18\left(m^3 - 1\right) = 0 \\ m\left(0\right) = m_0 \\ m^{'}\left(0\right) = -u_0 \end{cases} \tag{2.91}$$

We make the following assumption, noting that it is true in all physical situations tested in this study:

$$m(t) = 1 + \eta(t), \quad \eta \ll 1 \; \forall t \geq 0 \tag{2.92}$$

Thus, we have the linearized ODE:

$$\begin{cases} \frac{d^2\eta}{d\tau^2} + 15\frac{d\eta}{d\tau} + 54\eta = 0 \\ \eta(0) = m_0 - 1 \\ \eta^{'}(0) = -u_0 \end{cases} \tag{2.93}$$

This is a Sturm-Liouville equation with solution:

$$\eta(\tau) = \frac{e^{-9\tau}}{3}\left(ae^{3\tau} - b\right) \tag{2.94}$$

where

$$a = 9m_0 - u_0 - 9 \tag{2.95a}$$

$$b = 6m_0 - u_0 - 6 \tag{2.95b}$$

Thus, we also have:

$$u(\tau) = e^{-9\tau}\left(2ae^{3\tau} - 3b\right) \tag{2.96}$$

Denote the following:

$$m_{\Delta t} = 1 + \eta\left(\frac{2}{\tau_1}\left(\frac{\rho}{\rho_0}\right)^{\frac{7}{3}}\Delta t\right) \tag{2.97a}$$

$$u_{\Delta t} = u\left(\frac{2}{\tau_1}\left(\frac{\rho}{\rho_0}\right)^{\frac{7}{3}}\Delta t\right) \tag{2.97b}$$

Once these have been found, we have:

$$\frac{x_i + x_j + x_k}{3} = m_{\Delta t} \tag{2.98a}$$

$$\frac{(x_i - x_j)^2 + (x_j - x_k)^2 + (x_k - x_i)^2}{3} = u_{\Delta t} \tag{2.98b}$$

$$x_i x_j x_k = 1 \tag{2.98c}$$

This gives:

$$x_i = \frac{\Xi}{6} + \frac{u_{\Delta t}}{\Xi} + m_{\Delta t} \tag{2.99a}$$

$$x_j = \frac{1}{2}\left(\sqrt{\frac{x_i\left(3m_{\Delta t} - x_i\right)^2 - 4}{x_i}} + 3m_{\Delta t} - x_i\right) \tag{2.99b}$$

$$x_k = \frac{1}{x_i x_j} \tag{2.99c}$$

where

$$\Xi = \sqrt[3]{6\left(\sqrt{81\Delta^2 - 6u_{\Delta t}^3} + 9\Delta\right)} \tag{2.100a}$$

$$\Delta = -2m_{\Delta t}^3 + m_{\Delta t}u_{\Delta t} + 2 \tag{2.100b}$$

Note that taking the real parts of the above expression for x_i gives:

$$x_i = \frac{\sqrt{6u_{\Delta t}}}{3}\cos\left(\frac{\theta}{3}\right) + m_{\Delta t} \tag{2.101a}$$

$$\theta = \tan^{-1}\left(\frac{\sqrt{6u_{\Delta t}^3 - 81\Delta^2}}{9\Delta}\right) \tag{2.101b}$$

At this point it is not clear which values of $\{x_i, x_j, x_k\}$ are taken by x_1, x_2, x_3. However, this can be inferred from the fact that any relation $x_i \geq x_j \geq x_k$ is maintained over the lifetime of the system. Thus, the stiff ODE solver has been obviated by a few arithmetic operations.

2.2.4.3 Power Law Fluids

The stress-strain relationships for various kinds of fluids are shown in Figure 2.2 on page 59. Dilatants and pseudoplastics may be modeled using the following power law, with $n > 1$ and

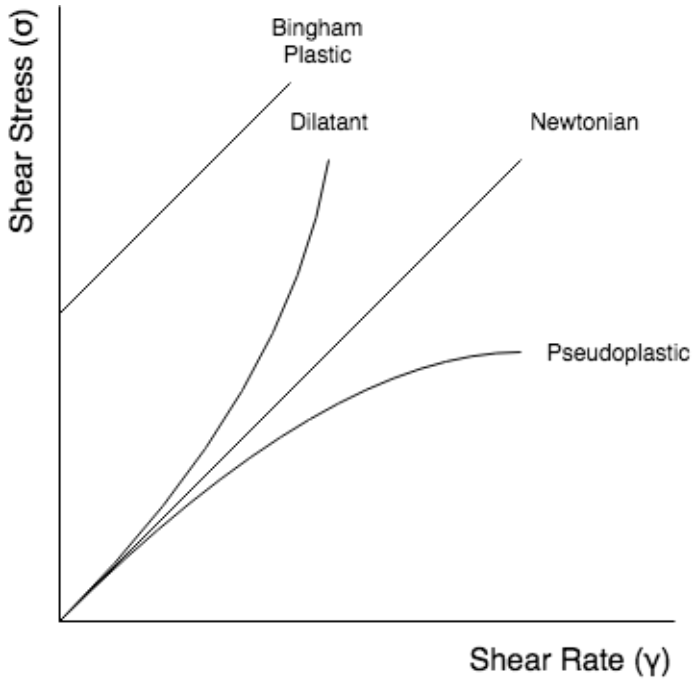

Figure 2.2: Stress-strain relationships for different kinds of fluids (source: [130])

$0 < n < 1$, respectively (see [122]):

$$\boldsymbol{\sigma} = K \left|\dot{\boldsymbol{\gamma}}\right|^{n-1} \dot{\boldsymbol{\gamma}} \tag{2.102}$$

$$\dot{\boldsymbol{\gamma}} = \nabla \boldsymbol{v} + \nabla \boldsymbol{v}^T - \frac{2 \operatorname{tr}(\nabla \boldsymbol{v})}{3} I \tag{2.103}$$

$K > 0$ is known as the *consistency*, and $K \left|\dot{\boldsymbol{\gamma}}\right|^{n-1}$ is the *apparent viscosity*. The norm is taken to be:

$$|X| = \sqrt{\frac{1}{2} X_{ij} X_{ij}} = \frac{\|X\|_F}{\sqrt{2}} \tag{2.104}$$

In [35] it was noted that when expressing the state variables as an asymptotic expansion in the relaxation parameter τ_1, to first order we have:

$$\boldsymbol{\sigma} = \frac{1}{6} \tau_1 \rho_0 c_s^2 \left(\nabla \boldsymbol{v} + \nabla \boldsymbol{v}^T - \frac{2}{3} \operatorname{tr}(\nabla \boldsymbol{v}) \boldsymbol{I} \right) \tag{2.105}$$

Thus, for a power law fluid, we require that:

$$\frac{1}{6} \tau_1 \rho_0 c_s^2 = K \left|\dot{\boldsymbol{\gamma}}\right|^{n-1} \tag{2.106}$$

Taking moduli of both sides of (2.105), we also have:

$$|\boldsymbol{\sigma}| = \frac{1}{6}\tau_1 \rho_0 c_s^2 \left|\dot{\boldsymbol{\gamma}}\right| \tag{2.107}$$

Combining these two relationships, we obtain:

$$\tau_1 = \frac{6K^{\frac{1}{n}}}{\rho_0 c_s^2}\left|\frac{1}{\boldsymbol{\sigma}}\right|^{\frac{1-n}{n}} := \tau_0 \left|\frac{1}{\boldsymbol{\sigma}}\right|^{\frac{1-n}{n}} \tag{2.108}$$

Take the singular value decomposition $A = U\Sigma V^T$. Note that:

$$\sigma = -\rho c_s^2 A^T A \,\mathrm{dev}\left(A^T A\right) = -\rho c_s^2 V \Sigma^2 \,\mathrm{dev}\left(\Sigma^2\right) V^T \tag{2.109}$$

Thus:

$$\|\sigma\|_F^k = \rho^k c_s^{2k} \left\|\Sigma^2 \,\mathrm{dev}\left(\Sigma^2\right)\right\|_F^k \tag{2.110}$$

Thus, according to (2.108), and letting $k = \frac{1-n}{n}$, we have:

$$\frac{d\Sigma}{dt} = -\frac{3}{\tau_0}\left(\frac{\rho}{\rho_0}\right)^{\frac{5}{3}} \frac{\rho^k c_s^{2k}}{2^{\frac{k}{2}}} \left\|\Sigma^2 \,\mathrm{dev}\left(\Sigma^2\right)\right\|_F^k \Sigma \,\mathrm{dev}\left(\Sigma^2\right) \tag{2.111}$$

Let:

$$x_i = \frac{a_i^2}{\det\left(A\right)^{\frac{2}{3}}} = \frac{a_i^2}{\left(\frac{\rho}{\rho_0}\right)^{\frac{2}{3}}} \tag{2.112}$$

then $\Sigma^2 = \det\left(A\right)^{\frac{2}{3}} X$ where $X = \mathrm{diag}\left(x_1, x_2, x_3\right)$. Thus, we have:

$$\frac{dx_i}{d\tilde{t}} = -3\left\|X \,\mathrm{dev}\left(X\right)\right\|_F^k x_i \left(x_i - \bar{x}\right) \tag{2.113}$$

where:

$$\tilde{t} = \frac{2}{\tau_0}\left(\frac{\rho}{\rho_0}\right)^{\frac{4k+7}{3}} \left(\frac{\rho c_s^2}{\sqrt{2}}\right)^k t \tag{2.114}$$

Note that:

$$\begin{aligned} 9\left\|X\,\mathrm{dev}\,(X)\right\|_F^2 = 4\left(x_1^4+x_2^4+x_3^4\right) \\ -2\left(x_1^2x_2^2+x_3^2x_2^2+x_1^2x_3^2\right) \\ +\sum_{i\neq j,j\neq k,k\neq i} x_i^2x_jx_k - 4\sum_{i\neq j} x_i^3x_j \end{aligned} \tag{2.115}$$

Defining m, u as before, we have:

$$\left\|X\,\mathrm{dev}\,(X)\right\|_F^2 = \frac{1}{2}u^2 + 4m^2u - 6m^4 + 6m \tag{2.116}$$

This leads to the following coupled system of ODEs:

$$\frac{du}{d\tilde{t}} = -18\frac{d\tau}{d\tilde{t}}\left(1 - m\left(m^2 - \frac{5}{6}u\right)\right) \tag{2.117a}$$

$$\frac{dm}{d\tilde{t}} = -\frac{d\tau}{d\tilde{t}}u \tag{2.117b}$$

where we have defined the variable τ by:

$$\frac{d\tau}{d\tilde{t}} = \left(\frac{1}{2}u^2 + 4m^2u - 6m^4 + 6m\right)^{\frac{k}{2}} \tag{2.118}$$

Using the approximation solution from before:

$$m\,(\tau) = 1 + \frac{e^{-9\tau}}{3}\left(ae^{3\tau} - b\right) \tag{2.119a}$$

$$u\,(\tau) = e^{-9\tau}\left(2ae^{3\tau} - 3b\right) \tag{2.119b}$$

It is straightforward to verify that:

$$\begin{aligned}\frac{d\tau}{d\tilde{t}} &= \frac{1}{54^{\frac{k}{2}}}\left(\begin{array}{c} 108ae^{-6\tau} - 324be^{-9\tau} \\ +180a^2e^{-12\tau} - 612abe^{-15\tau} \\ +459b^2e^{-18\tau} - 24a^2be^{-21\tau} \\ +\left(48ab^2 - 4a^4\right)e^{-24\tau} \\ +\left(16a^3b - 24b^3\right)e^{-27\tau} \\ -24a^2b^2e^{-30\tau} + 16ab^3e^{-33\tau} \\ -4b^4e^{-36\tau} \end{array}\right)^{\frac{k}{2}} \\ &\equiv \frac{f\left(\tau\right)^{\frac{k}{2}}}{54^{\frac{k}{2}}}\end{aligned} \tag{2.120}$$

$f\left(\tau\right)$ is approximated by $g\left(\tau\right) \equiv ce^{-\frac{c}{\lambda}\tau}$, where:

$$\begin{aligned} c &= 108a - 324b + 180a^2 - 612ab + 459b^2 \\ &\quad - 24\left(a^2b - 2ab^2 + b^3\right) - 4\left(a - b\right)^4 \end{aligned} \tag{2.121a}$$

$$\begin{aligned} \lambda &= 18a - 36b + 15a^2 - \frac{204ab}{5} + \frac{51b^2}{2} \\ &\quad - \frac{8a^2b}{7} + 2ab^2 - \frac{8b^3}{9} - \frac{a^4}{6} + \frac{16a^3b}{27} \\ &\quad - \frac{4a^2b^2}{5} + \frac{16ab^3}{33} - \frac{b^4}{9} \end{aligned} \tag{2.121b}$$

Note that $f\left(0\right) = g\left(0\right)$ and $\int_0^\infty \left(f\left(\tau\right) - g\left(\tau\right)\right)d\tau = 0$. Thus, we have:

$$\frac{d\tau}{d\tilde{t}} \approx \left(\frac{c}{54}\right)^{\frac{k}{2}} e^{-\frac{kc}{2\lambda}\tau} \tag{2.122}$$

Therefore:

$$\begin{aligned}\tau &\approx \frac{2\lambda}{kc}\log\left(\frac{kc}{2\lambda}\left(\frac{c}{54}\right)^{\frac{k}{2}}\tilde{t} + 1\right) \\ &= \frac{2\lambda}{kc}\log\left(\frac{kc}{\tau_0\lambda}\left(\frac{\rho}{\rho_0}\right)^{\frac{4k+7}{3}}\left(\frac{\sqrt{c}\rho c_s^2}{6\sqrt{3}}\right)^k t + 1\right)\end{aligned} \tag{2.123}$$

2.2.4.4 Elastoplastic Solids

For elastoplastic materials governed by the power law described in (15a):

$$\frac{d\Sigma}{dt} = -\frac{3}{\tau_0}\left(\frac{\rho}{\rho_0}\right)^{\frac{5}{3}} \frac{\left(\frac{3}{2}\right)^{\frac{n}{2}} \rho^n c_s^{2n} \left\|\operatorname{dev}\left(\Sigma^2 \operatorname{dev}\left(\Sigma^2\right)\right)\right\|_F^n}{\sigma_0^n} \Sigma \operatorname{dev}\left(\Sigma^2\right) \tag{2.124}$$

Thus, we have:

$$\frac{dx_i}{d\tilde{t}} = -3\left\|\operatorname{dev}\left(X \operatorname{dev}\left(X\right)\right)\right\|_F^n x_i\left(x_i - \bar{x}\right) \tag{2.125}$$

where:

$$\tilde{t} = \frac{2}{\tau_0}\left(\frac{\rho}{\rho_0}\right)^{\frac{4n+7}{3}} \left(\sqrt{\frac{3}{2}}\frac{\rho c_s^2}{\sigma_0}\right)^n t \tag{2.126}$$

Note that:

$$\begin{aligned}\frac{27}{2}\left\|\operatorname{dev}\left(X \operatorname{dev}\left(X\right)\right)\right\|_F^2 = \frac{3}{2}&\sum_{i\neq j, j\neq k, k\neq i} x_i^2 x_j x_k \\ &- 2\sum_{i\neq j} x_i^3 x_j \\ &- 3\left(x_1^2 x_2^2 + x_3^2 x_2^2 + x_1^2 x_3^2\right) \\ &+ 4\left(x_1^4 + x_2^4 + x_3^4\right)\end{aligned} \tag{2.127}$$

Thus we have:

$$\left\|\operatorname{dev}\left(X \operatorname{dev}\left(X\right)\right)\right\|_F^2 = \frac{1}{6}u^2 + 4m^2 u - 6m^4 + 6m \tag{2.128}$$

This leads to the following coupled system of ODEs:

$$\frac{du}{d\tilde{t}} = -18\frac{d\tau}{d\tilde{t}}\left(1 - m\left(m^2 - \frac{5}{6}u\right)\right) \tag{2.129a}$$

$$\frac{dm}{d\tilde{t}} = -\frac{d\tau}{d\tilde{t}}u \tag{2.129b}$$

where we have defined the variable τ by:

$$\frac{d\tau}{d\tilde{t}} = \left(\frac{1}{6}u^2 + 4m^2u - 6m^4 + 6m\right)^{\frac{n}{2}} \tag{2.130}$$

Then we have:

$$\frac{du}{d\tau} = -18\left(1 - m\left(m^2 - \frac{5}{6}u\right)\right) \tag{2.131a}$$

$$\frac{dm}{d\tau} = -u \tag{2.131b}$$

Using the approximate solution (2.119a), (2.119b) again, it is straightforward to verify that:

$$\begin{aligned}\frac{d\tau}{d\tilde{t}} &= \frac{1}{54^{\frac{n}{2}}}\begin{pmatrix} 108ae^{-6\tau} - 324be^{-9\tau} \\ +108a^2e^{-12\tau} - 396abe^{-15\tau} \\ +297b^2e^{-18\tau} - 24a^2be^{-21\tau} \\ +\left(48ab^2 - 4a^4\right)e^{-24\tau} \\ +\left(16a^3b - 24b^3\right)e^{-27\tau} \\ -24a^2b^2e^{-30\tau} + 16ab^3e^{-33\tau} \\ -4b^4e^{-36\tau}\end{pmatrix}^{\frac{n}{2}} \\ &\equiv \frac{f\left(\tau\right)^{\frac{n}{2}}}{54^{\frac{n}{2}}}\end{aligned} \tag{2.132}$$

$f\left(\tau\right)$ is approximated by $g\left(\tau\right) \equiv ce^{-\lambda\tau}$, where:

$$\begin{aligned}c &= 108a - 324b + 108a^2 - 396ab + 297b^2 \\ &\quad - 24\left(a^2b - 2ab^2 + b^3\right) - 4\left(a - b\right)^4\end{aligned} \tag{2.133a}$$

$$\begin{aligned}\lambda &= 18a - 36b + 9a^2 - \frac{132ab}{5} + \frac{33b^2}{2} \\ &\quad - \frac{8a^2b}{7} + 2ab^2 - \frac{8b^3}{9} - \frac{a^4}{6} \\ &\quad + \frac{16a^3b}{27} - \frac{4a^2b^2}{5} + \frac{16ab^3}{33} - \frac{b^4}{9}\end{aligned} \tag{2.133b}$$

Note that $f\left(0\right) = g\left(0\right)$ and $\int_0^\infty \left(f\left(\tau\right) - g\left(\tau\right)\right)d\tau = 0$. Thus, we have:

$$\frac{d\tau}{d\tilde{t}} \approx \left(\frac{c}{54}\right)^{\frac{n}{2}} e^{-\frac{nc}{2\lambda}\tau} \tag{2.134}$$

Therefore:

$$\begin{aligned}\tau &\approx \frac{2\lambda}{nc}\log\left(\frac{nc}{2\lambda}\left(\frac{c}{54}\right)^{\frac{n}{2}}\tilde{t}+1\right) \\ &= \frac{2\lambda}{nc}\log\left(\frac{nc}{\tau_0\lambda}\left(\frac{\rho}{\rho_0}\right)^{\frac{4n+7}{3}}\left(\frac{\sqrt{c}}{6}\frac{\rho c_s^2}{\sigma_0}\right)^{n}t+1\right)\end{aligned} \tag{2.135}$$

Thus, the value of A at time Δt is found by substituting the following into (2.119a), (2.119b):

$$\tau = \frac{2\lambda}{nc}\log\left(\frac{nc}{\tau_0\lambda}\left(\frac{\rho}{\rho_0}\right)^{\frac{4n+7}{3}}\left(\frac{\sqrt{c}}{6}\frac{\rho c_s^2}{\sigma_0}\right)^{n}\Delta t+1\right) \tag{2.136}$$

The results are in turn substituted into (2.101a), (2.99b), (2.99c).

2.2.5 Distortion Correction in Fluids

Owing to the linearization step in (2.93), the method presented will perform poorly if the mean of the normalized singular values of the distortion, m, deviates significantly from 1. To avert this, the following resetting procedure was applied globally for fluid flow problems when $m > 1.03$:

$$E \mapsto E - \frac{c_S^2}{4}\left\|\mathrm{dev}\,(G)\right\|_F^2 \tag{2.137a}$$

$$A \mapsto \left(\frac{\rho}{\rho_0}\right)^{1/3} I \tag{2.137b}$$

This is justified by the fact that the distortion is not a macroscopically-measurable quantity. This transformation leaves the density, pressure, and velocity of the fluid unchanged, and was found to improve the stability of the numerical scheme, while at the same time producing correct results, as demonstrated in the following section.

	ρ	p	$\boldsymbol{v}$	A	$\boldsymbol{J}$
$x < 0$	1	$1/\gamma$	$(0, -0.1, 0)$	I_3	$\mathbf{0}$
$x \geq 0$	1	$1/\gamma$	$(0, 0.1, 0)$	I_3	$\mathbf{0}$

Table 2.1: Initial conditions for the slow opposing shear flow test

2.3 Numerical Results

2.3.1 Newtonian Fluids & Elastic Solids

2.3.1.1 Strain Relaxation

In this section, the approximate analytic solver for the distortion ODEs, presented in 2.2.4.2, is compared with a numerical ODE solver. Initial data was taken from [10]:

$$A = \begin{pmatrix} 1 & 0 & 0 \\ -0.01 & 0.95 & 0.02 \\ -0.015 & 0 & 0.9 \end{pmatrix}^{-1} \tag{2.138}$$

Additionally, the following parameter values were used: $\rho_0 = 1, c_s = 1, \mu = 10^{-2}$, giving $\tau_1 = 0.06$. As can be seen in Figure 2.3 on page 67, Figure 2.4 on page 67, and Figure 2.5 on page 67, the approximate analytic solver compares well with the numerical solver in its results for the distortion tensor A, and thus also the internal energy and stress tensor. The numerical ODE solver was the odeint solver from SciPy 0.18.1, based on the LSODA solver from the FORTRAN library ODEPACK (see [95]).

2.3.1.2 Stokes' First Problem

This problem is one of the few test cases with an analytic solution for the Navier-Stokes equations. It consists of two ideal gases in an infinite domain, meeting at the plane $x = 0$, initially flowing with equal and opposite velocity ± 0.1 in the y-axis. The initial conditions are given in Table 2.1 on page 66.

The flow has a low Mach number of 0.1, and this test case is designed to demonstrate the efficacy of the numerical methods in this flow regime. The exact solution to the Navier-Stokes

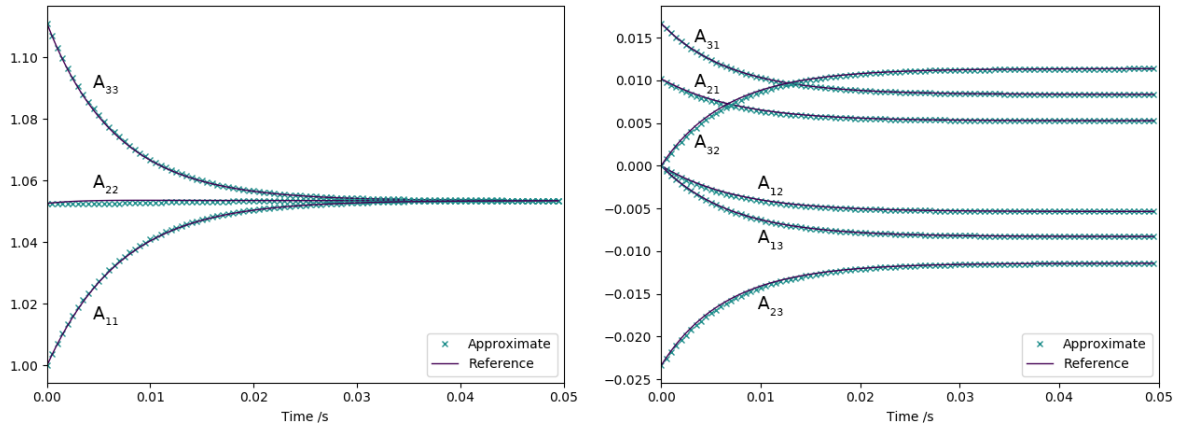

Figure 2.3: Components of the distortion tensor in the Strain Relaxation Test

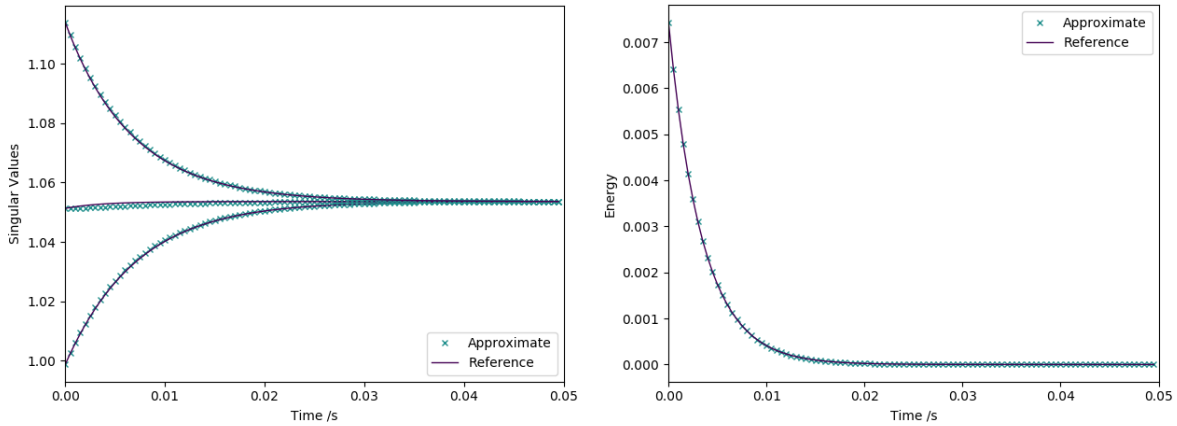

Figure 2.4: Singular values of the distortion tensor and the energy in the Strain Relaxation Test

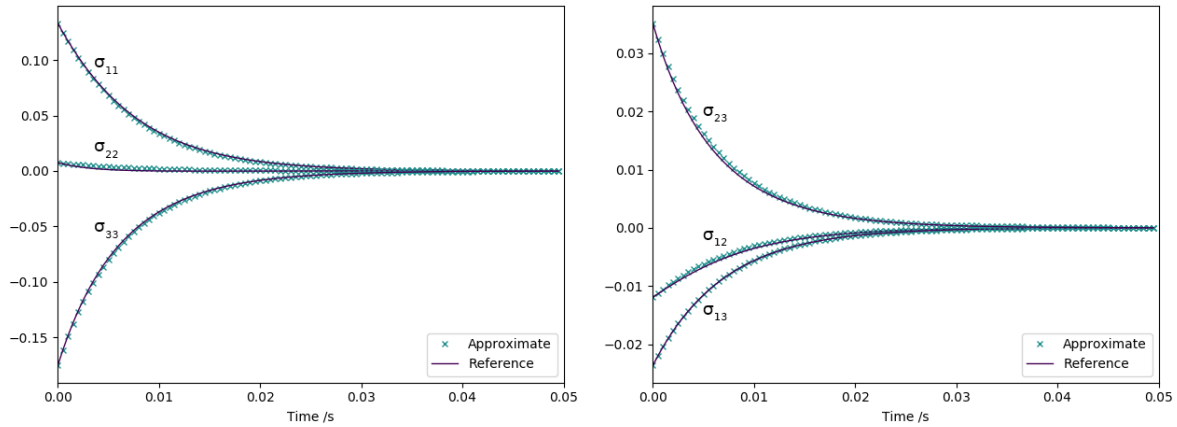

Figure 2.5: Components of the stress tensor in the Strain Relaxation Test

equations is given by[2]:

$$v = v_0 \operatorname{erf}\left(\frac{x}{2\sqrt{\mu t}}\right) \tag{2.139}$$

Heat conduction is neglected, and $\gamma = 1.4$, $c_v = 1$, $\rho_0 = 1$, $c_s = 1$. The viscosity is variously taken to be $\mu = 10^{-2}$, $\mu = 10^{-3}$, $\mu = 10^{-4}$ (resulting in $\tau_1 = 0.06$, $\tau_1 = 0.006$, $\tau_1 = 0.0006$, respectively). Due to the stiffness of the source terms in the equations governing A in the case that $\mu = 10^{-4}$, the step (2.50) in the WENO reconstruction under the Split-WENO method was not performed, and $\boldsymbol{w}_{\boldsymbol{p}}^{n+\frac{1}{2}} \equiv \boldsymbol{w}_{\boldsymbol{p}}^{n}$ was taken instead. This avoided the numerical diffusion that otherwise would have emerged at the interface at $x = 0$.

The results of simulations with 200 cells at time $t = 1$, using reconstruction polynomials of order $N = 2$, are presented in Figure 2.6 on page 69. The GPR model solved with both the ADER-WENO and Split-WENO methods closely matches the exact Navier-Stokes solution. Note that at $\mu = 10^{-2}$ and $\mu = 10^{-3}$, the ADER-WENO and Split-WENO methods are almost indistinguishable. At $\mu = 10^{-4}$ the Split-WENO method matches the curve of the velocity profile more closely, but overshoots slightly at the boundaries of the center region. This overshoot phenomenon is not visible in the ADER-WENO results.

2.3.1.3 Viscous Shock

This test is designed to demonstrate that the numerical methods used are also able to cope with fast flows. First demonstrated by Becker [14], the Navier-Stokes equations have an analytic solution for $P_r = 0.75$ (see Johnson [69] for a full analysis). As noted by Dumbser et al. [35], if the wave has non-dimensionalized upstream velocity $\bar{v} = 1$ and Mach number M_c, then its non-dimensionalized downstream velocity is:

$$a = \frac{1 + \frac{\gamma-1}{2} M_c^2}{\frac{\gamma+1}{2} M_c^2} \tag{2.140}$$

[2] In this problem, the Navier-Stokes equations reduce to $v_t = \mu v_{xx}$. Defining $\eta = \frac{x}{2\sqrt{\mu t}}$, and assuming $v = f(\eta)$, this becomes $f'' + 2\eta f' = 0$. The result follows by solving this equation with the boundary conditions $v(\pm\infty) = \pm v_0$.

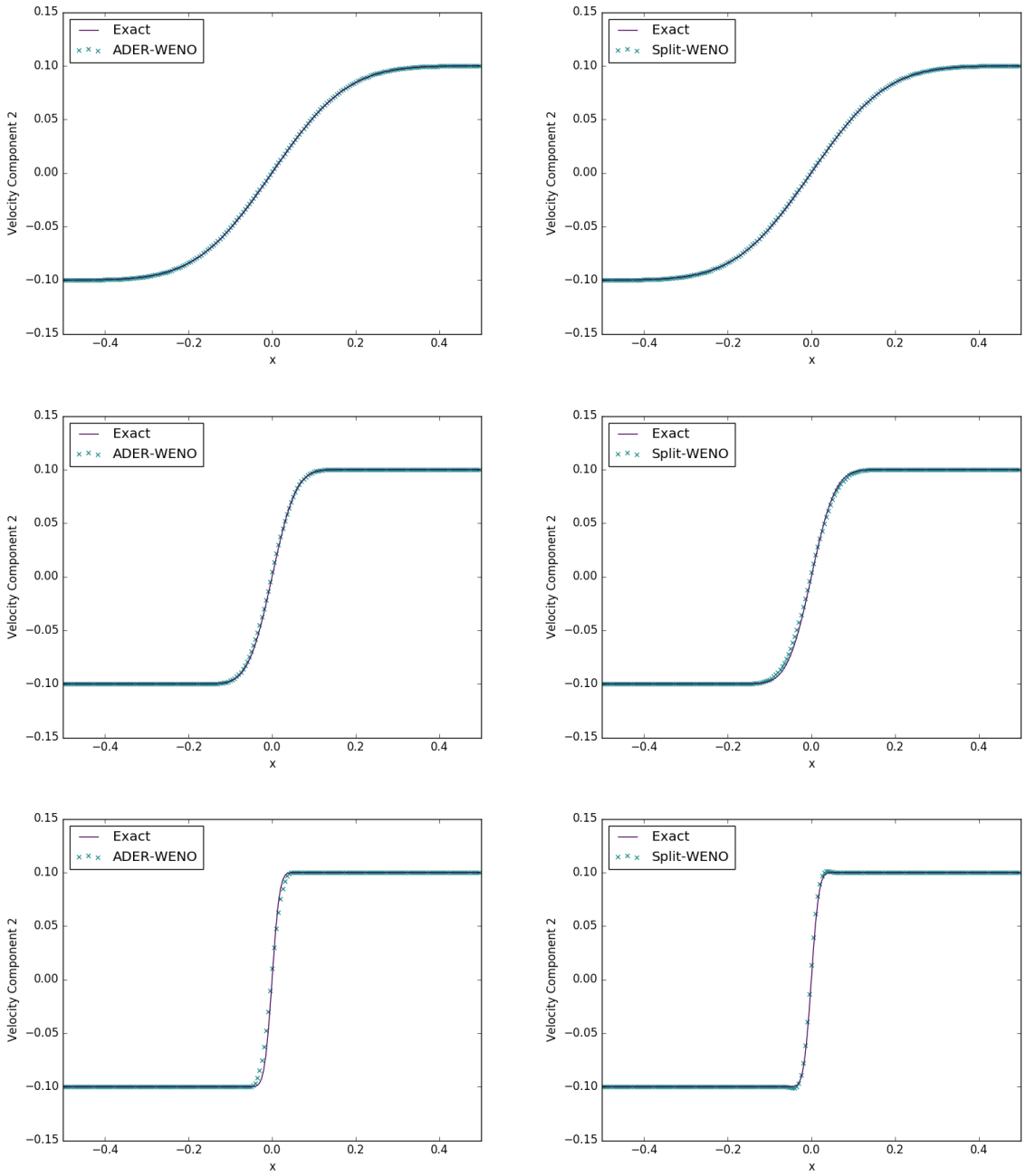

Figure 2.6: Velocity profiles in Stokes' First Problem (for $\mu = 10^{-2}, 10^{-3}, 10^{-4}$), solved with an ADER-WENO scheme and a Split-WENO scheme ($N = 2$)

The wave's velocity profile $\bar{v}(x)$ is given by the roots of the following equation:

$$\frac{1-\bar{v}}{(\bar{v}-a)^a} = c_1 \exp(-c_2 x) \tag{2.141a}$$

$$c_1 = \left(\frac{1-a}{2}\right)^{1-a} \tag{2.141b}$$

$$c_2 = \frac{3}{4} R_e \frac{M_c^2 - 1}{\gamma M_c^2} \tag{2.141c}$$

c_1, c_2 are constants that affect the position of the center of the wave, and its stretch factor, respectively. Following the analysis of Morduchow and Libby [90], the non-dimensional pressure and density profiles are given by:

$$\bar{p} = \frac{1}{\bar{v}}\left(1 + \frac{\gamma-1}{2} M_c^2 \left(1 - \bar{v}^2\right)\right) \tag{2.142}$$

$$\bar{\rho} = \frac{1}{\bar{v}} \tag{2.143}$$

To obtain an unsteady shock traveling into a region at rest, a constant velocity field $v = M_c c_0$ is imposed on the traveling wave solution presented here (where c_0 is the adiabatic sound speed). Thus, if p_0, ρ_0 are the downstream (reference) values for pressure and density:

$$v = M c_0 (1 - \bar{v}) \tag{2.144a}$$

$$p = p_0 \bar{p} \tag{2.144b}$$

$$\rho = \rho_0 \bar{\rho} \tag{2.144c}$$

These functions are used as initial conditions, along with $A = \sqrt[3]{\bar{\rho}} I$ and $\boldsymbol{J} = \mathbf{0}$. The downstream density and pressure are taken to be $\rho_0 = 1$ and $p_0 = \frac{1}{\gamma}$ (so that $c_0 = 1$). $M_c = 2$ and $R_e = 100$. The material parameters are taken to be: $\gamma = 1.4$, $p_\infty = 0$, $c_v = 2.5$, $c_s = 5$, $c_t = 5$, $\mu = 2 \times 10^{-2}$, $\kappa = \frac{28}{3} \times 10^{-2}$ (resulting in $\tau_1 = 0.0048$, $\tau_2 = 0.005226\dot{6}$).

The results of a simulation with 200 cells at time $t = 0.2$, using reconstruction polynomials of order $N = 2$, are presented in Figure 2.7 on page 72 and Figure 2.8 on page 73. The shock was initially centered at $x = 0.25$, reaching $x = 0.65$ at the final time. Note that the density, velocity, and pressure results for both methods match the exact solution well,

	ρ	p	$\boldsymbol{v}$	A	$\boldsymbol{J}$
$x < 0$	2	1	$\mathbf{0}$	$\sqrt[3]{2} \cdot I_3$	$\mathbf{0}$
$x \geq 0$	0.5	1	$\mathbf{0}$	$\frac{1}{\sqrt[3]{2}} \cdot I_3$	$\mathbf{0}$

Table 2.2: Initial conditions for the heat conduction test

with the ADER-WENO method appearing to produce a slightly more accurate solution. The results for the two methods for the stress tensor and heat flux are close.

2.3.1.4 Heat Conduction in a Gas

This is a simple test case to ensure that the heat transfer terms in the implementation are working correctly. Two ideal gases at different temperatures are initially in contact at position $x = 0$. The initial conditions for this problem are given in Table 2.2 on page 71.

The material parameters are taken to be: $\gamma = 1.4$, $c_v = 2.5$, $\rho_0 = 1$, $p_0 = 1$, $c_s = 1$, $c_t = 2$, $\mu = 10^{-2}$, $\kappa = 10^{-2}$ (resulting in $\tau_1 = 0.06$, $\tau_2 = 0.0025$). The results of a simulation with 200 cells at time $t = 1$, using reconstruction polynomials of order $N = 2$, are presented in Figure 2.9 on page 73. The ADER-WENO and Split-WENO methods are in perfect agreement for both the temperature and heat flux profiles. As demonstrated in [35], this means that they in turn agree very well with a reference Navier-Stokes-Fourier solution.

2.3.1.5 Elastic Riemann Problems

These two tests are taken from [18, 124]. The aim of the tests is to demonstrate the efficacy of the Split-WENO method in solving Riemann problems in purely elastic solids. Both tests comprise a 1D bar of copper, governed by the Godunov-Romenski EOS, with the following parameters (in CGS units): $\rho_0 = 8.9$, $c_v = 3.94 \times 10^{-4}$, $T^{ref} = 300$, $c_0 = 3.909$, $\alpha = 1$, $\beta = 3$, $\gamma = 2$, $b_0 = 2.1$. In both cases, the copper occupies the domain $x \in [0, 1]$, with transmissive boundary conditions imposed at each end. In the region $x \in [0.5, 1]$, we have

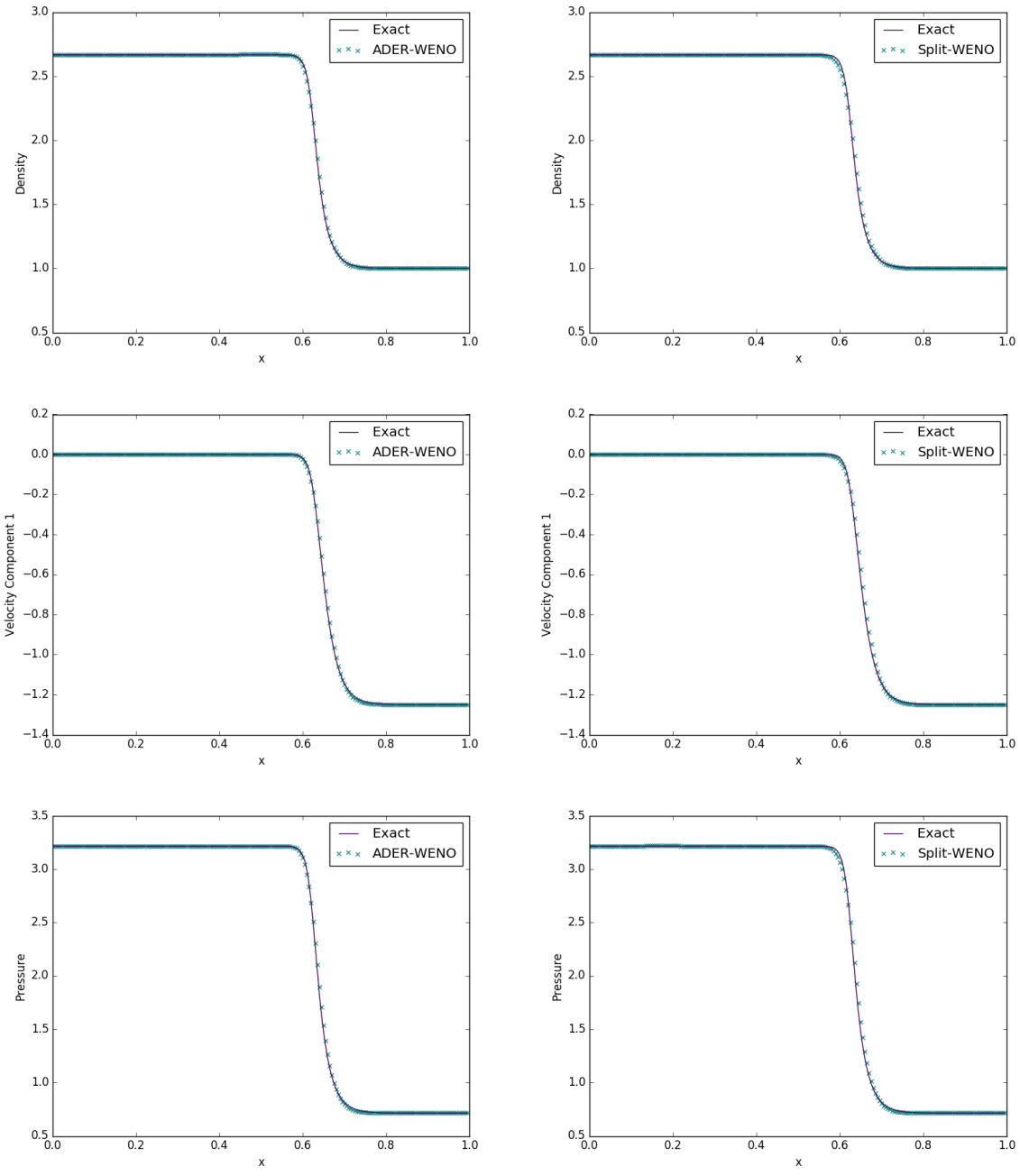

Figure 2.7: Density, velocity, and pressure for the Viscous Shock problem, solved with an ADER-WENO scheme and a Split-WENO scheme ($N = 2$)

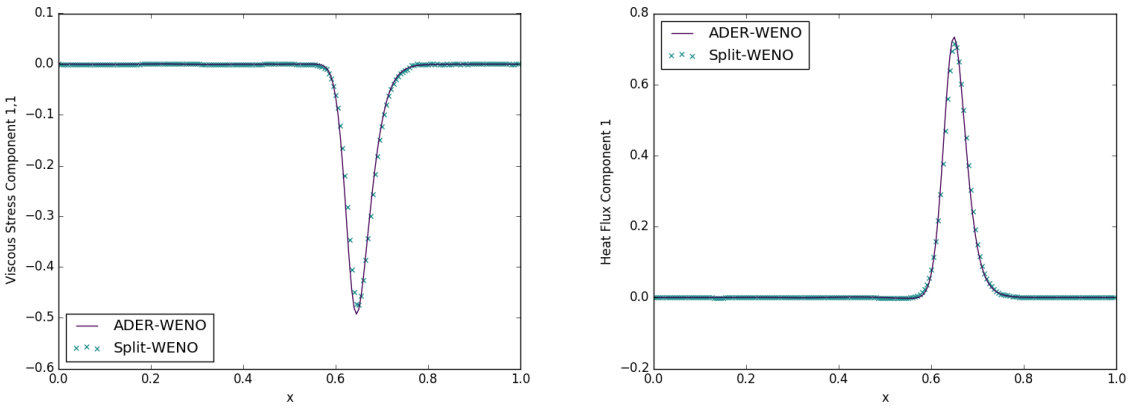

Figure 2.8: Viscous stress and heat flux for the Viscous Shock problem, solved with both an ADER-WENO scheme and a Split-WENO scheme ($N = 2$)

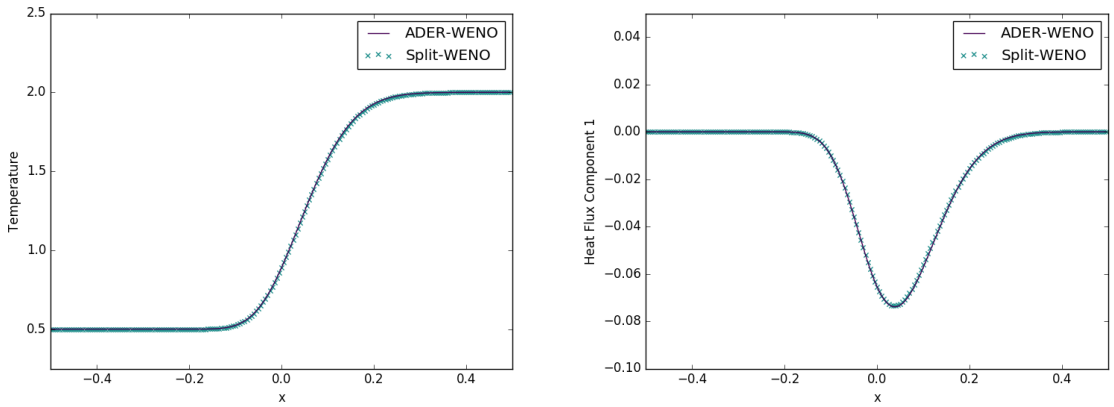

Figure 2.9: Temperature and heat flux in the problem of Heat Conduction in Gas, solved with an ADER-WENO scheme and a Split-WENO scheme ($N = 2$)

the values:

$$\rho = 8.9 \tag{2.145a}$$
$$E = 0 \tag{2.145b}$$
$$\mathbf{v} = \mathbf{0} \tag{2.145c}$$
$$A = I \tag{2.145d}$$

In the first test, the region $x \in [0, 0.5]$ starts with values:

$$\rho = 9.3684 \tag{2.146a}$$
$$E = 1.5180 \tag{2.146b}$$
$$\mathbf{v} = \mathbf{0} \tag{2.146c}$$
$$A = \begin{pmatrix} 20/19 & 0 & 0 \\ 0 & 1 & 0 \\ 0 & 0 & 1 \end{pmatrix} \tag{2.146d}$$

In the second test, the region $x \in [0, 0.5]$ starts with values:

$$\rho = 9.3684 \tag{2.147a}$$
$$E = 2.0257 \tag{2.147b}$$
$$\mathbf{v} = \begin{pmatrix} 0 & 1 & 0 \end{pmatrix}^T \tag{2.147c}$$
$$A = \begin{pmatrix} 20/19 & 0 & 0 \\ -1/19 & 1 & 0 \\ 0 & 0 & 1 \end{pmatrix} \tag{2.147d}$$

The tests are both run to final time $t = 0.06$. The resulting densities and y-velocities are shown in Figure 2.10 on page 75. The first test results in a 3-wave solution structure, comprising: a rarefaction wave traveling to the left, a contact discontinuity moving to the right with speed 0.3948, and a shock wave moving rightwards with speed 5.5380. The second test has a 5-wave solution structure: two rarefaction waves traveling to the left of the domain, and three waves towards the right. These constitute a contact discontinuity, a rarefaction, and a shock. As can be seen, the numerical method closely matches the exact solution, and are comparable in quality to the results obtained in [18], in which the authors employed a high-order ADER-WENO-ALE scheme.

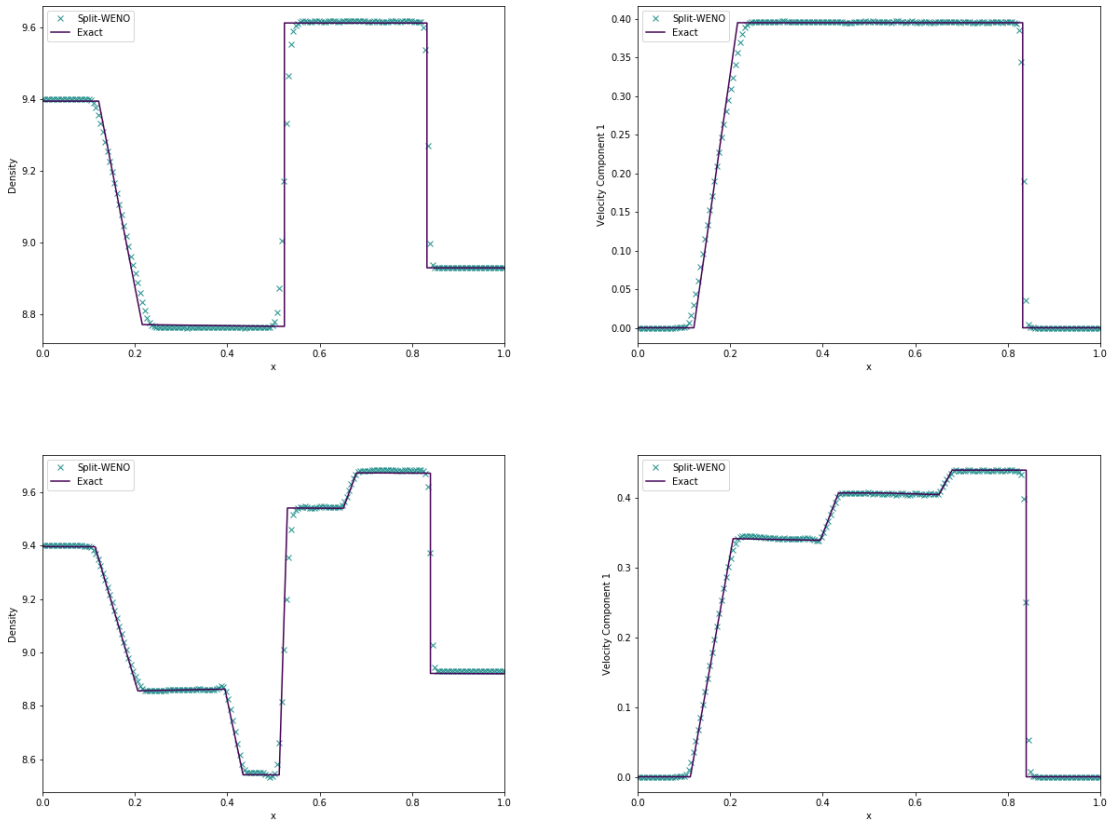

Figure 2.10: Density and velocity in the 3-wave and 5-wave purely elastic Riemann problems

2.3.1.6 Speed

Both the ADER-WENO scheme and the Split-WENO scheme used in this study were implemented in Python3. All array functions were precompiled with Numba's JIT capabilities and the root-finding procedure in the Galerkin predictor was performed using SciPy's Newton-Krylov solver, compiled against the Intel MKL. Clear differences in computational cost between the ADER-WENO and Split-WENO methods were apparent, as is to be expected, owing to the lack of Galerkin method in the Split-WENO scheme. The wall times for the various tests undertaken in this study are given in Table 2.3 on page 78, comparing the combined WENO and Galerkin methods of the ADER-WENO scheme to the combined WENO and ODE methods of the Split-WENO scheme. All computations were performed using an Intel Core i7-4910MQ, on a single core. The number of time steps taken are given in Table 2.4 on page 78. The differences between the methods in terms of the number of time steps taken in each test result from the fact that, for numerical stability, CFL numbers of 0.8 and 0.7 were required by the ADER-WENO method and the Split-WENO method, respectively.

Note that, unlike with the ADER-WENO scheme, the wall time for the Split-WENO scheme is unaffected by a decrease in the viscosity in Stokes' First Problem (and the corresponding increase in the stiffness of the source terms). This is because the analytic approximation to the distortion ODEs obviates the need for a stiff solver. The large difference in ADER-WENO solver times between the $\mu = 10^{-3}$ and $\mu = 10^{-4}$ cases is due to the fact that, in the latter case, a stiff solver must be employed for the initial guess to the root of the nonlinear system produced by the Discontinuous Galerkin method (as described in [58]).

2.3.1.7 Convergence

To assess the rate of convergence of the Split-WENO method, the convected isentropic vortex convergence study from [35] was performed. The initial conditions are given as $\rho = 1 + \delta\rho$,

$p = 1 + \delta p$, $\boldsymbol{v} = (1, 1, 0) + \delta \boldsymbol{v}$, $A = \sqrt[3]{\rho} I$, $\boldsymbol{J} = \boldsymbol{0}$, where:

$$\delta T = -\frac{(\gamma - 1)\,\epsilon^2}{8\gamma\pi^2} e^{1-r^2} \tag{2.148a}$$

$$\delta \rho = (1 + \delta T)^{\frac{1}{\gamma - 1}} - 1 \tag{2.148b}$$

$$\delta p = (1 + \delta T)^{\frac{\gamma}{\gamma - 1}} - 1 \tag{2.148c}$$

$$\delta \boldsymbol{v} = \frac{\epsilon}{2\pi} e^{\frac{1-r^2}{2}} \begin{pmatrix} -(y-5) \\ x - 5 \\ 0 \end{pmatrix} \tag{2.148d}$$

The 2D domain is taken to be $[0, 10]^2$. ϵ is taken to be 5. The material parameters are taken to be: $\gamma = 1.4$, $c_v = 2.5$, $\rho_0 = 1$, $p_0 = 1$, $c_s = 0.5$, $c_t = 1$, $\mu = 10^{-6}$, $\kappa = 10^{-6}$ (resulting in $\tau_1 = 2.4 \times 10^{-5}$, $\tau_2 = 10^{-6}$). Thus, this can be considered to be a stiff test case.

The convergence rates in the L_1, L_2, L_∞ norms for the density variable are given in Table 2.5 on page 78 and Table 2.6 on page 78 for WENO reconstruction polynomial orders of $N = 2$ and $N = 3$, respectively. As expected, both sets of tests attain roughly second order convergence. For comparison, the corresponding results for this test from [35] - solved using a third-order P2P2 scheme - are given in Table 2.7 on page 80 for comparison.

2.3.2 Non-Newtonian Fluids & Elastoplastic Solids

2.3.2.1 Strain Relaxation Test

The aim of this test is to gauge the accuracy of the approximate analytic solver for the distortion equations.

Take initial data used by [10]:

$$A = \begin{pmatrix} 1 & 0 & 0 \\ -0.01 & 0.95 & 0.02 \\ -0.015 & 0 & 0.9 \end{pmatrix}^{-1} \tag{2.149}$$

The following parameter values were used: $\rho_0 = 1, c_s = 0.219, n = 4, \sigma_0 = 9 \times 10^{-4}, \tau_0 = 0.1$.

	ADER-WENO	Split-WENO	Speed-up
Stokes' First Problem ($\mu = 10^{-2}$)	265s	38s	7.0
Stokes' First Problem ($\mu = 10^{-3}$)	294s	38s	7.7
Stokes' First Problem ($\mu = 10^{-4}$)	536s	38s	14.1
Viscous Shock	297s	56s	5.3
Heat Conduction in a Gas	544s	94s	5.8

Table 2.3: Wall time for various tests (all with 200 cells) under the ADER-WENO method and the Split-WENO method

	Timesteps (ADER-WENO)	Timesteps (Split-WENO)
Stokes' First Problem ($\mu = 10^{-2}$)	385	442
Stokes' First Problem ($\mu = 10^{-3}$)	386	443
Stokes' First Problem ($\mu = 10^{-4}$)	385	442
Viscous Shock	562	645
Heat Conduction in a Gas	942	1077

Table 2.4: Time steps taken for various tests (all with 200 cells) under the ADER-WENO method and the Split-WENO method

Grid Size	$\epsilon(L_1)$	$\epsilon(L_2)$	$\epsilon(L_\infty)$	$\mathcal{O}(L_1)$	$\mathcal{O}(L_2)$	$\mathcal{O}(L_\infty)$
20	2.87×10^{-3}	7.15×10^{-3}	6.21×10^{-2}			
40	5.81×10^{-4}	1.62×10^{-3}	1.73×10^{-2}	2.30	2.14	1.85
60	1.98×10^{-4}	5.39×10^{-4}	5.94×10^{-3}	2.65	2.70	2.63
80	1.23×10^{-4}	3.47×10^{-4}	3.41×10^{-3}	1.67	1.52	1.92

Table 2.5: Convergence rates for the Split-WENO method ($N = 2$)

Grid Size	$\epsilon(L_1)$	$\epsilon(L_2)$	$\epsilon(L_\infty)$	$\mathcal{O}(L_1)$	$\mathcal{O}(L_2)$	$\mathcal{O}(L_\infty)$
10	1.01×10^{-2}	2.58×10^{-2}	1.27×10^{-1}			
20	1.68×10^{-3}	4.02×10^{-3}	2.93×10^{-2}	2.59	2.68	2.11
30	5.34×10^{-4}	1.57×10^{-3}	1.70×10^{-2}	2.83	2.32	1.34
40	3.32×10^{-4}	8.94×10^{-4}	7.55×10^{-3}	1.65	1.95	2.82

Table 2.6: Convergence rates for the Split-WENO method ($N = 3$)

The evolution of the components of the distortion, according to both the approximate analytical solver and a stiff numerical ODE solver, are given in Figure 2.11 on page 80, Figure 2.12 on page 80, and Figure 2.13 on page 81. As can be seen, the approximate analytic solver compares well with the exact solution for the distortion, A, and thus also the stress tensor and the energy.

2.3.2.2 Poiseuille Flow

The aim of this test is to gauge both the performance of the modified formulation of the GPR model in simulating power-law fluids, and the accuracy of the new numerical scheme we have presented to solve it. The problem of poiseuille flow has been chosen due to the availability of an analytical solution against which to compare.

This test consists of a fluid traveling down a channel of constant width L, with a constant pressure gradient Δp along the length of the channel. No-slip boundary conditions are imposed on the channel walls. For a non-Newtonian fluid obeying a power law, the steady-state velocity profile across the channel is given by [47]:

$$v = \frac{\rho}{k}\left(\frac{\Delta p}{K}\right)^{1/n}\left(\left(\frac{L}{2}\right)^{k} - \left(x - \frac{L}{2}\right)^{k}\right) \tag{2.150a}$$

$$k = \frac{n+1}{n} \tag{2.150b}$$

where $x \in [0, L]$.

In this case, $L = 0.25$, $\Delta p = 0.48$, $K = 10^{-2}$. The fluid is initially at rest, with $\rho_0 = 1$, $A = I$, $p = 100/\gamma$. It follows an ideal gas EOS with $\gamma = 1.4$, $c_s = 1$. The pressure gradient is imposed by means of a body force, implemented as a constant source term to the momentum equation.

The final time was taken to be 20, so that in each case the system had reached steady state. 100 cells were taken across the width of the channel. A third order WENO method was used, with a CFL number of 0.6.

Results for various values of n are shown in Figure 2.14 on page 81. The exact solutions are shown as dotted lines, with the numerical solutions in solid colors. Note that there is good agreement between the numerical solutions and exact solutions for all values of n.

Grid Size	$\epsilon(L_1)$	$\epsilon(L_2)$	$\epsilon(L_\infty)$	$\mathcal{O}(L_1)$	$\mathcal{O}(L_2)$	$\mathcal{O}(L_\infty)$
20	9.44×10^{-3}	2.20×10^{-3}	2.16×10^{-3}			
40	1.95×10^{-3}	4.50×10^{-4}	4.27×10^{-4}	2.27	2.29	2.34
60	7.52×10^{-4}	1.74×10^{-4}	1.48×10^{-4}	2.35	2.35	2.61
80	3.72×10^{-4}	8.66×10^{-5}	7.40×10^{-5}	2.45	2.42	2.41

Table 2.7: Convergence rates for the ADER-DG PNPM method ($N, M = 2$)

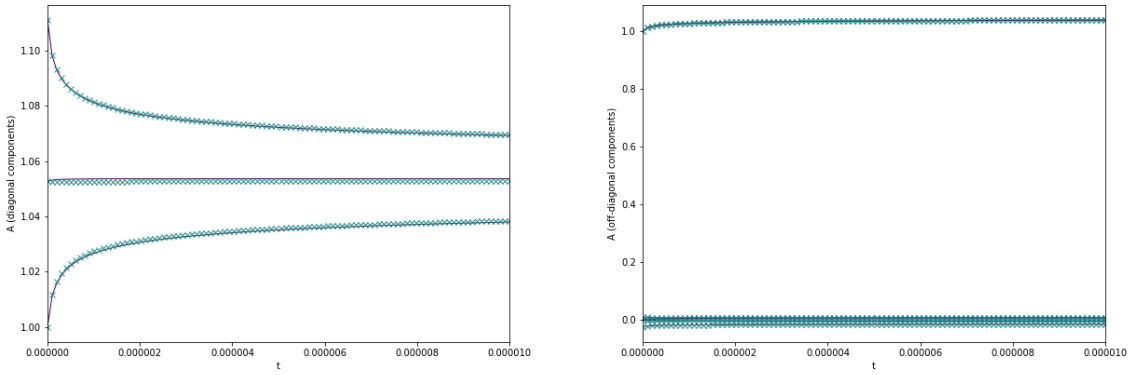

Figure 2.11: Distortion components during the Strain Relaxation Test: approximate analytical solution (crosses) and numerical ODE solution (solid line)

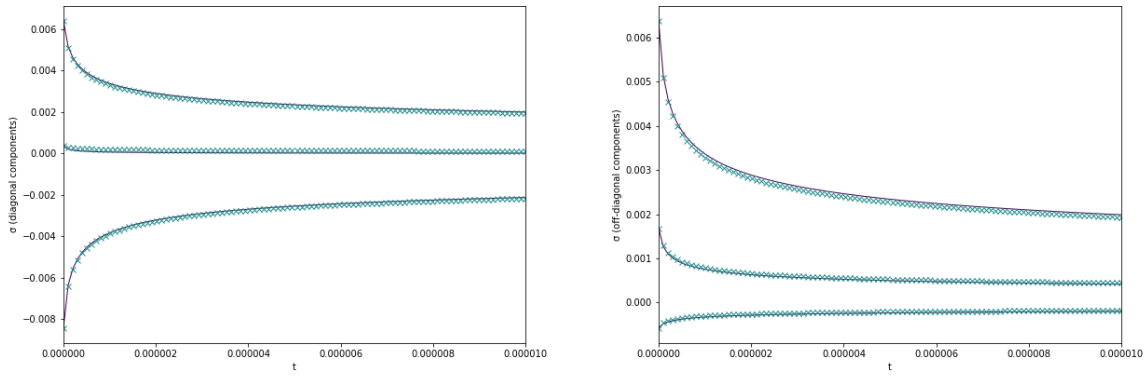

Figure 2.12: Stress tensor components during the Strain Relaxation Test: approximate analytical solution (crosses) and numerical ODE solution (solid line)

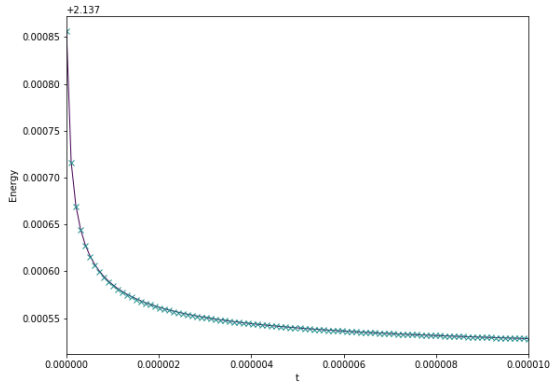

Figure 2.13: Total energy during the Strain Relaxation Test: approximate analytical solution (crosses) and numerical ODE solution (solid line)

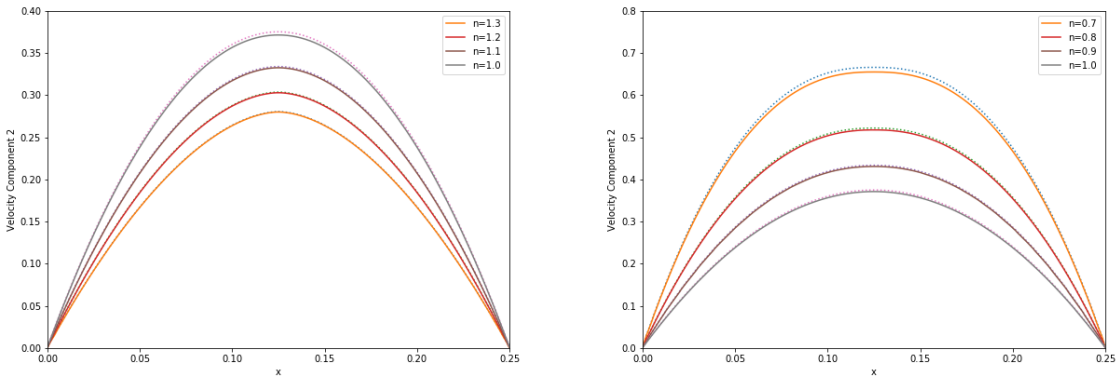

Figure 2.14: Velocity profiles for different dilatants (left) and pseudoplastics (right), in steady Poiseuille flow

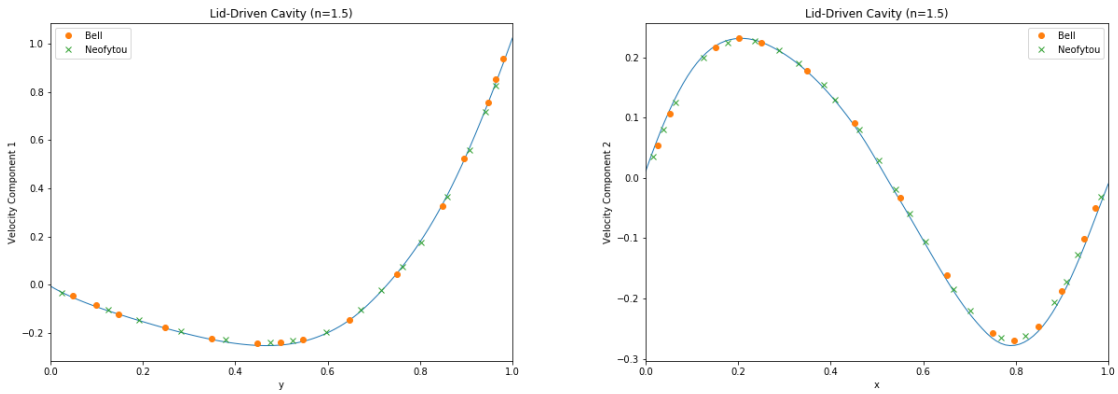

Figure 2.15: Velocity profiles for the Lid-Driven Cavity Test under the new formulation (solid line), for a dilatant with $n = 1.5$. Slices are taken through the center of the domain, in both axes, and compared with those of [15] and [92].

2.3.2.3 Lid-Driven Cavity

This lid-driven cavity test has been chosen here as a famous multidimensional problem against which the power-law fluid framework we have presented can be benchmarked. See [122] for detailed analysis of this problem, under power-law fluids and other non-Newtonian fluids.

The test consists of a square grid, with one side at a constant velocity of 1, and the other three stationary, with no-slip boundary conditions imposed. The fluid obeys an ideal gas EOS with $\gamma = 1.4$ and $c_s = 1$. It obeys a viscosity power law with $K = 10^{-2}$, for various n. It is initially at rest, with $\rho = 1$, $p = 1$, $A = I$.

The grid is chosen to have size 100×100. A third order WENO method is used, with a CFL number of 0.5.

Figure 2.15 on page 82 and Figure 2.16 on page 83 show the results of running the system to steady state, for $n = 1.5$ and $n = 0.5$, respectively. The results are compared with those of [15] and [92]. As can be seen, there is very good agreement for the case $n = 1.5$, with the split solver performing slightly less well for the case $n = 0.5$. The 2D streamline plots found in Figure 2.17 on page 83 take the characteristic forms found in the aforementioned literature.

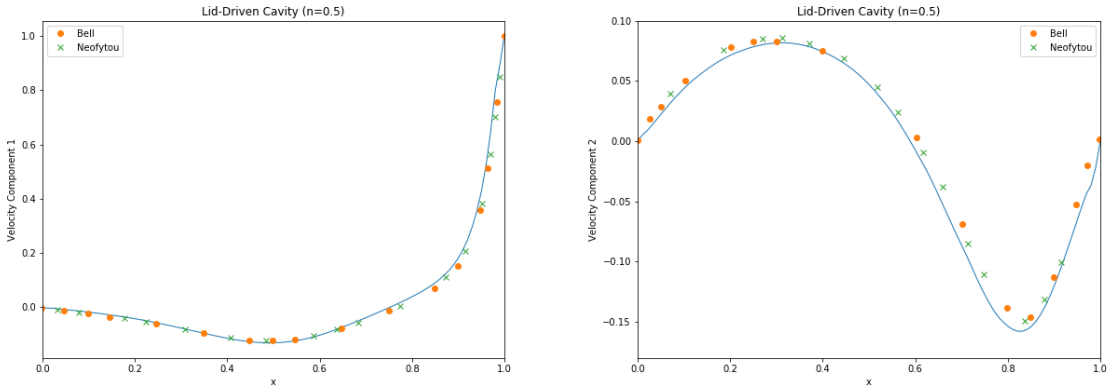

Figure 2.16: Velocity profiles for the Lid-Driven Cavity Test under the new formulation (solid line), for a pseudoplastic with $n = 0.5$. Slices are taken through the center of the domain, in both axes, and compared with those of [15] and [92].

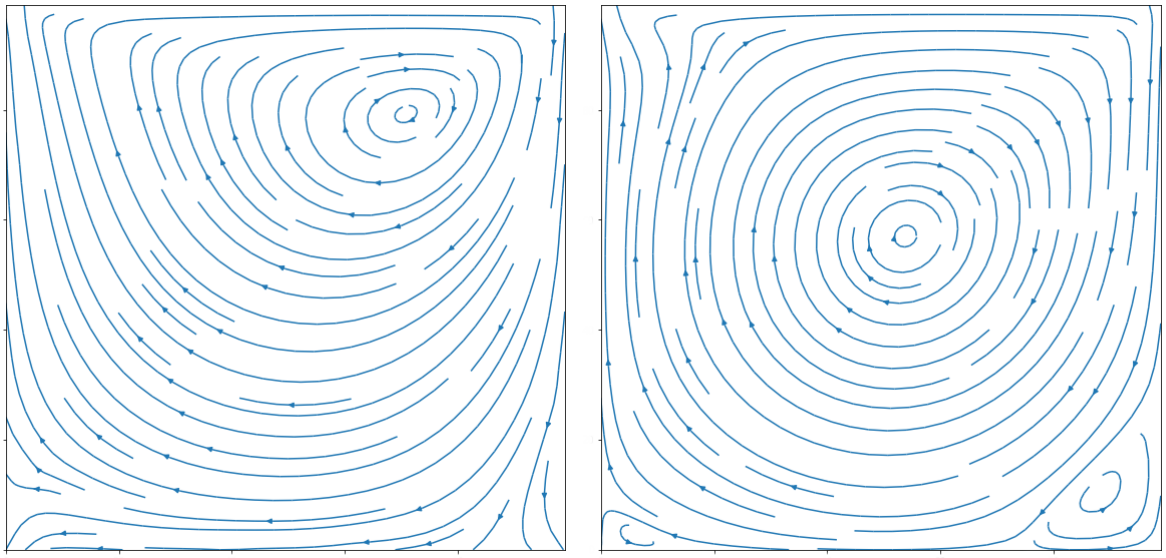

Figure 2.17: Streamplots for the Lid-Driven Cavity Test, for a pseudoplastic with $n = 0.5$ (left) and a dilatant with $n = 1.5$ (right)

2.3.2.4 Elastoplastic Piston

We now demonstrate the ability of our new numerical scheme to deal with problems involving elastoplastic materials. This test is taken from [99], with exact solutions found in [80].

In this test, a piston with speed $20ms^{-1}$ is driven into copper initially at rest. An elastic shock wave develops, followed by a plastic shock wave. The following parameters were used: $\rho_0 = 8930, c_s = 2244, \sigma_0 = 9 \times 10^7, \tau_0 = 1$. The shock Mie-Gruneisen EOS is used for the internal energy, with $p_0 = 0, c_0 = 3940, \Gamma_0 = 2, s = 1.48$. 400 grid cells were used, with a third order WENO method, and a CFL number of 0.7.

Figure 2.18 on page 85 and Figure 2.19 on page 85 demonstrate the results using the split solver for various values of n. These results are compared with the exact solution to the problem under ideal plasticity (to which the former results should converge as $n \to \infty$). The split solver is able to cope with larger values of n than those that have been presented in [99]. The results here are correspondingly closer to the ideal plasticity solution that they approximate, than those found in the aforementioned paper.

2.3.2.5 Cylindrical Shock

The purpose of this test is to demonstrate the efficacy of the split solver in multidimensional elastoplastic problems.

This test is taken from [12]. It consists of a slab of copper, occupying the domain $[0, 20]^2$, initially at rest. The region $r \leq 2$ is at ambient conditions, with zero pressure. The region $r > 2$ is at raised pressure 10^{10} and temperature 600.

The simulation is run to time $t = 10^{-5}$, on a grid of shape 500×500. A fourth order WENO scheme is used, with a CFL number of 0.8. The resulting radial density, velocity, stress tensor, and temperature profiles are given in Figure 2.20 on page 87, Figure 2.21 on page 87, Figure 2.22 on page 88, Figure 2.23 on page 88, and 2D heatmaps for density and speed are given in Figure 2.24 on page 92.

The results are compared with those of the 1D radially-symmetric scheme found in [12], which are in turn compared with the 2D results from the same publication. As can be seen, the 2D results computed using the new split solver for the GPR model more closely match the

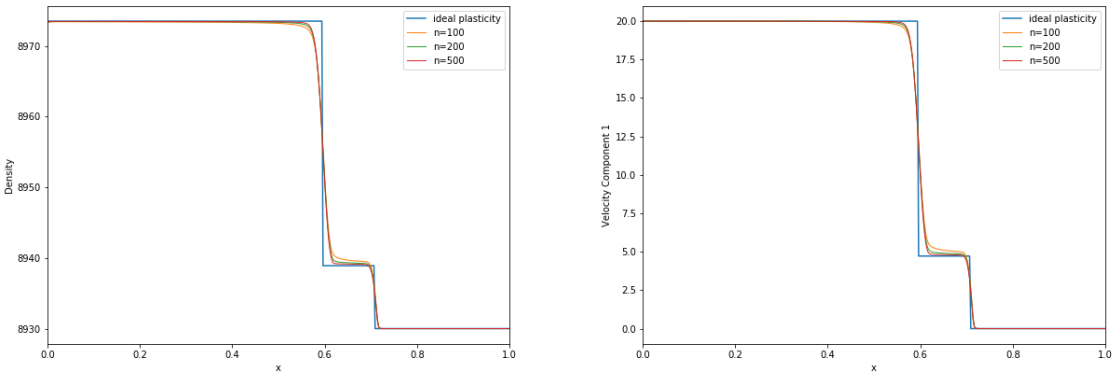

Figure 2.18: Density and velocity in the elastoplastic piston test, for various values of power-law parameter n

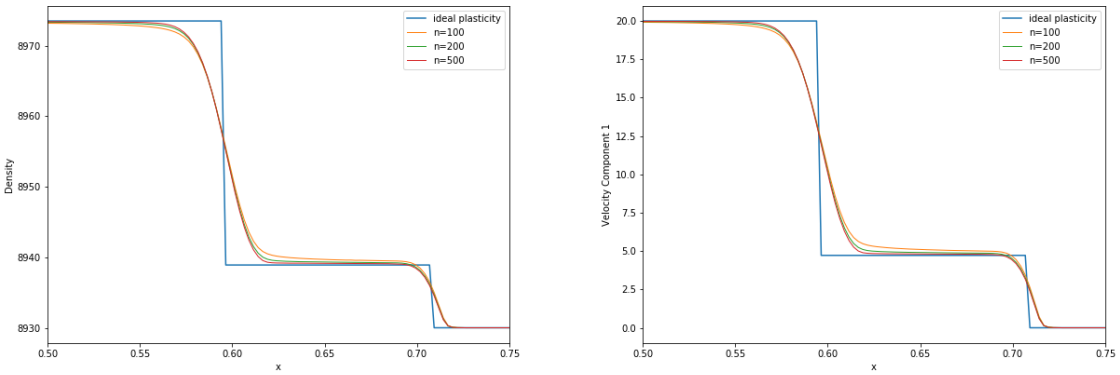

Figure 2.19: Zoom view of density and velocity in the elastoplastic piston test, for various values of power-law parameter n

1D radially-symmetric results than the 2D results from the aforementioned publication, with the spikes in both variables around $r = 2$ and the wave around $r = 6$ being more accurately resolved. Additionally, the temperature jump around $r = 2$ is more sharply resolved.

2.4 Conclusions

2.4.1 Newtonian Fluids & Elastic Solids

In summary, a new numerical method based on an operator splitting, and including some analytical results, has been proposed for the GPR model of continuum mechanics. It has been demonstrated that this method is able to match current ADER-WENO methods in terms of accuracy on a range of test cases. It is significantly faster than the other currently available methods, and it is easier to implement. The author would recommend that if very high order-of-accuracy is required, and computational cost is not important, then ADER-WENO methods may present a better option, as by design the new method cannot achieve better than second-order accuracy. This new method clearly has applications in which it will prove useful, however.

In a similar manner to the operator splitting method presented in [75], the Split-WENO method is second-order accurate and stable even for very stiff problems (in particular, the reader is referred to the results of the $\mu = 10^{-4}$ variation of Stokes' First Problem in 2.3.1.2 and the convergence study in 2.3.1.7). However, it will inevitably suffer from the incorrect speed of propagation of discontinuities on regular, structured grids. This is due to a lack of spatial resolution in evaluating the source terms, as detailed in [75]. This issue can be rectified by the use of some form of shock tracking or mesh refinement, as noted in the cited paper. It is noted in [33] that operator splitting-based methods can result in schemes that are neither well-balanced nor asymptotically consistent. The extent to which these two conditions are violated by the Split-WENO method - and the severity in practice of any potential violation - is a topic of further research.

It should be noted that the assumption (2.92) used to derive the approximate analytical solver may break down for situations where the flow is compressed heavily in one direction but not the others. The reason for this is that one of the singular values of the distortion tensor will be much larger than the others, and the mean of the squares of the singular values will not be close to its geometric mean, meaning that the subsequent linearization of the

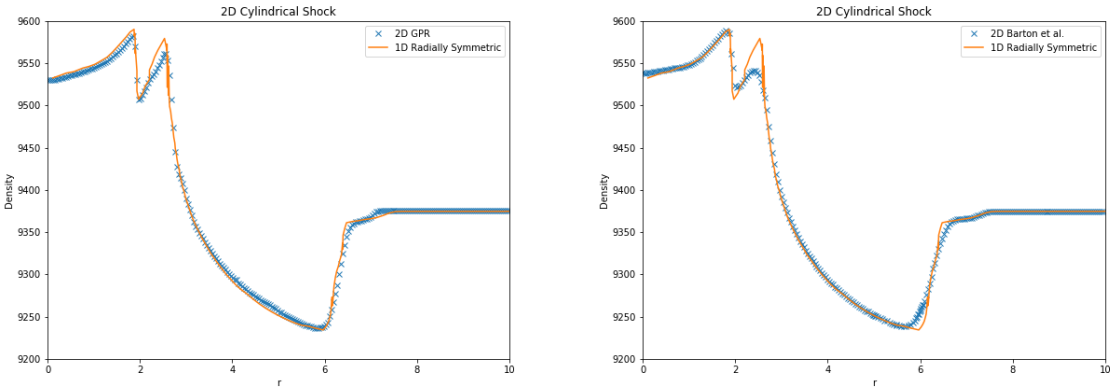

Figure 2.20: 1D density profiles for the 2D Cylindrical Shock Test: GPR model with split solver (left) and results from [12] (right)

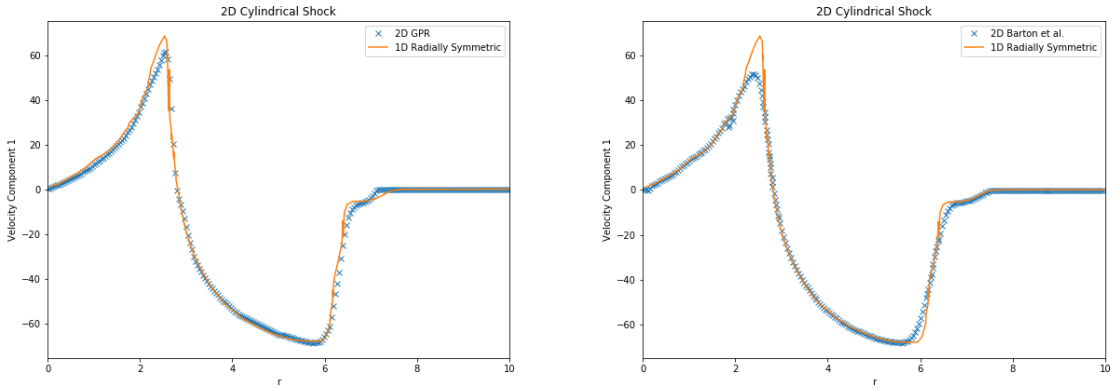

Figure 2.21: 1D velocity profiles for the 2D Cylindrical Shock Test: GPR model with split solver (left) and results from [12] (right)

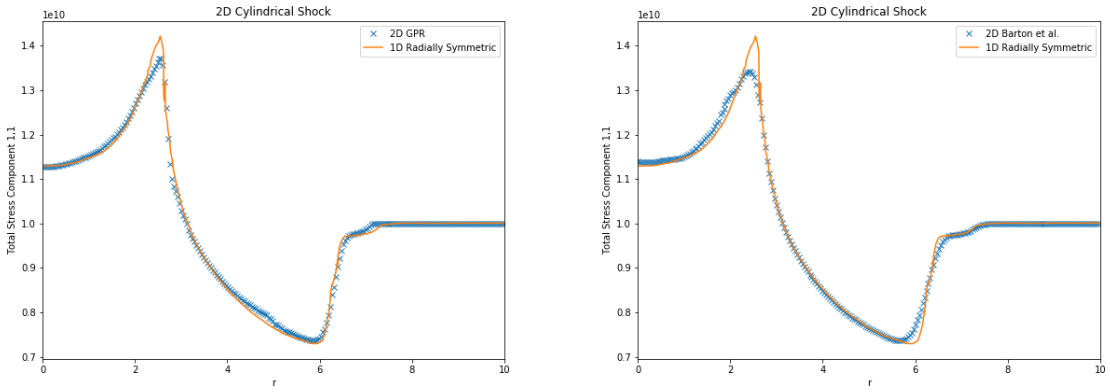

Figure 2.22: 1D stress tensor profiles for the 2D Cylindrical Shock Test: GPR model with split solver (left) and results from [12] (right)

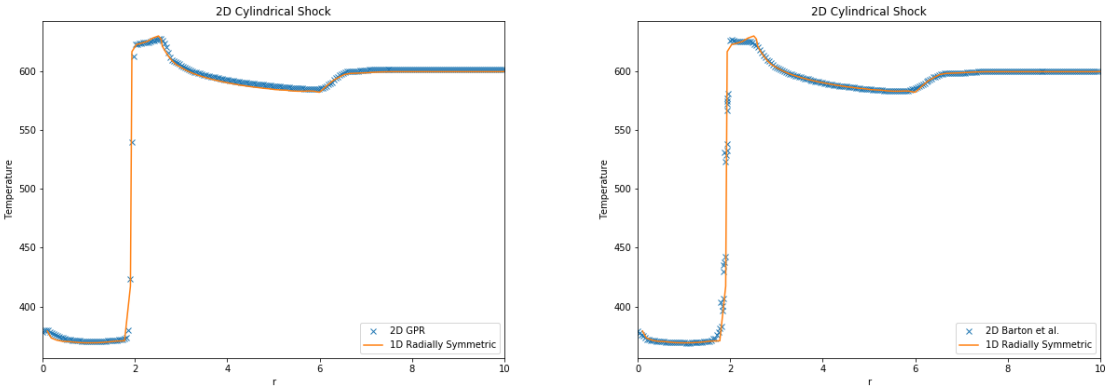

Figure 2.23: 1D temperature profiles for the 2D Cylindrical Shock Test: GPR model with split solver (left) and results from [12] (right)

ODE governing the mean of the singular values fails. It should be noted that none of the situations covered in this study presented problems for the approximate analytical solver, and situations which may be problematic are in some sense unusual. In any case, a stiff ODE solver can be used to solve the system (2.74) if necessary, utilizing the Jacobians derived in the appendix, and so the Split-WENO method is still very much usable in these situations, albeit slightly slower.

It should be noted that both the ADER-WENO and Split-WENO methods, as described in this study, are trivially parallelizable on a cell-wise basis. Thus, given a large number of computational cores, deficiencies in the Split-WENO method in terms of its order of accuracy may be overcome by utilizing a larger number of computational cells and cores. The computational cost of each time step is significantly smaller than with the ADER-WENO method, and the number of grid cells that can be used scales roughly linearly with number of cores, at constant time per iteration.

2.4.2 Non-Newtonian Fluids & Elastoplastic Solids

In summary, a formulation for modeling power-law dilatants and pseudoplastics under the GPR model has been presented. A new numerical method - based on an operator splitting, combined with some analytical results - has also been presented for solving this version of the GPR model, and this numerical method has been applied also to the case of elastoplastic solids under a power-law plasticity model. It has been demonstrated through numerical simulation that the modified GPR formulation is able to accurately describe the evolution of non-Newtonian fluids, and the new numerical scheme has been shown to be an effective method by which to solve this system, and the existing corresponding system for elastoplastic solids.

Under circumstances in which the flow is compressed heavily in one direction relative to the other directions, it should be noted that the linearization assumption (2.92) used to derive the approximate analytical solver may break down. As discussed in [63], this is due to the fact that one of the singular values of the distortion will be much larger than the others, and the mean of the squares of the singular values will be distant to the geometric mean. The subsequent linearization of the ODE governing the mean of the singular values will then fail. It should be noted that none of the situations covered in this study presented problems for the approximate analytical solver, and situations which may be problematic are in some sense

unusual. In any case, a stiff ODE solver can be used to solve the systems (2.47a), (2.47b) if necessary, and so this method is still very much usable in these situations, albeit slightly slower.

It may be that it is possible to find a more efficient (yet still sufficiently accurate) numerical method to solve (2.45a) than the WENO method that was used in this study. This method was chosen due to its well-known performance characteristics (see [7, 40, 68]), but the authors are aware that further performance gains may be possible, and this is an area of further investigation.

As detailed in [75], solvers based on a temporal splitting suffer from a lack of spatial resolution in evaluating the source terms. Thus, it should be noted that the operator splitting method presented here may suffer from the incorrect speed of propagation of discontinuities on regular, structured grids. This issue can be rectified, however, by the use of some form of shock tracking or mesh refinement, as noted in the cited paper. The effect on the propagation speeds of discontinuities can be more evident if the underlying temporal ODEs have non-zero equilibrium states. Noting that the singular values of the distortion cannot be 0 (as this would imply zero density), we have, by (2.73), that at equilibrium the scaled squares of the singular values obey the follow relations:

$$x_1 - \frac{x_1 + x_2 + x_3}{3} = 0 \tag{2.151a}$$

$$x_2 - \frac{x_1 + x_2 + x_3}{3} = 0 \tag{2.151b}$$

$$x_3 - \frac{x_1 + x_2 + x_3}{3} = 0 \tag{2.151c}$$

The set of solutions to this system is $x_1 = x_2 = x_3$. As $x_1 x_2 x_3 = 1$ for all time (due to the constraint (17)), we have that the only equilibrium solution of the ODE system is $x_1, x_2, x_3 = 1$. Given any initial values for x_1, x_2, x_3, the system tends towards this state.

[33] note that operator splitting-based methods can result in schemes that are neither well-balanced, nor asymptotically consistent. The extent to which these two conditions are violated by this method – and the severity in practice of any potential violation – is a topic of further research.

It should be noted that the new numerical scheme presented in this study is trivially parallelizable on a cell-wise basis. Thus, given a large number of computational cores, deficiencies in this method in terms of its order of accuracy may be overcome by utilizing a larger number

of computational cells and cores. The number of grid cells that can be used scales roughly linearly with number of cores, at constant time per iteration.

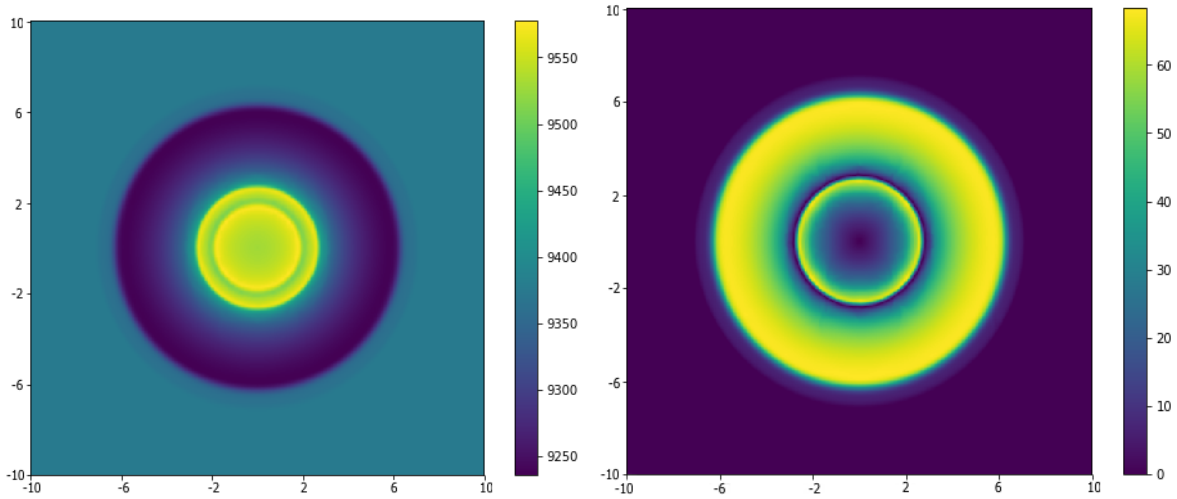

Figure 2.24: 2D plots of density and speed for the Cylindrical Shock Test

Chapter 3

Objective 3: Simulating Material Interfaces

The material in this section is published in [67].

A framework for simulating the interactions between multiple different continua is presented. Each constituent material is governed by the same set of equations, differing only in terms of their equations of state and strain dissipation functions. The interfaces between any combination of fluids, solids, and vacuum are handled by a new Riemann Ghost Fluid Method (RGFM), which is agnostic to the type of material on either side (depending only on the desired boundary conditions).

The Godunov-Peshkov-Romenski (GPR) model is used for modeling the continua (having recently been used to solve a range of problems involving Newtonian and non-Newtonian fluids, and elastic and elastoplastic solids), and this study represents a novel approach for handling multimaterial problems under this model.

The resulting framework is simple, yet capable of accurately reproducing a wide range of different physical scenarios. It is demonstrated here to accurately reproduce analytical results for known Riemann problems, and to produce expected results in other cases, including some featuring heat conduction across interfaces, and impact-induced deformation and detonation of combustible materials. The framework thus has the potential to streamline development of simulation software for scenarios involving multiple materials and phases of matter, by reducing the number of different systems of equations that require solvers, and cutting down on the amount of theoretical work required to deal with the interfaces between materials.

3.1 Ghost Fluid Methods

Ghost fluid methods, combined with level set methods, are used to model the evolution of interfaces between different materials. They are detailed here, as it is with such a method that this study proposes to model the interfaces between different materials described by the GPR model.

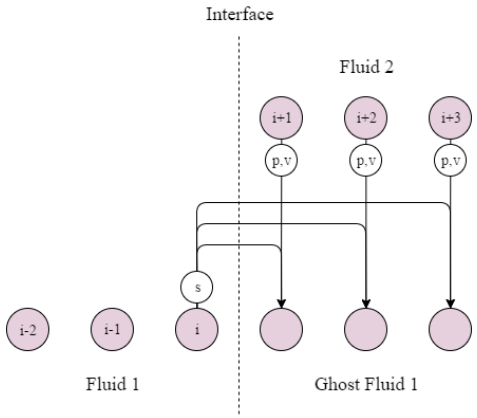

Figure 3.1: Original Ghost Fluid Method

3.1.1 Level Set Methods

Given a function $\phi : \mathbb{R}^n \to \mathbb{R}$, the level set of ϕ at level c is defined as:

$$\Gamma_c = \{\boldsymbol{x} : \phi(\boldsymbol{x}) = c\} \tag{3.1}$$

In this study, problems involving m different materials were assigned the functions $\phi_1, \ldots, \phi_{m-1} : \mathbb{R}^n \to \mathbb{R}$, such that the region occupied by material i is considered to be exactly that in which $\phi_1, \ldots, \phi_{i-1} > 0$, $\phi_i, \ldots, \phi_{m-1} < 0$. The locations of the zero level sets correspond to the locations of the interfaces.

Given the local velocity field $\boldsymbol{v} : \mathbb{R}^n \to \mathbb{R}^3$, the functions ϕ are advected according to the level set equation [96]:

$$\frac{\partial \phi}{\partial t} = \boldsymbol{v} \cdot \nabla \phi \tag{3.2}$$

$\phi_1, \ldots, \phi_{m-1}$ are renormalized to resemble a straight line at every time step, to avoid unwanted distortions such as becoming a multivalued function.

3.1.2 Original Ghost Fluid Method

The Original Ghost Fluid Method of Fedkiw et al. [45] (an adaptation of the work of Glimm et al. [50]) is a numerical method for the Euler equations for simulating interfaces

between multiple materials. The primitive variables for the Euler equations in 1D are given by $\boldsymbol{P} = \begin{pmatrix} \rho & v & p \end{pmatrix}^T$.

Suppose the interface between two fluids is modeled on spatial domain $[0, 1]$, divided into N cells with width $\Delta x = \frac{1}{N}$. Let the time step be Δt and let $\boldsymbol{P_i^n}$ be the set of primitive variables in cell i at time $t_n = n\Delta t$. Let the level set function f have root x_n where $x_n \in \left[\left(i + \frac{1}{2}\right)\Delta x, \left(i + \frac{3}{2}\right)\Delta x\right]$. Thus, at time t_n the interface lies between the cells with primitive variables $\boldsymbol{P_i^n}, \boldsymbol{P_{i+1}^n}$. Define two sets of primitive variables:

$$\boldsymbol{P_j^{(1)}} = \begin{cases} \boldsymbol{P_j^n} & j \leq i \\ \begin{pmatrix} \rho\left(s_i^n, p_j^n, \gamma_i^n\right) & v_j^n & p_j^n \end{pmatrix} & j > i \end{cases} \tag{3.3}$$

$$\boldsymbol{P_j^{(2)}} = \begin{cases} \boldsymbol{P_j^n} & j \geq i+1 \\ \begin{pmatrix} \rho\left(s_{i+1}^n, p_j^n, \gamma_{i+1}^n\right) & v_j^n & p_j^n \end{pmatrix} & j < i+1 \end{cases} \tag{3.4}$$

where:

$$\rho\left(s, p, \gamma\right) = \left(\frac{p}{s}\right)^{\frac{1}{\gamma}} \tag{3.5}$$

All cells in $\boldsymbol{P^{(1)}}$ to the left of the interface have the same state variables as those of $\boldsymbol{P^n}$. All cells to the right have the same pressure and velocity as their counterparts in $\boldsymbol{P^n}$, but the same entropy as $\boldsymbol{P_i^n}$. This affects their density. The situation is analogous for $\boldsymbol{P^{(2)}}$. This is demonstrated in Figure 3.1 on page 94.

$\boldsymbol{P^{(1)}}, \boldsymbol{P^{(2)}}$ are stepped forward by time step Δt using a standard Eulerian method. f is advected using (3.2), taking the velocity in each cell to be that of $\boldsymbol{P^n}$. Now let $f\left(x_{n+1}\right) = 0$ where $x_{n+1} \in \left[\left(k + \frac{1}{2}\right)\Delta x, \left(k + \frac{3}{2}\right)\Delta x\right]$ for some k. Define:

$$\boldsymbol{P_j^{n+1}} = \begin{cases} \boldsymbol{P_j^{(1)}} & j \leq k \\ \boldsymbol{P_j^{(2)}} & j > k \end{cases} \tag{3.6}$$

The rationale behind the original GFM is that in most applications, pressure and velocity are continuous across the interface, and thus the ghost cells may take the real pressure and velocity values. Entropy is generally discontinuous at a contact discontinuity, resulting in large truncation errors if a standard finite difference scheme is used to solve the system.

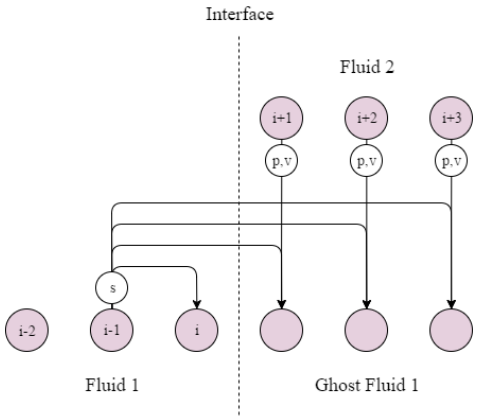

Figure 3.2: Original Ghost Fluid Method, with the isobaric fix

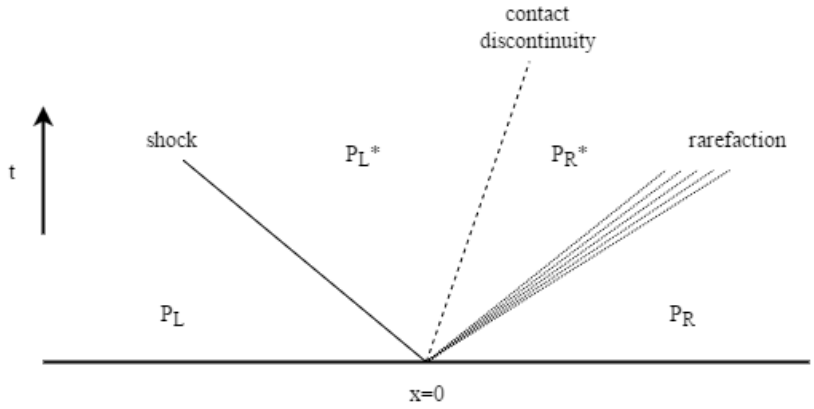

Figure 3.3: Qualitative structure of the solution to the Riemann Problem, showing the different possible types of waves

Thus, entropy is extrapolated as a constant from the interface boundary cell into the ghost region.

Fedkiw et al. advised to use the *isobaric fix* technique. This involves setting the entropy of cell i, and all cells in the right ghost region, to that of cell $i-1$, and setting the entropy of cell $i+1$, and all cells in the left ghost region, to that of cell $i+2$. This is demonstrated in Figure 3.2 on page 96.

Effectively, the ghost regions behave like they are composed of the same fluid as the regions they extend (as they have the same entropy), facilitating calculation of the next time step, but they have the same pressure and velocity profiles as the real fluids they replace, meaning the boundary conditions at the interface are upheld.

3.1.3 Riemann Ghost Fluid Method

The Riemann Problem in its general form is the solution of the following initial value problem. Given a set of variables $\boldsymbol{P}$ dependent on space and time, and a hyperbolic set of equations which govern their spatio-temporal evolution, $\boldsymbol{P}(x,t)$ is sought for $t > 0$, given the initial condition:

$$\boldsymbol{P}(x,0) = \begin{cases} \boldsymbol{P_L} & x < 0 \\ \boldsymbol{P_R} & x > 0 \end{cases} \tag{3.7}$$

This problem is denoted by $RP(\boldsymbol{P_L}, \boldsymbol{P_R})$. Exact solvers exist for the Riemann Problem for various sets of governing equations, such as the Euler equations [126], the equations of non-linear elasticity [11], or the shallow water equations [3], among others. There also exist approximate solvers for general conservative [77, 87] or non-conservative [29] hyperbolic systems of PDEs. The references given here form a very small sample of the work that has been done in this area.

The solution of the Riemann Problem usually takes the form of a set of waves, between which $\boldsymbol{P}$ is constant. The waves can either be a contact discontinuity (across which pressure and velocity are continuous), a shock (across which all variables may be discontinuous), or a rarefaction (along which the variables vary continuously between their values on either side of the wave). The number and form of the waves are determined by the governing equations and the initial conditions. The states of the variables either side of the contact discontinuity in the middle are known as the *star states*. This qualitative description is depicted in Figure 3.3 on page 96.

Liu et al. [76] demonstrated that the original GFM fails to resolve strong shocks at material interfaces. This is because the method effectively solves two separate single-fluid Riemann problems. The waves present in these Riemann problems do not necessarily correspond to those in the real Riemann problem across the interface. The Riemann Ghost Fluid Method of Sambasivan et al. [116, 117] aims to rectify this.

Given $\boldsymbol{P^n}$ and $x_n \in \left[\left(i+\frac{1}{2}\right)\Delta x, \left(i+\frac{3}{2}\right)\Delta x\right]$, the ghost cells for fluid 1 are populated with the left star state of $RP\left(\boldsymbol{P^n_{i-1}}, \boldsymbol{P^n_{i+2}}\right)$, and the ghost cells for fluid 2 are populated with the right star state. $RP\left(\boldsymbol{P^n_{i-1}}, \boldsymbol{P^n_{i+2}}\right)$ is solved rather than $RP\left(\boldsymbol{P^n_i}, \boldsymbol{P^n_{i+1}}\right)$, as $\boldsymbol{P^n_i}, \boldsymbol{P^n_{i+1}}$ often contain errors generated by the fact that they lie on the material interface. $\boldsymbol{P^{n+1}}$ is

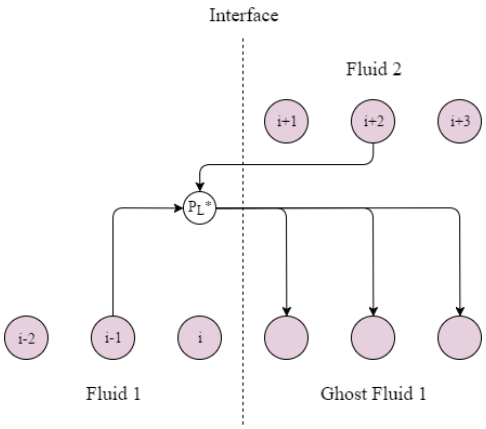

Figure 3.4: Riemann Ghost Fluid Method

then generated as before from the newly formed $\boldsymbol{P}^{(1)}, \boldsymbol{P}^{(2)}$. This process is demonstrated in Figure 3.4 on page 98.

3.2 A Riemann Ghost Fluid Method for the GPR Model

3.2.1 Solving the Riemann Problem

Barton et al. have presented an RGFM for the equations of non-linear elasticity [10, 13]. Owing to the similarity of the structure of the non-linear elasticity equations to those of the GPR model (differing only in the presence of source terms, the form of the shear stress tensor, and possibly the EOS), their method is built upon here. The resulting method is named the *GPR-RGFM*.

The Riemann Problem of the GPR model takes the form demonstrated in Figure 3.5 on page 99. Assuming all waves are distinct, there are four waves on either side of the contact discontinuity. On each side, one wave corresponds to the thermal impulse (manifesting as a heat wave) and the other three correspond to the distortion components in the axis in which the Riemann Problem is considered (manifesting as two shear waves and one longitudinal pressure wave). It is important to note that - owing to the source terms - the star states are not constant in the spacetime region in which they reside, so the method presented here produces only an approximation to them.

The method is presented here along the first spatial axis. It can easily be adapted along

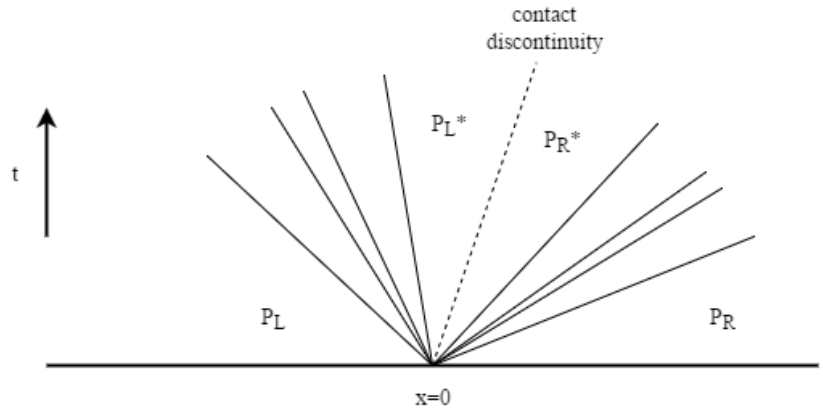

Figure 3.5: Riemann Problem for the GPR model, assuming all waves are distinct

any axis by taking the components of all relevant vector quantities (velocity, distortion, and thermal impulse) in the direction normal to the interface.

Denote the vector of primitive variables by $\boldsymbol{P}$. Take the set of left eigenvectors L (B.28) with eigenvalues $\{\lambda_i\}$. We have the standard set of relations along characteristics (curves along which $\frac{dx}{dt} = \lambda_i$):[1]

$$L \cdot d\boldsymbol{P} = dt \cdot L \cdot \boldsymbol{S} \tag{3.8}$$

In what follows, we enact an operator splitting of the two processes present in the system (3.8):

$$L \cdot d\boldsymbol{P} = \boldsymbol{0} \tag{3.9a}$$

$$\frac{d\boldsymbol{P}}{dt} = \boldsymbol{S} \tag{3.9b}$$

$\boldsymbol{P}^{*\boldsymbol{K}}$ is now sought, where $K = L$ or $K = R$, denoting the left or right sides of the interface,

[1] Take the hyperbolic system $\frac{\partial \boldsymbol{P}}{\partial t} + M\frac{\partial \boldsymbol{P}}{\partial x} = \boldsymbol{S}$. Let $\boldsymbol{l_i}^T M = \lambda_i \boldsymbol{l_i}^T$. Along characteristics corresponding to λ_i:

$$\begin{aligned} \boldsymbol{l_i^T}\left(\frac{\partial \boldsymbol{P}}{\partial t} + M\frac{\partial \boldsymbol{P}}{\partial x}\right) &= \boldsymbol{l_i^T}\left(\frac{\partial \boldsymbol{P}}{\partial t} + \frac{dx}{dt}\frac{\partial \boldsymbol{P}}{\partial x}\right) \\ &= \boldsymbol{l_i^T}\frac{d\boldsymbol{P}}{dt} = \boldsymbol{l_i^T}\boldsymbol{S} \end{aligned}$$

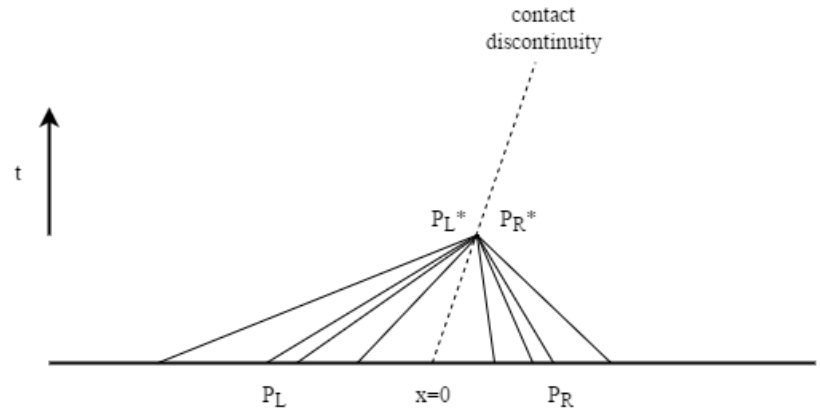

Figure 3.6: Different sets of characteristic curves, traveling from their respective initial points to the star region

respectively. Take the following linearization:

$$d\boldsymbol{P}^{\boldsymbol{K}} \approx \boldsymbol{P}^{*\boldsymbol{K}} - \boldsymbol{P}^{\boldsymbol{K}} \tag{3.10}$$

13 relations from (3.9a) are taken: 4 regarding the 4 sets of characteristics traveling into the contact discontinuity from side K (with speeds greater or less than v for $K = L$ or $K = R$, respectively), and 9 relating to the contact discontinuity itself. This is demonstrated in Figure 3.6 on page 100. 4 more relations must be derived to solve the system for $\boldsymbol{P}^{*\boldsymbol{K}}$.

Define the total stress tensor as:

$$\Sigma \equiv pI - \sigma \tag{3.11}$$

The values of Σ, T under variables $\boldsymbol{P}^{*\boldsymbol{K}}$ are obtained by expanding the following Taylor series:

$$\Sigma^* = \Sigma + (\rho^* - \rho)\frac{\partial \Sigma}{\partial \rho} + (p^* - p)\frac{\partial \Sigma}{\partial p} + (A^*_{mn} - A_{mn})\frac{\partial \Sigma}{\partial A_{mn}} + O\left(d\boldsymbol{P}^2\right) \tag{3.12a}$$

$$T^* = T + (\rho^* - \rho)\frac{\partial T}{\partial \rho} + (p^* - p)\frac{\partial T}{\partial p} + O\left(d\boldsymbol{P}^2\right) \tag{3.12b}$$

Thus, we have:

$$\Sigma^* - \Sigma \approx (p^* - p)\, I - (\rho^* - \rho)\, \frac{\partial \sigma}{\partial \rho} - (A^*_{mn} - A_{mn})\, \frac{\partial \sigma}{\partial A_{mn}} \tag{3.13a}$$

$$T^* - T \approx (\rho^* - \rho)\, \frac{\partial T}{\partial \rho} + (p^* - p)\, \frac{\partial T}{\partial p} \tag{3.13b}$$

These are the extra required relations. Thus we have:

$$\hat{L}^K \cdot \left(\boldsymbol{P}^{*\boldsymbol{K}} - \boldsymbol{P}^{\boldsymbol{K}} \right) = \boldsymbol{c}^{\boldsymbol{K}} \tag{3.14}$$

where $\hat{L}^K$ takes the form found in (3.29), with $\xi = -1$ for $K = R$ and $\xi = 1$ for $K = L$, and:

$$\boldsymbol{c}^{\boldsymbol{K}} = \begin{pmatrix} \boldsymbol{\Sigma}_{\mathbf{1}}^{*\boldsymbol{K}} - \boldsymbol{\Sigma}_{\mathbf{1}}^{\boldsymbol{K}} \\ T^{*K} - T^K \\ \mathbf{0} \end{pmatrix} \tag{3.15}$$

The inverse of $\hat{L}^K$ takes the form found in (3.30).

$\hat{L}^K, \hat{L}^{K-1}$ are evaluated at $\boldsymbol{P}^{\boldsymbol{K}}$. It remains to find expressions for Σ^* and T^* in terms of $\boldsymbol{P}^{\boldsymbol{L}}, \boldsymbol{P}^{\boldsymbol{R}}$ to close the system. The obtained values depend on the boundary conditions chosen, as explained below.

3.2.1.1 Stick Boundary Conditions

The following boundary conditions are used:

$$\boldsymbol{\Sigma}_{\mathbf{1}}^{*\boldsymbol{L}} = \boldsymbol{\Sigma}_{\mathbf{1}}^{*\boldsymbol{R}} \tag{3.16a}$$

$$T^{*L} = T^{*R} \tag{3.16b}$$

$$\boldsymbol{v}^{*\boldsymbol{L}} = \boldsymbol{v}^{*\boldsymbol{R}} \tag{3.16c}$$

$$q_1^{*L} = q_1^{*R} \tag{3.16d}$$

Taking the relevant rows of $\boldsymbol{P}^{*\boldsymbol{K}} = \boldsymbol{P}^{\boldsymbol{K}} + \hat{L}^{K-1} \boldsymbol{c}^{\boldsymbol{K}}$:

$$\begin{pmatrix} \boldsymbol{v}^* \\ J_1^* \end{pmatrix} = \begin{pmatrix} \boldsymbol{v}^{\boldsymbol{K}} \\ J_1^K \end{pmatrix} + Y^K \left(\begin{pmatrix} \boldsymbol{\Sigma}_{\mathbf{1}}^* \\ T^* \end{pmatrix} - \begin{pmatrix} \boldsymbol{\Sigma}_{\mathbf{1}}^{\boldsymbol{K}} \\ T^K \end{pmatrix} \right) \tag{3.17}$$

Thus:

$$\begin{pmatrix} \boldsymbol{\Sigma_1^*} \\ T^* \end{pmatrix} = \left(Y^L - Y^R\right)^{-1} \left(\begin{pmatrix} \boldsymbol{v^R} \\ J_1^R \end{pmatrix} - \begin{pmatrix} \boldsymbol{v^L} \\ J_1^L \end{pmatrix} + Y^L \begin{pmatrix} \boldsymbol{\Sigma_1^L} \\ T^L \end{pmatrix} - Y^R \begin{pmatrix} \boldsymbol{\Sigma_1^R} \\ T^R \end{pmatrix} \right) \tag{3.18}$$

3.2.1.2 Slip Boundary Conditions

The following boundary conditions are used:

$$\Sigma_{11}^{*L} = \Sigma_{11}^{*R} \tag{3.19a}$$
$$\Sigma_{12}^{*L}, \Sigma_{12}^{*R} = 0 \tag{3.19b}$$
$$\Sigma_{13}^{*L}, \Sigma_{13}^{*R} = 0 \tag{3.19c}$$
$$T^{*L} = T^{*R} \tag{3.19d}$$
$$v_1^{*L} = v_1^{*R} \tag{3.19e}$$
$$q_1^{*L} = q_1^{*R} \tag{3.19f}$$

Taking the relevant rows of $\boldsymbol{P^{*K}} = \boldsymbol{P^K} + \hat{L}^{K-1}\boldsymbol{c^K}$:

$$\begin{pmatrix} v_1^* \\ J_1^* \end{pmatrix} = \begin{pmatrix} v_1^K \\ J_1^K \end{pmatrix} + \tilde{Y}^K \left(\begin{pmatrix} \Sigma_{11}^* \\ 0 \\ 0 \\ T^* \end{pmatrix} - \begin{pmatrix} \Sigma_{11}^K \\ \Sigma_{12}^K \\ \Sigma_{13}^K \\ T^K \end{pmatrix} \right) \tag{3.20}$$

where

$$\tilde{Y}^K = \begin{pmatrix} \boldsymbol{Y_1^K} \\ \boldsymbol{Y_4^K} \end{pmatrix} \tag{3.21}$$

Thus:

$$\begin{pmatrix} \Sigma_{11}^* \\ T^* \end{pmatrix} = \left(\hat{Y}^L - \hat{Y}^R\right)^{-1} \left(\begin{pmatrix} v_1^R \\ J_1^R \end{pmatrix} - \begin{pmatrix} v_1^K \\ J_1^L \end{pmatrix} + Y^L \begin{pmatrix} \boldsymbol{\Sigma_1^L} \\ T^L \end{pmatrix} - Y^R \begin{pmatrix} \boldsymbol{\Sigma_1^R} \\ T^R \end{pmatrix} \right) \tag{3.22}$$

where

$$\hat{Y}^K = \begin{pmatrix} Y_{11}^K & Y_{14}^K \\ Y_{41}^K & Y_{44}^K \end{pmatrix} \tag{3.23}$$

3.2.1.3 Vacuum Boundary Conditions

The following boundary conditions are used:

$$\boldsymbol{\Sigma_1^*} = \mathbf{0} \tag{3.24a}$$
$$q_1^* = 0 \tag{3.24b}$$

Taking the relevant row of $\boldsymbol{P^{*K}} = \boldsymbol{P^K} + \hat{L}^{K-1}\boldsymbol{c^K}$:

$$J_1^* = J_1^K + \boldsymbol{Y_4^K} \cdot \left(\begin{pmatrix} \mathbf{0} \\ T^* \end{pmatrix} - \begin{pmatrix} \boldsymbol{\Sigma_1^K} \\ T^K \end{pmatrix} \right) \tag{3.25}$$

As $q_1^* = 0$ implies that $J_1^* = 0$, we have:

$$T^* = \frac{1}{Y_{44}^K} \left(\boldsymbol{Y_4^K} \cdot \begin{pmatrix} \boldsymbol{\Sigma_1^K} \\ T^K \end{pmatrix} - J_1^K \right) = T^K + \frac{\boldsymbol{Y_{4,:3}^K} \cdot \boldsymbol{\Sigma_1^K} - J_1^K}{Y_{44}^K} \tag{3.26}$$

3.2.1.4 Iteration

(3.14) is solved for $\boldsymbol{P^{*K}}$, which is taken to be the star state if the following conditions are satisfied:

$$\frac{\left| \boldsymbol{\Sigma_1^{*L}} - \boldsymbol{\Sigma_1^{*R}} \right|}{\min\left(\rho_0^L, \rho_0^R\right) \times \min\left(c_s^L, c_s^R\right)^2} < TOL \tag{3.27a}$$
$$\frac{\left| v_1^L - v_1^R \right|}{\min\left(c_s^L, c_s^R\right)} < TOL \tag{3.27b}$$
$$\frac{\left| q_1^L - q_1^R \right|}{\min\left(\tilde{q}^L, \tilde{q}^R\right)} < TOL \tag{3.27c}$$
$$\frac{\left| T^L - T^R \right|}{\min\left(T_0^L, T_0^R\right)} < TOL \tag{3.27d}$$

where

$$\tilde{q} = \frac{c_t^2}{\rho_0}\sqrt{\frac{T_0^3}{c_V}} \tag{3.28}$$

These convergence criteria are chosen so that the variables required to be less than TOL are dimensionless. At every iteration, (3.9b) is solved using the ODE solvers described in 2.2.4.

3.2.2 Linear Conditions

We now obtain $\hat{L}^K$ and its inverse in order to solve (3.14). Replacing the first four lines of (B.28) with the conditions (3.13a), (3.13b), we have:

$$\hat{L}^K = \left\{ \begin{array}{c} \begin{pmatrix} -\frac{\partial \boldsymbol{\sigma_d}}{\partial \rho} & \boldsymbol{e_d} & -\Pi_1 & -\Pi_2 & -\Pi_3 & 0_{3,6} \\ \frac{\partial T}{\partial \rho} & \frac{\partial T}{\partial p} & 0_{1,3} & 0_{1,3} & 0_{1,3} & 0_{1,6} \end{pmatrix} \\ \begin{pmatrix} Q\Xi_1 & -\frac{1}{\rho}Q_{:,1:3}\Pi_2 & -\frac{1}{\rho}Q_{:,1:3}\Pi_3 & \xi DQ & 0_{4,2} \end{pmatrix} \\ \begin{pmatrix} -\frac{1}{\rho} & 0 & \boldsymbol{e_d^T}A^{-1} & \boldsymbol{e_d^T}A^{-1}\Pi_1^{-1}\Pi_2 & \boldsymbol{e_d^T}A^{-1}\Pi_1^{-1}\Pi_3 & 0_{1,6} \end{pmatrix} \\ \begin{pmatrix} 0_{3,5} & I_3 & 0_{3,3} & 0_{3,6} \\ 0_{3,5} & 0_{3,3} & I_3 & 0_{3,6} \end{pmatrix} \\ \begin{pmatrix} 0_{2,15} & I_2 \end{pmatrix} \end{array} \right\} \tag{3.29}$$

Thus, the inverse of the left-eigenvector matrix becomes:

$$\hat{L}^{K-1} = \left\{ \begin{pmatrix} X^{-1}I_{5,4} \\ 0_{6,4} \\ Y \\ 0_{2,4} \end{pmatrix}, \begin{pmatrix} 0_{11,4} \\ \xi\,(DQ)^{-1} \\ 0_{2,4} \end{pmatrix}, \begin{pmatrix} -cT_p \\ cT_\rho \\ c\Pi_d^{-1}\boldsymbol{w} \\ 0_{12,1} \end{pmatrix}, \begin{pmatrix} 0_{2,3} & 0_{2,3} \\ -\Pi_1^{-1}\Pi_2 & -\Pi_1^{-1}\Pi_3 \\ I_3 & 0_{3,3} \\ 0_{3,3} & I_3 \\ 0_{6,3} & 0_{6,3} \end{pmatrix}, \begin{pmatrix} 0_{15,2} \\ I_2 \end{pmatrix} \right\} \tag{3.30}$$

where:

$$X = \begin{pmatrix} \tilde{B}_{11} & \tilde{B}_{12} & (-\Pi_1)_{11} & (-\Pi_1)_{12} & (-\Pi_1)_{13} \\ \tilde{B}_{21} & \tilde{B}_{22} & (-\Pi_1)_{21} & (-\Pi_1)_{22} & (-\Pi_1)_{23} \\ \tilde{B}_{31} & \tilde{B}_{32} & (-\Pi_1)_{31} & (-\Pi_1)_{32} & (-\Pi_1)_{33} \\ \tilde{D}_{11} & \tilde{D}_{12} & \tilde{C}_{11} & \tilde{C}_{12} & \tilde{C}_{13} \\ \tilde{D}_{21} & \tilde{D}_{22} & \tilde{C}_{21} & \tilde{C}_{22} & \tilde{C}_{23} \end{pmatrix} \tag{3.31a}$$

$$Y = -\xi Q^{-1} D^{-1} Q \Xi_1 X^{-1} I_{5,4} \tag{3.31b}$$

and also:

$$\tilde{B} = \begin{pmatrix} -\frac{\partial \boldsymbol{\sigma_d}}{\partial \rho} & \boldsymbol{e_d} \end{pmatrix} \tag{3.32a}$$

$$\tilde{C} = \begin{pmatrix} 0 & 0 & 0 \\ A_{d1}^{-1} & A_{d2}^{-1} & A_{d3}^{-1} \end{pmatrix} \tag{3.32b}$$

$$\tilde{D} = \begin{pmatrix} \frac{\partial T}{\partial \rho} & \frac{\partial T}{\partial p} \\ -\frac{1}{\rho} & 0 \end{pmatrix} \tag{3.32c}$$

By inversion of block matrices[2]:

$$X^{-1} = \begin{pmatrix} \tilde{D}^{-1}\tilde{C}Z^{-1} & \tilde{D}^{-1}\left(I - \tilde{C}Z^{-1}\tilde{B}\tilde{D}^{-1}\right) \\ -Z^{-1} & Z^{-1}\tilde{B}\tilde{D}^{-1} \end{pmatrix} \tag{3.33}$$

where

$$Z = \Pi_1 + \frac{\rho}{T_p}\left(T_p \frac{\partial \boldsymbol{\sigma_d}}{\partial \rho} + T_\rho \boldsymbol{e_d}\right) \boldsymbol{e_d^T} A^{-1} \tag{3.34}$$

3.2.3 Systems without Heat Conduction

If the heat conduction terms are dropped from the GPR model, the eigenstructure of the system changes, along with the solution of the linear conditions. Ξ retains the same definition, but is now a 3×3 matrix (comprising the top-left corner of Ξ under heat conduction). Thus,

[2] $\begin{pmatrix} A & B \\ C & D \end{pmatrix}^{-1} = \begin{pmatrix} \left(A - BD^{-1}C\right)^{-1} & -\left(A - BD^{-1}C\right)^{-1} BD^{-1} \\ -D^{-1}C\left(A - BD^{-1}C\right)^{-1} & D^{-1}\left(I + C\left(A - BD^{-1}C\right)^{-1} BD^{-1}\right) \end{pmatrix}$

Q, D are also 3×3 matrices. Taking the eigenvectors (B.42), the linear conditions become:

$$\hat{L}^K = \left\{ \begin{array}{c} \begin{pmatrix} -\frac{\partial \boldsymbol{\sigma_d}}{\partial \rho} & \boldsymbol{e_d} & -\Pi_1 & -\Pi_2 & -\Pi_3 \end{pmatrix} \\ \begin{pmatrix} Q\Xi_1 & -\frac{1}{\rho} Q\Pi_2 & -\frac{1}{\rho} Q\Pi_3 & \xi DQ \end{pmatrix} \\ (I - BA^{-1}C)^{-1} \begin{pmatrix} I_2 & -BA^{-1} & -BA^{-1}\Pi_1^{-1}\Pi_2 & -BA^{-1}\Pi_1^{-1}\Pi_3 & 0_{2,3} \end{pmatrix} \\ \begin{pmatrix} 0_{3,5} & I_3 & 0_{3,3} & 0_{3,3} \end{pmatrix} \\ \begin{pmatrix} 0_{3,5} & 0_{3,3} & I_3 & 0_{3,3} \end{pmatrix} \end{array} \right\} \tag{3.35}$$

$$\hat{L}^{K-1} = \left\{ \begin{pmatrix} X^{-1} I_{5,4} \\ 0_{6,3} \\ Y \end{pmatrix}, \begin{pmatrix} 0_{11,3} \\ \xi \left(DQ\right)^{-1} \end{pmatrix}, \begin{pmatrix} 1 & 0 \\ 0 & 1 \\ -\Pi_1^{-1} \frac{\partial \boldsymbol{\sigma_1}}{\partial \rho} & \Pi_1^{-1} \boldsymbol{e_1} \\ \mathbf{0_9} & \mathbf{0_9} \end{pmatrix}, \begin{pmatrix} 0_{2,3} & 0_{2,3} \\ -\Pi_1^{-1}\Pi_2 & -\Pi_1^{-1}\Pi_3 \\ I_3 & 0_{3,3} \\ 0_{3,3} & I_3 \\ 0_{3,3} & 0_{3,3} \end{pmatrix} \right\} \tag{3.36}$$

where:

$$X = \begin{pmatrix} \tilde{B}_{11} & \tilde{B}_{12} & (-\Pi_1)_{11} & (-\Pi_1)_{12} & (-\Pi_1)_{13} \\ \tilde{B}_{21} & \tilde{B}_{22} & (-\Pi_1)_{21} & (-\Pi_1)_{22} & (-\Pi_1)_{23} \\ \tilde{B}_{31} & \tilde{B}_{32} & (-\Pi_1)_{31} & (-\Pi_1)_{32} & (-\Pi_1)_{33} \\ \Delta_{11}^{-1} & \Delta_{12}^{-1} & (-\Delta^{-1}BA^{-1})_{11} & (-\Delta^{-1}BA^{-1})_{12} & (-\Delta^{-1}BA^{-1})_{13} \\ \Delta_{21}^{-1} & \Delta_{22}^{-1} & (-\Delta^{-1}BA^{-1})_{21} & (-\Delta^{-1}BA^{-1})_{22} & (-\Delta^{-1}BA^{-1})_{23} \end{pmatrix} \tag{3.37a}$$

$$Y = -\xi Q^{-1} D^{-1} Q \Xi_1 X^{-1} I_{5,4} \tag{3.37b}$$

where

$$\Delta = I - BA^{-1}C \tag{3.38a}$$

$$\tilde{B} = \begin{pmatrix} -\frac{\partial \boldsymbol{\sigma_1}}{\partial \rho} & \boldsymbol{e_1} \end{pmatrix} \tag{3.38b}$$

$$B = \begin{pmatrix} \rho & 0 & 0 \\ \left(\rho c_0^2 + \sigma_{11} - \rho \frac{\partial \sigma_{11}}{\partial \rho}\right) & \left(\sigma_{21} - \rho \frac{\partial \sigma_{21}}{\partial \rho}\right) & \left(\sigma_{31} - \rho \frac{\partial \sigma_{31}}{\partial \rho}\right) \end{pmatrix} \tag{3.38c}$$

By inversion of block matrices:

$$X^{-1} = \begin{pmatrix} -BA^{-1}\tilde{Z} & \left(I + BA^{-1}\tilde{Z}\tilde{B}\right)\left(I - BA^{-1}\Pi_1^{-1}\tilde{B}\right) \\ -\tilde{Z} & \tilde{Z}\tilde{B}\left(I - BA^{-1}\Pi_1^{-1}\tilde{B}\right) \end{pmatrix} \tag{3.39}$$

where

$$\tilde{Z} = \left(\Pi_1 - \tilde{B}BA^{-1}\right)^{-1} \tag{3.40}$$

3.3 Numerical Results

The GPR-RGFM is now assessed. The first fives tests in this chapter are Riemann problems that have appeared elsewhere in the literature. Reference solutions to these problems have been calculated by various methods, as described for each test individually. The sixth test is new; it assess the ability of the GPR-RGFM to correctly model heat conduction across interfaces. The last two tests are well-known two-dimensional problems, to demonstrate the applicability of the method to multiple dimensions. The stiffened gas EOS parameters for three commonly-used fluids are given in Table 3.1 on page 107.

	ρ_0	c_v	γ	p_∞	c_s	c_t	μ	P_r
Air	1.18	718	1.4	-	55	50	1.85×10^{-5}	0.714
Helium	0.163	3127	5/3	-	55	50	1.99×10^{-5}	0.688
Water	997	950	4.4	6×10^8	1	1	10^{-3}	7

Table 3.1: EOS parameters for different fluids (using SI units)

3.3.1 Helium Bubble

The interface between two different gases is now modeled. As in Test B of Wang et al. [129], a bubble of helium - surrounded by air - initially occupies the region $x \in [0.4, 0.6]$. A shock front in the air, initially at $x = 0.05$, travels towards the helium bubble. The initial conditions are given in Table 3.2 on page 108 and the EOS parameters for each material are given in Table 3.1 on page 107.

200 cells are used. Reference solutions are computed using the exact solver for mixed ideal gas Riemann problems under the Euler equations (presented in [126]). The results for times $t = 7 \times 10^{-4}$ and $t = 14 \times 10^{-4}$ are displayed in Figure 3.7 on page 109. In the former, the shock is about to hit the helium bubble (corresponding to the region of low density). In the latter, the shock has traveled through the helium bubble, compressing it slightly, and the

bubble itself has moved almost 0.1 spatial units to the right. There is good correspondence with the results in [129] and the sharp discontinuity in density is maintained.

	ρ	p	$\boldsymbol{v}$	A	$\boldsymbol{J}$
$x < 0.05$	1.3333	1.5×10^5	$\begin{pmatrix} 35.35\sqrt{10} & 0 & 0 \end{pmatrix}$	$\left(\frac{1.3333}{1.18}\right)^{\frac{1}{3}} I_3$	$\mathbf{0}$
$0.05 \leq x < 0.4$	1	10^5	$\mathbf{0}$	$\left(\frac{1}{1.18}\right)^{\frac{1}{3}} I_3$	$\mathbf{0}$
$0.4 \leq x < 0.6$	0.1379	10^5	$\mathbf{0}$	$\left(\frac{0.1379}{0.163}\right)^{\frac{1}{3}} I_3$	$\mathbf{0}$
$0.6 \leq x \leq 1$	1	10^5	$\mathbf{0}$	$\left(\frac{1}{1.18}\right)^{\frac{1}{3}} I_3$	$\mathbf{0}$

Table 3.2: Initial conditions for the helium bubble test

3.3.2 Water-Air Shock Tube

This test comprises an interface between water and air, with initial data taken from Chinnayya et al. [22] (see Table 3.3 on page 108). The aim of this test is to evaluate the ability of the GPR-RGFM at capturing interfaces between qualitatively different fluids. The water is initially at high pressure, and the air at atmospheric pressure. Due to the large difference in state variables and qualitative characteristics of the two fluids, this is an example of a test with which the original GFM for the Euler equations does not perform well.

The results using the GPR-RGFM with 200 cells are shown in Figure 3.8 on page 110, along with the exact solution to the Euler equations (computed using the extension to the stiffened gas equations of the exact Riemann solver presented in [126]). As can be seen, the material interface is captured well, with the correct intermediate density found by the numerical method.

	ρ	p	$\boldsymbol{v}$	A	$\boldsymbol{J}$
$0 \leq x < 0.7$	1000	10^9	$\mathbf{0}$	I_3	$\mathbf{0}$
$0.7 \leq x \leq 1$	50	10^5	$\mathbf{0}$	$\sqrt[3]{50} \cdot I_3$	$\mathbf{0}$

Table 3.3: Initial conditions for the water-air shock tube test

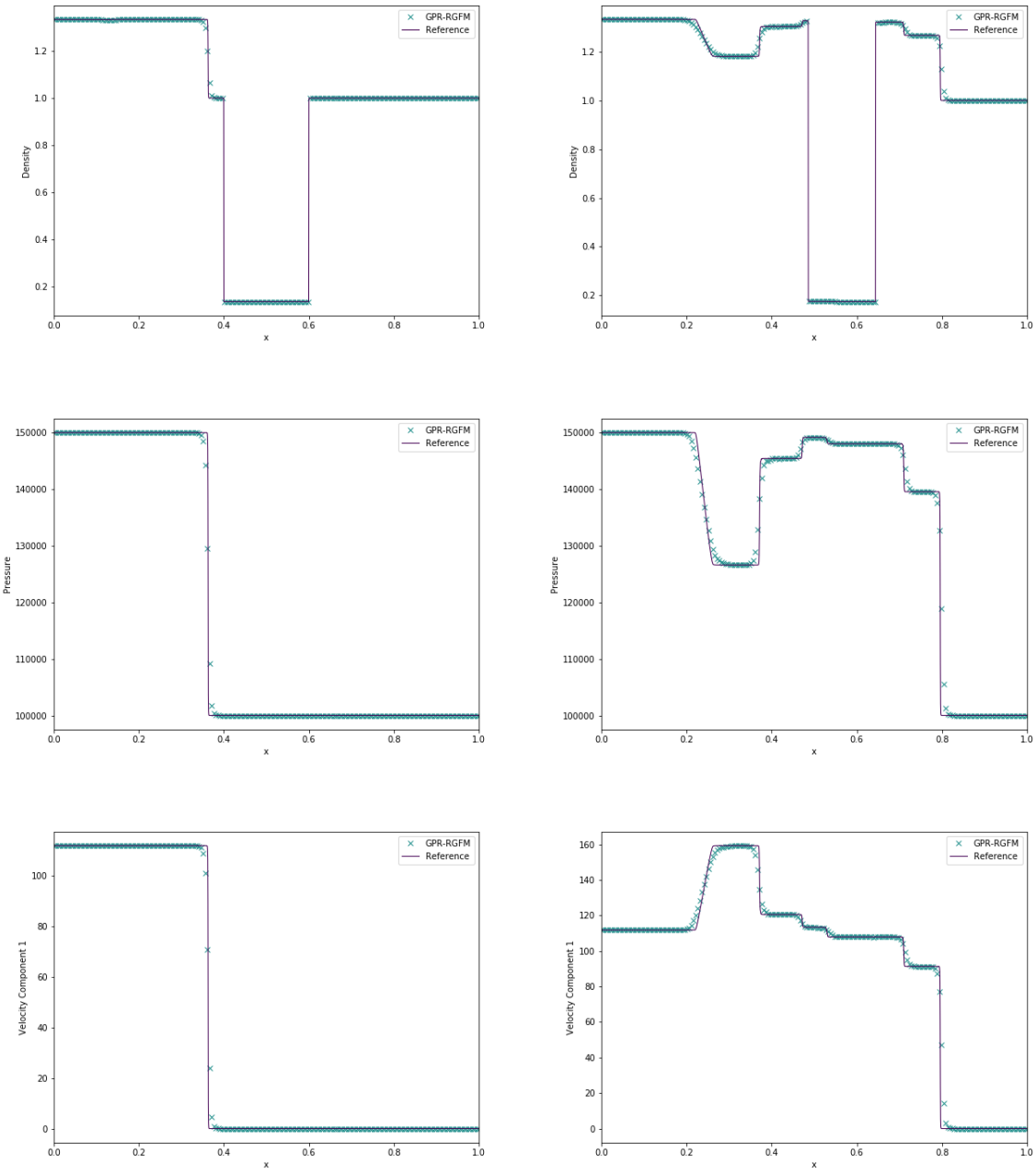

Figure 3.7: Density, pressure, and velocity for the helium bubble test with GPR-RGFM at times $t = 7 \times 10^{-4}$ (left) and $t = 14 \times 10^{-4}$ (right)

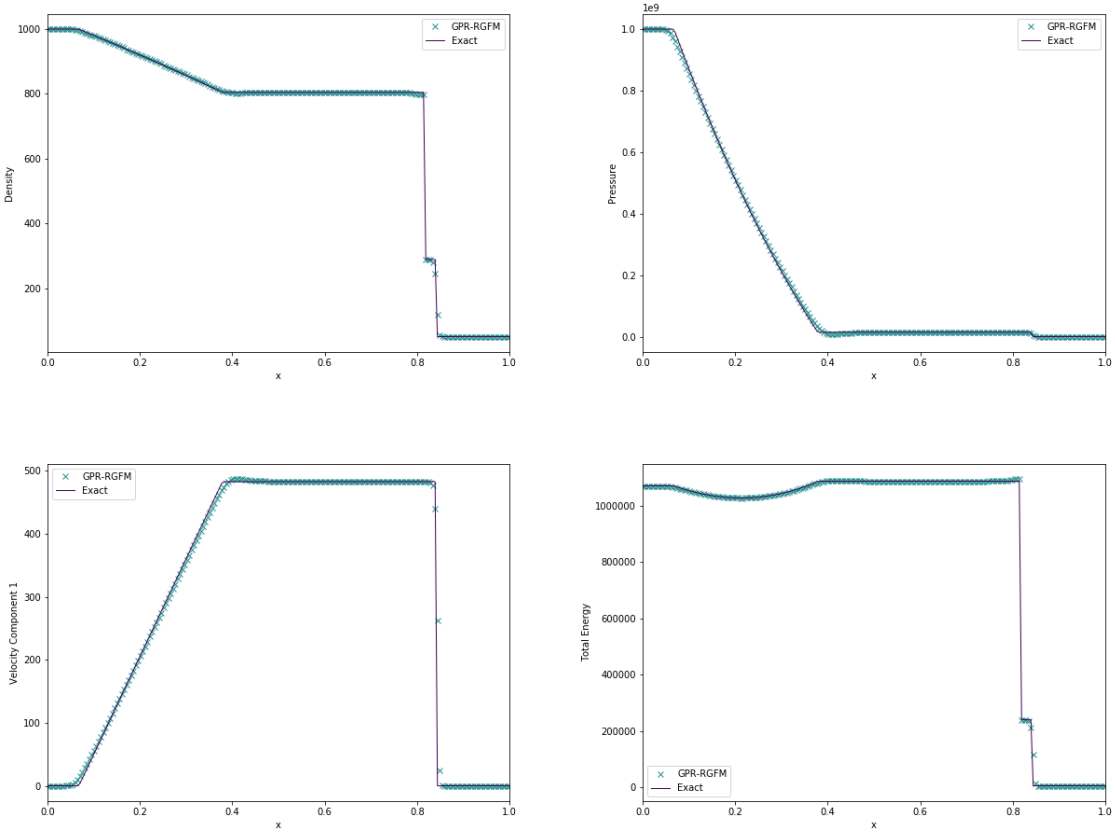

Figure 3.8: Density, pressure, velocity, and internal energy for the water-air shock tube test with GPR-RGFM

3.3.3 PBX9404-Copper Shock Tube

This test is taken from [13], with the aim of testing the ability of the GPR-RGFM to model interfaces between fluids and solids. High pressure, reacted PBX9404 is in contact with copper at position $x = 0.5$ on domain $x \in [0, 1]$, with both materials initially at rest. The pressure of the PBX is initially $18.9GPa$, and the entropy of the copper is initially 0. The PBX follows an ideal gas EOS, with parameters $\rho_0 = 1840$, $\gamma = 2.85$, $c_s = 1$, $\mu = 10^{-2}$. The copper follows the Godunov-Romenski EOS, with parameters $\rho_0 = 8930$, $c_v = 390$, $T_0 = 300$, $c_0 = 3939$, $\alpha = 1$, $\beta = 3$, $\gamma = 2$, $b_0 = 2141$. The test is run until time $t = 0.5 \times 10^{-6}$, using 500 cells.

The exact solution to this test is calculated using the iterative solver described in [11]. The error in the wavespeeds is calculated from the residual error in the traction and velocities across the central contact, as required by the Rankine–Hugoniot conditions and boundary conditions. The wavespeeds are found by iteratively reducing the residual using the Newton–Raphson method.

Plots for density, velocity, and total stress are given in Figure 3.9 on page 112. As can be seen, the GPR-RGFM is able to reproduce the solution to high fidelity, with a perfectly sharp discontinuity in the density, and a very well resolved discontinuity in the total stress.

3.3.4 Aluminium in Vacuum

This test is taken from [10]. The initial conditions of the test consist of a slab of aluminium, initially with velocity $\begin{pmatrix} 2 & 0 & 0.1 \end{pmatrix}$, meeting a vacuum at point $x = 0.5$, on the domain $x \in [0, 1]$. The distortion of the aluminium is initially given by:

$$A = \begin{pmatrix} 1 & 0 & 0 \\ -0.01 & 0.95 & 0.02 \\ -0.015 & 0 & 0.9 \end{pmatrix}^{-1} \tag{3.41}$$

The initial density of the aluminium is thus given as $\rho = \rho_0 \det(A)$. The aluminium is modeled using the Godunov-Romenski EOS, with parameters $\rho_0 = 2.71$, $c_v = 9 \times 10^{-4}$, $T_0 = 300$, $c_0 = 5.037$, $\alpha = 1$, $\beta = 3.577$, $\gamma = 2.088$, $b_0 = 3.16$, $c_t = 2$, $\kappa = 204$.

The test was run until time $t = 0.06$, using 500 cells. The results of solving this problem with the GPR-RGFM, not including thermal conduction (as in [10]), are given in Figure 3.10

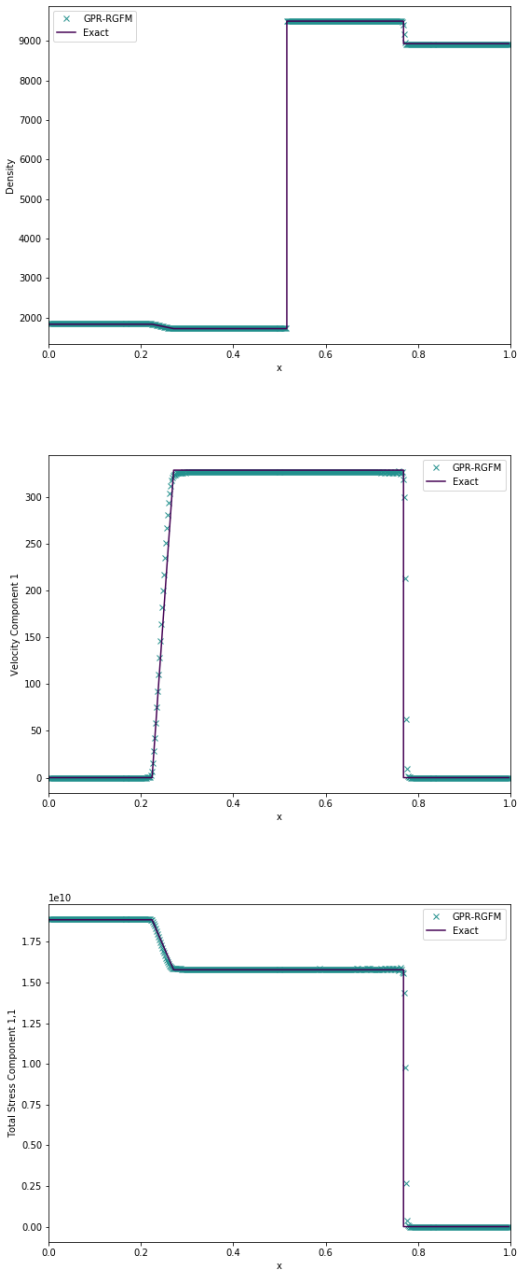

Figure 3.9: Density, velocity, and total stress for the Copper-PBX test with GPR-RGFM

	ρ	p	$\boldsymbol{v}$	A	$\boldsymbol{J}$
$x < 0$	2	1	$\mathbf{0}$	$\sqrt[3]{2} \cdot I_3$	$\mathbf{0}$
$x \geq 0$	0.5	1	$\mathbf{0}$	$\frac{1}{\sqrt[3]{2}} \cdot I_3$	$\mathbf{0}$

Table 3.4: Initial conditions for the heat conduction test

on page 114. The results of solving the problem, including thermal conduction, are given in Figure 3.11 on page 115. The exact solutions are calculated using the iterative method presented in [11], as described in the previous test.

As can be seen, in both cases, the GPR-RGFM is able to accurately capture the longitudinal wave and the two transverse shock waves that propagate to the left side of the initial point of contact. Note that at $t = 0.06$, the vacuum occupies the region $[\sim 0.65, 1]$. As this region is empty, the plots in the aforementioned figures are shown over the interval $[0, 0.7]$, to give greater resolution to the region of interest.

Without thermal conduction, the interface suffers from a "heating error" of the same kind discussed in [10], manifesting itself as a slight undershoot in the density of the metal at the interface. Note that by incorporating thermal conduction into the numerical method, this heating error completely disappears, without the use of an entropy fix (as in [10]). It must be noted that, in this case, the waves in the state variables now appear to be slightly more diffused than the reference solution. This is the expected effect of incorporating the phenomenon of thermal conduction into this physical problem.

3.3.5 Heat Conduction in a Gas

This test is based on the Heat Conduction in a Gas Test of Dumbser et al. [35]. Two ideal gases at different temperatures are initially in contact at position $x = 0$. The initial conditions for this problem are given in Table 3.4 on page 113.

The material parameters are taken to be: $\gamma = 1.4$, $c_v = 2.5$, $\rho_0 = 1$, $p_0 = 1$, $c_s = 1$, $c_t = 1$, $\mu = 10^{-2}$, $\kappa = 10^{-2}$. An interface is initially placed between the two volumes of air at $x = 0.5$. The final time is taken to be $t = 1$, and 200 cells are used. Results are displayed in Figure 3.12 on page 117, using the results from [35] as a reference. The material interface is denoted by a dashed vertical line.

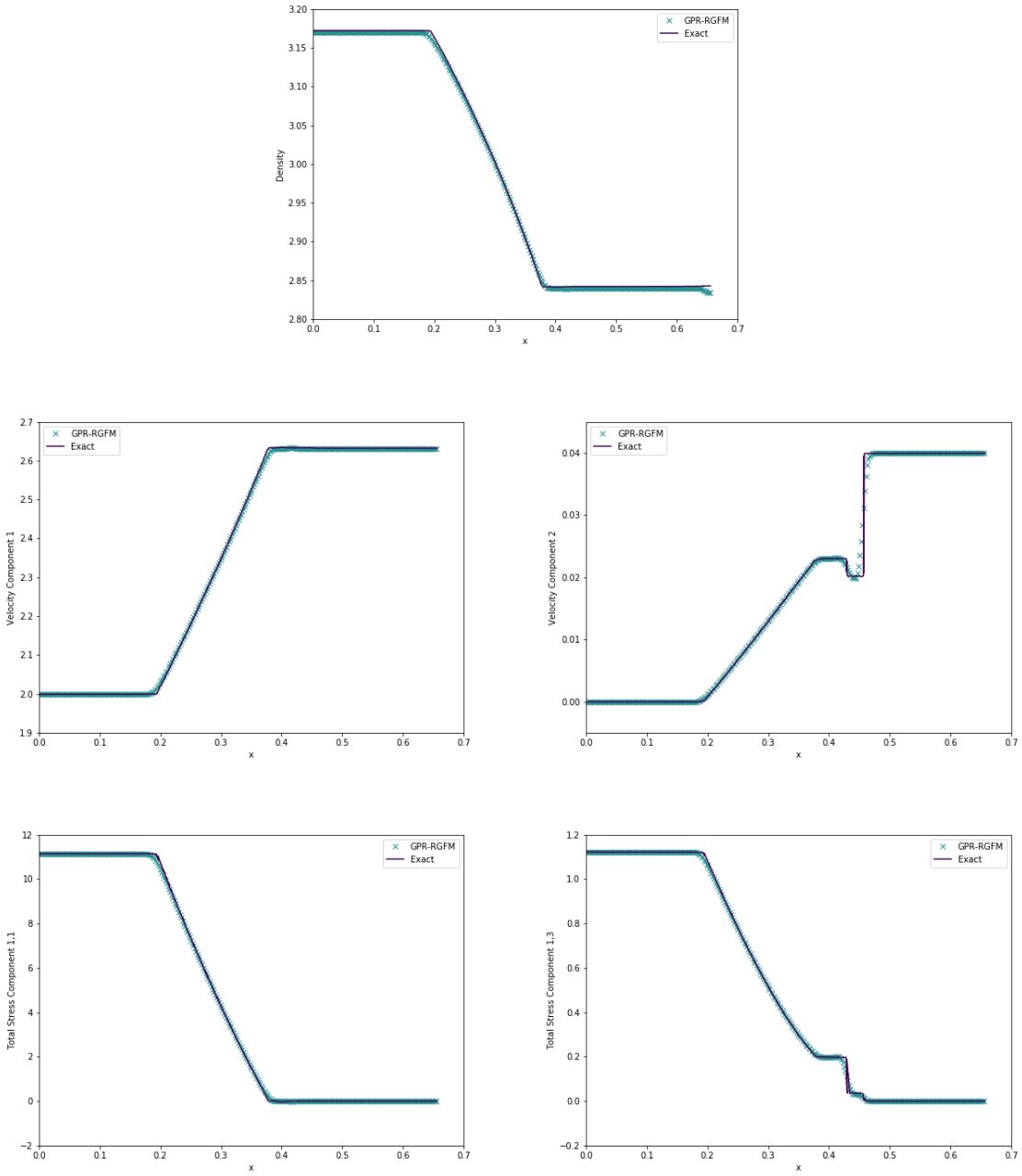

Figure 3.10: Density, velocity, and total stress for the aluminium-vacuum test with GPR-RGFM, not including thermal conduction

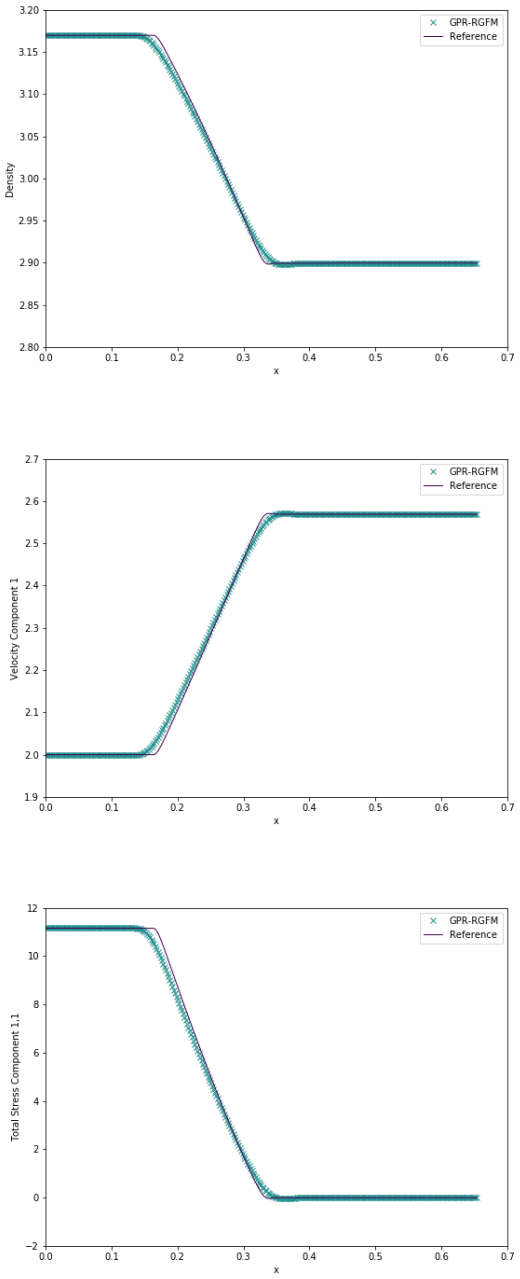

Figure 3.11: Density, velocity, and total stress for the aluminium-vacuum test with GPR-RGFM, including thermal conduction

The temperature curve generated using the GPR-RGFM matches very well the reference solution. The interface has moved to $x = 0.53756$, as is to be expected, as the cooler gas on the left expands as it heats up, and the hotter gas on the right contracts as it cools. Initially, the mass of the left volume is 1 and the right volume is 0.25. At $t = 1$, these masses are 0.9997 and 0.2503, respectively. Thus, mass on either side is conserved to a good approximation. Although the GPR-RGFM results for the heat flux match the reference solution well over most of the domain, there are aberrations in a small region around the interface. Although this doesn't affect the temperature curve, these discrepancies are undesirable, and possible methods to rectify them are discussed in Chapter 4.2.

3.3.6 Inter-Material Heating-Induced Acoustic Wave

The test assesses the ability of the GPR-RGFM to conduct heat between two different materials. Take the material parameters for air and helium from Section 3.3.1. Take the scaled spatial variable x^* defined by:

$$x = \frac{\mu^{air} c_0^{air}}{p_0 \gamma^{air}} x^* \tag{3.42}$$

The domain $x^* \in [0, 90]$ is used. Thermal energy is added at the left boundary at a high power of $\frac{\gamma^{air} p_0 c_0^{air}}{P_r^{air}(\gamma^{air}-1)}$ (around $1.7 \times 10^8 W m^{-2}$). Three scenarios are tested:

1. The domain is filled with air.
2. The domain comprises two volumes of air, initially separated at $x^* = 22.5$.
3. The domain comprises a volume of air (left) and a volume of helium (right), initially separated at $x^* = 22.5$.

The initial conditions for the two gases in all scenarios are given in Table 3.5 on page 118. The results of the test are shown in Figure 3.13 on page 119 and Figure 3.14 on page 120 for various times. The material interface is represented by a dashed vertical line in scenarios 2 and 3. All simulations used 400 cells.

As the left wall heats up, a temperature gradient develops and the acoustic wave described appears. The results for scenarios 1 and 2 are indistinguishable, as they should be, and there

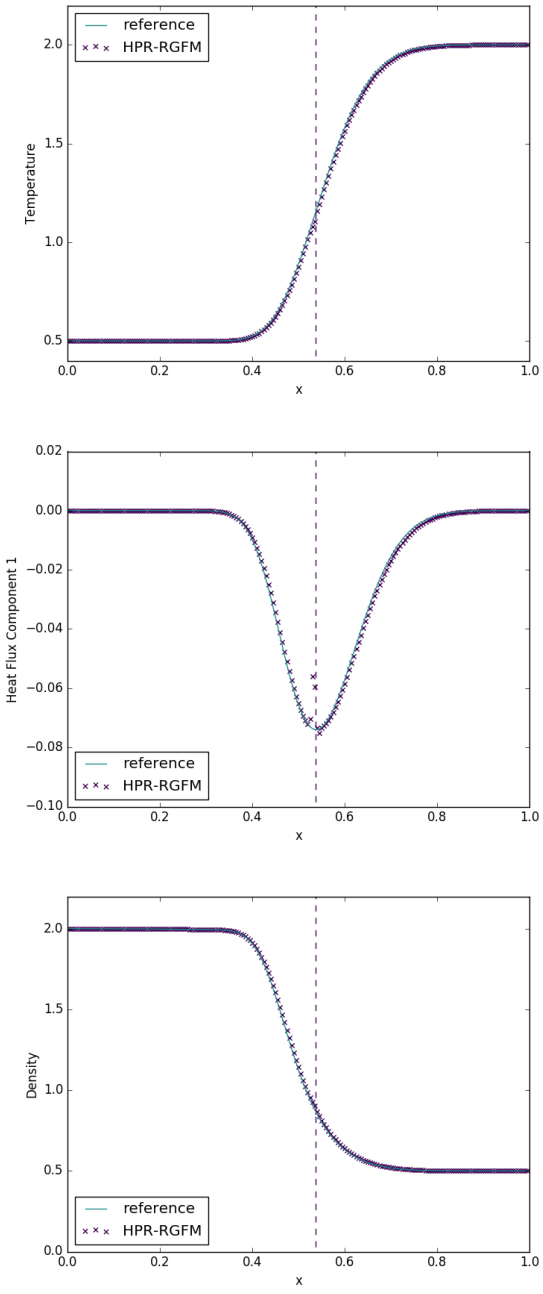

Figure 3.12: Temperature, heat flux, and density for the inter-material heat conduction test with GPR-RGFM

	ρ	p	$\boldsymbol{v}$	A	$\boldsymbol{J}$
air	1.18	101325	$\mathbf{0}$	I_3	$\mathbf{0}$
helium	0.164	101325	$\mathbf{0}$	I_3	$\mathbf{0}$

Table 3.5: Initial conditions for the inter-material heating-induced acoustic wave test

are no aberrations around the material interface in scenario 2. In scenario 3, the acoustic wave hits the interface at around $t = 2 \times 10^{-9}$ and then speeds up (as it should, the speed of sound in helium being around three times that of air). The heat flux wave increases in intensity after passing into the helium, owing to the fact that the wave is traveling faster. As expected, all variables displayed are continuous across the interface.

In scenarios 2 and 3 the interface moves to the right as the air heats up and expands. The masses of the air volumes in these two scenarios at various times are given in Table 3.6 on page 118, demonstrating that mass is conserved well as the interface moves.

Time ($\times 10^{-9}$)	0	1	2	3	4	5
Mass in Scenario 2 ($\times 10^{-6}$)	1.254	1.255	1.253	1.252	1.252	1.253
Mass in Scenario 3 ($\times 10^{-6}$)	1.254	1.253	1.248	1.254	1.255	1.255

Table 3.6: Mass of the air volume in scenarios 2 and 3 at various times

3.3.7 Convergence Study

In order to determine the order of convergence of the Riemann Ghost Fluid Method presented in this study, the tests from 3.3.2, 3.3.3, and 3.3.4 were run with cell counts of $50, 100, 150, 200, 250, 300$, and the error as compared with the exact solutions were calculated at the interfaces. The reason for choosing these two tests was to incorporate a range of different interface types (gas-liquid, fluid-solid, and solid-vacuum). The results are displayed in Table 3.7 on page 121. As can be seen, in all tests, the convergence rate is roughly first-order.

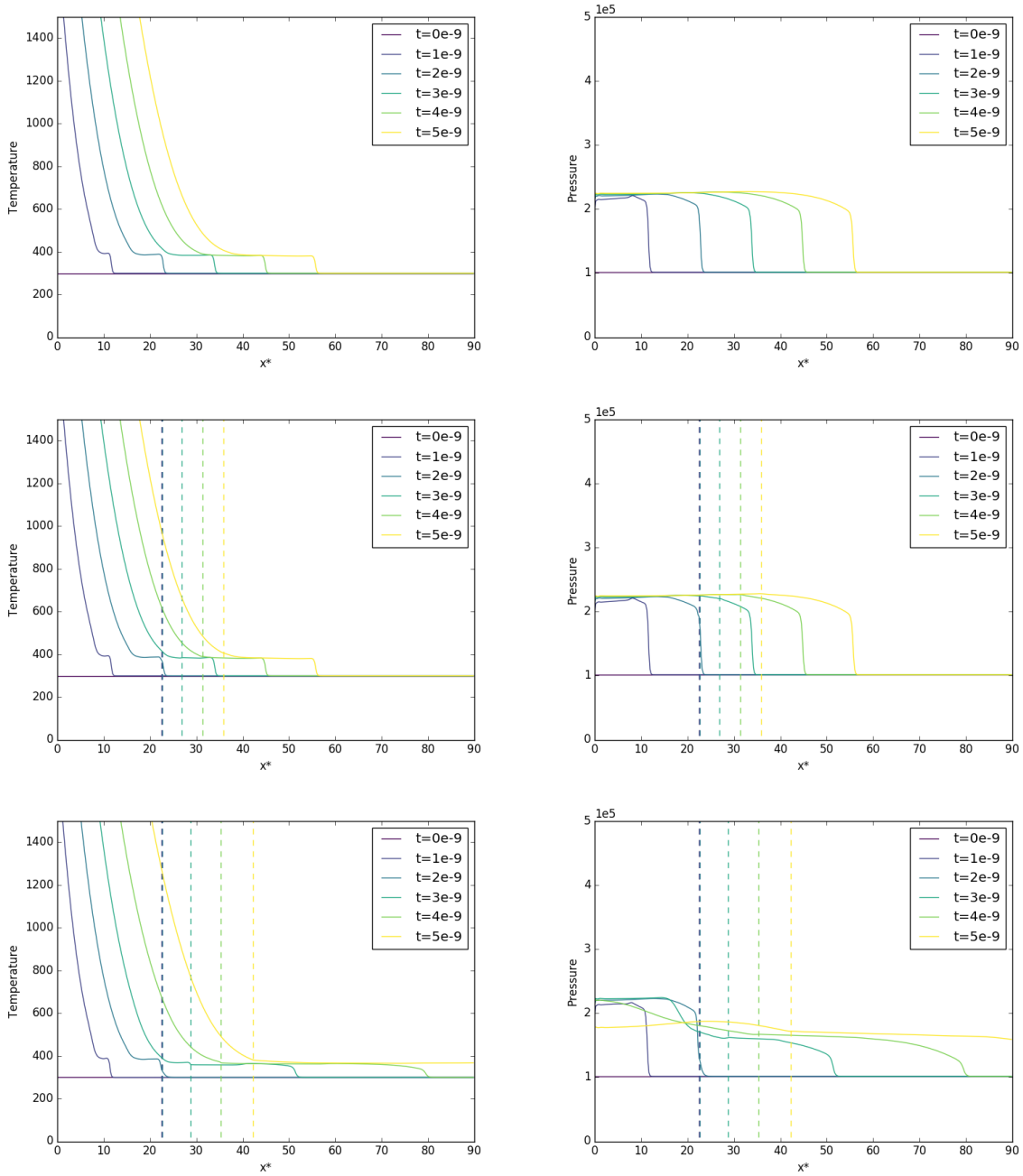

Figure 3.13: Temperature and pressure for the inter-material heating-induced acoustic wave test with: a single volume of air (top); two volumes of air initially separated at $x^* = 22.5$ (middle); air and helium initially separated at $x^* = 22.5$ (bottom).

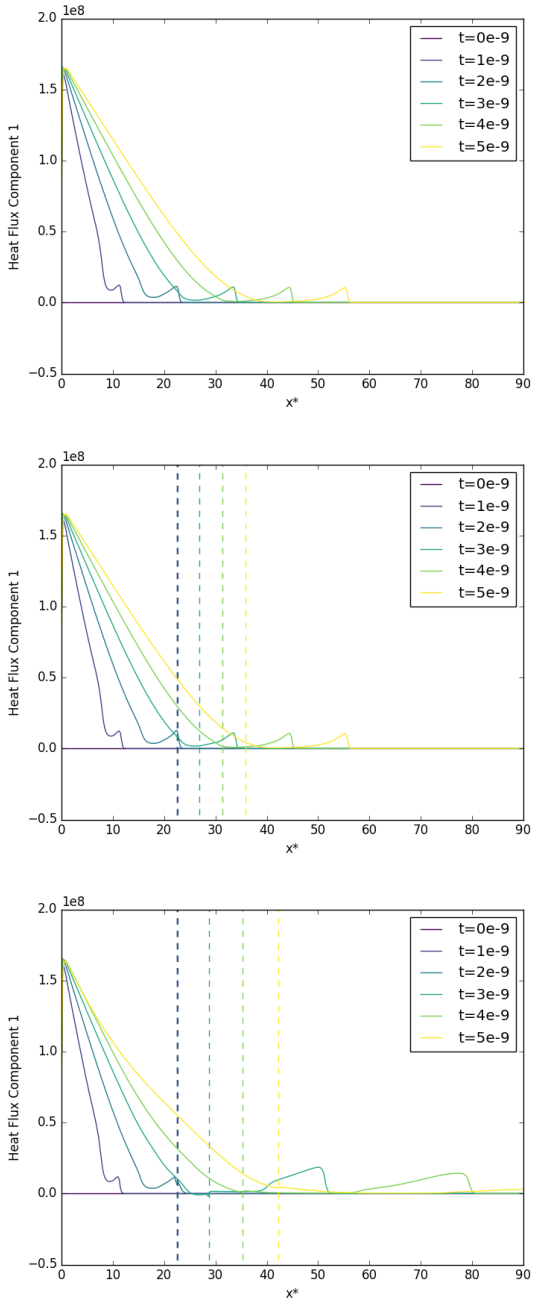

Figure 3.14: Heat flux for the inter-material heating-induced acoustic wave test with: a single volume of air (top); two volumes of air initially separated at $x^* = 22.5$ (middle); air and helium initially separated at $x^* = 22.5$ (bottom).

	Water-Air Test		PBX-Copper Test		Aluminium-Vacuum Test	
# Cells	Error	Rate	Error	Rate	Error	Rate
50	17.67419797		20.27348796		0.04232714	
100	7.98596866	1.146	10.14165497	0.999	0.02180830	0.957
150	5.20404021	1.056	6.57517319	1.069	0.01365700	1.154
200	4.19411427	0.750	4.99100631	0.958	0.01005346	1.065
250	3.32431075	1.042	3.73732754	1.296	0.00793378	1.061
300	2.77425968	0.992	3.10851219	1.010	0.00571356	1.800

Table 3.7: Convergence Rates for the Water-Air Test, PBX-Copper Test, and Aluminium-Vacuum Test

3.4 Discussion

The Riemann Ghost Fluid Method presented in this study has been demonstrated to be an effective way of accurately simulating the interfaces between several different materials (in all three main phases of matter, plus vacuum), described by the GPR model. Unlike in many existing implementations, heat conduction across the interface was simulated accurately, leading to the representation of physical phenomena that are often overlooked, and to the redundancy of numerical techniques that are sometimes used to enforce more empirically-accurate results (such as entropy and temperature fixes).

The framework presented here greatly simplifies the conceptual framework required for multimaterial interactions. Implementation should be easier and quicker, and future work can be more focused on a single model, rather than several fundamentally different frameworks.

3.4.1 Limitations

Throughout this study, the various fluids have been assumed to be immiscible. Whilst this is a common assumption in situations where mixing is low or practically non-existent, there are many problems which may require it. An area of further research would be the implementation of a mixture model such as that proposed by Romenski et al. [109, 112], which uses the same thermal conduction system as the GPR model.

The truncation of the Taylor series expansions (3.12a) and (3.12b) used to find the star states of the heat flux and the viscous stress tensor implicitly assumes that there are only small differences between the side states and the star states of the variables upon which

$q_1^*, \boldsymbol{\sigma}_1^*$ depend (ρ, p, J_1, and $\boldsymbol{A_1}$). If this is the case, higher order terms of the expansion can be neglected. If it is not, however, the method may fail. The linearized nature of the GPR-RGFM solver also implicitly assumes that all waves of interest present in the Riemann Problem are shocks. Thus, strong rarefactions may cause the method to fail.

3.4.2 Potential Improvements

As noted in Section 3.3.5, the GPR-RGFM method does not necessarily ensure the continuity of the normal component of heat flux across interfaces that feature discontinuous temperature jumps. This is despite the method accurately modeling both the heat conduction across the interface over time, and the corresponding evolution to thermal equilibrium between the two materials. The reason for this is that the star states produced by the linearized solver presented in 3.2.1 represent the state of the system at a time slightly beyond the point in time at which they are applied to neighboring ghost cells. With more simple systems of PDEs - such as the Euler equations - this often doesn't matter, as the star states are constant in time, or their time evolution is easily calculated. Owing to the source terms in the GPR equations, however, the star states evolve in a manner for which an analytical solution is not available. Thus, when the star states are applied to the ghost cells, they contain higher heat fluxes and slightly different temperatures to the actual values at the interface at that moment in time, leading to the slight aberration apparent in the heat flux in Figure 3.12 on page 117.

A possible solution to this is as follows: Take materials L and R either side of an interface. Given the states straddling the interface, Q_L, Q_R, derive Q_L^* using the procedure outlined in 3.2.1. Then, by inverting this procedure, derive a state $\tilde{Q}_R$ such that if $Q_L, \tilde{Q}_R$ are both states for material L (rather than for materials L and R, respectively), following the procedure in 3.2.1 obtains the same star state, Q_L^*. The derivation of such an inverse mapping should be feasible, possibly with the addition of some physical constraints. In this way, $\tilde{Q}_R$ represents a state for the righthand cell at the current time, which - if cell R were occupied by material L - would result in the same state on the lefthand side of the interface at the end of the current timestep as if the righthand cell were occupied by Q_R and material R.

Another clear improvement to the GPR-RGFM method presented would be to use a better Riemann solver than the iterative, linearized solver devised in 3.2.1. Let L be the matrix of left eigenvectors of the primitive system. As noted previously, the solver relies upon the fact

that each of the following relations holds along the characteristic to which it corresponds:

$$L \cdot \frac{d\boldsymbol{P}}{dt} = L \cdot \boldsymbol{S} \tag{3.43}$$

Methods to accurately integrate (3.43) from the left and right interface boundary states to their respective star states warrant further research.

Alternatively, a completely different approximate Riemann solver could be employed, such as the universal HLLEM solver of Dumbser et al. [29]. This path-conservative formulation of the HLLEM solver works for general non-conservative systems (such as the GPR model) and is simple to implement. It's based upon a new path-conservative HLL method (building on the original method of Harten, Lax, and van Leer [54]) but is claimed to be able to represent linearly degenerate intermediate waves "with a minimum of smearing" by evaluating the eigenvalues and eigenvectors of the intermediate characteristic fields (given in Chapter B).

There are iterative exact Riemann solvers for the equations of non-linear elasticity (to which the GPR model reduces as $\tau_1 \to \infty$). Thus, they will work for applications of the GPR model to solids problems (and perhaps to very viscous fluids problems too). Although these solvers are computationally expensive, they are only used once at each material interface point at each time step, and thus the added accuracy that they provide may be desirable. There are two ways to formulate the equations of non-linear elasticity: one in which the deformation tensor (the analogue of the inverse of the GPR model's distortion tensor) is evolved in time, and one in which its inverse (the analogue of A) is evolved instead. Miller's exact solver [87] uses the first formulation and the solver of Barton et al. [11] uses the second. The former can be used to evolve A^{-1}, from which A can be calculated. Unfortunately, both solvers critically assume that the source terms of the system vanish, and so are unlikely to produce the correct boundary conditions for the GPR-RGFM when modeling relatively inviscid fluids. It should also be noted that they cannot be used for problems involving heat conduction across material interfaces, and they do not take the thermal conduction subsystem of the GPR model into account.

Chapter 4

Impact-Induced Detonation in an Elastoplastic Confiner

The material in this section is published in [67].

4.1 Numerical Results

4.1.1 Taylor Bar

This follows a similar form to that found in [18, 80]. A bar of aluminium of dimensions 100×500 travels towards a solid wall at speed 0.015. The surrounding environment is a vacuum. The aluminium bar is modeled by the shock Mie-Gruneisen equation of state, with parameters $\rho_0 = 2.785$, $c_v = 9 \times 10^{-4}$, $c_0 = 0.533$, $\Gamma_0 = 2$, $s = 1.338$. The aluminium also follows a plasticity law with parameters $b_0 = 0.305$, $\sigma_Y = 0.003$, $\tau_0 = 1$, $n = 20$. The domain has dimensions 300×510, with $\Delta x, \Delta y = 1$.

The density and plastic deformation of the bar at times $t = 0.0025$ and $t = 0.005$ are shown in Figure 4.1 on page 125. Unfortunately there are no experimental results for this test, but the reader is asked to note the good agreement here with the results found in [80]. In that study, the boundary between the bar and the vacuum is captured using a Lagrangian scheme, and it is reassuring that the same behavior is captured here with a characteristically different numerical method.

4.1.2 Aluminum Plate Impact

This test follows the form found in Michael & Nikiforakis [84] (based on the original formulation found in [61]). An aluminum projectile impacts upon an aluminum plate at speed 400. The domain is $[0, 0.03] \times [0, 0.04]$, with the projectile initially occupying $[0.001, 0.006] \times [0.014, 0.026]$, and the plate occupying $[0.006, 0.028] \times [0.003, 0.037]$. We have $\Delta x, \Delta y = 10^{-4}$. The surroundings are taken to be a vacuum. The aluminium follows a Godunov-Romenski EOS with parameters $\rho_0 = 2710$, $c_v = 900$, $T_0 = 300$, $c_0 = 5037$, $\alpha = 1$,

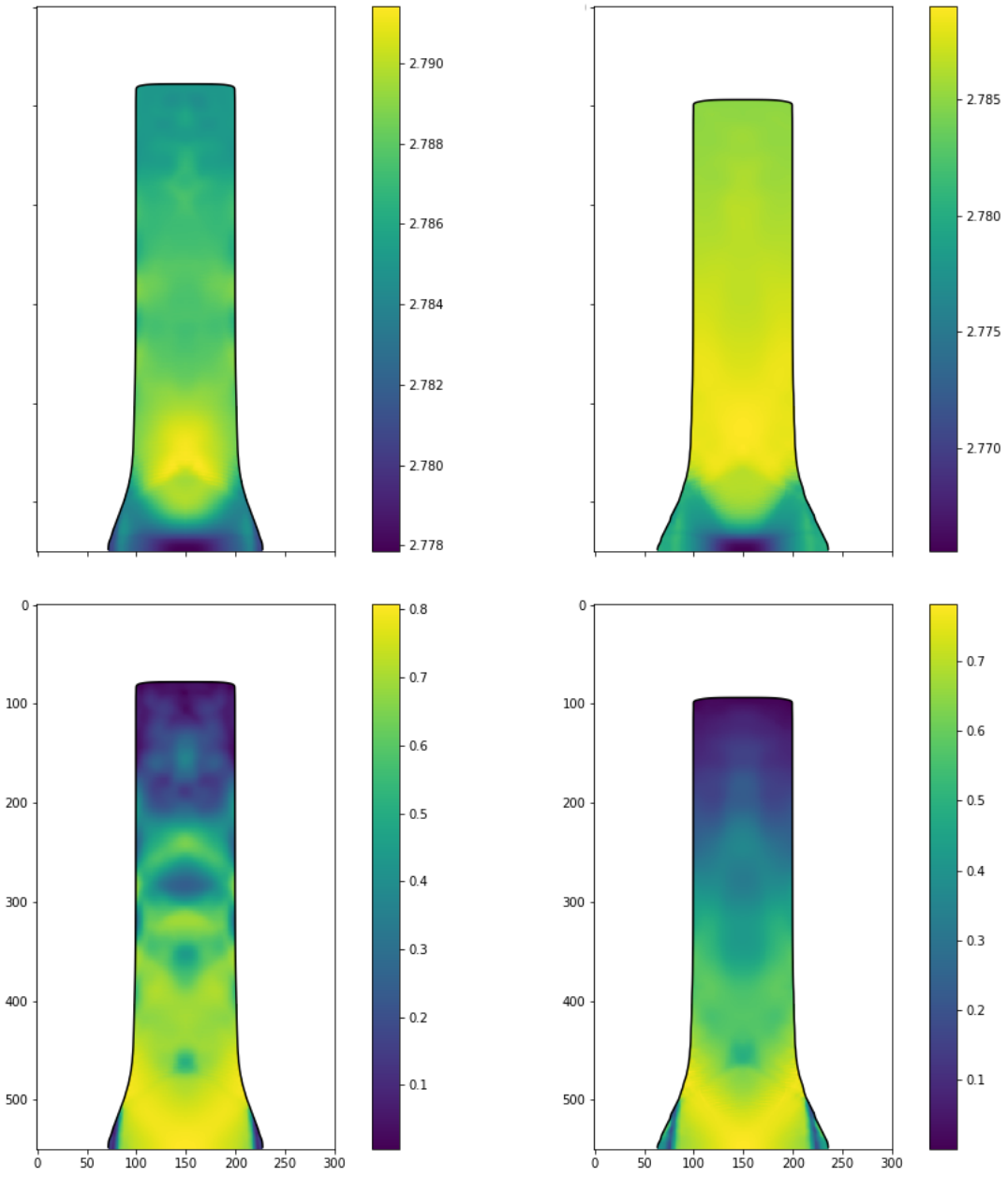

Figure 4.1: Density (top) and plastic deformation (bottom) for the Taylor bar test, at times $t = 0.0025$ (left) and $t = 0.005$ (right)

$\beta = 3.577$, $\gamma = 2.088$, $b_0 = 3160$, $\sigma_Y = 4 \times 10^8$, $\tau_0 = 1$, $n = 100$. Gauges are placed initially at $x = 0.0078125$, 0.0114375, 0.0150625, 0.0186875, 0.0223125 to measure the state variables over time, and these gauges are permitted to move with the local velocity of the material. The test is run until time $t = 5 \times 10^{-6}$.

The pressure contours throughout the aluminium at various times are shown in Figure 4.2 on page 127. Despite relying on a slightly different plasticity model to that found in [84], it can be seen that these plots are in very good agreement with those found in the aforementioned publication. Note that release waves can be seen on the sides of the plate, in agreement with Michael & Nikiforakis.

Plots over time of the x-velocity, pressure, density, and total stress - as measured by the gauges - are given in Figure 4.3 on page 128. Note the good agreement between these plots and those found in [61, 84], both in terms of their qualitative shape, and the arrival times of the waves that they represent. One can clearly see the separation between the elastic precursor wave and the trailing plastic wave in the impacted plate, and the subsequent return waves that are generated once these waves reach the end of the plate. This implies that the GPR-RGFM has correctly captured the aluminium-vacuum interface.

4.1.3 Confined C4 Detonation without Back Plate

This test is a variation of that found in [84]. A steel bar of length 0.03 and width 0.018 impacts upon a steel plate of depth 0.003, which is covering a region of depth 0.009 composed of C4 . The bar is initially traveling with speed 700. The system is surrounded by air.

The steel is modeled using a shock Mie-Gruneisen EOS, with parameters $\rho_0 = 7870$, $c_v = 134$, $c_0 = 4569$, $\Gamma_0 = 2.17$, $s = 1.49$, $b_0 = 3235$, $\sigma_Y = 0.53 \times 10^9$, $\tau_0 = 1$, $n = 10$. The C4 is modeled using a JWL EOS, with parameters $\rho_0 = 1601$, $c_v = 2.487 \times 10^6/1601$, $\Gamma_0 = 0.8938$, $A = 7.781 \times 10^{13}$, $B = -5.031 \times 10^9$, $R_1 = 11.3$, $R_2 = 1.13$, $b_0 = 1487$. The air is modeled using an ideal gas EOS, with parameters $\rho_0 = 1.18$, $c_v = 718$, $\gamma = 1.4$, $b_0 = 50$, $\mu = 1.85 \times 10^{-5}$. The reaction of the C4 is captured using the ignition and growth model, with parameters $Q = 9 \times 10^9/1601$, $I = 4 \times 10^6$, $G_1 = 1.4 \times 10^{-20}$, $G_2 = 0$, $a = 0.0367$, $b = 2/3$, $c = 2/3$, $d = 1/3$, $x = 7$, $y = 2$, $\phi_I = 0.022$, $\phi_{G1} = 1$.

Figure 4.5 on page 130 displays the resulting pressure and C4 concentration at times $t = 2.4 \times 10^{-6}$ and $t = 4.9 \times 10^{-6}$. As can be seen, the kinetic energy of the bar is correctly transmitted

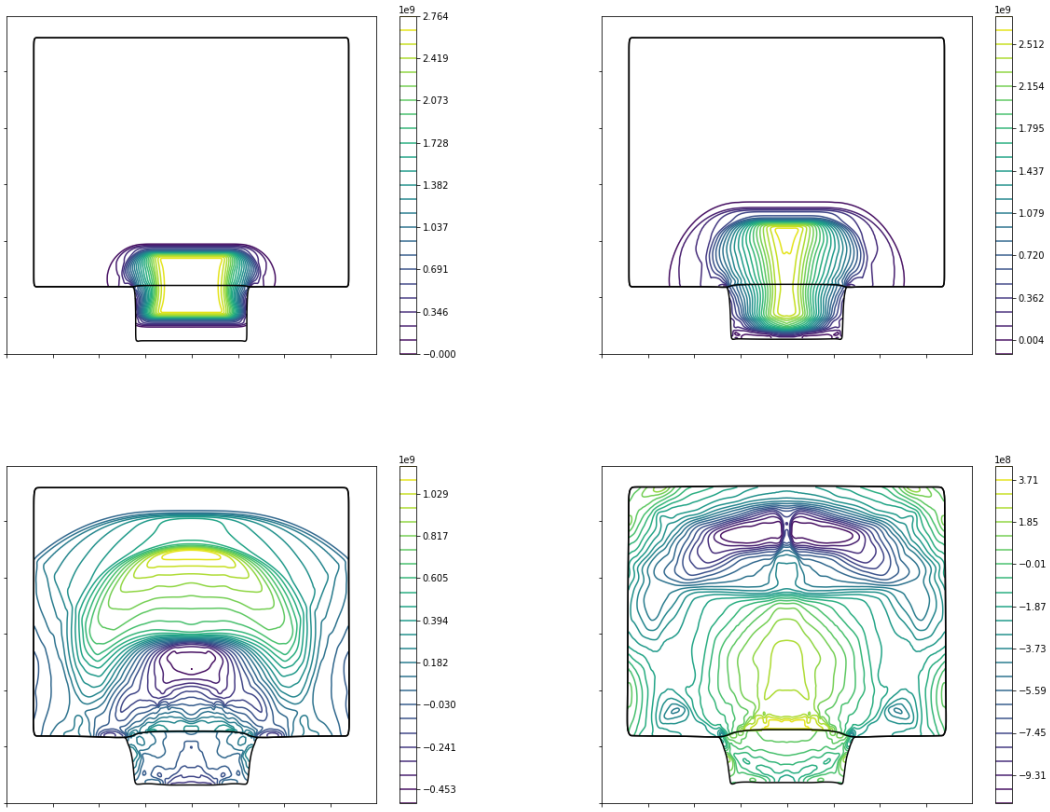

Figure 4.2: Pressure contour plots for the aluminium plate impact test, at times $0.5\mu s$, $1\mu s$, $3\mu s$, $5\mu s$

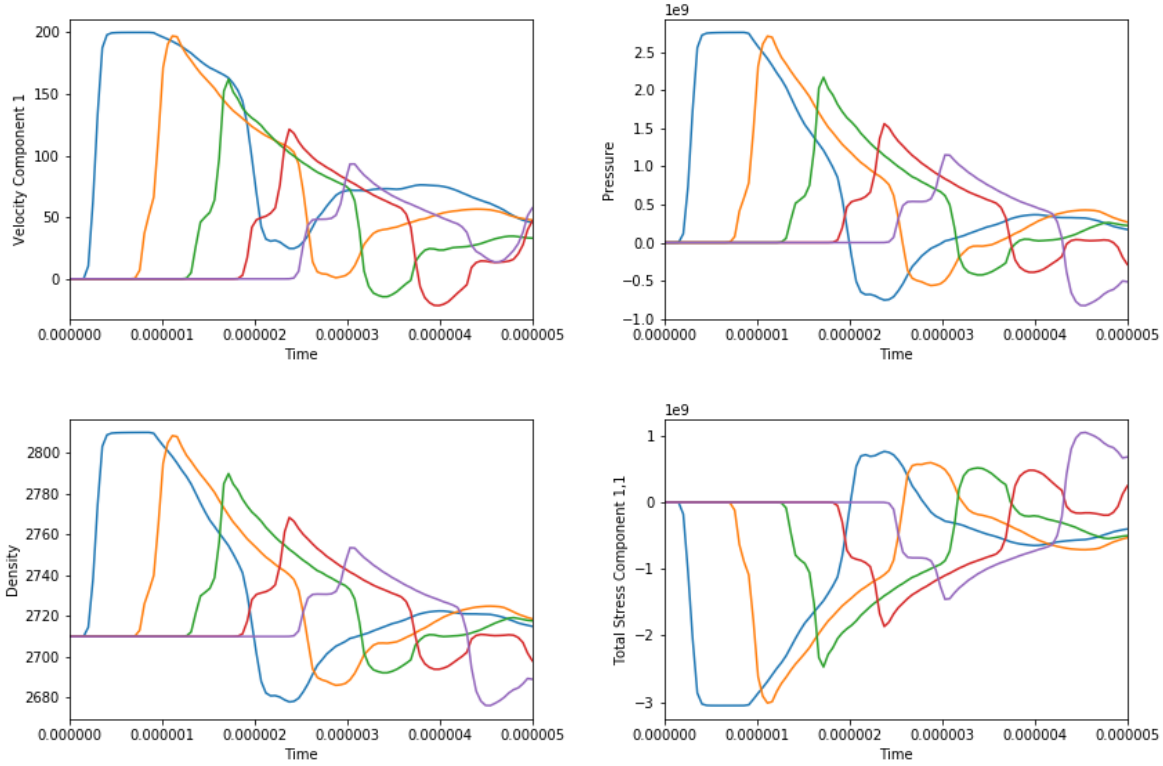

Figure 4.3: x-velocity, pressure, density, and total stress over time, as measured by the various gauges of the aluminium plate impact test

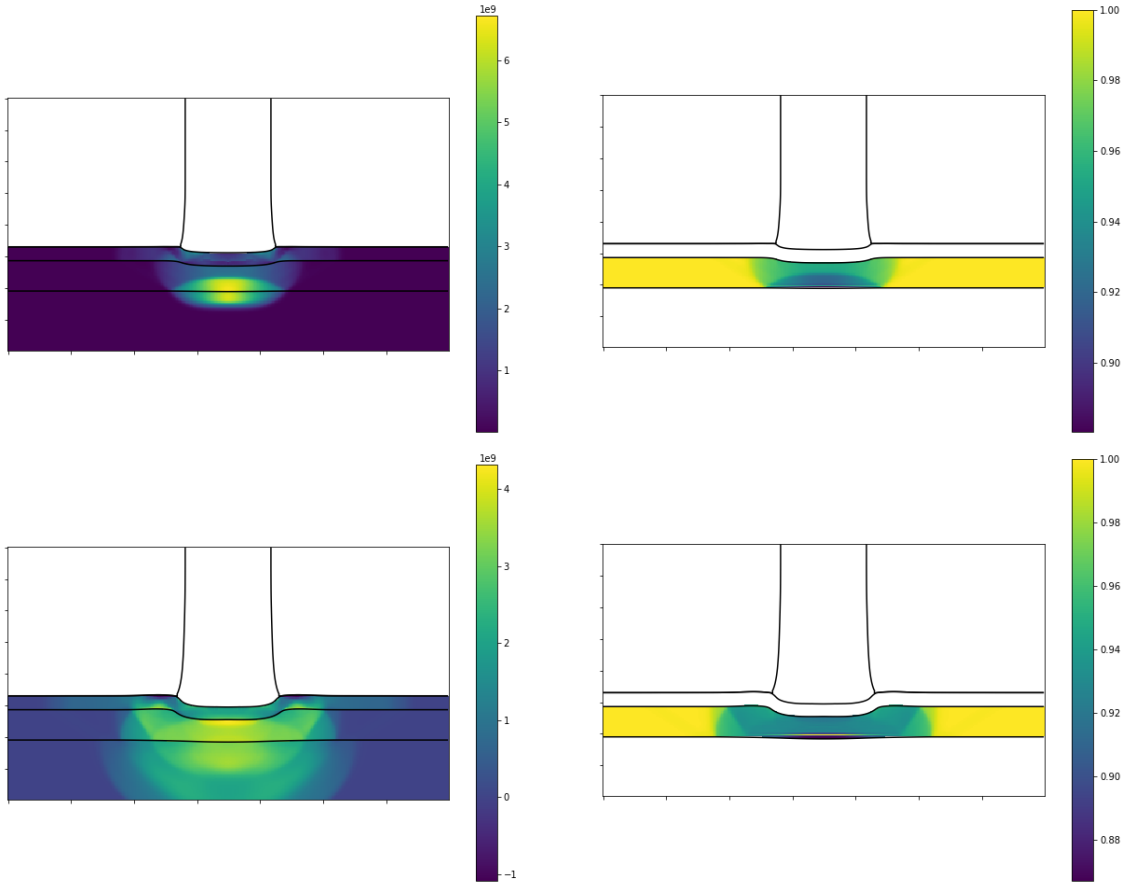

Figure 4.4: Pressure (left) and reactant concentration (right) for the confined detonation test, at times $2.4\mu s$ (top) and $4.9\mu s$ (bottom)

to the steel plate, with the plate deforming in a manner qualitatively identical to that found in [84]. This energy is in turn transmitted to the C4, leading to an exothermic reaction and a symmetrical wavefront that travels through the material. The C4 concentration is depleted to 0.93 at time $t = 2.4 \times 10^{-6}$ and to 0.915 at time $t = 4.9 \times 10^{-6}$.

4.1.4 Confined C4 Detonation

This test is identical to the previous test, except a steel plate of depth 0.003 is now placed behind the C4, so that the explosive is entirely confined. As can be seen from Figure 4.4 on page 129, the kinetic energy of the bar is once again correctly transmitted to the steel plate and C4, with the same deformation occurring in the first steel plate. At time $t = 2.4\times10^{-6}$ we see the wave in the C4 both partially rebounding off the backplate back into the reactant, and partially traveling on through the backplate. At the earlier time, the reactant concentration

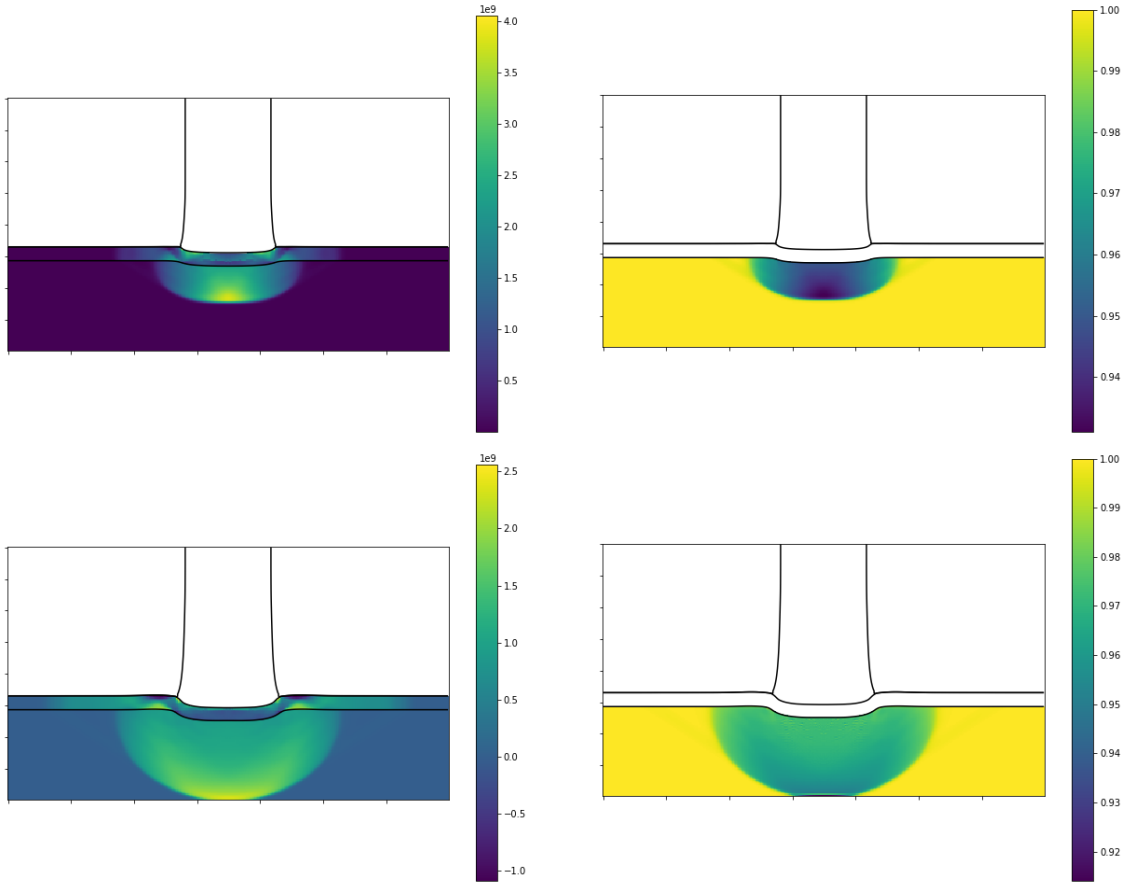

Figure 4.5: Pressure (left) and reactant concentration (right) for the confined detonation test (without back plate), at times $2.4\mu s$ (top) and $4.9\mu s$ (bottom)

has been depleted to 0.88, and at the later time to 0.865. This corroborates the results of [84], in that the presence of the backplate accelerates the reactive processes.

4.1.5 Confined C4 Detonation with Air Gap

This problem is designed to test the ability of the framework presented in this study to capture the interaction of widely varying media. It is identical to the previous problem, except an air gap is now placed between the first steel plate and the C4. The air has the same EOS parameters as the surrounding air.

As can be seen in Figure 4.6 on page 131, the rod displaces the air (with the numerical method coping with contact of the region representing the plate with the region representing the C4). The displacement of the air enables the kinetic energy of the rod to be transmitted

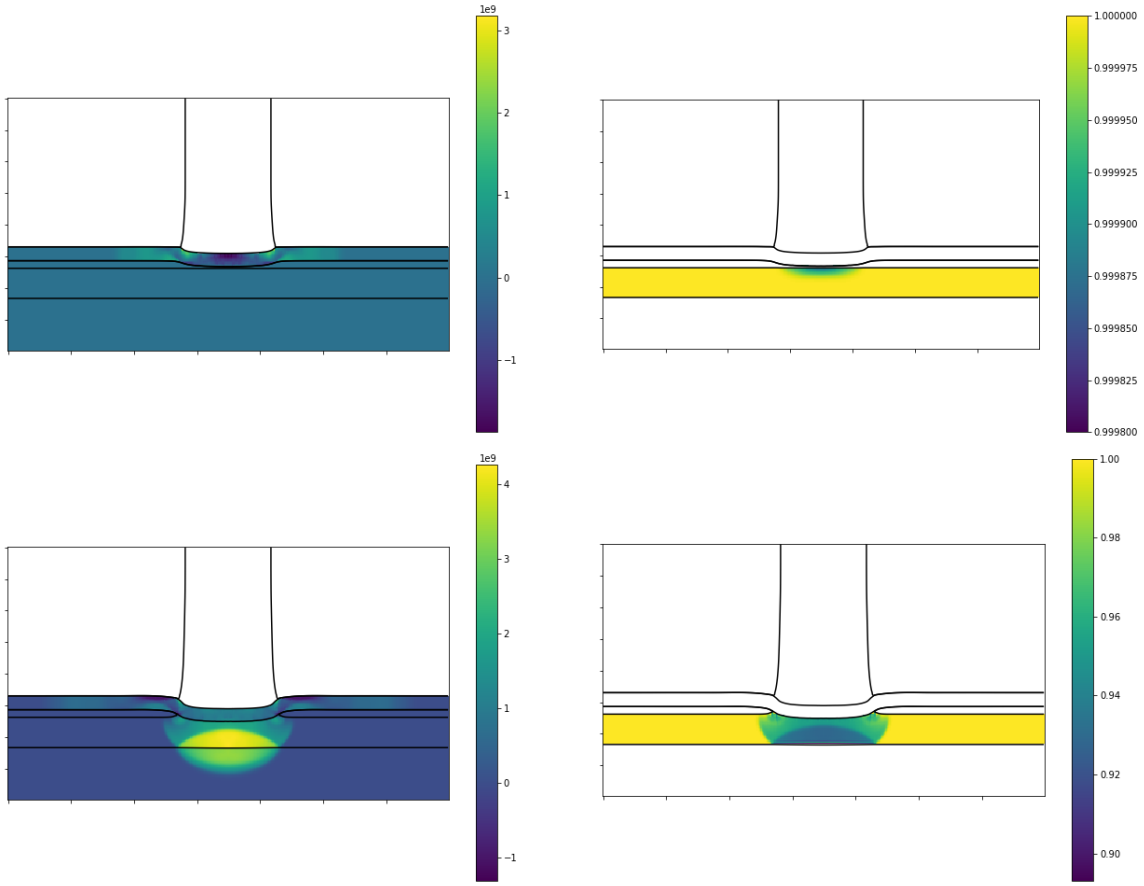

Figure 4.6: Pressure (left) and reactant concentration (right) for the confined detonation test (with air gap), at times $2.4\mu s$ (top) and $4.9\mu s$ (bottom)

through the plate and into the C4, as before. The earlier time of $t = 2.4 \times 10^{-6}$ corresponds with the instant after the plate makes contact with the C4. The concentration is depleted to 0.9998 at $t = 2.4 \times 10^{-6}$ and 0.894 at $t = 4.9 \times 10^{-6}$. The latter value is lower than the corresponding value in the previous test, as the reaction has been delayed by the presence of the air gap.

4.2 Discussion

4.2.1 Conclusions

The results of these numerical tests demonstrate the power of combining the several different novel ideas presented in this study into a coherent framework. The tests feature all three

major phases of matter, reactive species, and the vacuum, and the results corroborate those obtained in previous studies.

In achieving these results, it was necessary to first perform the analytical work present in Section 1.1 and Section 1.2, to enable the use of a broad set of equations of state with the GPR model, and to extend the GPR model to incorporate reactive species. Next, it was required to develop new numerical methods to solve this (extended) model (in Section 2.2), to allow for the solution of these problems in significantly less time than with the previously-used ADER-WENO method, while retaining a reasonable order of accuracy. In 2.2.4, the relaxation mechanism of the GPR model was modified to allow for the simulation of non-Newtonian viscous fluids and elastoplastic solids (as required for the elastoplastic confiner of the impact-induced detonation problem). Finally, it was required to derive a Riemann Ghost Fluid Method for this extended GPR model in Section 3.2 (for both problems involving both heat conduction and no heat conduction) to allow for modeling the evolution of interfaces between every possible pairing of material types.

For completeness and reproducibility, explicit forms of mathematical objects appearing in the GPR model have been provided in Chapter A, the eigenstructure analysis of the GPR model is given in Chapter B, and parameters pertaining to the various different materials encountered in this study are given in Chapter C. It should be straightforward for others to implement and validate the methods developed in this study, enabling them to leverage a unified framework for simulating a vast array of different physical phenomena. This should bring the aforementioned benefits of reducing the conceptual work required to implement such simulations; saving time and streamlining development of simulation software by reducing the number of different systems of equations that require solvers.

4.2.2 Future Research

The generality of the physical phenomena captured by the framework presented in this study allows it to be extended in many different ways. Two major avenues of further investigation are presented in this section.

4.2.2.1 Different constitutive equations

Equations of State Although the tests in this study have demonstrated the suitability of this framework to model materials governed by a wide range of Mie-Gruneisen-type equations

of state (discussed in 1.1.1), there are many other kinds of EOS that can be used. As mentioned in 0.2.2, it is straightforward to utilize other EOSs that express the internal energy in terms of the density, entropy, pressure, or temperature (if required), and other more exotic EOSs such as tabulated EOSs. The derivatives of the internal energy with respect to ρ, p are required in the computation of eigenvalues and eigenvectors of the system matrix, for both the Finite Volume flux updates (see 0.3.3) and the RGFM method (see 3.2.1). Ideally, these derivatives would have an analytical expression, but they can also be calculated numerically, if required. Of course, it is required to validate the use of such EOSs by solving well-understood physical problems numerically.

Relaxation Functions Another material-dependent aspect of this framework is the choice of functions θ_1, θ_2 that govern the relaxation mechanisms of the distortion tensor and the thermal impulse vector respectively (see 0.2.2). In this study, we have used pre-existing forms of θ_1 for inviscid and Newtonian viscous fluids, elastic solids, and elastoplastic solids governed by a power law in the stress tensor. A new form for θ_1 was presented in 2.2.4.3 for (power-law) non-Newtonian fluids. There are many more relationships that can be explored, however, between the stress tensor and the strain or other variables such as temperature and pressure.

One other such class of materials is Bingham plastics. These are materials that do not strain until the stress reaches a specific minimum σ_Y:

$$\dot{\boldsymbol{\gamma}} = \begin{cases} 0 & |\boldsymbol{\sigma}| \leq \sigma_Y \\ \frac{1}{\mu}\left(1 - \frac{\sigma_Y}{|\boldsymbol{\sigma}|}\right)\boldsymbol{\sigma} & |\boldsymbol{\sigma}| \geq \sigma_Y \end{cases} \tag{4.1}$$

Taking the analysis from 2.2.4.3, under the GPR model we have (to first order):

$$\boldsymbol{\sigma} = \frac{1}{6}\tau_1 \rho_0 c_s^2 \dot{\boldsymbol{\gamma}} \tag{4.2}$$

Thus, the definition of θ_1 in (14a) can be used with:

$$\tau_1 = \begin{cases} \infty & |\boldsymbol{\sigma}| \leq \sigma_Y \\ \frac{6\mu}{\rho_0 c_s^2\left(1 - \frac{\sigma_Y}{|\boldsymbol{\sigma}|}\right)} & |\boldsymbol{\sigma}| \geq \sigma_Y \end{cases} \tag{4.3}$$

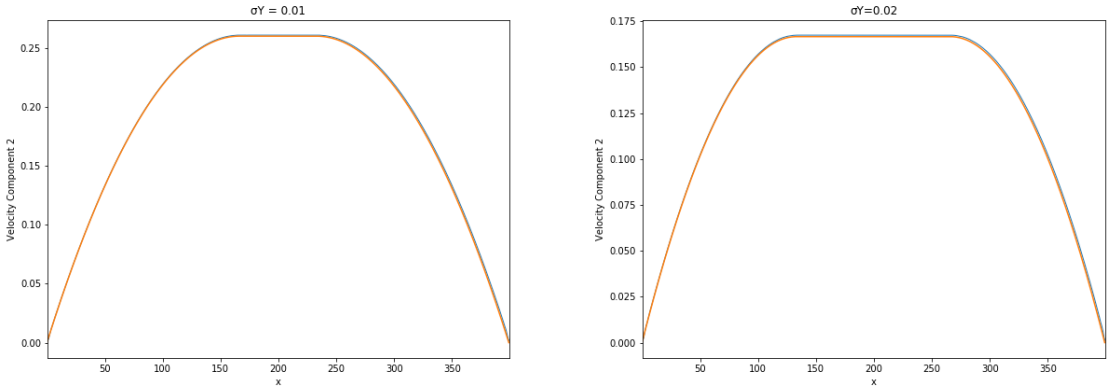

Figure 4.7: The steady-state solution to Poiseuille flow problem for a Bingham plastic with $\sigma_Y = 0.01$ (left) and $\sigma_Y = 0.02$ (right). The numerical solution is in orange, and the exact solution in blue.

Figure 4.7 on page 134 demonstrates the results of the Poiseuille flow problem from 2.3.2.2, now featuring Bingham plastics with $\sigma_Y = 0.01, 0.02$. Solved with the ADER-WENO method on a grid of 400 cells, it is demonstrated that the numerical and exact steady-state solutions almost perfectly coincide. This is a promising result for the usage of our unified framework with more exotic materials, but more work remains to be done in applying the methodology to more tests, and adapting the new solver presented in Section 2.2 to this new form for τ_1.

Many different models of solid plasticity have been presented over the years (e.g. see [9, 12, 41, 79, 86, 88] for a sample), and there exist more advanced concepts such as damage in the realm of solid mechanics (e.g. [8]). The solids models referenced here are similar in mathematical structure to the GPR model, differing mainly in the form of the relaxation function θ_1. Some of the models incorporate extra state variables to track the more complex properties that they describe. It is conceivable - but remains to be demonstrated - that these features are compatible with the RGFM presented in Section 3.2.

Reactive Models Reaction pathways and networks for reactive species can become arbitrarily complex (see [98] for a recent review of complex kinetic modeling methodologies), and there is much potential work in extended the framework presented in this study to encompass reactive systems such as those presented in the aforementioned paper. Care needs to be taken when multiple reactants and products are present, with different properties such as viscosity and thermal conduction, as these affect the relaxation rates of the distortion tensor and thermal impulse vector (now representing the distortion and thermal impulse of

the mixture of the different materials present). Appropriate mixture models must be used for μ, κ (see [4, 16, 52, 53, 57, 131] for several different approaches that have been devised over the years).

4.2.2.2 Extensions to the GPR model

Several extensions to the GPR model have been presented over the last few years since its initial presentation by Peshkov and Romenski, allowing it to simulate more exotic physical phenomena. They will be briefly noted here. In each case, work remains to be done in extended the solvers presented in Section 2.2, and the RGFM presented in Section 3.2 to operate under these extended models.

Electrodynamics Dumbser et al [36] have coupled the GPR model with electrodynamics, enabling modeling of moving elastoplastic dielectric solids and inviscid or viscous fluids in the presence of electromagnetic fields. The resulting PDE system tends in the stiff limit to the viscous and resistive magnetohydrodynamics (MHD) equations. The density, distortion, and thermal impulse evolution equations (1a), (1c), (1d) take their usual form, with the momentum and energy evolution equations (1b), (3) taking the modified form below, along with new evolution equations for the electric field $\mathbf{D}$, magnetic field $\mathbf{B}$, and the artificial scalar ϕ:

$$\frac{\partial (\rho v_i)}{\partial t} + \frac{\partial (\rho v_i v_k + p\delta_{ik} - \sigma_{ik} + \beta_{ik})}{\partial x_k} = 0 \tag{4.4a}$$

$$\frac{\partial D_i}{\partial t} + \frac{\partial (v_k D_i - v_i D_k - \epsilon_{ikj} b_j)}{\partial x_k} + v_i \frac{\partial D_k}{\partial x_k} = -\frac{d_i}{\eta} \tag{4.4b}$$

$$\frac{\partial B_i}{\partial t} + \frac{\partial (v_k B_i - v_i B_k + \epsilon_{ikj} d_j + \phi\delta_{ik})}{\partial x_k} + v_i \frac{\partial B_k}{\partial x_k} = 0 \tag{4.4c}$$

$$\frac{\partial (\rho E)}{\partial t} + \frac{\partial (\rho E v_k + (p\delta_{ik} - \sigma_{ik} + \beta_{ik}) v_i + q_k + \epsilon_{ijk} d_i b_j)}{\partial x_k} = 0 \tag{4.4d}$$

$$\frac{\partial \phi}{\partial t} + \frac{\partial (c_h^2 B_k)}{\partial x_k} = 0 \tag{4.4e}$$

where ϵ_{ijk} is the Levi-Civita tensor, η is the resistivity, and $\mathbf{d}, \mathbf{b}$ are the electric and magnetic

fields in the comoving frame:

$$\mathbf{d} = \frac{1}{\epsilon'}\mathbf{D} + \mathbf{v} \times \mathbf{B} \tag{4.5a}$$

$$\mathbf{b} = \frac{1}{\mu'}\mathbf{B} - \mathbf{v} \times \mathbf{D} \tag{4.5b}$$

where ϵ', μ' are the electric permittivity and magnetic permeability of the material.

The following contribution is added to E in the EOS (6):

$$E_{em} = \frac{1}{2\rho}\left(\frac{1}{\epsilon'}\mathbf{D}^2 + \frac{1}{\mu'}\mathbf{B}^2\right) \tag{4.6}$$

The Maxwell stress, β takes the form:

$$\beta = \rho E_{em} I - \frac{1}{\epsilon'}\mathbf{D} \otimes \mathbf{D} - \frac{1}{\mu'}\mathbf{B} \otimes \mathbf{B} \tag{4.7}$$

It is straightforward to solve the resulting homogeneous system of PDEs with the methods presented in 2.2.2. Combining (4.4b) and (4.5a), the new temporal ODE to solve is:

$$\frac{dD_i}{dt} = -\frac{1}{\eta\epsilon'}D_i - \frac{1}{\eta}\left(\mathbf{v} \times \mathbf{B}\right)_i \tag{4.8}$$

Denoting D_i^t as the value of D_i at time t after the current timestep:

$$D_i^{\Delta t} = \left(D_i^0 + \epsilon'\left(\mathbf{v} \times \mathbf{B}\right)_i\right) e^{-\frac{\Delta t}{\eta\epsilon'}} - \epsilon'\left(\mathbf{v} \times \mathbf{B}\right)_i \tag{4.9}$$

Thus, it should be possible to solve this system in the framework presented in Section 2.2. To use the RGFM with this system, a similar eigenstructure analysis to that performed in Chapter B will need to be undertaken, and new boundary conditions will need to devised in the methodology presented in 3.2.1.

Multiphase Systems Romenski et al [111] have recently proposed an extension to the GPR model for simulating multiphase mixtures (in particular the problem of compressible fluid flows in elastoplastic porous media). The model features 2 types of phase interaction: phase pressure relaxation to a common value, and interfacial friction.

Taking two phases, let the volume fraction, phase mass fraction, and velocity of the ith phase be denoted by $\alpha^{(i)}, c^{(i)}, \mathbf{v^{(i)}}$. Note that $c^{(1)} + c^{(2)} = 1$ and $v_i = c^{(1)} v_i^{(1)} + c^{(2)} v_i^{(2)}$. The density and distortion evolution equations (1a), (1c) take their usual form, with the momentum and energy evolution equations (1b), (3) taking the modified form below, along with new evolution equations for the relative phase velocity $\mathbf{w} = \mathbf{v^{(1)}} - \mathbf{v^{(2)}}$, $c^{(1)}$, and $\alpha^{(1)}$.

$$\frac{\partial \left(\rho v_i\right)}{\partial t} + \frac{\partial \left(\rho v_i v_k + p\delta_{ik} - \sigma_{ik} + w_i E_{w_k}\right)}{\partial x_k} = 0 \tag{4.10a}$$

$$\frac{\partial \left(\rho c^{(1)}\right)}{\partial t} + \frac{\partial \left(\rho c^{(1)} v_k + \rho E_{w_k}\right)}{\partial x_k} = 0 \tag{4.10b}$$

$$\frac{\partial w_k}{\partial t} + \frac{\partial \left(w_l v_l + E_{c^{(1)}}\right)}{\partial x_k} + v_l \left(\frac{\partial w_k}{\partial x_l} - \frac{\partial w_l}{\partial x_k}\right) = -\frac{\lambda_k}{\tilde{\theta}} \tag{4.10c}$$

$$\frac{\partial \left(\rho \alpha^{(1)}\right)}{\partial t} + \frac{\partial \left(\rho \alpha^{(1)} v_k\right)}{\partial x_k} = -\frac{\rho \phi}{\hat{\theta}} \tag{4.10d}$$

$$\frac{\partial \left(\rho E\right)}{\partial t} + \frac{\partial \left(\rho E v_k + v_i \left(p\delta_{ik} - \sigma_{ik} + \rho w_i E_{w_k}\right) + \rho E_{c^{(1)}} E_{w_k}\right)}{\partial x_k} = 0 \tag{4.10e}$$

where $\tilde{\theta}, \hat{\theta}$ characterize the rate of pressure and velocity relaxation. The total energy now contains contributions from the volume fractions, phase mass fractions, and the relative phase velocity. Depending on the form chosen for $\tilde{\theta}, \hat{\theta}$, it may be possible to derive semi-analytical solutions for the temporal ODEs presented by this system, in a similar manner to those performed in 2.2.4. Care must be taken when choosing the RGFM boundary conditions between regions occupied by different multiphase mixtures, if it is desired to apply the theory from Section 3.2 to this system.

Another similar, recent attempt at modeling multiphase systems in a GPR-like framework is that of Groom et al [51]. This paper presents a one-dimensional theory, working towards the formulation of a three-dimensional, hyperbolic, two-phase, two-pressure, two-velocity, two-temperature model for viscous, miscible and compressible fluids. This system may also be amenable to being incorporated into the framework developed in this study.

Yet another GPR-like model of multiphase systems was presented in [100]. Here, a framework is presented for simulating two-phase continua experiencing stress-induced solid–fluid transitions. It is similar to the GPR system, with the addition of four extra state variables: the Burgers tensor $\mathbf{B}$, the defect flux density $\mathbf{D}$, and both of their divergence vectors. The source term for the distortion tensor takes a different form to that used in this study, and the Burgers tensor and defect flux density contain source terms also. Thus, a significant amount

of work will need to be performed to adapt the operator splitting numerical solver presented in Chapter 2 to this system, but it may be possible. Once again, care must be taken in choosing boundary conditions involving $\mathbf{B}, \mathbf{D}$ and their divergence vectors, if the RGFM of Chapter 3 is used to simulate impermeable interfaces between different regions occupied by materials that can undergo stress-induced phase transitions, described by this model.

Riemann-Cartan Geometry and General Relativity Peshkov et al [103] have recently applied elements of Riemann-Cartan geometry to fluid mechanics, with the aim of modeling turbulence effects. The authors associate the rotational degrees of freedom of the the distortion tensor field with the dynamics of microscopic, unresolved vortexes. The concept of the rank-3 four-torsion tensor is introduced, and is used to characterize the distortion field's spin. Two new evolution equations are introduced, for rank-2 components $\mathbf{B}, \mathbf{D}$ of the rank-3 four-torsion tensor. These are similar in structure to the magnetic and electric fields encountered in (4.4c), (4.4b) (although $\mathbf{B}, \mathbf{D}$ are now rank-2, rather than rank-1). It may be that this system is amenable to solution in a similar manner to the method given in (4.9).

Another recent development in this area - in part building upon the material of the aforementioned study - is the introduction of general relativistic effects into the GPR system [105, 110]. A significant amount of work lies ahead with regards to this extended model, in the construction of numerical solvers of the kind developed in this study, and the implementation of immiscible multimaterial modeling. The resulting framework has the potential to be very powerful, however.

References

[1] A. Afzal, Z. Ansari, A. R. Faizabadi, and M. K. Ramis, *Parallelization Strategies for Computational Fluid Dynamics Software: State of the Art Review*, Archives of Computational Methods in Engineering, 24 (2017), pp. 337–363.

[2] M. Aivazis, W. Goddard, D. Meiron, M. Ortiz, J. Pool, and J. Shepherd, *A virtual test facility for simulating the dynamic response of materials*, Computing in Science & Engineering, 2 (2000), pp. 39–50.

[3] F. Alcrudo and F. Benkhaldoun, *Exact solutions to the Riemann problem of the shallow water equations with a bottom step*, Computers & Fluids, 30 (2001), pp. 643–671.

[4] H. Alkandry, I. Boyd, and A. Martin, *Comparison of Models for Mixture Transport Properties for Numerical Simulations of Ablative Heat-Shields*, in 51st AIAA Aerospace Sciences Meeting including the New Horizons Forum and Aerospace Exposition, Grapevine (Dallas/Ft. Worth Region), Texas, Jan. 2013, American Institute of Aeronautics and Astronautics.

[5] S. Arrhenius, *The heat of dissociation of electrolytes and the influence of temperature on the degree of dissociation*, Wilhelm Engelmann, 1889.

[6] ——, *On the Reaction Velocity of the Inversion of Cane Sugar by Acids*, Zeitschrift fur Physikalische Chemie, 4 (1889), pp. 226–248.

[7] D. S. Balsara, T. Rumpf, M. Dumbser, and C. D. Munz, *Efficient, high accuracy ADER-WENO schemes for hydrodynamics and divergence-free magnetohydrodynamics*, Journal of Computational Physics, 228 (2009), pp. 2480–2516.

[8] P. T. Barton, *An Eulerian method for finite deformation anisotropic damage with application to high strain-rate problems*, International Journal of Plasticity, 83 (2016), pp. 225–251.

[9] P. T. Barton, R. Deiterding, D. Meiron, and D. Pullin, *Eulerian adaptive finite-difference method for high-velocity impact and penetration problems*, Journal of Computational Physics, 240 (2013), pp. 76–99.

[10] P. T. Barton and D. Drikakis, *An Eulerian method for multi-component problems in non-linear elasticity with sliding interfaces*, Journal of Computational Physics, 229 (2010), pp. 5518–5540.

[11] P. T. Barton, D. Drikakis, E. Romenski, and V. a. Titarev, *Exact and approximate solutions of Riemann problems in non-linear elasticity*, Journal of Computational Physics, 228 (2009), pp. 7046–7068.

[12] P. T. Barton, D. Drikakis, and E. I. Romenski, *An Eulerian finite-volume scheme for large elastoplastic deformations in solids*, International Journal for Numerical Methods in Engineering, 81 (2011), pp. 453–484.

[13] P. T. Barton, B. Obadia, and D. Drikakis, *A conservative level-set based method for compressible solid/fluid problems on fixed grids*, Journal of Computational Physics, 230 (2011), pp. 7867–7890.

[14] R. Becker, *Impact Waves and Detonation*, Zeitschrift fur Physik, 8 (1929), pp. 381–381.

[15] B. C. Bell and K. S. Surana, *p-version least squares finite element formulation for two-dimensional, incompressible, non-Newtonian isothermal and non-isothermal fluid flow*, International Journal for Numerical Methods in Fluids, 18 (1994), pp. 127–162.

[16] F. G. Blottner, M. Johnson, and M. Ellis, *Chemically Reacting Viscous Flow Program For Multi-Component Gas Mixtures*, tech. rep., Sandia Labs., Albuquerque, N. Mex., 1971.

[17] J. Boettger, K. G. Honnell, J. H. Peterson, C. Greeff, and S. Crockett, *Tabular equation of state for gold*, AIP Conference Proceedings, 1426 (2012), pp. 812–815.

[18] W. Boscheri, M. Dumbser, and R. Loubere, *Cell centered direct Arbitrary-Lagrangian-Eulerian ADER-WENO finite volume schemes for nonlinear hyperelasticity*, Computers and Fluids, 134-135 (2016), pp. 111–129.

[19] A. d. Brauer, A. Iollo, and T. Milcent, *A Cartesian Scheme for Compressible Multimaterial Hyperelastic Models with Plasticity*, Communications in Computational Physics, 22 (2017), pp. 1362–1384.

[20] N. Buyukcizmeci, A. S. Botvina, and I. N. Mishustin, *Tabulated Equation of State for Supernova Matter Including Full Nuclear Ensemble*, The Astrophysical Journal, 789 (2014), p. 33.

[21] D. L. Chapman, *On the Rate of Explosion in Gases*, Philosophical Magazine Series 5, 47 (1899), pp. 90–104.

[22] A. Chinnayya, E. Daniel, and R. Saurel, *Modelling detonation waves in heterogeneous energetic materials*, Journal of Computational Physics, 196 (2004), pp. 490–538.

[23] J. F. Clarke, D. R. Kassoy, and N. Riley, *Shocks generated in a confined gas due to rapid heat addition at the boundary*, Proceedings of the Royal Society of London A, 393 (1984), pp. 309–329.

[24] J. F. Clarke, D. R. Kassoy, and N. Riley, *On the direct initiation of a plane detonation wave*, Proc. Roy. Soc. London, (1986).

[25] J. F. Clarke, D. R. Kassoy, and N. Riley, *On the evolution of plane detonations*, Proceedings of the Royal Society of London A, 429 (1990), pp. 259–283.

[26] A. de Brauer, A. Iollo, and T. Milcent, *A Cartesian scheme for compressible multimaterial models in 3d*, Journal of Computational Physics, 313 (2016), pp. 121–143.

[27] J. Donea, S. Giuliani, and J. P. Halleux, *An arbitrary lagrangian-eulerian finite element method for transient dynamic fluid-structure interactions*, Computer Methods in Applied Mechanics and Engineering, 33 (1982), pp. 689–723.

[28] W. Doring, *On detonation processes in gases*, Annalen der Physik, 43 (1943), pp. 421–436.

[29] M. Dumbser and D. S. Balsara, *A new efficient formulation of the HLLEM Riemann solver for general conservative and non-conservative hyperbolic systems*, Journal of Computational Physics, 304 (2016), pp. 275–319.

[30] M. Dumbser, D. S. Balsara, E. F. Toro, and C.-D. Munz, *A unified framework for the construction of one-step finite volume and discontinuous Galerkin schemes on unstructured meshes*, Journal of Computational Physics, 227 (2008), pp. 8209–8253.

[31] M. Dumbser and W. Boscheri, *High-Order Unstructured Lagrangian One-Step WENO Finite Volume Schemes for Non-conservative Hyperbolic Systems: Applications to Compressible Multi-Phase Flows*, Elsevier Science, (2013).

[32] M. Dumbser, M. Castro, C. Pares, and E. F. Toro, *ADER schemes on unstructured meshes for nonconservative hyperbolic systems: Applications to geophysical flows*, Computers & Fluids, 38 (2009), pp. 1731–1748.

[33] M. Dumbser, C. Enaux, and E. F. Toro, *Finite volume schemes of very high order of accuracy for stiff hyperbolic balance laws*, Journal of Computational Physics, 227 (2008), pp. 3971–4001.

[34] M. Dumbser, A. Hidalgo, and O. Zanotti, *High order space-time adaptive ADER-WENO finite volume schemes for non-conservative hyperbolic systems*, Computer Methods in Applied Mechanics and Engineering, 268 (2014), pp. 359–387.

[35] M. Dumbser, I. Peshkov, E. Romenski, and O. Zanotti, *High order ADER schemes for a unified first order hyperbolic formulation of continuum mechanics: viscous heat-conducting fluids and elastic solids*, Journal of Computational Physics, 314 (2015), pp. 824–862.

[36] ——, *High order ADER schemes for a unified first order hyperbolic formulation of Newtonian continuum mechanics coupled with electro-dynamics*, Journal of Computational Physics, 348 (2017), pp. 298–342.

[37] M. Dumbser and E. F. Toro, *On universal Osher-type schemes for general nonlinear hyperbolic conservation laws*, Communications in Computational Physics, 10 (2011), pp. 635–671.

[38] M. Dumbser and E. F. Toro, *A simple extension of the Osher Riemann solver to non-conservative hyperbolic systems*, Journal of Scientific Computing, 48 (2011), pp. 70–88.

[39] M. Dumbser and O. Zanotti, *Very high order PNPM schemes on unstructured meshes for the resistive relativistic MHD equations*, Journal of Computational Physics, 228 (2009), pp. 6991–7006.

[40] M. Dumbser, O. Zanotti, A. Hidalgo, and D. S. Balsara, *ADER-WENO finite volume schemes with space-time adaptive mesh refinement*, Journal of Computational Physics, 248 (2013), pp. 257–286.

[41] N. Favrie and S. Gavrilyuk, *Dynamics of shock waves in elastic-plastic solids*, ESAIM: Proceedings, 33 (2011), pp. 50–67.

[42] N. Favrie and S. L. Gavrilyuk, *Diffuse interface model for compressible fluid - Compressible elastic-plastic solid interaction*, Journal of Computational Physics, 231 (2012), pp. 2695–2723.

[43] N. Favrie, S. L. Gavrilyuk, and R. Saurel, *Solid-fluid diffuse interface model in cases of extreme deformations*, Journal of Computational Physics, 228 (2009), pp. 6037–6077.

[44] R. Fedkiw, T. Aslam, B. Merriman, and S. Osher, *A Non-oscillatory Eulerian Approach to Interfaces in Multimaterial Flows (the Ghost Fluid Method)*, Journal of Computational Physics, 152 (1999), pp. 457–492.

[45] R. Fedkiw and X. Liu, *The ghost fluid method for viscous flows*, (1998), pp. 1–33.

[46] R. P. Fedkiw, *Coupling an Eulerian Fluid Calculation to a Lagrangian Solid Calculation with the Ghost Fluid Method*, Journal of Computational Physics, 175 (2002), pp. 200–224.

[47] L. L. Ferras, J. M. Nobrega, and F. T. Pinho, *Analytical solutions for Newtonian and inelastic non-Newtonian flows with wall slip*, Journal of Non-Newtonian Fluid Mechanics, 175-176 (2012), pp. 76–88.

[48] J. Frenkel, *Kinetic Theory of Liquids*, Oxford University Press, 1947.

[49] M. B. Giles, *An extended collection of matrix derivative results for forward and reverse mode algorithmic differentiation*, Tech. Rep. 9783540689355, 2008.

[50] J. Glimm and D. Marchesin, *A Numerical Method for Two Phase Flow with an Unstable Interface*, Journal of Computational Physics, 39 (1981), pp. 179–200.

[51] M. Groom, B. Thornber, and E. Romenski, *A first-order hyperbolic system of governing equations for miscible and viscous compressible fluids*, Barcelona, Spain, 2018, p. 12.

[52] L. GRUNBERG and A. H. NISSAN, *Mixture Law for Viscosity*, Nature, 164 (1949), p. 799.

[53] R. N. Gupta, J. M. Yos, R. A. Thompson, and K.-P. Lee, *A review of reaction rates and thermodynamic and transport properties for an 11-species air model for chemical and thermal nonequilibrium calculations to 30000 K*, (1990).

[54] A. Harten, P. D. Lax, and B. van Leer, *On Upstream Differencing and Godunov-Type Schemes for Hyperbolic Conservation Laws*, Society for Industrial and Applied Mathematics, 25 (1983), pp. 35–61.

[55] C. Helzel, R. J. Leveque, and G. Warnecke, *A Modified Fractional Step Method for the Accurate Approximation of Detonation Waves*, SIAM Journal on Scientific Computing, 22 (2000), pp. 1489–1510.

[56] F. Hempert, S. Boblest, T. Ertl, F. Sadlo, P. Offenhauser, C. W. Glass, M. Hoffmann, A. Beck, C. D. Munz, and U. Iben, *Simulation of real gas effects in supersonic methane jets using a tabulated equation of state with a discontinuous Galerkin spectral element method*, Computers & Fluids, 145 (2017), pp. 167–179.

[57] F. Herning and L. Zipperer, *Calculation of the viscosity of technical gas mixtures from the viscosity of the individual gases*, Gas u. Wasserfach, 79 (1936), p. 69.

[58] A. Hidalgo and M. Dumbser, *ADER schemes for nonlinear systems of stiff advection-diffusion-reaction equations*, Journal of Scientific Computing, 48 (2011), pp. 173–189.

[59] C. W. Hirt and B. D. Nichols, *Volume of fluid (VOF) method for the dynamics of free boundaries*, Journal of Computational Physics, 39 (1981), pp. 201–225.

[60] G. Hou, J. Wang, and A. Layton, *Numerical methods for fluid-structure interaction - A review*, Communications in Computational Physics, 12 (2012), pp. 337–377.

[61] B. Howell and G. Ball, *A Free Lagrange Augmented Godunov Method for the Simulation of Elastic Plastic Solids*, Journal of Computational Physics, 175 (2002), pp. 128–167.

[62] B. Hubner, E. Walhorn, and D. Dinkler, *A monolithic approach to fluid-structure interaction using space-time finite elements*, Computer Methods in Applied Mechanics & Engineering, 193 (2004), pp. 2087–2104.

[63] H. Jackson, *A Fast Numerical Scheme for the Godunov-Peshkov-Romenski Model of Continuum Mechanics*, Journal of Computational Physics, 348 (2017), pp. 514–533.

[64] ——, *On the Eigenvalues of the ADER-WENO Galerkin Predictor*, Journal of Computational Physics, 333 (2017), pp. 409–413.

[65] ——, *The Montecinos-Balsara ADER-FV polynomial basis: Convergence properties & extension to non-conservative multidimensional systems*, Computers & Fluids, 163 (2018), pp. 50–53.

[66] H. Jackson and N. Nikiforakis, *A numerical scheme for non-Newtonian fluids and plastic solids under the GPR model*, Journal of Computational Physics, 387 (2019), pp. 410–429.

[67] ——, *A unified Eulerian framework for multimaterial continuum mechanics*, Journal of Computational Physics, (2019).

[68] G. S. Jiang and C. W. Shu, *Efficient implementation of weighted WENO schemes*, Journal of Computational Physics, 126 (1996), pp. 202–228.

[69] B. M. Johnson, *Analytical shock solutions at large and small Prandtl number*, Journal of Fluid Mechanics, 726 (2013).

[70] E. Jouget, *On the Propagation of Chemical Reactions in Gases*, Journal de Mathematiques Pures et Appliquees, 1 (1905), pp. 347–425.

[71] A. Kapila, D. W. Schwendeman, J. J. Quirk, and T. Hawa, *Mechanisms of detonation formation due to a temperature gradient*, Combustion Theory & Modelling, 6 (2002), pp. 553–594.

[72] E. L. Lee and C. M. Tarver, *Phenomenological model of shock initiation in heterogeneous explosives*, Physics of Fluids, 23 (1980), p. 2362.

[73] A. Legay, J. Chessa, and T. Belytschko, *An Eulerian-Lagrangian method for fluid-structure interaction based on level sets*, Computer Methods in Applied Mechanics & Engineering, 195 (2006), pp. 2070–2087.

[74] P. R. Levashov and K. V. Khishchenko, *Tabular multiphase equations of state for metals and their applications*, AIP Conference Proceedings, 955 (2007), pp. 59–62.

[75] R. Leveque and H. Yee, *A Study of Numerical Methods for Hyperbolic Conservation Laws with Stiff Source Terms*, Journal of Computational Physics, 86 (1990), pp. 187–210.

[76] T. G. Liu, B. C. Khoo, and K. S. Yeo, *Ghost fluid method for strong shock impacting on material interface*, Journal of Computational Physics, 190 (2003), pp. 651–681.

[77] T.-P. Liu, *The Riemann problem for general systems of conservation laws*, Journal of Differential Equations, 18 (1975), pp. 218–234.

[78] X.-D. Liu, S. Osher, and T. Chan, *Weighted Essentially Non-oscillatory Schemes*, Journal of Computational Physics, 115 (1994), pp. 200–212.

[79] A. Lopez Ortega, M. Lombardini, D. I. Pullin, and D. I. Meiron, *Numerical simulation of elastic-plastic solid mechanics using an Eulerian stretch tensor approach and HLLD Riemann solver*, Journal of Computational Physics, 257 (2014), pp. 414–441.

[80] P. H. Maire, R. Abgrall, J. Breil, R. Loubere, and B. Rebourcet, *A nominally second-order cell-centered Lagrangian scheme for simulating elastic-plastic flows on two-dimensional unstructured grids*, Journal of Computational Physics, 235 (2013), pp. 626–665.

[81] A. N. Malyshev and E. I. Romenskii, *Hyperbolic equations for heat transfer. Global solvability of the Cauchy problem*, Siberian Mathematical Journal, 27 (1986), pp. 734–740.

[82] A. McAdams, A. Selle, R. Tamstorf, J. Teran, and E. Sifakis, *Computing the Singular Value Decomposition of 3 x 3 matrices with minimal branching and elementary floating point operations*, University of Wisconsin Madison, (2011).

[83] R. Menikoff, *Complete Mie-Gruneisen Equation of State*, tech. rep., 2016.

[84] L. Michael and N. Nikiforakis, *A multi-physics methodology for the simulation of reactive flow and elastoplastic structural response*, Journal of Computational Physics, 367 (2018), pp. 1–27.

[85] C. Michler, S. J. Hulshoff, E. H. van Brummelen, and R. de Borst, *A monolithic approach to fluid-structure interaction*, Computers & Fluids, 33 (2004), pp. 839–848.

[86] G. Miller and P. Colella, *A Conservative Three-Dimensional Eulerian Method for Coupled Solid-Fluid Shock Capturing*, Journal of Computational Physics, 183 (2002), pp. 26–82.

[87] G. H. Miller, *An iterative Riemann solver for systems of hyperbolic conservation laws, with application to hyperelastic solid mechanics*, Journal of Computational Physics, 193 (2004), pp. 198–225.

[88] G. H. Miller and P. Colella, *A High-Order Eulerian Godunov Method for Elastic-Plastic Flow in Solids*, Journal of Computational Physics, 167 (2001), pp. 131–176.

[89] G. I. Montecinos and D. S. Balsara, *A cell-centered polynomial basis for efficient Galerkin predictors in the context of ADER finite volume schemes. The one-dimensional case*, Computers & Fluids, 156 (2017), pp. 220–238.

[90] M. Morduchow and P. A. Libby, *On a Complete Solution of the One-Dimensional Flow Equations of a Viscous, Heat-Conducting, Compressible Gas*, tech. rep., 1949.

[91] S. Ndanou, N. Favrie, and S. Gavrilyuk, *Multi-solid and multi-fluid diffuse interface model: Applications to dynamic fracture and fragmentation*, Journal of Computational Physics, 295 (2015), pp. 523–555.

[92] P. Neofytou, *A 3rd order upwind finite volume method for generalised Newtonian fluid flows*, Advances in Engineering Software, 36 (2005), pp. 664–680.

[93] E. D. Nering, *Linear Algebra and Matrix Theory*, 1970.

[94] B. D. Nichols, C. W. Hirt, and R. S. Hotchkiss, *SOLA-VOF: A solution algorithm for transient fluid flow with multiple free boundaries*, NASA STI/Recon Technical Report N, 81 (1980).

[95] T. E. Oliphant, *Python for Scientific Computing*, Computing in Science & Engineering, 9 (2007), pp. 10–20.

[96] S. Osher and R. Fedkiw, *Level set methods and dynamic implicit surfaces*, 2003.

[97] S. Osher and R. P. Fedkiw, *Level Set Methods: An Overview and Some Recent Results*, Journal of Computational Physics, 169 (2001), pp. 463–502.

[98] L. Pereira De Oliveira, D. P. Hudebine, D. P. Guillaume, and J. J. Verstraete, *A Review of Kinetic Modeling Methodologies for Complex Processes*, Oil & Gas Science and Technology - Revue d'IFP Energies nouvelles, 71 (2016), p. 45.

[99] I. Peshkov, W. Boscheri, R. Loubere, E. Romenski, and M. Dumbser, *Theoretical and numerical comparison of hyperelastic and hypoelastic formulations for Eulerian non-linear elastoplasticity*, Journal of Computational Physics, 387 (2019), pp. 481–521.

[100] I. Peshkov, M. Grmela, and E. Romenski, *Irreversible mechanics and thermodynamics of two-phase continua experiencing stress-induced solid-fluid transitions*, Continuum Mechanics and Thermodynamics, 27 (2015), pp. 905–940.

[101] I. Peshkov and E. Romenski, *A hyperbolic model for viscous Newtonian flows*, Continuum Mechanics and Thermodynamics, 28 (2016), pp. 85–104.

[102] I. Peshkov, E. Romenski, and M. Dumbser, *A unified hyperbolic formulation for viscous fluids and elastoplastic solids*, (2017).

[103] ——, *Continuum mechanics with torsion*, Continuum Mechanics and Thermodynamics, 31 (2019), pp. 1517–1541.

[104] I. Peshkov, E. Romenski, M. Dumbser, and F. Fambri, *General Relativistic formulation of dissipative continuum mechanics*, 2018.

[105] I. Peshkov, E. Romenski, F. Fambri, and M. Dumbser, *A new causal general relativistic formulation for dissipative continuum fluid and solid mechanics and its solution with high-order ADER schemes*, arXiv:1910.02687 [gr-qc], (2019). arXiv: 1910.02687.

[106] J. H. Peterson, K. G. Honnell, C. Greeff, J. D. Johnson, J. Boettger, and S. Crockett, *Global equation of state for copper*, Chicago, Illinois, 2012, pp. 763–766.

[107] F. D. Pin, S. Idelsohn, E. Onate, and R. Aubry, *The ALE/Lagrangian Particle Finite Element Method: A new approach to computation of free-surface flows and fluid-object interactions*, Computers & Fluids, 36 (2007), pp. 27–38.

[108] W. J. Rider and D. B. Kothe, *Reconstructing Volume Tracking*, Journal of Computational Physics, 141 (1998), pp. 112–152.

[109] E. Romenski, D. Drikakis, and E. Toro, *Conservative models and numerical methods for compressible two-phase flow*, Journal of Scientific Computing, 42 (2010), pp. 68–95.

[110] E. Romenski, I. Peshkov, M. Dumbser, and a. F. Fambri, *A new continuum model for general relativistic viscous heat-conducting media*, arXiv:1910.03298 [gr-qc], (2019). arXiv: 1910.03298.

[111] E. Romenski, G. Reshetova, I. Peshkov, and M. Dumbser, *Modeling wavefields in saturated elastic porous media based on thermodynamically compatible system theory for multiphase mixtures*, arXiv:1910.04207 [physics], (2019). arXiv: 1910.04207.

[112] E. Romenski, A. D. Resnyansky, and E. F. Toro, *Conservative hyperbolic model for compressible two-phase flow with different phase pressures and temperatures*, Quarterly of applied mathematics, 65(2) (2007), pp. 259–279.

[113] E. I. Romenski, *Hyperbolic equations of Maxwell's nonlinear model of elastoplastic heat-conducting media*, Siberian Mathematical Journal, 30 (1989), pp. 606–625.

[114] R. Rossi and E. Onate, *Analysis of some partitioned algorithms for fluid-structure interaction*, Engineering Computations, 27 (2010), pp. 20–56.

[115] P. B. Ryzhakov, R. Rossi, S. R. Idelsohn, and E. Onate, *A monolithic Lagrangian approach for fluid-structure interaction problems*, Computational Mechanics, 46 (2010), pp. 883–899.

[116] S. K. Sambasivan and H. S. UdayKumar, *Ghost Fluid Method for Strong Shock Interactions Part 1: Fluid-Fluid Interfaces*, AIAA Journal, 47 (2009), pp. 2907–2922.

[117] ——, *Ghost Fluid Method for Strong Shock Interactions Part 2: Immersed Solid Boundaries*, AIAA Journal, 47 (2009), pp. 2923–2937.

[118] R. Saurel and R. Abgrall, *A Multiphase Godunov Method for Compressible Multifluid and Multiphase Flows*, Journal of Computational Physics, 150 (1999), pp. 425–467.

[119] R. Scardovelli and S. Zaleski, *Direct numerical simulation of free-surface and interfacial flow*, Annual Review of Fluid Mechanics, 31 (1999), pp. 567–603.

[120] S. Schoch, K. Nordin-Bates, and N. Nikiforakis, *An Eulerian algorithm for coupled simulations of elastoplastic-solids and condensed-phase explosives*, Journal of Computational Physics, 252 (2013), pp. 163–194.

[121] M. Short, *On the Critical Conditions for the Initiation of a Detonation in a Nonuniformly Perturbed Reactive Fluid*, SIAM Journal on Applied Mathematics, 57 (1997), pp. 1242–1280.

[122] K. Sverdrup, N. Nikiforakis, and A. Almgren, *Highly parallelisable simulations of time-dependent viscoplastic fluid flow with structured adaptive mesh refinement*, Physics of Fluids, 30 (2018), p. 093102.

[123] V. Titarev and E. Toro, *ADER: Arbitrary high order godunov approach*, Journal of Scientific Computing, 17 (2002), pp. 609–618.

[124] V. A. Titarev, E. Romenski, and E. F. Toro, *MUSTA-type upwind fluxes for non-linear elasticity*, International Journal for Numerical Methods in Engineering, 73 (2008), pp. 897–926.

[125] E. Toro and V. Titarev, *Solution of the generalized Riemann problem for advection-reaction equations*, Proceedings of the Royal Society A: Mathematical, Physical and Engineering Sciences, 458 (2002), pp. 271–281.

[126] E. F. Toro, *Reimann Solvers and Numerical Methods for fluid dynamics*, vol. 40, 2009.

[127] E. F. Toro, R. C. Millington, and L. A. M. Nejad, *Towards Very High Order Godunov Schemes*, in Godunov Methods: Theory and Applications, E. F. Toro, ed., Springer US, Boston, MA, 2001, pp. 907–940.

[128] J. von Neumann, *Theory of Detonation Waves*, tech. rep., 1942.

[129] S. P. Wang, M. H. Anderson, J. G. Oakley, M. L. Corradini, and R. Bonazza, *A thermodynamically consistent and fully conservative treatment of contact discontinuities for compressible multicomponent flows*, Journal of Computational Physics, 195 (2004), pp. 528–559.

[130] {Wikipedia contributors}, *Non-Newtonian fluid — {Wikipedia}{,} The Free Encyclopedia*, 2019.

[131] C. R. Wilke, *A viscosity equation for gas mixtures*, The journal of chemical physics, 18 (1950), pp. 517–519.

[132] O. Zanotti and M. Dumbser, *Efficient conservative ADER schemes based on WENO reconstruction and space-time predictor in primitive variables*, Computational Astrophysics and Cosmology, 3 (2016), pp. 1–1.

[133] Y. B. Zeldovich, *On the Theory of the Propagation of Detonation in Gaseous Systems*, Journal of Experimental & Theoretical Physics, 10 (1940), pp. 542–568.

Appendix A

System Matrices

A.1 Fluxes, Sources, and Non-Conservative Terms

The mixed-material GPR model takes the form $\frac{\partial \boldsymbol{Q}}{\partial t} + \frac{\partial \boldsymbol{F}(\boldsymbol{Q})}{\partial x} + B(\boldsymbol{Q}) \cdot \frac{\partial \boldsymbol{Q}}{\partial x} = \boldsymbol{S}(\boldsymbol{Q})$ where $\boldsymbol{Q}, \boldsymbol{F}, B, \boldsymbol{S}$ are given in (A.1), (A.2), (A.3).

A.2 Jacobians

Jacobian of the Conserved System

Define the following variables:

$$\tilde{\psi} = \rho \left. \frac{\partial E}{\partial A} \right|_{\rho,p} \tag{A.4a}$$

$$\Psi_{ij} = \rho v_i v_j - \sigma_{ij} \tag{A.4b}$$

$$\Phi_{ij} = v_i v_j - \frac{\partial \sigma_{ij}}{\partial \rho} \tag{A.4c}$$

$$\aleph_{ij}^{mn} = -\frac{\partial \sigma_{mn}}{\partial A_{ij}} \tag{A.4d}$$

$$\Omega_{ij}^{k} = v_k \tilde{\psi}_{ij} + v_m \aleph_{ij}^{mk} \tag{A.4e}$$

$$\Delta_i = v_i \left(E + \rho \left. \frac{\partial E}{\partial \rho} \right|_{p,A} \right) - \frac{\partial \sigma_{im}}{\partial \rho} v_m + \frac{\partial T}{\partial \rho} H_i \tag{A.4f}$$

$$\Pi_i = v_i \left(\rho \frac{\partial E}{\partial p} + 1 \right) + \frac{\partial T}{\partial p} H_i \tag{A.4g}$$

$$\Upsilon = \Gamma \left(\|\boldsymbol{v}\|^2 + c_t^2 \|\boldsymbol{J}\|^2 + Q\lambda - \left(E + \rho \left. \frac{\partial E}{\partial \rho} \right|_{p,A} \right) \right) \tag{A.4h}$$

The Jacobians of the GPR system are given in (A.5), (A.6), (A.7), (A.8), (A.9).

$$
\boldsymbol{Q} = \begin{pmatrix} \rho \\ \rho E \\ \rho v_1 \\ \rho v_2 \\ \rho v_3 \\ A_{11} \\ A_{12} \\ A_{13} \\ A_{21} \\ A_{22} \\ A_{23} \\ A_{31} \\ A_{32} \\ A_{33} \\ \rho J_1 \\ \rho J_2 \\ \rho J_3 \\ \rho\lambda \end{pmatrix}
\quad
\boldsymbol{F_1} = \begin{pmatrix} \rho v_1 \\ \rho v_1 E + v_1 p - v_m \sigma_{m1} + q_1 \\ \rho v_1^2 + p - \sigma_{11} \\ \rho v_1 v_2 - \sigma_{21} \\ \rho v_1 v_3 - \sigma_{31} \\ A_{1m} v_m \\ 0 \\ 0 \\ A_{2m} v_m \\ 0 \\ 0 \\ A_{3m} v_m \\ 0 \\ 0 \\ \rho J_1 v_1 + T \\ \rho J_2 v_1 \\ \rho J_3 v_1 \\ \rho\lambda v_1 \end{pmatrix}
\quad
\boldsymbol{F_2} = \begin{pmatrix} \rho v_2 \\ \rho v_2 E + v_2 p - v_m \sigma_{m2} + q_2 \\ \rho v_1 v_2 - \sigma_{12} \\ \rho v_2^2 + p - \sigma_{22} \\ \rho v_2 v_3 - \sigma_{32} \\ 0 \\ A_{1m} v_m \\ 0 \\ 0 \\ A_{2m} v_m \\ 0 \\ 0 \\ A_{3m} v_m \\ 0 \\ \rho J_1 v_2 \\ \rho J_2 v_2 + T \\ \rho J_3 v_2 \\ \rho\lambda v_2 \end{pmatrix}
\quad
\boldsymbol{F_3} = \begin{pmatrix} \rho v_3 \\ \rho v_3 E + v_3 p - v_m \sigma_{m3} + q_3 \\ \rho v_1 v_3 - \sigma_{13} \\ \rho v_2 v_3 - \sigma_{23} \\ \rho v_3^2 + p - \sigma_{33} \\ 0 \\ 0 \\ A_{1m} v_m \\ 0 \\ 0 \\ A_{2m} v_m \\ 0 \\ 0 \\ A_{3m} v_m \\ \rho J_1 v_3 \\ \rho J_2 v_3 \\ \rho J_3 v_3 + T \\ \rho\lambda v_3 \end{pmatrix}
\tag{A.1}
$$

$$B_1 = \left(\begin{array}{cccccccccccccccccc}
0 & 0 & 0 & 0 & 0 & 0 & 0 & 0 & 0 & 0 & 0 & 0 & 0 & 0 & 0 & 0 & 0 & 0 \\
0 & 0 & 0 & 0 & 0 & 0 & 0 & 0 & 0 & 0 & 0 & 0 & 0 & 0 & 0 & 0 & 0 & 0 \\
0 & 0 & 0 & 0 & 0 & 0 & 0 & 0 & 0 & 0 & 0 & 0 & 0 & 0 & 0 & 0 & 0 & 0 \\
0 & 0 & 0 & 0 & 0 & 0 & 0 & 0 & 0 & 0 & 0 & 0 & 0 & 0 & 0 & 0 & 0 & 0 \\
0 & 0 & 0 & 0 & 0 & 0 & 0 & 0 & 0 & 0 & 0 & 0 & 0 & 0 & 0 & 0 & 0 & 0 \\
0 & 0 & 0 & 0 & 0 & 0 & 0 & 0 & -v_2 & 0 & 0 & -v_3 & 0 & 0 & 0 & 0 & 0 & 0 \\
0 & 0 & 0 & 0 & 0 & 0 & 0 & 0 & 0 & -v_2 & 0 & 0 & -v_3 & 0 & 0 & 0 & 0 & 0 \\
0 & 0 & 0 & 0 & 0 & 0 & 0 & 0 & 0 & 0 & -v_2 & 0 & 0 & -v_3 & 0 & 0 & 0 & 0 \\
0 & 0 & 0 & 0 & 0 & 0 & 0 & 0 & v_1 & 0 & 0 & 0 & 0 & 0 & 0 & 0 & 0 & 0 \\
0 & 0 & 0 & 0 & 0 & 0 & 0 & 0 & 0 & v_1 & 0 & 0 & 0 & 0 & 0 & 0 & 0 & 0 \\
0 & 0 & 0 & 0 & 0 & 0 & 0 & 0 & 0 & 0 & v_1 & 0 & 0 & 0 & 0 & 0 & 0 & 0 \\
0 & 0 & 0 & 0 & 0 & 0 & 0 & 0 & 0 & 0 & 0 & v_1 & 0 & 0 & 0 & 0 & 0 & 0 \\
0 & 0 & 0 & 0 & 0 & 0 & 0 & 0 & 0 & 0 & 0 & 0 & v_1 & 0 & 0 & 0 & 0 & 0 \\
0 & 0 & 0 & 0 & 0 & 0 & 0 & 0 & 0 & 0 & 0 & 0 & 0 & v_1 & 0 & 0 & 0 & 0 \\
0 & 0 & 0 & 0 & 0 & 0 & 0 & 0 & 0 & 0 & 0 & 0 & 0 & 0 & 0 & 0 & 0 & 0 \\
0 & 0 & 0 & 0 & 0 & 0 & 0 & 0 & 0 & 0 & 0 & 0 & 0 & 0 & 0 & 0 & 0 & 0 \\
0 & 0 & 0 & 0 & 0 & 0 & 0 & 0 & 0 & 0 & 0 & 0 & 0 & 0 & 0 & 0 & 0 & 0 \\
0 & 0 & 0 & 0 & 0 & 0 & 0 & 0 & 0 & 0 & 0 & 0 & 0 & 0 & 0 & 0 & 0 & 0
\end{array}\right)
\quad
B_2 = \left(\begin{array}{cccccccccccccccccc}
0 & 0 & 0 & 0 & 0 & 0 & 0 & 0 & 0 & 0 & 0 & 0 & 0 & 0 & 0 & 0 & 0 & 0 \\
0 & 0 & 0 & 0 & 0 & 0 & 0 & 0 & 0 & 0 & 0 & 0 & 0 & 0 & 0 & 0 & 0 & 0 \\
0 & 0 & 0 & 0 & 0 & 0 & 0 & 0 & 0 & 0 & 0 & 0 & 0 & 0 & 0 & 0 & 0 & 0 \\
0 & 0 & 0 & 0 & 0 & 0 & 0 & 0 & 0 & 0 & 0 & 0 & 0 & 0 & 0 & 0 & 0 & 0 \\
0 & 0 & 0 & 0 & 0 & 0 & 0 & 0 & 0 & 0 & 0 & 0 & 0 & 0 & 0 & 0 & 0 & 0 \\
0 & 0 & 0 & 0 & 0 & v_2 & 0 & 0 & 0 & 0 & 0 & 0 & 0 & 0 & 0 & 0 & 0 & 0 \\
0 & 0 & 0 & 0 & 0 & 0 & v_2 & 0 & 0 & 0 & 0 & 0 & 0 & 0 & 0 & 0 & 0 & 0 \\
0 & 0 & 0 & 0 & 0 & 0 & 0 & v_2 & 0 & 0 & 0 & 0 & 0 & 0 & 0 & 0 & 0 & 0 \\
0 & 0 & 0 & 0 & 0 & -v_1 & 0 & 0 & 0 & 0 & 0 & -v_3 & 0 & 0 & 0 & 0 & 0 & 0 \\
0 & 0 & 0 & 0 & 0 & 0 & -v_1 & 0 & 0 & 0 & 0 & 0 & -v_3 & 0 & 0 & 0 & 0 & 0 \\
0 & 0 & 0 & 0 & 0 & 0 & 0 & -v_1 & 0 & 0 & 0 & 0 & 0 & -v_3 & 0 & 0 & 0 & 0 \\
0 & 0 & 0 & 0 & 0 & 0 & 0 & 0 & 0 & 0 & 0 & v_2 & 0 & 0 & 0 & 0 & 0 & 0 \\
0 & 0 & 0 & 0 & 0 & 0 & 0 & 0 & 0 & 0 & 0 & 0 & v_2 & 0 & 0 & 0 & 0 & 0 \\
0 & 0 & 0 & 0 & 0 & 0 & 0 & 0 & 0 & 0 & 0 & 0 & 0 & v_2 & 0 & 0 & 0 & 0 \\
0 & 0 & 0 & 0 & 0 & 0 & 0 & 0 & 0 & 0 & 0 & 0 & 0 & 0 & 0 & 0 & 0 & 0 \\
0 & 0 & 0 & 0 & 0 & 0 & 0 & 0 & 0 & 0 & 0 & 0 & 0 & 0 & 0 & 0 & 0 & 0 \\
0 & 0 & 0 & 0 & 0 & 0 & 0 & 0 & 0 & 0 & 0 & 0 & 0 & 0 & 0 & 0 & 0 & 0 \\
0 & 0 & 0 & 0 & 0 & 0 & 0 & 0 & 0 & 0 & 0 & 0 & 0 & 0 & 0 & 0 & 0 & 0
\end{array}\right) \tag{A.2}$$

$$
\boldsymbol{S} = -\frac{1}{\theta_1}\begin{pmatrix}
0 & 0 & 0 & 0 & 0 \\
0 & 0 & 0 & 0 & 0 \\
0 & 0 & 0 & 0 & 0 \\
0 & 0 & 0 & 0 & 0 \\
0 & 0 & 0 & 0 & 0 \\
\psi_{11} & \psi_{12} & \psi_{13} & 0 & 0 \\
\psi_{21} & \psi_{22} & \psi_{23} & 0 & 0 \\
\psi_{31} & \psi_{32} & \psi_{33} & 0 & 0 \\
0 & 0 & 0 & \rho H_1 & 0 \\
0 & 0 & 0 & \rho H_2 & 0 \\
0 & 0 & 0 & \rho H_3 & 0 \\
0 & 0 & 0 & 0 & \rho K
\end{pmatrix} + \frac{1}{\theta_2}\begin{pmatrix}
0 & 0 & 0 & 0 & 0 \\
0 & 0 & 0 & 0 & 0 \\
0 & 0 & 0 & 0 & 0 \\
0 & 0 & 0 & 0 & 0 \\
0 & 0 & 0 & 0 & 0 \\
0 & 0 & 0 & 0 & 0 \\
0 & 0 & 0 & 0 & 0 \\
0 & 0 & 0 & 0 & 0 \\
0 & 0 & 0 & 0 & 0 \\
0 & 0 & 0 & 0 & 0 \\
0 & 0 & 0 & 0 & 0 \\
0 & 0 & 0 & 0 & 0
\end{pmatrix} \tag{A.3}
$$

$$
B_3 = \begin{pmatrix}
0\,0\,0\,0\,0 & 0 & 0 & 0 & 0\,0\,0\,0\,0\,0\,0 \\
0\,0\,0\,0\,0 & 0 & 0 & 0 & 0\,0\,0\,0\,0\,0\,0 \\
0\,0\,0\,0\,0 & 0 & 0 & 0 & 0\,0\,0\,0\,0\,0\,0 \\
0\,0\,0\,0\,0 & 0 & 0 & 0 & 0\,0\,0\,0\,0\,0\,0 \\
0\,0\,0\,0\,0 & 0 & 0 & 0 & 0\,0\,0\,0\,0\,0\,0 \\
0\,0\,0\,0\,0 & v_3 & 0 & 0 & 0\,0\,0\,0\,0\,0\,0 \\
0\,0\,0\,0\,0 & 0 & v_3 & 0 & 0\,0\,0\,0\,0\,0\,0 \\
0\,0\,0\,0\,0 & 0 & 0 & v_3 & 0\,0\,0\,0\,0\,0\,0 \\
0\,0\,0\,0\,0 & 0 & 0 & 0 & 0\,0\,0\,0\,0\,0\,0 \\
0\,0\,0\,0\,0 & 0 & 0 & 0 & 0\,0\,0\,0\,0\,0\,0 \\
0\,0\,0\,0\,0 & 0 & 0 & 0 & 0\,0\,0\,0\,0\,0\,0 \\
0\,0\,0\,0\,0 & 0 & 0 & 0 & 0\,0\,0\,0\,0\,0\,0
\end{pmatrix}
\begin{pmatrix}
0\,0\,0\,0\,0 & 0 & 0 & 0 & 0\,0\,0\,0\,0\,0\,0 \\
0\,0\,0\,0\,0 & 0 & 0 & 0 & 0\,0\,0\,0\,0\,0\,0 \\
0\,0\,0\,0\,0 & 0 & 0 & 0 & 0\,0\,0\,0\,0\,0\,0 \\
0\,0\,0\,0\,0 & 0 & 0 & 0 & 0\,0\,0\,0\,0\,0\,0 \\
0\,0\,0\,0\,0 & 0 & 0 & 0 & 0\,0\,0\,0\,0\,0\,0 \\
0\,0\,0\,0\,0 & 0 & 0 & 0 & 0\,0\,0\,0\,0\,0\,0 \\
0\,0\,0\,0\,0 & 0 & 0 & 0 & 0\,0\,0\,0\,0\,0\,0 \\
0\,0\,0\,0\,0 & 0 & 0 & 0 & 0\,0\,0\,0\,0\,0\,0 \\
0\,0\,0\,0\,0 & 0 & 0 & 0 & 0\,0\,0\,0\,0\,0\,0 \\
0\,0\,0\,0\,0 & 0 & 0 & 0 & 0\,0\,0\,0\,0\,0\,0 \\
0\,0\,0\,0\,0 & 0 & 0 & 0 & 0\,0\,0\,0\,0\,0\,0 \\
0\,0\,0\,0\,0 & 0 & 0 & 0 & 0\,0\,0\,0\,0\,0\,0
\end{pmatrix}
$$

$$
\frac{\partial \boldsymbol{Q}}{\partial \boldsymbol{P}} =
\begin{pmatrix}
1 & 0 & 0 & 0 & 0 & 0 & 0 & 0 & 0 & 0 & 0 & 0 & 0 & 0 & 0 & 0 & 0 & 0 \\
\left(E + \rho\frac{\partial E}{\partial \rho}\right) & \frac{1}{\Gamma}\rho v_1 & \rho v_2 & \rho v_3 & \tilde{\psi}_{11} & \tilde{\psi}_{12} & \tilde{\psi}_{13} & \tilde{\psi}_{21} & \tilde{\psi}_{22} & \tilde{\psi}_{23} & \tilde{\psi}_{31} & \tilde{\psi}_{32} & \tilde{\psi}_{33} & \rho H_1 & \rho H_2 & \rho H_3 & \rho Q \\
v_1 & 0 & \rho & 0 & 0 & 0 & 0 & 0 & 0 & 0 & 0 & 0 & 0 & 0 & 0 & 0 & 0 & 0 \\
v_2 & 0 & 0 & \rho & 0 & 0 & 0 & 0 & 0 & 0 & 0 & 0 & 0 & 0 & 0 & 0 & 0 & 0 \\
v_3 & 0 & 0 & 0 & \rho & 0 & 0 & 0 & 0 & 0 & 0 & 0 & 0 & 0 & 0 & 0 & 0 & 0 \\
0 & 0 & 0 & 0 & 0 & 1 & 0 & 0 & 0 & 0 & 0 & 0 & 0 & 0 & 0 & 0 & 0 & 0 \\
0 & 0 & 0 & 0 & 0 & 0 & 1 & 0 & 0 & 0 & 0 & 0 & 0 & 0 & 0 & 0 & 0 & 0 \\
0 & 0 & 0 & 0 & 0 & 0 & 0 & 1 & 0 & 0 & 0 & 0 & 0 & 0 & 0 & 0 & 0 & 0 \\
0 & 0 & 0 & 0 & 0 & 0 & 0 & 0 & 1 & 0 & 0 & 0 & 0 & 0 & 0 & 0 & 0 & 0 \\
0 & 0 & 0 & 0 & 0 & 0 & 0 & 0 & 0 & 1 & 0 & 0 & 0 & 0 & 0 & 0 & 0 & 0 \\
0 & 0 & 0 & 0 & 0 & 0 & 0 & 0 & 0 & 0 & 1 & 0 & 0 & 0 & 0 & 0 & 0 & 0 \\
0 & 0 & 0 & 0 & 0 & 0 & 0 & 0 & 0 & 0 & 0 & 1 & 0 & 0 & 0 & 0 & 0 & 0 \\
0 & 0 & 0 & 0 & 0 & 0 & 0 & 0 & 0 & 0 & 0 & 0 & 1 & 0 & 0 & 0 & 0 & 0 \\
J_1 & 0 & 0 & 0 & 0 & 0 & 0 & 0 & 0 & 0 & 0 & 0 & 0 & \rho & 0 & 0 & 0 & 0 \\
J_2 & 0 & 0 & 0 & 0 & 0 & 0 & 0 & 0 & 0 & 0 & 0 & 0 & 0 & \rho & 0 & 0 & 0 \\
J_3 & 0 & 0 & 0 & 0 & 0 & 0 & 0 & 0 & 0 & 0 & 0 & 0 & 0 & 0 & \rho & 0 & 0 \\
\lambda & 0 & 0 & 0 & 0 & 0 & 0 & 0 & 0 & 0 & 0 & 0 & 0 & 0 & 0 & 0 & 0 & \rho
\end{pmatrix}
\tag{A.5}
$$

$$\frac{\partial \boldsymbol{P}}{\partial \boldsymbol{Q}} = -\begin{pmatrix}
-1 & 0 & 0 & 0 & 0 & 0 & 0 & 0 & 0 & 0 & 0 & 0 & 0 & 0 & 0 & 0 & 0 & 0 & 0 & 0 \\
-\Upsilon & -\Gamma & \Gamma v_1 & \Gamma v_2 & \Gamma v_3 & \Gamma\tilde{\psi}_{11} & \Gamma\tilde{\psi}_{12} & \Gamma\tilde{\psi}_{13} & \Gamma\tilde{\psi}_{21} & \Gamma\tilde{\psi}_{22} & \Gamma\tilde{\psi}_{23} & \Gamma\tilde{\psi}_{31} & \Gamma\tilde{\psi}_{32} & \Gamma\tilde{\psi}_{33} & \Gamma H_1 & \Gamma H_2 & \Gamma H_3 & \Gamma Q \\
\frac{v_1}{\rho} & 0 & \frac{-1}{\rho} & 0 & 0 & 0 & 0 & 0 & 0 & 0 & 0 & 0 & 0 & 0 & 0 & 0 & 0 & 0 & 0 \\
\frac{v_2}{\rho} & 0 & 0 & \frac{-1}{\rho} & 0 & 0 & 0 & 0 & 0 & 0 & 0 & 0 & 0 & 0 & 0 & 0 & 0 & 0 & 0 \\
\frac{v_3}{\rho} & 0 & 0 & 0 & \frac{-1}{\rho} & 0 & 0 & 0 & 0 & 0 & 0 & 0 & 0 & 0 & 0 & 0 & 0 & 0 & 0 \\
0 & 0 & 0 & 0 & 0 & -1 & 0 & 0 & 0 & 0 & 0 & 0 & 0 & 0 & 0 & 0 & 0 & 0 & 0 \\
0 & 0 & 0 & 0 & 0 & 0 & -1 & 0 & 0 & 0 & 0 & 0 & 0 & 0 & 0 & 0 & 0 & 0 & 0 \\
0 & 0 & 0 & 0 & 0 & 0 & 0 & -1 & 0 & 0 & 0 & 0 & 0 & 0 & 0 & 0 & 0 & 0 & 0 \\
0 & 0 & 0 & 0 & 0 & 0 & 0 & 0 & -1 & 0 & 0 & 0 & 0 & 0 & 0 & 0 & 0 & 0 & 0 \\
0 & 0 & 0 & 0 & 0 & 0 & 0 & 0 & 0 & -1 & 0 & 0 & 0 & 0 & 0 & 0 & 0 & 0 & 0 \\
0 & 0 & 0 & 0 & 0 & 0 & 0 & 0 & 0 & 0 & -1 & 0 & 0 & 0 & 0 & 0 & 0 & 0 & 0 \\
0 & 0 & 0 & 0 & 0 & 0 & 0 & 0 & 0 & 0 & 0 & -1 & 0 & 0 & 0 & 0 & 0 & 0 & 0 \\
0 & 0 & 0 & 0 & 0 & 0 & 0 & 0 & 0 & 0 & 0 & 0 & -1 & 0 & 0 & 0 & 0 & 0 & 0 \\
0 & 0 & 0 & 0 & 0 & 0 & 0 & 0 & 0 & 0 & 0 & 0 & 0 & -1 & 0 & 0 & 0 & 0 & 0 \\
\frac{J_1}{\rho} & 0 & 0 & 0 & 0 & 0 & 0 & 0 & 0 & 0 & 0 & 0 & 0 & 0 & \frac{-1}{\rho} & 0 & 0 & 0 & 0 \\
\frac{J_2}{\rho} & 0 & 0 & 0 & 0 & 0 & 0 & 0 & 0 & 0 & 0 & 0 & 0 & 0 & 0 & \frac{-1}{\rho} & 0 & 0 & 0 \\
\frac{J_3}{\rho} & 0 & 0 & 0 & 0 & 0 & 0 & 0 & 0 & 0 & 0 & 0 & 0 & 0 & 0 & 0 & \frac{-1}{\rho} & 0 & 0 \\
\frac{\lambda}{\rho} & 0 & 0 & 0 & 0 & 0 & 0 & 0 & 0 & 0 & 0 & 0 & 0 & 0 & 0 & 0 & 0 & \frac{-1}{\rho} & 0
\end{pmatrix} \tag{A.6}$$

$$
\frac{\partial \boldsymbol{F_1}}{\partial \boldsymbol{P}} =
\begin{pmatrix}
v_1 & 0 & \rho & 0 & 0 & 0 & 0 & 0 & 0 & 0 & 0 & 0 & 0 & 0 & 0 & 0 & 0 & 0 & 0 \\
\Delta_1 & \Pi_1 & (\Psi_{11}+\rho E+p) & \Psi_{12} & \Psi_{13} & \Omega_{11}^1 & \Omega_{12}^1 & \Omega_{13}^1 & \Omega_{21}^1 & \Omega_{22}^1 & \Omega_{23}^1 & \Omega_{31}^1 & \Omega_{32}^1 & \Omega_{33}^1 & (\rho v_1 H_1 + c_t^2 T) & \rho v_1 H_2 & \rho v_1 H_3 & \rho v_1 Q \\
\Phi_{11} & 1 & 2\rho v_1 & 0 & 0 & \aleph_{11}^{11} & \aleph_{12}^{11} & \aleph_{13}^{11} & \aleph_{21}^{11} & \aleph_{22}^{11} & \aleph_{23}^{11} & \aleph_{31}^{11} & \aleph_{32}^{11} & \aleph_{33}^{11} & 0 & 0 & 0 & 0 \\
\Phi_{12} & 0 & \rho v_2 & \rho v_1 & 0 & \aleph_{11}^{12} & \aleph_{12}^{12} & \aleph_{13}^{12} & \aleph_{21}^{12} & \aleph_{22}^{12} & \aleph_{23}^{12} & \aleph_{31}^{12} & \aleph_{32}^{12} & \aleph_{33}^{12} & 0 & 0 & 0 & 0 \\
\Phi_{13} & 0 & \rho v_3 & 0 & \rho v_1 & \aleph_{11}^{13} & \aleph_{12}^{13} & \aleph_{13}^{13} & \aleph_{21}^{13} & \aleph_{22}^{13} & \aleph_{23}^{13} & \aleph_{31}^{13} & \aleph_{32}^{13} & \aleph_{33}^{13} & 0 & 0 & 0 & 0 \\
0 & 0 & A_{11} & A_{12} & A_{13} & v_1 & v_2 & v_3 & 0 & 0 & 0 & 0 & 0 & 0 & 0 & 0 & 0 & 0 \\
0 & 0 & 0 & 0 & 0 & 0 & 0 & 0 & 0 & 0 & 0 & 0 & 0 & 0 & 0 & 0 & 0 & 0 \\
0 & 0 & 0 & 0 & 0 & 0 & 0 & 0 & 0 & 0 & 0 & 0 & 0 & 0 & 0 & 0 & 0 & 0 \\
0 & 0 & A_{21} & A_{22} & A_{23} & 0 & 0 & 0 & v_1 & v_2 & v_3 & 0 & 0 & 0 & 0 & 0 & 0 & 0 \\
0 & 0 & 0 & 0 & 0 & 0 & 0 & 0 & 0 & 0 & 0 & 0 & 0 & 0 & 0 & 0 & 0 & 0 \\
0 & 0 & 0 & 0 & 0 & 0 & 0 & 0 & 0 & 0 & 0 & 0 & 0 & 0 & 0 & 0 & 0 & 0 \\
0 & 0 & A_{31} & A_{32} & A_{33} & 0 & 0 & 0 & 0 & 0 & 0 & v_1 & v_2 & v_3 & 0 & 0 & 0 & 0 \\
0 & 0 & 0 & 0 & 0 & 0 & 0 & 0 & 0 & 0 & 0 & 0 & 0 & 0 & 0 & 0 & 0 & 0 \\
0 & 0 & 0 & 0 & 0 & 0 & 0 & 0 & 0 & 0 & 0 & 0 & 0 & 0 & 0 & 0 & 0 & 0 \\
v_1 J_1 + \frac{\partial T}{\partial \rho} & \frac{\partial T}{\partial p} & \rho J_1 & 0 & 0 & 0 & 0 & 0 & 0 & 0 & 0 & 0 & 0 & 0 & \rho v_1 & 0 & 0 & 0 \\
v_1 J_2 & 0 & \rho J_2 & 0 & 0 & 0 & 0 & 0 & 0 & 0 & 0 & 0 & 0 & 0 & 0 & \rho v_1 & 0 & 0 \\
v_1 J_3 & 0 & \rho J_3 & 0 & 0 & 0 & 0 & 0 & 0 & 0 & 0 & 0 & 0 & 0 & 0 & 0 & \rho v_1 & 0 \\
v_1 \lambda & 0 & \rho\lambda & 0 & 0 & 0 & 0 & 0 & 0 & 0 & 0 & 0 & 0 & 0 & 0 & 0 & 0 & \rho v_1
\end{pmatrix}
\tag{A.7}
$$

$$
\frac{\partial \boldsymbol{F_2}}{\partial \boldsymbol{P}} =
\begin{pmatrix}
v_2 & 0 & 0 & \rho & 0 & 0 & 0 & 0 & 0 & 0 & 0 & 0 & 0 & 0 & 0 & 0 & 0 & 0 \\
\Delta_2 & \Pi_2 & \Psi_{21} & (\Psi_{22}+\rho E+p) & \Psi_{23} & \Omega_{11}^2 & \Omega_{12}^2 & \Omega_{13}^2 & \Omega_{21}^2 & \Omega_{22}^2 & \Omega_{23}^2 & \Omega_{31}^2 & \Omega_{32}^2 & \Omega_{33}^2 & \rho v_2 H_1 & (\rho v_2 H_2 + c_t^2 T) & \rho v_2 H_3 & \rho v_2 Q \\
\Phi_{21} & 0 & \rho v_2 & \rho v_1 & 0 & \aleph_{11}^{21} & \aleph_{12}^{21} & \aleph_{13}^{21} & \aleph_{21}^{21} & \aleph_{22}^{21} & \aleph_{23}^{21} & \aleph_{31}^{21} & \aleph_{32}^{21} & \aleph_{33}^{21} & 0 & 0 & 0 & 0 \\
\Phi_{22} & 1 & 0 & 2\rho v_2 & 0 & \aleph_{11}^{22} & \aleph_{12}^{22} & \aleph_{13}^{22} & \aleph_{21}^{22} & \aleph_{22}^{22} & \aleph_{23}^{22} & \aleph_{31}^{22} & \aleph_{32}^{22} & \aleph_{33}^{22} & 0 & 0 & 0 & 0 \\
\Phi_{23} & 0 & 0 & \rho v_3 & \rho v_2 & \aleph_{11}^{23} & \aleph_{12}^{23} & \aleph_{13}^{23} & \aleph_{21}^{23} & \aleph_{22}^{23} & \aleph_{23}^{23} & \aleph_{31}^{23} & \aleph_{32}^{23} & \aleph_{33}^{23} & 0 & 0 & 0 & 0 \\
0 & 0 & 0 & 0 & 0 & 0 & 0 & 0 & 0 & 0 & 0 & 0 & 0 & 0 & 0 & 0 & 0 & 0 \\
0 & 0 & A_{11} & A_{12} & A_{13} & v_1 & v_2 & v_3 & 0 & 0 & 0 & 0 & 0 & 0 & 0 & 0 & 0 & 0 \\
0 & 0 & 0 & 0 & 0 & 0 & 0 & 0 & 0 & 0 & 0 & 0 & 0 & 0 & 0 & 0 & 0 & 0 \\
0 & 0 & 0 & 0 & 0 & 0 & 0 & 0 & 0 & 0 & 0 & 0 & 0 & 0 & 0 & 0 & 0 & 0 \\
0 & 0 & A_{21} & A_{22} & A_{23} & 0 & 0 & 0 & v_1 & v_2 & v_3 & 0 & 0 & 0 & 0 & 0 & 0 & 0 \\
0 & 0 & 0 & 0 & 0 & 0 & 0 & 0 & 0 & 0 & 0 & 0 & 0 & 0 & 0 & 0 & 0 & 0 \\
0 & 0 & 0 & 0 & 0 & 0 & 0 & 0 & 0 & 0 & 0 & 0 & 0 & 0 & 0 & 0 & 0 & 0 \\
0 & 0 & A_{31} & A_{32} & A_{33} & 0 & 0 & 0 & 0 & 0 & 0 & v_1 & v_2 & v_3 & 0 & 0 & 0 & 0 \\
0 & 0 & 0 & 0 & 0 & 0 & 0 & 0 & 0 & 0 & 0 & 0 & 0 & 0 & 0 & 0 & 0 & 0 \\
v_2 J_1 & 0 & 0 & \rho J_1 & 0 & 0 & 0 & 0 & 0 & 0 & 0 & 0 & 0 & 0 & \rho v_2 & 0 & 0 & 0 \\
v_2 J_2 + \frac{\partial T}{\partial \rho} & \frac{\partial T}{\partial p} & 0 & \rho J_2 & 0 & 0 & 0 & 0 & 0 & 0 & 0 & 0 & 0 & 0 & 0 & \rho v_2 & 0 & 0 \\
v_2 J_3 & 0 & 0 & \rho J_3 & 0 & 0 & 0 & 0 & 0 & 0 & 0 & 0 & 0 & 0 & 0 & 0 & \rho v_2 & 0 \\
v_2 \lambda & 0 & 0 & \rho \lambda & 0 & 0 & 0 & 0 & 0 & 0 & 0 & 0 & 0 & 0 & 0 & 0 & 0 & \rho v_2
\end{pmatrix}
\tag{A.8}
$$

$$
\frac{\partial \boldsymbol{F_3}}{\partial \boldsymbol{P}} =
\begin{pmatrix}
v_3 & 0 & 0 & 0 & 0 & \rho & 0 & 0 & 0 & 0 & 0 & 0 & 0 & 0 & 0 & 0 & 0 & 0 & 0 & 0 & 0 & 0 & 0 \\
\Delta_3 & \Pi_3 & \Psi_{11} & \Psi_{12} & (\Psi_{13}+\rho E+p) & \Omega^3_{11} & \Omega^3_{12} & \Omega^3_{13} & \Omega^3_{21} & \Omega^3_{22} & \Omega^3_{23} & \Omega^3_{31} & \Omega^3_{32} & \Omega^3_{33} & \rho v_3 H_1 & \rho v_3 H_2 & \left(\rho v_3 H_3 + c_t^2 T\right) & \rho v_3 Q \\
\Phi_{31} & 0 & \rho v_3 & 0 & \rho v_1 & \aleph^{31}_{11} & \aleph^{31}_{12} & \aleph^{31}_{13} & \aleph^{31}_{21} & \aleph^{31}_{22} & \aleph^{31}_{23} & \aleph^{31}_{31} & \aleph^{31}_{32} & \aleph^{31}_{33} & 0 & 0 & 0 & 0 \\
\Phi_{32} & 0 & 0 & \rho v_3 & \rho v_2 & \aleph^{32}_{11} & \aleph^{32}_{12} & \aleph^{32}_{13} & \aleph^{32}_{21} & \aleph^{32}_{22} & \aleph^{32}_{23} & \aleph^{32}_{31} & \aleph^{32}_{32} & \aleph^{32}_{33} & 0 & 0 & 0 & 0 \\
\Phi_{33} & 1 & 0 & 0 & 2\rho v_3 & \aleph^{33}_{11} & \aleph^{33}_{12} & \aleph^{33}_{13} & \aleph^{33}_{21} & \aleph^{33}_{22} & \aleph^{33}_{23} & \aleph^{33}_{31} & \aleph^{33}_{32} & \aleph^{33}_{33} & 0 & 0 & 0 & 0 \\
0 & 0 & 0 & 0 & 0 & 0 & 0 & 0 & 0 & 0 & 0 & 0 & 0 & 0 & 0 & 0 & 0 & 0 \\
0 & 0 & 0 & 0 & 0 & 0 & 0 & 0 & 0 & 0 & 0 & 0 & 0 & 0 & 0 & 0 & 0 & 0 \\
0 & 0 & A_{11} & A_{12} & A_{13} & v_1 & v_2 & v_3 & 0 & 0 & 0 & 0 & 0 & 0 & 0 & 0 & 0 & 0 \\
0 & 0 & 0 & 0 & 0 & 0 & 0 & 0 & 0 & 0 & 0 & 0 & 0 & 0 & 0 & 0 & 0 & 0 \\
0 & 0 & 0 & 0 & 0 & 0 & 0 & 0 & 0 & 0 & 0 & 0 & 0 & 0 & 0 & 0 & 0 & 0 \\
0 & 0 & A_{21} & A_{22} & A_{23} & 0 & 0 & 0 & v_1 & v_2 & v_3 & 0 & 0 & 0 & 0 & 0 & 0 & 0 \\
0 & 0 & 0 & 0 & 0 & 0 & 0 & 0 & 0 & 0 & 0 & 0 & 0 & 0 & 0 & 0 & 0 & 0 \\
0 & 0 & 0 & 0 & 0 & 0 & 0 & 0 & 0 & 0 & 0 & 0 & 0 & 0 & 0 & 0 & 0 & 0 \\
0 & 0 & A_{31} & A_{32} & A_{33} & 0 & 0 & 0 & 0 & 0 & 0 & v_1 & v_2 & v_3 & 0 & 0 & 0 & 0 \\
v_3 J_1 & 0 & 0 & 0 & \rho J_1 & 0 & 0 & 0 & 0 & 0 & 0 & 0 & 0 & 0 & \rho v_3 & 0 & 0 & 0 \\
v_3 J_2 & 0 & 0 & 0 & \rho J_2 & 0 & 0 & 0 & 0 & 0 & 0 & 0 & 0 & 0 & 0 & \rho v_3 & 0 & 0 \\
v_3 J_3 + \frac{\partial T}{\partial \rho} & 0 & 0 & 0 & \rho J_3 & 0 & 0 & 0 & 0 & 0 & 0 & 0 & 0 & 0 & 0 & 0 & \rho v_3 & 0 \\
v_3 \lambda & 0 & 0 & 0 & \rho \lambda & 0 & 0 & 0 & 0 & 0 & 0 & 0 & 0 & 0 & 0 & 0 & 0 & \rho v_3
\end{pmatrix}
\tag{A.9}
$$

Jacobian of Distortion ODEs

The Jacobian of the source function is used to speed up numerical integration of the ODE. It is derived thus:

$$\frac{\partial \operatorname{dev}(G)_{ij}}{\partial A_{mn}} = \delta_{in}A_{mj} + \delta_{jn}A_{mi} - \frac{2}{3}\delta_{ij}A_{mn} \tag{A.10}$$

Thus:

$$\begin{aligned}\frac{\partial \left(A \operatorname{dev}(G)\right)_{ij}}{\partial A_{mn}} &= \frac{\partial A_{it}}{\partial A_{mn}} \operatorname{dev}(G)_{tj} + A_{it}\frac{\partial \operatorname{dev}(G)_{tj}}{\partial A_{mn}} \\ &= \begin{array}{c}\delta_{im}\delta_{tn}\left(A_{kt}A_{kj} - \frac{1}{3}A_{kl}A_{kl}\delta_{tj}\right) \\ +A_{it}\left(\delta_{tn}A_{mj} + \delta_{jn}A_{mt} - \frac{2}{3}\delta_{tj}A_{mn}\right)\end{array} \\ &= \delta_{im}A_{kn}A_{kj} - \frac{1}{3}\delta_{im}\delta_{jn}A_{kl}A_{kl} + A_{in}A_{mj} + \delta_{jn}A_{ik}A_{mk} - \frac{2}{3}A_{ij}A_{mn}\end{aligned} \tag{A.11}$$

Thus:

$$\begin{aligned}J_A &\equiv \frac{-3}{\tau_1}\frac{\partial\left(\det(A)^{\frac{5}{3}} A \operatorname{dev}(G)\right)_{ij}}{\partial A_{mn}} \\ &= \frac{-3}{\tau_1}\det(A)^{\frac{5}{3}}\begin{pmatrix}\frac{5}{3}\left(A\operatorname{dev}(G)\right)_{ij}A^{-T}_{mn} + A_{in}A_{mj} + \delta_{jn}G'_{im} + \delta_{im}G_{jn} \\ -\frac{1}{3}\delta_{im}\delta_{jn}A_{kl}A_{kl} - \frac{2}{3}A_{ij}A_{mn}\end{pmatrix} \\ &= \frac{-1}{\tau_1}\det(A)^{\frac{5}{3}}\begin{pmatrix}5\left(A\operatorname{dev}(G)\right)\otimes A^{-T} - 2A\otimes A + 3\left(A\otimes A\right)^{1,3} \\ -\|A\|_F^2\left(I\otimes I\right)^{2,3} + 3\left(G'\otimes I + I\otimes G\right)^{2,3}\end{pmatrix}\end{aligned} \tag{A.12}$$

where $G' = AA^T$ and $X^{a,b}$ refers to tensor X with indices a, b transposed.

Jacobian of Thermal Impulse ODEs

As demonstrated in 2.2.3, we have:

$$\frac{dJ_i}{dt} = \frac{J_i}{2}\left(-a + b\left(J_1^2 + J_2^2 + J_3^2\right)\right) \tag{A.13}$$

where

$$a = \frac{2\rho_0}{\tau_2 T_0 \rho c_v} \left(E - E_{2A}\left(A\right) - E_3\left(\boldsymbol{v}\right)\right) \tag{A.14a}$$

$$b = \frac{\rho_0 c_t^2}{\tau_2 T_0 \rho c_v} \tag{A.14b}$$

Thus, the Jacobian of the thermal impulse ODEs is:

$$\begin{pmatrix} \frac{b}{2}\left(3J_1^2 + J_2^2 + J_3^2\right) - \frac{a}{2} & bJ_1J_2 & bJ_1J_3 \\ bJ_1J_2 & \frac{b}{2}\left(J_1^2 + 3J_2^2 + J_3^2\right) - \frac{a}{2} & bJ_2J_3 \\ bJ_1J_3 & bJ_2J_3 & \frac{b}{2}\left(J_1^2 + J_2^2 + 3J_3^2\right) - \frac{a}{2} \end{pmatrix} \tag{A.15}$$

Appendix B

Eigenstructure

B.1 Primitive System

Taking the ordering $\boldsymbol{P}$ of primitive variables in (B.17), note that (3), (1b), (1c), (1d) can be stated as:

$$\frac{D\rho}{Dt} + \rho\frac{\partial v_k}{\partial x_k} = 0 \tag{B.1a}$$

$$\frac{Dv_i}{Dt} + \frac{1}{\rho}\frac{\partial \Sigma_{ik}}{\partial x_k} = 0 \tag{B.1b}$$

$$\frac{DA_{ij}}{Dt} + A_{ik}\frac{\partial v_k}{\partial x_j} = -\frac{\psi_{ij}}{\theta_1} \tag{B.1c}$$

$$\frac{DJ_i}{Dt} + \frac{1}{\rho}\frac{\partial T\delta_{ik}}{\partial x_k} = -\frac{H_i}{\theta_2} \tag{B.1d}$$

$$\frac{DE}{Dt} + \frac{1}{\rho}\frac{\partial\left(\Sigma_{ik}v_i + TH_k\right)}{\partial x_k} = 0 \tag{B.1e}$$

$$\frac{D\lambda}{Dt} = -K \tag{B.1f}$$

where the total stress tensor $\Sigma = pI + \rho A^T\psi$. Note that:

$$\begin{aligned}\frac{DE}{Dt} = & \frac{\partial E}{\partial p}\frac{Dp}{Dt} + \frac{\partial E}{\partial \rho}\frac{D\rho}{Dt} + v_i\frac{Dv_i}{Dt} \\ & + \frac{\partial E}{\partial A_{ij}}\frac{DA_{ij}}{Dt} + H_i\frac{DJ_i}{Dt} + \frac{\partial E}{\partial \lambda}\frac{D\lambda}{Dt} \\ = & \frac{\partial E}{\partial p}\frac{Dp}{Dt} - \rho\frac{\partial E}{\partial \rho}\frac{\partial v_k}{\partial x_k} - \frac{1}{\rho}v_i\frac{\partial \Sigma_{ik}}{\partial x_k} \\ & - \frac{\partial E}{\partial A_{ij}}\left(A_{ik}\frac{\partial v_k}{\partial x_j} + \frac{\psi_{ij}}{\theta_1}\right) - H_i\left(\frac{1}{\rho}\frac{\partial T\delta_{ik}}{\partial x_k} + \frac{H_i}{\theta_2}\right) - \frac{\partial E}{\partial \lambda}K\end{aligned} \tag{B.2}$$

Thus, the energy equation becomes:

$$\begin{aligned}\frac{\partial E}{\partial p}\frac{Dp}{Dt} - \rho\frac{\partial E}{\partial \rho}\frac{\partial v_k}{\partial x_k} - \frac{1}{\rho}v_i\frac{\partial \Sigma_{ik}}{\partial x_k} - \frac{\partial E}{\partial A_{ij}}A_{ik}\frac{\partial v_k}{\partial x_j} - \frac{H_k}{\rho}\frac{\partial T}{\partial x_k} + \frac{1}{\rho}\frac{\partial(\Sigma_{ik}v_i + TH_k)}{\partial x_k} \\ = \frac{\partial E}{\partial A_{ij}}\frac{\psi_{ij}}{\theta_1} + \frac{H_iH_i}{\theta_2} + \frac{\partial E}{\partial \lambda}K\end{aligned} \tag{B.3}$$

Simplifying:

$$\begin{aligned}\frac{Dp}{Dt} + \frac{1}{\rho E_p}\left(\Sigma_{ik} - \rho A_{ji}\frac{\partial E}{\partial A_{jk}} - \rho^2\frac{\partial E}{\partial \rho}\delta_{ik}\right)\frac{\partial v_i}{\partial x_k} + \frac{T}{\rho E_p}\frac{\partial H_k}{\partial x_k} \\ = \frac{\partial E}{\partial A_{ij}}\frac{\psi_{ij}}{\theta_1 E_p} + \frac{H_i H_i}{\theta_2 E_p} + \frac{E_\lambda}{E_p}K\end{aligned} \tag{B.4}$$

We have[1][2][3]:

$$\frac{p - \rho^2 E_\rho}{\rho E_p} = \rho c_0^2 \tag{B.9a}$$

$$\frac{c_t^2 T}{\rho E_p} = \frac{\rho c_h^2}{T_p} \tag{B.9b}$$

$$\left.\frac{\partial E}{\partial A}\right|_{\rho,p} = \left(1 - 2\rho^2 E_p \frac{\partial \log(c_s)}{\partial \rho}\right)\psi \tag{B.9c}$$

$$-\rho A^T \left.\frac{\partial E}{\partial A}\right|_{\rho,p} = \sigma + \rho^2 E_p\left(\frac{\sigma}{\rho} - \frac{\partial \sigma}{\partial \rho}\right) \tag{B.9d}$$

---

[1]

$$\begin{aligned}\frac{p - \rho^2 E_\rho}{\rho E_p} &= \frac{\rho^2\ E_\rho|_s - \rho^2\ E_\rho|_p}{\rho\ E_p|_\rho} = \rho\frac{E_\rho|_s - \left(E_\rho|_s + E_s|_\rho\ s_\rho|_p\right)}{E_s|_\rho\ s_p|_\rho} \\ &= \rho\frac{-\ s_\rho|_p}{s_p|_\rho} = \rho\left.\frac{\partial p}{\partial \rho}\right|_s\end{aligned} \tag{B.5}$$

[2]

$$\frac{c_t^2 T}{\rho E_p} = \frac{c_t^2 T}{\rho c_v T_p} = \frac{\rho c_h^2}{T_p} \tag{B.6}$$

[3]

$$\left.\frac{\partial E}{\partial A}\right|_{\rho,p} = \left(c_s^2 - \frac{\rho}{\Gamma}\frac{\partial c_s^2}{\partial \rho}\right)\frac{\psi}{c_s^2} = \left(1 - 2\frac{\rho^2}{\rho\Gamma}\frac{\partial \log(c_s)}{\partial \rho}\right)\psi \tag{B.7}$$

$$\begin{aligned}\frac{\partial \sigma}{\partial \rho} &= \frac{\partial}{\partial \rho}\left(-\rho c_s^2 A^T \frac{\psi}{c_s^2}\right) = -c_s^2 A^T \frac{\psi}{c_s^2} - \rho\frac{\partial c_s^2}{\partial \rho}A^T\frac{\psi}{c_s^2} \\ &= \frac{\sigma}{\rho} + 2\frac{\partial \log(c_s)}{\partial \rho}\sigma\end{aligned} \tag{B.8}$$

The full system then becomes:

$$\frac{D\rho}{Dt} + \rho\frac{\partial v_k}{\partial x_k} = 0 \tag{B.10a}$$

$$\frac{Dp}{Dt} + \rho c_0^2\frac{\partial v_i}{\partial x_i} + \left(\sigma_{ik} - \rho\frac{\partial \sigma_{ik}}{\partial \rho}\right)\frac{\partial v_i}{\partial x_k} + \frac{\rho c_h^2}{T_p}\frac{\partial J_k}{\partial x_k} = \tilde{c}_s\frac{\|\psi\|_F^2}{\theta_1 E_p} + \frac{\|H\|^2}{\theta_2 E_p} + \frac{E_\lambda}{E_p}K \tag{B.10b}$$

$$\frac{DA_{ij}}{Dt} + A_{ik}\frac{\partial v_k}{\partial x_j} = -\frac{\psi_{ij}}{\theta_1} \tag{B.10c}$$

$$\frac{Dv_i}{Dt} - \frac{1}{\rho}\frac{\partial \sigma_{ik}}{\partial \rho}\frac{\partial \rho}{\partial x_k} + \frac{1}{\rho}\frac{\partial p}{\partial x_i} - \frac{1}{\rho}\frac{\partial \sigma_{ik}}{\partial A_{mn}}\frac{\partial A_{mn}}{\partial x_k} = 0 \tag{B.10d}$$

$$\frac{DJ_i}{Dt} + \frac{T_\rho}{\rho}\frac{\partial \rho}{\partial x_i} + \frac{T_p}{\rho}\frac{\partial p}{\partial x_i} = -\frac{H_i}{\theta_2} \tag{B.10e}$$

$$\frac{D\lambda}{Dt} = -K \tag{B.10f}$$

where:

$$\tilde{c}_s\left(\rho, p, A\right) = 1 - 2\rho^2 E_p\frac{\partial \log\left(c_s\right)}{\partial \rho} \tag{B.11}$$

Thus, the GPR system can be written in the following form:

$$\frac{\partial \boldsymbol{P}}{\partial t} + \boldsymbol{M}\cdot\nabla\boldsymbol{P} = \boldsymbol{S_p} \tag{B.12}$$

Defining the following variables:

$$\tilde{\aleph}_{ij} = -\frac{\partial \sigma_{ij}}{\partial \rho} \tag{B.13a}$$

$$\tilde{\Omega}_{ij} = \rho\sigma_{ij} + \rho^2\tilde{\aleph}_{ij} \tag{B.13b}$$

we have $\mathbf{M}$ taking the form given in (B.14), (B.15), (B.16), and $\mathbf{P}, \mathbf{S_P}$ taking the forms given in (B.17).

$$
M_1 = v_1 I + \frac{1}{\rho}
\begin{pmatrix}
0 & 0 & 0 & 0 & 0 & 0 & 0 & 0 & 0 & \rho^2 & 0 & 0 & 0 & 0 & 0 & 0 \\
0 & 0 & 0 & 0 & 0 & 0 & 0 & 0 & 0 & \tilde{\Omega}_{11}+\rho^2 c_0^2 & \tilde{\Omega}_{21} & \tilde{\Omega}_{31} & \frac{\rho^2 c_h^2}{T_p} & 0 & 0 & 0 \\
0 & 0 & 0 & 0 & 0 & 0 & 0 & 0 & 0 & \rho A_{11} & \rho A_{12} & \rho A_{13} & 0 & 0 & 0 & 0 \\
0 & 0 & 0 & 0 & 0 & 0 & 0 & 0 & 0 & \rho A_{21} & \rho A_{22} & \rho A_{23} & 0 & 0 & 0 & 0 \\
0 & 0 & 0 & 0 & 0 & 0 & 0 & 0 & 0 & \rho A_{31} & \rho A_{32} & \rho A_{33} & 0 & 0 & 0 & 0 \\
0 & 0 & 0 & 0 & 0 & 0 & 0 & 0 & 0 & 0 & 0 & 0 & 0 & 0 & 0 & 0 \\
0 & 0 & 0 & 0 & 0 & 0 & 0 & 0 & 0 & 0 & 0 & 0 & 0 & 0 & 0 & 0 \\
0 & 0 & 0 & 0 & 0 & 0 & 0 & 0 & 0 & 0 & 0 & 0 & 0 & 0 & 0 & 0 \\
0 & 0 & 0 & 0 & 0 & 0 & 0 & 0 & 0 & 0 & 0 & 0 & 0 & 0 & 0 & 0 \\
0 & 0 & 0 & 0 & 0 & 0 & 0 & 0 & 0 & 0 & 0 & 0 & 0 & 0 & 0 & 0 \\
\tilde{\aleph}_{11} & 1 & \aleph_{11}^{11} & \aleph_{21}^{11} & \aleph_{31}^{11} & \aleph_{12}^{11} & \aleph_{22}^{11} & \aleph_{32}^{11} & \aleph_{13}^{11} & \aleph_{23}^{11} & \aleph_{33}^{11} & 0 & 0 & 0 & 0 & 0 & 0 \\
\tilde{\aleph}_{12} & 0 & \aleph_{11}^{12} & \aleph_{21}^{12} & \aleph_{31}^{12} & \aleph_{12}^{12} & \aleph_{22}^{12} & \aleph_{32}^{12} & \aleph_{13}^{12} & \aleph_{23}^{12} & \aleph_{33}^{12} & 0 & 0 & 0 & 0 & 0 & 0 \\
\tilde{\aleph}_{13} & 0 & \aleph_{11}^{13} & \aleph_{21}^{13} & \aleph_{31}^{13} & \aleph_{12}^{13} & \aleph_{22}^{13} & \aleph_{32}^{13} & \aleph_{13}^{13} & \aleph_{23}^{13} & \aleph_{33}^{13} & 0 & 0 & 0 & 0 & 0 & 0 \\
T_\rho & T_p & 0 & 0 & 0 & 0 & 0 & 0 & 0 & 0 & 0 & 0 & 0 & 0 & 0 & 0 & 0 \\
0 & 0 & 0 & 0 & 0 & 0 & 0 & 0 & 0 & 0 & 0 & 0 & 0 & 0 & 0 & 0 \\
0 & 0 & 0 & 0 & 0 & 0 & 0 & 0 & 0 & 0 & 0 & 0 & 0 & 0 & 0 & 0 \\
0 & 0 & 0 & 0 & 0 & 0 & 0 & 0 & 0 & 0 & 0 & 0 & 0 & 0 & 0 & 0
\end{pmatrix}
\tag{B.14}
$$

$$
M_2 = v_2 I + \frac{1}{\rho}
\begin{pmatrix}
0 & 0 & 0 & 0 & 0 & 0 & 0 & 0 & 0 & 0 & \rho^2 & 0 & 0 & 0 & 0 & 0 \\
0 & 0 & 0 & 0 & 0 & 0 & 0 & 0 & 0 & \tilde{\Omega}_{12} & \tilde{\Omega}_{22} + \rho^2 c_0^2 & \tilde{\Omega}_{32} & 0 & \frac{\rho^2 c_h^2}{T_p} & 0 & 0 \\
0 & 0 & 0 & 0 & 0 & 0 & 0 & 0 & 0 & 0 & 0 & 0 & 0 & 0 & 0 & 0 \\
0 & 0 & 0 & 0 & 0 & 0 & 0 & 0 & 0 & 0 & 0 & 0 & 0 & 0 & 0 & 0 \\
0 & 0 & 0 & 0 & 0 & 0 & 0 & 0 & 0 & 0 & 0 & 0 & 0 & 0 & 0 & 0 \\
0 & 0 & 0 & 0 & 0 & 0 & 0 & 0 & 0 & \rho A_{11} & \rho A_{12} & \rho A_{13} & 0 & 0 & 0 & 0 \\
0 & 0 & 0 & 0 & 0 & 0 & 0 & 0 & 0 & \rho A_{21} & \rho A_{22} & \rho A_{23} & 0 & 0 & 0 & 0 \\
0 & 0 & 0 & 0 & 0 & 0 & 0 & 0 & 0 & \rho A_{31} & \rho A_{32} & \rho A_{33} & 0 & 0 & 0 & 0 \\
0 & 0 & 0 & 0 & 0 & 0 & 0 & 0 & 0 & 0 & 0 & 0 & 0 & 0 & 0 & 0 \\
0 & 0 & 0 & 0 & 0 & 0 & 0 & 0 & 0 & 0 & 0 & 0 & 0 & 0 & 0 & 0 \\
0 & 0 & 0 & 0 & 0 & 0 & 0 & 0 & 0 & 0 & 0 & 0 & 0 & 0 & 0 & 0 \\
\tilde{\aleph}_{21} & 1 & \aleph_{11}^{21} & \aleph_{21}^{21} & \aleph_{31}^{21} & \aleph_{12}^{21} & \aleph_{22}^{21} & \aleph_{32}^{21} & \aleph_{13}^{21} & \aleph_{23}^{21} & \aleph_{33}^{21} & 0 & 0 & 0 & 0 & 0 & 0 \\
0 & 0 & 0 & 0 & 0 & 0 & 0 & 0 & 0 & 0 & 0 & 0 & 0 & 0 & 0 & 0 \\
0 & 0 & 0 & 0 & 0 & 0 & 0 & 0 & 0 & 0 & 0 & 0 & 0 & 0 & 0 & 0 \\
\tilde{\aleph}_{22} & 0 & \aleph_{11}^{22} & \aleph_{21}^{22} & \aleph_{31}^{22} & \aleph_{12}^{22} & \aleph_{22}^{22} & \aleph_{32}^{22} & \aleph_{13}^{22} & \aleph_{23}^{22} & \aleph_{33}^{22} & 0 & 0 & 0 & 0 & 0 & 0 \\
0 & 0 & 0 & 0 & 0 & 0 & 0 & 0 & 0 & 0 & 0 & 0 & 0 & 0 & 0 & 0 \\
0 & 0 & 0 & 0 & 0 & 0 & 0 & 0 & 0 & 0 & 0 & 0 & 0 & 0 & 0 & 0 \\
\tilde{\aleph}_{23} & 0 & \aleph_{11}^{23} & \aleph_{21}^{23} & \aleph_{31}^{23} & \aleph_{12}^{23} & \aleph_{22}^{23} & \aleph_{32}^{23} & \aleph_{13}^{23} & \aleph_{23}^{23} & \aleph_{33}^{23} & 0 & 0 & 0 & 0 & 0 & 0 \\
0 & 0 & 0 & 0 & 0 & 0 & 0 & 0 & 0 & 0 & 0 & 0 & 0 & 0 & 0 & 0 \\
0 & 0 & 0 & 0 & 0 & 0 & 0 & 0 & 0 & 0 & 0 & 0 & 0 & 0 & 0 & 0 \\
T_\rho & T_p & 0 & 0 & 0 & 0 & 0 & 0 & 0 & 0 & 0 & 0 & 0 & 0 & 0 & 0 \\
0 & 0 & 0 & 0 & 0 & 0 & 0 & 0 & 0 & 0 & 0 & 0 & 0 & 0 & 0 & 0 \\
0 & 0 & 0 & 0 & 0 & 0 & 0 & 0 & 0 & 0 & 0 & 0 & 0 & 0 & 0 & 0
\end{pmatrix}
\tag{B.15}
$$

$$
M_3 = v_3 I + \frac{1}{\rho}
\begin{pmatrix}
0 & 0 & 0 & 0 & 0 & 0 & 0 & 0 & 0 & 0 & 0 & \rho^2 & 0 & 0 & 0 & 0 \\
0 & 0 & 0 & 0 & 0 & 0 & 0 & 0 & 0 & \tilde{\Omega}_{13} & \tilde{\Omega}_{23} & \tilde{\Omega}_{33} + \rho^2 c_0^2 & 0 & 0 & \frac{\rho^2 c_h^2}{T_p} & 0 \\
0 & 0 & 0 & 0 & 0 & 0 & 0 & 0 & 0 & 0 & 0 & 0 & 0 & 0 & 0 & 0 \\
0 & 0 & 0 & 0 & 0 & 0 & 0 & 0 & 0 & 0 & 0 & 0 & 0 & 0 & 0 & 0 \\
0 & 0 & 0 & 0 & 0 & 0 & 0 & 0 & 0 & 0 & 0 & 0 & 0 & 0 & 0 & 0 \\
0 & 0 & 0 & 0 & 0 & 0 & 0 & 0 & 0 & 0 & 0 & 0 & 0 & 0 & 0 & 0 \\
0 & 0 & 0 & 0 & 0 & 0 & 0 & 0 & 0 & 0 & 0 & 0 & 0 & 0 & 0 & 0 \\
0 & 0 & 0 & 0 & 0 & 0 & 0 & 0 & 0 & \rho A_{11} & \rho A_{12} & \rho A_{13} & 0 & 0 & 0 & 0 \\
0 & 0 & 0 & 0 & 0 & 0 & 0 & 0 & 0 & \rho A_{21} & \rho A_{22} & \rho A_{23} & 0 & 0 & 0 & 0 \\
0 & 0 & 0 & 0 & 0 & 0 & 0 & 0 & 0 & \rho A_{31} & \rho A_{32} & \rho A_{33} & 0 & 0 & 0 & 0 \\
\tilde{\aleph}_{31} & 1 & \aleph_{11}^{31} & \aleph_{21}^{31} & \aleph_{31}^{31} & \aleph_{12}^{31} & \aleph_{22}^{31} & \aleph_{32}^{31} & \aleph_{13}^{31} & \aleph_{23}^{31} & \aleph_{33}^{31} & 0 & 0 & 0 & 0 & 0 \\
\tilde{\aleph}_{32} & 0 & \aleph_{11}^{32} & \aleph_{21}^{32} & \aleph_{31}^{32} & \aleph_{12}^{32} & \aleph_{22}^{32} & \aleph_{32}^{32} & \aleph_{13}^{32} & \aleph_{23}^{32} & \aleph_{33}^{32} & 0 & 0 & 0 & 0 & 0 \\
\tilde{\aleph}_{33} & 0 & \aleph_{11}^{33} & \aleph_{21}^{33} & \aleph_{31}^{33} & \aleph_{12}^{33} & \aleph_{22}^{33} & \aleph_{32}^{33} & \aleph_{13}^{33} & \aleph_{23}^{33} & \aleph_{33}^{33} & 0 & 0 & 0 & 0 & 0 \\
0 & 0 & 0 & 0 & 0 & 0 & 0 & 0 & 0 & 0 & 0 & 0 & 0 & 0 & 0 & 0 \\
0 & 0 & 0 & 0 & 0 & 0 & 0 & 0 & 0 & 0 & 0 & 0 & 0 & 0 & 0 & 0 \\
T_\rho & T_p & 0 & 0 & 0 & 0 & 0 & 0 & 0 & 0 & 0 & 0 & 0 & 0 & 0 & 0 \\
0 & 0 & 0 & 0 & 0 & 0 & 0 & 0 & 0 & 0 & 0 & 0 & 0 & 0 & 0 & 0
\end{pmatrix}
\tag{B.16}
$$

$$
\boldsymbol{P} = \begin{pmatrix} \rho \\ p \\ A_{11} \\ A_{21} \\ A_{31} \\ A_{12} \\ A_{22} \\ A_{32} \\ A_{13} \\ A_{23} \\ A_{33} \\ v_1 \\ v_2 \\ v_3 \\ J_1 \\ J_2 \\ J_3 \end{pmatrix}
$$

$$
\boldsymbol{S_p} = - \begin{pmatrix} 0 \\ -\frac{\tilde{c}_s \|\psi\|_F^2}{E_p} \\ \psi_{11} \\ \psi_{21} \\ \psi_{31} \\ \psi_{12} \\ \psi_{22} \\ \psi_{32} \\ \psi_{13} \\ \psi_{23} \\ \psi_{33} \\ 0 \\ 0 \\ 0 \\ 0 \\ 0 \\ 0 \end{pmatrix} \frac{1}{\theta_1} + \begin{pmatrix} 0 \\ -\frac{\|\boldsymbol{H}\|^2}{E_p} \\ 0 \\ 0 \\ 0 \\ 0 \\ 0 \\ 0 \\ 0 \\ 0 \\ 0 \\ 0 \\ 0 \\ 0 \\ H_1 \\ H_2 \\ H_3 \\ 0 \end{pmatrix} \frac{1}{\theta_2} + \begin{pmatrix} 0 \\ -\frac{E_\Delta}{E_p} \\ 0 \\ 0 \\ 0 \\ 0 \\ 0 \\ 0 \\ 0 \\ 0 \\ 0 \\ 0 \\ 0 \\ 0 \\ 0 \\ 0 \\ 0 \\ K \end{pmatrix}
$$

(B.17)

B.2 Eigenvalues

Considering the primitive system matrix (B.14), it is clear that the eigenvalues of the GPR system in the first spatial axis consist of v_1 repeated 8 times, along with the roots of:

$$\begin{vmatrix} (v_1 - \lambda) I & \Xi_2 \\ \Xi_1 & (v_1 - \lambda) I \end{vmatrix} = 0 \tag{B.18}$$

where

$$\Xi_1 = -\frac{1}{\rho} \begin{pmatrix} \frac{\partial \sigma_{11}}{\partial \rho} & -1 & \frac{\partial \sigma_{11}}{\partial A_{11}} & \frac{\partial \sigma_{11}}{\partial A_{21}} & \frac{\partial \sigma_{11}}{\partial A_{31}} \\ \frac{\partial \sigma_{21}}{\partial \rho} & 0 & \frac{\partial \sigma_{21}}{\partial A_{11}} & \frac{\partial \sigma_{21}}{\partial A_{21}} & \frac{\partial \sigma_{21}}{\partial A_{31}} \\ \frac{\partial \sigma_{31}}{\partial \rho} & 0 & \frac{\partial \sigma_{31}}{\partial A_{11}} & \frac{\partial \sigma_{31}}{\partial A_{21}} & \frac{\partial \sigma_{31}}{\partial A_{31}} \\ -T_\rho & -T_p & 0 & 0 & 0 \end{pmatrix} \tag{B.19}$$

$$\Xi_2 = \begin{pmatrix} \rho & 0 & 0 & 0 \\ \left(\rho c_0^2 + \sigma_{11} - \rho \frac{\partial \sigma_{11}}{\partial \rho}\right) & \left(\sigma_{21} - \rho \frac{\partial \sigma_{21}}{\partial \rho}\right) & \left(\sigma_{31} - \rho \frac{\partial \sigma_{31}}{\partial \rho}\right) & \frac{\rho c_h^2}{T_p} \\ A_{11} & A_{12} & A_{13} & 0 \\ A_{21} & A_{22} & A_{23} & 0 \\ A_{31} & A_{32} & A_{33} & 0 \end{pmatrix} \tag{B.20}$$

By the properties of block matrices[4], the remaining eigenvalues are v_1 and the roots of $\left|(v_1 - \lambda)^2 I - \Xi_1 \Xi_2\right| = 0$. Thus, $\lambda_i = v_1 \pm \sqrt{\tilde{\lambda}_i}$ where the $\tilde{\lambda}_i$ are the eigenvalues of the following matrix:

$$\Xi = \Xi_1 \Xi_2 = \begin{pmatrix} \Omega_{11}^1 + \left(c_0^2 + \frac{\sigma_{11}}{\rho} - \frac{\partial \sigma_{11}}{\partial \rho}\right) & \Omega_{12}^1 + \left(\frac{\sigma_{21}}{\rho} - \frac{\partial \sigma_{21}}{\partial \rho}\right) & \Omega_{13}^1 + \left(\frac{\sigma_{31}}{\rho} - \frac{\partial \sigma_{31}}{\partial \rho}\right) & \frac{c_h^2}{T_p} \\ \Omega_{21}^1 & \Omega_{22}^1 & \Omega_{23}^1 & 0 \\ \Omega_{31}^1 & \Omega_{32}^1 & \Omega_{33}^1 & 0 \\ T_\rho + T_p \left(c_0^2 + \frac{\sigma_{11}}{\rho} - \frac{\partial \sigma_{11}}{\partial \rho}\right) & T_p \left(\frac{\sigma_{21}}{\rho} - \frac{\partial \sigma_{21}}{\partial \rho}\right) & T_p \left(\frac{\sigma_{31}}{\rho} - \frac{\partial \sigma_{31}}{\partial \rho}\right) & c_h^2 \end{pmatrix} \tag{B.21}$$

where Ω is given shortly. Similar results hold for the other two spatial directions. In general it is not possible to express the eigenvalues of Ξ in terms of the eigenvalues of its submatrices. Note, however, that if $c_t = 0$ then one of the eigenvalues is 0 and the remaining eigenvalues can be found analytically, using the form given in the appendix of [35].

[4] If A is invertible, $\det \begin{pmatrix} A & B \\ C & D \end{pmatrix} = \det(A) \det\left(D - CA^{-1}B\right)$

It is straightforward to verify the following:

$$\frac{\partial \sigma_{ij}}{\partial A_{mn}} = -c_s^2 \rho \begin{pmatrix} \delta_{in} \left(A \operatorname{dev}(G)\right)_{mj} + \delta_{jn} \left(A \operatorname{dev}(G)\right)_{mi} \\ + A_{mi} G_{jn} + A_{mj} G_{in} - \frac{2}{3} G_{ij} A_{mn} \end{pmatrix} \tag{B.22}$$

The quantity Ω is named here the *acoustic tensor*, due to its similarity to the acoustic tensor described in [11]:

$$\begin{aligned} \Omega_{ij}^d &= -\frac{1}{\rho} \frac{\partial \sigma_{id}}{\partial A_{kd}} A_{kj} - \frac{\sigma_{id}}{\rho} \delta_{dj} \\ &= c_s^2 \begin{pmatrix} \delta_{id} \left(G \operatorname{dev}(G)\right)_{dj} + \left(G \operatorname{dev}(G)\right)_{id} \delta_{dj} \\ + \left(G \operatorname{dev}(G)\right)_{ij} + G_{ij} G_{dd} + \frac{1}{3} G_{dj} G_{id} \end{pmatrix} \\ &= c_s^2 \left(E^d G \operatorname{dev}(G) + G \operatorname{dev}(G) E^d + G \operatorname{dev}(G) + G_{dd} G + \frac{1}{3} G_d G_d^T \right) \end{aligned} \tag{B.23}$$

where $E_{ij}^d = \delta_{id} \delta_{jd}$.

B.3 Eigenvectors

With Heat Conduction

By hyperbolicity of the system, Ξ can be expressed as:

$$\Xi = Q^{-1} D^2 Q \tag{B.24}$$

where D is a diagonal matrix with positive diagonal entries. The eigenvectors corresponding to $\lambda_i = v_1 \pm \sqrt{\tilde{\lambda}_i}$ take the form $\begin{pmatrix} \hat{u} & 0_6 & \tilde{u} & 0_2 \end{pmatrix}^T$ where $\hat{\boldsymbol{u}} \in \mathbb{R}^5, \tilde{\boldsymbol{u}} \in \mathbb{R}^4$ satisfy:

$$\begin{pmatrix} v_1 I & \Xi_2 \\ \Xi_1 & v_1 I \end{pmatrix} \begin{pmatrix} \hat{\boldsymbol{u}} \\ \tilde{\boldsymbol{u}} \end{pmatrix} = \left(v_1 \pm \sqrt{\tilde{\lambda}_i} \right) \begin{pmatrix} \hat{\boldsymbol{u}} \\ \tilde{\boldsymbol{u}} \end{pmatrix} \tag{B.25}$$

Thus, $\Xi_2 \tilde{\boldsymbol{u}} = \pm \sqrt{\tilde{\lambda}_i} \hat{\boldsymbol{u}}$ and $\Xi_1 \hat{\boldsymbol{u}} = \pm \sqrt{\tilde{\lambda}_i} \tilde{\boldsymbol{u}}$. Combining these results, $\Xi \tilde{\boldsymbol{u}} = \tilde{\lambda}_i \tilde{\boldsymbol{u}}$. Thus, $\tilde{\boldsymbol{u}}$ is a right eigenvector of Ξ and, taking the form $Q^{-1} \boldsymbol{e_i}$ for some $i = 1 \ldots 4$.

The four eigenvectors corresponding to eigenvalues of the form $v_1 + \sqrt{\tilde{\lambda}_i}$ are columns 1-4 of matrix R in (B.26). Those corresponding to eigenvalues of the form $v_1 - \sqrt{\tilde{\lambda}_i}$ are columns 5-8. By inspection (using the system matrix (B.14)), it can be verified that the remaining 9 eigenvectors (corresponding to eigenvalue v_1) are the remaining columns.

Note that the index d appearing in these representations should be taken as $1, 2, 3$ for eigenvectors in directions x, y, z, respectively. $0_{m,n}$ is defined to be the 0-matrix of shape (m, n) and I_n the identity matrix of size n.

$$R = \left\{ \begin{pmatrix} \frac{1}{2}\Xi_2 \left(D^2Q\right)^{-1} & \frac{1}{2}\Xi_2 \left(D^2Q\right)^{-1} \\ 0_{6,4} & 0_{6,4} \\ \frac{1}{2}\left(DQ\right)^{-1} & -\frac{1}{2}\left(DQ\right)^{-1} \\ 0_{2,4} & 0_{2,4} \end{pmatrix}, \begin{pmatrix} -cT_p \\ cT_\rho \\ c\Pi_d^{-1}\boldsymbol{w} \\ 0_{12,1} \end{pmatrix}, \begin{pmatrix} 0_{2,3} & 0_{2,3} \\ -\Pi_1^{-1}\Pi_2 & -\Pi_1^{-1}\Pi_3 \\ I_3 & 0_{3,3} \\ 0_{3,3} & I_3 \\ 0_{6,3} & 0_{6,3} \end{pmatrix}, \begin{pmatrix} 0_{15,2} \\ I_2 \end{pmatrix} \right\} \tag{B.26}$$

where

$$\left(\Pi_k\right)_{ij} = \frac{\partial \sigma_{id}}{\partial A_{jk}} \tag{B.27a}$$

$$\boldsymbol{w} = T_p \frac{\partial \boldsymbol{\sigma_d}}{\partial \rho} + T_\rho \boldsymbol{e_d} \tag{B.27b}$$

$$c = \frac{1}{\boldsymbol{e_d^T}\left(\Pi_d A\right)^{-1}\boldsymbol{w} + \frac{T_p}{\rho}} \tag{B.27c}$$

A similar analysis yields the left eigenvectors as the rows of (B.28).

$$L = \left\{ \begin{pmatrix} Q\Xi_1 & -\frac{1}{\rho}Q_{:,1:3}\Pi_2 & -\frac{1}{\rho}Q_{:,1:3}\Pi_3 & DQ & 0_{4,2} \\ Q\Xi_1 & -\frac{1}{\rho}Q_{:,1:3}\Pi_2 & -\frac{1}{\rho}Q_{:,1:3}\Pi_3 & -DQ & 0_{4,2} \end{pmatrix}, \begin{pmatrix} -\frac{1}{\rho} & 0 & \boldsymbol{e_d^T}A^{-1} & \boldsymbol{e_d^T}A^{-1}\Pi_1^{-1}\Pi_2 & \boldsymbol{e_d^T}A^{-1}\Pi_1^{-1}\Pi_3 & 0_{1,6} \end{pmatrix}, \begin{pmatrix} 0_{3,5} & I_3 & 0_{3,3} & 0_{3,6} \\ 0_{3,5} & 0_{3,3} & I_3 & 0_{3,6} \end{pmatrix}, \begin{pmatrix} 0_{2,15} & I_2 \end{pmatrix} \right\} \tag{B.28}$$

Without Heat Conduction

If the system does not include the heat conduction terms, the eigenstructure of the system matrix changes. Ξ_1, Ξ_2, Ξ now take the following values:

$$\Xi_1 = -\frac{1}{\rho}\begin{pmatrix} \frac{\partial \sigma_{11}}{\partial \rho} & -1 & \frac{\partial \sigma_{11}}{\partial A_{11}} & \frac{\partial \sigma_{11}}{\partial A_{21}} & \frac{\partial \sigma_{11}}{\partial A_{31}} \\ \frac{\partial \sigma_{21}}{\partial \rho} & 0 & \frac{\partial \sigma_{21}}{\partial A_{11}} & \frac{\partial \sigma_{21}}{\partial A_{21}} & \frac{\partial \sigma_{21}}{\partial A_{31}} \\ \frac{\partial \sigma_{31}}{\partial \rho} & 0 & \frac{\partial \sigma_{31}}{\partial A_{11}} & \frac{\partial \sigma_{31}}{\partial A_{21}} & \frac{\partial \sigma_{31}}{\partial A_{31}} \end{pmatrix} \tag{B.29}$$

$$\Xi_2 = \begin{pmatrix} \rho & 0 & 0 \\ \left(\rho c_0^2 + \sigma_{11} - \rho \frac{\partial \sigma_{11}}{\partial \rho}\right) & \left(\sigma_{21} - \rho \frac{\partial \sigma_{21}}{\partial \rho}\right) & \left(\sigma_{31} - \rho \frac{\partial \sigma_{31}}{\partial \rho}\right) \\ A_{11} & A_{12} & A_{13} \\ A_{21} & A_{22} & A_{23} \\ A_{31} & A_{32} & A_{33} \end{pmatrix} \tag{B.30}$$

$$\Xi = \Xi_1 \Xi_2 = \begin{pmatrix} \Omega_{11}^1 + \left(c_0^2 + \frac{\sigma_{11}}{\rho} - \frac{\partial \sigma_{11}}{\partial \rho}\right) & \Omega_{12}^1 + \left(\frac{\sigma_{21}}{\rho} - \frac{\partial \sigma_{21}}{\partial \rho}\right) & \Omega_{13}^1 + \left(\frac{\sigma_{31}}{\rho} - \frac{\partial \sigma_{31}}{\partial \rho}\right) \\ \Omega_{21}^1 & \Omega_{22}^1 & \Omega_{23}^1 \\ \Omega_{31}^1 & \Omega_{32}^1 & \Omega_{33}^1 \end{pmatrix} \tag{B.31}$$

Using the eigendecomposition $\Xi = Q^{-1} D^2 Q$ as before, we have:

$$R = \left\{ \begin{pmatrix} \frac{1}{2}\Xi_2 \left(D^2 Q\right)^{-1} & \frac{1}{2}\Xi_2 \left(D^2 Q\right)^{-1} \\ 0_{6,3} & 0_{6,3} \\ \frac{1}{2}\left(DQ\right)^{-1} & -\frac{1}{2}\left(DQ\right)^{-1} \end{pmatrix}, \begin{pmatrix} 1 & 0 \\ 0 & 1 \\ -\Pi_1^{-1} \frac{\partial \boldsymbol{\sigma_1}}{\partial \rho} & \Pi_1^{-1} \boldsymbol{e_1} \\ \mathbf{0_9} & \mathbf{0_9} \end{pmatrix}, \begin{pmatrix} 0_{2,3} & 0_{2,3} \\ -\Pi_1^{-1}\Pi_2 & -\Pi_1^{-1}\Pi_3 \\ I_3 & 0_{3,3} \\ 0_{3,3} & I_3 \\ 0_{3,3} & 0_{3,3} \end{pmatrix} \right\} \tag{B.32}$$

By considering their products with the first 8 columns of R, two of the left eigenvectors corresponding the the 7th and 8th right eigenvectors must come in the form of the rows of the following matrix:

$$\begin{pmatrix} W & X & Y & Z \end{pmatrix} \tag{B.33}$$

where $W \in \mathbb{R}^{2,5}$ and $X, Y, Z \in \mathbb{R}^{2,3}$, and:

$$W\Xi_2 \left(D^2 Q\right)^{-1} + Z\,(DQ)^{-1} = 0 \tag{B.34a}$$

$$W\Xi_2 \left(D^2 Q\right)^{-1} - Z\,(DQ)^{-1} = 0 \tag{B.34b}$$

$$W \begin{pmatrix} 0_{2,3} \\ -\Pi_1^{-1}\Pi_2 \end{pmatrix} + X = 0 \tag{B.34c}$$

$$W \begin{pmatrix} 0_{2,3} \\ -\Pi_1^{-1}\Pi_3 \end{pmatrix} + Y = 0 \tag{B.34d}$$

Solving this system for X, Y, Z:

$$Z = 0 \tag{B.35a}$$

$$X = W_{:,3:5}\Pi_1^{-1}\Pi_2 \tag{B.35b}$$

$$Y = W_{:,3:5}\Pi_1^{-1}\Pi_3 \tag{B.35c}$$

Define:

$$\begin{aligned} \aleph &\equiv \begin{pmatrix} (\Xi_2)_{11} & (\Xi_2)_{12} & (\Xi_2)_{13} & 1 & 0 \\ (\Xi_2)_{21} & (\Xi_2)_{22} & (\Xi_2)_{23} & 0 & 1 \\ (\Xi_2)_{31} & (\Xi_2)_{32} & (\Xi_2)_{33} & C_{11} & C_{12} \\ (\Xi_2)_{41} & (\Xi_2)_{42} & (\Xi_2)_{43} & C_{21} & C_{22} \\ (\Xi_2)_{51} & (\Xi_2)_{52} & (\Xi_2)_{53} & C_{31} & C_{32} \end{pmatrix} \\ &= \begin{pmatrix} B_{11} & B_{12} & B_{13} & 1 & 0 \\ B_{21} & B_{22} & B_{23} & 0 & 1 \\ A_{11} & A_{12} & A_{13} & C_{11} & C_{12} \\ A_{21} & A_{22} & A_{23} & C_{21} & C_{22} \\ A_{31} & A_{32} & A_{33} & C_{31} & C_{32} \end{pmatrix} \end{aligned} \tag{B.36}$$

where

$$B = \begin{pmatrix} \rho & 0 & 0 \\ \left(\rho c_0^2 + \sigma_{11} - \rho\frac{\partial \sigma_{11}}{\partial \rho}\right) & \left(\sigma_{21} - \rho\frac{\partial \sigma_{21}}{\partial \rho}\right) & \left(\sigma_{31} - \rho\frac{\partial \sigma_{31}}{\partial \rho}\right) \end{pmatrix} \tag{B.37a}$$

$$C = \Pi_1^{-1}\left(-\frac{\partial \boldsymbol{\sigma_1}}{\partial \rho}\ \boldsymbol{e_1}\right) \tag{B.37b}$$

By the properties of block matrices:

$$\aleph^{-1} = \begin{pmatrix} -A^{-1}C\left(I - BA^{-1}C\right)^{-1} & A^{-1}\left(I + C\left(I - BA^{-1}C\right)^{-1}BA^{-1}\right) \\ \left(I - BA^{-1}C\right)^{-1} & -\left(I - BA^{-1}C\right)^{-1}BA^{-1} \end{pmatrix} \tag{B.38}$$

By the orthonormality of eigenvectors, we must have:

$$W\aleph = \begin{pmatrix} 0 & 0 & 0 & 1 & 0 \\ 0 & 0 & 0 & 0 & 1 \end{pmatrix} \tag{B.39}$$

Thus, it is straightforward to confirm that:

$$W = \begin{pmatrix} \left(I - BA^{-1}C\right)^{-1} & -\left(I - BA^{-1}C\right)^{-1}BA^{-1} \end{pmatrix} \tag{B.40}$$

Thus, we have:

$$W = \left(I - BA^{-1}C\right)^{-1}\begin{pmatrix} I_2 & -BA^{-1} \end{pmatrix} \tag{B.41a}$$

$$X = -\left(I - BA^{-1}C\right)^{-1}BA^{-1}\Pi_1^{-1}\Pi_2 \tag{B.41b}$$

$$Y = -\left(I - BA^{-1}C\right)^{-1}BA^{-1}\Pi_1^{-1}\Pi_3 \tag{B.41c}$$

Finally, combining the preceding results with (B.33), we have:

$$L = \left\{ \begin{array}{c} \begin{pmatrix} Q\Xi_1 & -\frac{1}{\rho}Q\Pi_2 & -\frac{1}{\rho}Q\Pi_3 & DQ \\ Q\Xi_1 & -\frac{1}{\rho}Q\Pi_2 & -\frac{1}{\rho}Q\Pi_3 & -DQ \end{pmatrix} \\ \left(I_2 - BA^{-1}C\right)^{-1}\begin{pmatrix} I_2 & -BA^{-1} & -BA^{-1}\Pi_1^{-1}\Pi_2 & -BA^{-1}\Pi_1^{-1}\Pi_3 & 0_{2,3} \end{pmatrix} \\ \begin{pmatrix} 0_{3,5} & I_3 & 0_{3,3} & 0_{3,3} \\ 0_{3,5} & 0_{3,3} & I_3 & 0_{3,3} \end{pmatrix} \end{array} \right\} \tag{B.42}$$

Appendix C

Model Parameters

The parameters for different materials under different equations of state are given in the tables below. All variables are given in SI units.

C.1 Material Properties

Material	ρ_0	p_0	T_0	c_v	c_s	μ	c_t	κ	P_r
Air	1.18	10100		721	1	1.85×10^{-5}	1		0.714
Helium	0.163	10100		3127	1	1.99×10^{-5}	1		0.688
Water	1000	10000		950	10^{-4}	10^{-3}	10^{-4}		7
PBX	1840	10000		-	10^{-4}	10^{-5}	-		-
Aluminium	2710	0	300	900	3160	-			-
Copper	8930	0	300	390	2141	-			-
Steel	7860	0	298	134	2888	-			-
C4	1590								

Table C.1: Reference parameters for various materials

C.2 Equation of State Parameters

	Ideal/Stiffened Gas		Shock Mie-Gruneisen			Godunov-Romenski			
	γ	p_∞	c_0	Γ_0	s	c_0	α	β	γ
Air	1.4	-				-	-	-	-
Helium	1.66	-				-	-	-	-
Water	4.4	6×10^8				-	-	-	-
PBX	2.85	-				-	-	-	-
Aluminium	-	-				5037	1	3.577	2.088
Copper	-	-	3939	2	1.5	3939	1	3	2
Steel	-	-	4030	1.43	1.24				
C4	-	-							

Table C.2: Parameters for the Ideal-/Stiffened-Gas, Shock Mie-Gruneisen, and Godunov-Romenski equations of state

Material	τ_1	σ_Y	n
Copper	0.1	9×10^8	10
Aluminium	1	4×10^8	20

Table C.3: Plasticity parameters for various materials